JNRS

JOURNAL OF NEW RESULTS IN SCIENCE

http://dergipark.gov.tr/jnrs

ISSN: 1304 - 7981

VOLUME : 14
NUMBER : 2
YEAR : 2025

jnrs@gop.edu.tr

Journal of New Results in Science (abbreviated as J. New Results Sci. or JNRS) is an international, peer-reviewed, and open-access journal.

J. New Results Sci. is a science journal focusing on new theories and their applications.

JNRS was founded in 2011, and its first issue was published on 01 January 2012.

Language: As of 2023, JNRS accepts contributions in **American English** only.

Frequency: 3 Issues Per Year.

Publication Dates: April, August, and December

ISSN: 1304-7981

Editor-in-Chief: Ali Yakar

Email: togu.jnrs@gmail.com

Publisher: Tokat Gaziosmanpaşa University

APC: JNRS incurs no article processing charges.

Review Process: Single-Blind Peer Review.

DOI Numbers: The published papers are assigned DOI numbers.

Journal Boards

Editor-in-Chief

Section Editors

CONTENT

Journal of New Results in Science
dergipark.org.tr/en/pub/jnrs
Open Access

ISSN: 1304-7981 14 (2) (2025) 73-81 doi.org/10.54187/jnrs.1611847

On the Structure of Hybrid Subalgebras in Bd-Algebras

Damla Yılmaz[1]

Article Info
Received: 14 Mar 2025
Accepted: 23 Jul 2025
Published: 31 Aug 2025
Research Article

Abstract − By combining the properties of fuzzy and soft set theories, hybrid structures provide a more flexible framework for handling uncertainty. In this work, we define hybrid subalgebras of Bd-algebras and investigate related properties. We examine the properties of some special sets with hybrid structures. More precisely, we investigate situations where we can describe these sets as Bd-subalgebras. We show that the hybrid intersections of hybrid Bd-subalgebras are also hybrid Bd-subalgebras, but we give an example that hybrid union of hybrid Bd-subalgebras may not be a hybrid Bd-subalgebra. Furthermore, we prove that every homomorphic preimage of a hybrid Bd-algebra is a hybrid Bd-subalgebra.

Keywords − *Hybrid subalgebra, d-algebra, Bd-algebra, Bd-ideal, hybrid intersection*

1. Introduction

Fuzzy set theory, which deals with uncertainty of situations and preferences, was introduced by Zadeh [1]. Subsequently, this theory became an active research area in many fields such as artificial intelligence, control engineering, computer science, and robotics. The concept of soft sets was introduced by Molodtsov as a new mathematical tool for dealing with uncertainties [2]. Jun et al. introduced the concept of hybrid structure by combining fuzzy sets and soft sets in the initial universe [3]. Ideal theory of BCK/BCI-algebras based on hybrid structures and the notions of hybrid ideals and hybrid closed ideals in BCK/BCI-algebras were introduced and related properties were investigated in [4].

Imai and Iseki initiated theory of BCK/BCI algebras as a generalization of the concepts of set theoretical differences and propositional calculus [5-6]. In this rapidly developing theory, more focus was placed on the ideal theory of BCK/BCI algebras.

One of the generalizations of BCK-algebras, d-algebras, was presented by Neggers and Kim [7]. The notions of d-subalgebra, d-ideal, and some related concepts were defined, and relations among them were investigated by Neggers et al. [8]. Shortly after, Neggers and Sik gave properties of B-algebras [9], Kim and Park showed that 0-commutative B-algebras are semisimple BCI-algebras [10]. Bd-algebras were introduced by Bantaojai et al. in 2022 [11]. Studies in which hybrid structures have been applied to many algebraic structures have been studied in recent years. As examples of these studies, we reference the studies of hybrid k-ideals of semirings [12], hybrid ordered ideals of ordered semirings [13], hybrid ideals of near rings [14], regularity of semigroups with the help of hybrid ideals [15], hybrid nil radical of a ring [16], hybrid bi-ideals in near-subtraction semigroups [17], hybrid ideals of BCK/BCI-algebras [18].

[1]damla.yilmaz@erzurum.edu.tr
[1]Department of Mathematics, Faculty of Science, Erzurum Technical University, Erzurum, Türkiye

In this work, we introduce a new notion called hybrid structures of Bd-algebras and examine some of its basic properties and some special cases for Bd-subalgebras. The rest of the paper is organized as follows: Section 2 provides the basic definitions that will be used in the article about Bd-algebras and hybrid structures. Section 3 presents properties and examples obtained when hybrid structures are applied to subalgebras of Bd-algebras. Section 4 discusses the possibility of working on generalizations of this type of algebra where hybrid structures are applied.

2. Preliminaries

The basic structures used in the creation of this article are listed in this section. We reference sources [3, 7, 9, 11] for the information used in these requirements.

Definition 2.1. If an algebra $A = (A;* ,0)$ of type $(2,0)$ satisfies:

i. $(\forall b \in A)\ (b * b = 0)$

ii. $(\forall b \in A)\ (b * 0 = b)$

iii. $(\forall b, c, d \in A)\ \big((b * c) * d = b * \big(d * (0 * c)\big)\big)$

then, we call A a B-algebra.

Definition 2.2. A d-algebra is an algebra $A = (A;* ,0)$ of type $(2,0)$ satisfying the following conditions:

i. $(\forall b \in A)\ (b * b = 0)$

ii. $(\forall b \in A)\ (b * 0 = b)$

iii. $(\forall b, c \in A)\ (b * c = 0, c * b = 0 \Rightarrow b = c)$

In 2022, Bantaojai et al. created a combination of B-algebras and d-algebras and presented Bd-algebras.

Definition 2.3. A Bd-algebra is an algebra $A = (A;* ,0)$ of type $(2,0)$ satisfying the following conditions:

i. $(\forall a \in A)\ (a * 0 = a)$

ii. $(\forall a, b \in A)\ (a * b = 0, b * a = 0 \Rightarrow a = b)$

Note that every $BCI/BH/BZ$-algebra is a Bd-algebra. It has been shown that the inverse is not true.

Definition 2.4. A non-empty subset S of a Bd-algebra A is called a Bd-subalgebra of A if

i. $0 \in S$

ii. $(\forall a, b \in S)\ (a * b \in S)$

Definition 2.5. A subset K of a Bd-algebra A is called a Bd-ideal of A if it satisfies:

i. $0 \in K$

ii. $(\forall a, b \in K)\ (a * b, b \in K \Rightarrow a \in K)$

iii. $(\forall a \in K, b \in A)\ (a * b \in K)$

We know that $\{0\}$ is a Bd-subalgebra, but it is not a Bd-ideal.

Definition 2.6. Let $A = (A;*, 0_A)$ and $B = (B;., 0_B)$ be Bd-algebras. A function $\eta: A \to B$ defined by

i. $\eta(0_A) = 0_B$

ii. $(\forall a_1, a_2 \in A)\ \big(\eta(a_1 * a_2) = \eta(a_1).\eta(a_2)\big)$

is a homomorphism between Bd-algebras.

In this paper, the power set of an initial universe set E, a set of parameters, and the unit interval are denoted by $P(E), B$ and I, respectively.

Hybrid structure in B over E defined by the following map:

$$\Phi_{\lambda}^{\sim} \coloneqq (\Phi^{\sim}, \lambda): B \to P(E) \times I, \quad b \mapsto (\Phi^{\sim}(b), \lambda(b))$$

where $\Phi^{\sim}: B \to P(E)$ and $\lambda: B \to I$ are mappings.

The set of all hybrid structures in B over E is denoted by the symbol $H(B)$. In $H(B)$, we define an order "$\leq$" as follows:

$$\left(\forall \Phi_{\lambda}^{\sim}, \Psi_{\gamma}^{\sim} \in H(B)\right)\left(\Phi_{\lambda}^{\sim} \leq \Psi_{\gamma}^{\sim} \Leftrightarrow \Phi^{\sim} \Subset \Psi^{\sim}, \lambda \gtrsim \gamma\right)$$

where $\Phi^{\sim} \Subset \Psi^{\sim}$, $\lambda \gtrsim \gamma$ mean $\Phi^{\sim}(b) \subseteq \Psi^{\sim}(b)$, $\lambda(b) \geq \gamma(b)$ for all $b \in B$, respectively. Hence, $(H(B), \leq)$ is a poset.

Let $\Phi_{\lambda}^{\sim}$ and $\Psi_{\gamma}^{\sim}$ be hybrid structures in B over E. Hence, the hybrid intersection of $\Phi_{\lambda}^{\sim}$ and $\Psi_{\gamma}^{\sim}$ is defined to be a hybrid structure

$$\Phi_{\lambda}^{\sim} \Cap \Psi_{\gamma}^{\sim}: B \to P(E) \times I, \quad b \mapsto ((\Phi^{\sim} \cap^{\sim} \Psi^{\sim})(b), (\lambda \vee \gamma)(b))$$

for all $b \in B$, where

$$\Phi^{\sim} \cap^{\sim} \Psi^{\sim}: B \to P(E), \ b \mapsto \Phi^{\sim}(b) \cap \Psi^{\sim}(b)$$

$$\lambda \vee \gamma: B \to I, \ b \mapsto \vee\{\lambda(b), \gamma(b)\}$$

Let $\Phi_{\lambda}^{\sim}$ and $\Psi_{\gamma}^{\sim}$ be hybrid structures in B over E. Hence, the hybrid union of $\Phi_{\lambda}^{\sim}$ and $\Psi_{\gamma}^{\sim}$ is defined to be a hybrid structure

$$\Phi_{\lambda}^{\sim} \Cup \Psi_{\gamma}^{\sim}: B \to P(E) \times I, \quad b \mapsto ((\Phi^{\sim} \cup^{\sim} \Psi^{\sim})(b), (\lambda \wedge \gamma)(b))$$

for all $b \in B$, where

$$\Phi^{\sim} \cup^{\sim} \Psi^{\sim}: B \to P(E), \ b \mapsto \Phi^{\sim}(b) \cup \Psi^{\sim}(b)$$

$$\lambda \wedge \gamma: B \to I, \ b \mapsto \wedge\{\lambda(b), \gamma(b)\}$$

3. Hybrid Structures Applied to Subalgebras in Bd-Algebras

In this section, we apply hybrid structures to subalgebras of Bd-algebras. We explore the key properties they provide and give examples.

Definition 3.1. Assume that B is a Bd-algebra and $\Phi_{\lambda}^{\sim}$ is a hybrid structure in B over E. Thus, $\Phi_{\lambda}^{\sim}$ is called hybrid Bd-subalgebra of B over E if it satisfies

i. $(\forall b \in B)\left(\Phi^{\sim}(b) \subseteq \Phi^{\sim}(0), \lambda(b) \geq \lambda(0)\right)$

ii. $(\forall b, c \in B)(\Phi^{\sim}(b * c) \supseteq \Phi^{\sim}(b) \cap \Phi^{\sim}(c), \lambda(b * c) \leq \vee\{\lambda(b), \lambda(c)\})$

Example 3.2. Let $B = \{0, b_1, b_2, b_3\}$ be a set of parameters and $E = \{e_1, e_2, e_3, e_4\}$ be the initial universe set given by the following Cayley table:

Table 1. Cayley table of the binary operation "$*$"

$*$	**0**	$\mathbf{b_1}$	$\mathbf{b_2}$	$\mathbf{b_3}$
0	0	b_1	b_1	b_1
$\mathbf{b_1}$	b_1	b_1	b_1	b_1
$\mathbf{b_2}$	b_2	b_2	b_2	b_2
$\mathbf{b_3}$	b_3	b_1	b_1	b_1

Then, $(B;*,0)$ is a Bd-algebra. Let $\Phi_\lambda^{\sim}$ be hybrid structure in B over E which is given by the following table:

Table 2. The hybrid structure $\Phi_\lambda^{\sim}$

B	**Φ**	**λ**
0	E	0,3
$\mathbf{b_1}$	$\{e_1, e_2, e_4\}$	0,6
$\mathbf{b_2}$	$\{e_1\}$	0,9
$\mathbf{b_3}$	$\{e_1, e_4\}$	0,8

It is routine to verify that $\Phi_\lambda^{\sim}$ is a Bd-subagebra of B over E.

Proposition 3.3. Let B be a Bd-algebra and $\Phi_\lambda^{\sim}$ be a hybrid Bd-subalgebra in B over E. Then, the following assertions are equivalent:

i. $(\forall b_1, b_2 \in B)\big(\Phi^{\sim}(b_1 * b_2) \supseteq \Phi^{\sim}(b_2),\ \lambda(b_1 * b_2) \leq \lambda(b_2)\big)$

ii. $(\forall b_1 \in B)\big(\Phi^{\sim}(0) = \Phi^{\sim}(b_1),\ \lambda(0) = \lambda(b_1)\big)$

Proof. If we write $b_2 = 0$ in *(i)*, then we get $\Phi^{\sim}(0) \subseteq \Phi^{\sim}(b_1 * 0) = \Phi^{\sim}(b_1)$ and $\lambda(b_1 * 0) = \lambda(b_1) \leq \lambda(0)$ for all $b_1 \in B$. Combining this and definition of hybrid Bd-subalgebra, we get $\Phi^{\sim}(0) = \Phi^{\sim}(b_1)$ and $\lambda(0) = \lambda(b_1)$, for all $b_1 \in B$.

Suppose that *(ii)* is valid. Then

$$\Phi^{\sim}(b_2) = \Phi^{\sim}(0) \cap \Phi^{\sim}(b_2) = \Phi^{\sim}(b_1) \cap \Phi^{\sim}(b_2) \subseteq \Phi^{\sim}(b_1 * b_2)$$

and

$$\lambda(b_2) = \vee\{\lambda(0), \lambda(b_2)\} = \vee\{\lambda(b_1), \lambda(b_2)\} \geq \lambda(b_1 * b_2)$$

for all $b_1 \in B$.

Proposition 3.4. Let B be a Bd-algebra. Then every hybrid Bd-subalgebra $\Phi_\lambda^{\sim}$ in B over E satisfies the following assertion:

$$(\forall b_1, b_2 \in B)\big(\Phi^{\sim}\big(b_1 * (0 * b_2)\big) \supseteq \Phi^{\sim}(b_1) \cap \Phi^{\sim}(b_2),\ \lambda\big(b_1 * (0 * b_2)\big) \leq \vee\{\lambda(b_1), \lambda(b_2)\}\big).$$

Proof. By the definition of hybrid Bd-subalgebra, we get

$$\Phi^{\sim}\big(b_1 * (0 * b_2)\big) \supseteq \Phi^{\sim}(b_1) \cap \Phi^{\sim}(0 * b_2) \supseteq \Phi^{\sim}(b_1) \cap \Phi^{\sim}(0) \cap \Phi^{\sim}(b_2) = \Phi^{\sim}(b_1) \cap \Phi^{\sim}(b_2)$$

and

$$\lambda\big(b_1 * (0 * b_2)\big) \leq \vee\{\lambda(b_1), \lambda(0 * b_2)\} \leq \vee\big\{\lambda(b_1), \vee\{\lambda(0), \lambda(b_2)\}\big\} = \vee\{\lambda(b_1), \lambda(b_2)\}$$

for all $b_1, b_2 \in B$.

Definition 3.5. For a hybrid structure $\Phi_\lambda^{\sim}$ in B over E, we define two sets:

$\Phi_\lambda^{\sim}(\alpha) = \{b \in B | \alpha \subseteq \Phi^{\sim}(b)\}$ and $\Phi_\lambda^{\sim}(t) = \{b \in B | \lambda(b) \leq t\}$, where $\alpha \in P(E)$ and $t \in I$.

Theorem 3.6. Let B be a Bd-algebra and $\Phi_\lambda^{\sim}$be a hybrid structure in B over E. Thus, the following assertions are equivalent:

i. $\Phi_\lambda^{\sim}$ is a hybrid Bd-subalgebra of B over E.

ii. For any $\alpha \in P(E)$ and $t \in I$, $\Phi_\lambda^{\sim}(\alpha)$ and $\Phi_\lambda^{\sim}(t)$ are Bd-subalgebra of B whenever they are non-empty sets.

Proof. Assume that condition (i) of the theorem is satisfied. Let $\alpha \in P(E)$ and $t \in I$ be such that $\Phi_\lambda^{\sim}(\alpha) \neq \emptyset$ and $\Phi_\lambda^{\sim}(t) \neq \emptyset$. Let $b \in \Phi_\lambda^{\sim}(\alpha) \cap \Phi_\lambda^{\sim}(t)$. Then $\Phi^{\sim}(b) \supseteq \alpha, \lambda(b) \leq t$. It follows from the definition of hybrid Bd-subalgebra that $\Phi^{\sim}(0) \supseteq \Phi^{\sim}(b) \supseteq \alpha$ and $\lambda(0) \leq \lambda(b) \leq t$. Thus, $0 \in \Phi_\lambda^{\sim}(\alpha) \cap \Phi_\lambda^{\sim}(t)$.

If $b, c \in \Phi_\lambda^{\sim}(\alpha) \cap \Phi_\lambda^{\sim}(t)$, then we have $\Phi^{\sim}(b) \supseteq \alpha, \lambda(b) \leq t$ and $\Phi^{\sim}(c) \supseteq \alpha, \lambda(c) \leq t$. Using Definition 3.1.*ii*, we have

$$\Phi^{\sim}(b * c) \supseteq \Phi^{\sim}(b) \cap \Phi^{\sim}(c) \supseteq \alpha$$

and

$$\lambda(b * c) \leq \vee\{\lambda(b), \lambda(c)\} \leq t.$$

Thus, $b * c \in \Phi_\lambda^{\sim}(\alpha) \cap \Phi_\lambda^{\sim}(t)$ and so the required results are obtained.

Conversely, suppose that (*ii*) is valid. Let $b, c \in B$ be such that $\Phi^{\sim}(b) = \alpha_b$ and $\Phi^{\sim}(c) = \alpha_c$. If we take $\alpha = \alpha_b \cap \alpha_c$, then $b, c \in \Phi_\lambda^{\sim}(\alpha)$ and so $b * c \in \Phi_\lambda^{\sim}(\alpha)$. Thus, we get $\Phi^{\sim}(b * c) \supseteq \alpha = \alpha_b \cap \alpha_c = \Phi^{\sim}(b) \cap \Phi^{\sim}(c)$. Let $t \coloneqq \vee\{\lambda(b), \lambda(c)\}$ for any $b, c \in B$. Thus, we get $b, c \in \Phi_\lambda^{\sim}(t)$. It implies that $b * c \in \Phi_\lambda^{\sim}(t)$ and so $\lambda(b * c) \leq t = \vee\{\lambda(b), \lambda(c)\}$. Therefore, $\Phi_\lambda^{\sim}$ is a hybrid Bd-subalgebra of B over E. □

Theorem 3.7. Let B be a Bd-algebra. If $\Phi_\lambda^{\sim}$ and $\Psi_\gamma^{\sim}$ are hybrid Bd-subalgebras of B over E, then the hybrid intersection $\Phi_\lambda^{\sim} \Cap \Psi_\gamma^{\sim}$ is a hybrid Bd-subalgebra of B over E.

Proof. For any $b_1 \in B$,

$$(\Phi^{\sim} \cap^{\sim} \Psi^{\sim})(b_1) = \Phi^{\sim}(b_1) \cap \Psi^{\sim}(b_1) \subseteq \Phi^{\sim}(0) \cap \Psi^{\sim}(0) = (\Phi^{\sim} \cap^{\sim} \Psi^{\sim})(0)$$

and

$$(\lambda \vee \gamma)(b_1) = \vee\{\lambda(b_1), \gamma(b_1)\} \geq \vee\{\lambda(0), \gamma(0)\} = (\lambda \vee \gamma)(0)\ .$$

Let $b_1, b_2 \in B$. Then

$$\begin{aligned}(\Phi^{\sim} \cap^{\sim} \Psi^{\sim})(b_1 * b_2) &= \Phi^{\sim}(b_1 * b_2) \cap \Psi^{\sim}(b_1 * b_2)\\ &\supseteq \big(\Phi^{\sim}(b_1) \cap \Phi^{\sim}(b_2)\big) \cap \big(\Psi^{\sim}(b_1) \cap \Psi^{\sim}(b_2)\big)\\ &= \big(\Phi^{\sim}(b_1) \cap \Psi^{\sim}(b_1)\big) \cap \big(\Phi^{\sim}(b_2) \cap \Psi^{\sim}(b_2)\big)\\ &= (\Phi^{\sim} \cap^{\sim} \Psi^{\sim})(b_1) \cap (\Phi^{\sim} \cap^{\sim} \Psi^{\sim})(b_2)\end{aligned}$$

and

$$\begin{aligned}(\lambda \vee \gamma)(b_1 * b_2) &= \vee\{\lambda(b_1 * b_2), \gamma(b_1 * b_2)\}\\ &\leq \vee\big\{\vee\{\lambda(b_1), \lambda(b_2)\}, \vee\{\gamma(b_1), \gamma(b_2)\}\big\}\\ &= \vee\big\{\vee\{\lambda(b_1), \gamma(b_1)\}, \vee\{\lambda(b_2), \gamma(b_2)\}\big\}\\ &= \vee\{(\lambda \vee \gamma)(b_1), (\lambda \vee \gamma)(b_2)\}\end{aligned}$$

Therefore, $\Phi_\lambda^{\sim} \Cap \Psi_\gamma^{\sim}$ is a hybrid Bd-subalgebra of B over E.

The following example shows that the hybrid union of hybrid Bd-subalgebras may not be a hybrid Bd-subalgebra.

Example 3.8. Let $B = \{0, b_1, b_2, b_3\}$ be a set of parameters and $E = \{e_1, e_2, e_3, e_4, e_5\}$ be the initial universe set given by the following Cayley table:

Table 3. Cayley table of the binary operation "$*$"

$*$	**0**	$\boldsymbol{b_1}$	$\mathbf{b_2}$	$\mathbf{b_3}$
0	0	0	b_3	0
$\mathbf{b_1}$	b_1	0	b_2	b_3
$\mathbf{b_2}$	b_2	b_2	b_2	b_3
$\mathbf{b_3}$	b_3	b_2	b_2	b_3

Then, $(B;*,0)$ is a Bd-algebra. Let $\Phi_\lambda^\sim$ and $\Psi_\gamma^\sim$ be hybrid structures in B over E which are given by following tables, respectively.

Table 4. The hybrid structure $\Phi_\lambda^\sim$

B	$\boldsymbol{\Phi}^\sim$	$\boldsymbol{\lambda}$
0	E	0,1
$\mathbf{b_1}$	$\{e_1\}$	0,6
$\mathbf{b_2}$	$\{e_1, e_2\}$	0,4
$\mathbf{b_3}$	$\{e_1, e_2, e_3, e_4\}$	0,3

Table 5. The hybrid structure $\Psi_\gamma^\sim$

B	$\boldsymbol{\Psi}^\sim$	$\boldsymbol{\gamma}$
0	E	0,3
$\mathbf{b_1}$	$\{e_1, e_2, e_4\}$	0,5
$\mathbf{b_2}$	$\{e_1, e_2\}$	0,8
$\mathbf{b_3}$	$\{e_1, e_2\}$	0,8

Then, the hybrid union $\Phi_\lambda^\sim \Cup \Psi_\gamma^\sim$ is represented by following table:

Table 6. The hybrid structure $\Phi_\lambda^\sim \Cup \Psi_\gamma^\sim$

B	$\boldsymbol{\Phi}_\lambda^\sim \cup^\sim \boldsymbol{\Psi}_\gamma^\sim$	$\boldsymbol{\lambda \wedge \gamma}$
0	E	0,1
$\mathbf{b_1}$	$\{e_1, e_2, e_4\}$	0,5
$\mathbf{b_2}$	$\{e_1, e_2\}$	0,4
$\mathbf{b_3}$	$\{e_1, e_2, e_3, e_4\}$	0,3

By routine verifications, we see that $\Phi_\lambda^\sim$ and $\Psi_\gamma^\sim$ are hybrid Bd-subalgebras in B over E. But the hybrid union $\Phi_\lambda^\sim \Cup \Psi_\gamma^\sim$ is not a hybrid Bd- subalgebra in B over E since

$$(\Phi^\sim \cup^\sim \Psi^\sim)(b_3 * b_1) = (\Phi^\sim \cup^\sim \Psi^\sim)(b_2) = \{e_1, e_2\}$$
$$\not\supseteq \{e_1, e_2, e_4\} = (\Phi^\sim \cup^\sim \Psi^\sim)(b_3) \cap (\Phi^\sim \cup^\sim \Psi^\sim)(b_1).$$

Let $\Phi_\lambda^\sim$ be a hybrid structure in B over E and $\Phi_\lambda^{\sim *} := (\Phi^{\sim *}, \lambda^*)$ a hybrid structure in B over E defined by:

$$\Phi^{\sim *}: B \to P(E), b \mapsto \begin{cases} \Phi^\sim(b), & b \in \Phi_\lambda^\sim(\alpha) \\ \beta, & otherwise \end{cases}$$

and

$$\lambda^*: B \to I,\ b \mapsto \begin{cases} \lambda(b),\ b \in \Phi_\lambda^\sim(\alpha) \\ s,\ otherwise \end{cases},$$

where $\alpha, \beta \in P(E)$ and $s, t \in I$ with $\beta \subsetneq \Phi^\sim(b)$ and $s > \lambda(b)$.

Theorem 3.9. Assume that B is a Bd-algebra. If $\Phi_\lambda^\sim$ is a hybrid Bd-subalgebra of B over E, then $\Phi_\lambda^{\sim *}$ is a hybrid Bd-subalgebra of B over E.

Proof. Let $\Phi_\lambda^\sim$ be a hybrid Bd-subalgebra of B over E. By Theorem 3.6, $\Phi_\lambda^\sim(\alpha)$ and $\Phi_\lambda^\sim(t)$ are Bd-subalgebras of B for all $\alpha \in P(E)$ and $\lambda \in I$ if they are non-empty sets.

Let $b, c \in B$. If $b, c \in \Phi_\lambda^\sim(\alpha)$ then $b * c \in \Phi_\lambda^\sim(\alpha)$. So,

$\Phi^{\sim *}(b * c) = \Phi^\sim(b * c) \supseteq \Phi^\sim(b) \cap \Phi^\sim(c) = \Phi^{\sim *}(b) \cap \Phi^{\sim *}(c)$ and $\Phi^{\sim *}(0) = \Phi^\sim(0) \supseteq \Phi^\sim(b) = \Phi^{\sim *}(b)$

since $0 \in \Phi_\lambda^\sim(\alpha)$.

If $b \notin \Phi_\lambda^{\sim}(\alpha)$ or $c \notin \Phi_\lambda^{\sim}(\alpha)$, then $\Phi^{\sim*}(b) = \beta$ or $\Phi^{\sim*}(c) = \beta$. Thus,

$$\Phi^{\sim*}(b * c) \supseteq \beta = \Phi^{\sim}(b) \cap \Phi^{\sim}(c).$$

If $b, c \in \Phi_\lambda^{\sim}(t)$ then $b * c \in \Phi_\lambda^{\sim}(t)$. Hence, $\lambda^*(b * c) = \lambda(b * c) \leq \vee\{\lambda(b), \lambda(c)\} = \vee\{\lambda^*(b), \lambda^*(c)\}$ and $\lambda^*(b) = \lambda(b) \geq \lambda(0)$. If $b \notin \Phi_\lambda^{\sim}(t)$ or $c \notin \Phi_\lambda^{\sim}(t)$, then $\lambda^*(b) = s$ or $\lambda^*(c) = s$. Thus,

$$\lambda^*(b * c) \leq s = \vee\{\lambda^*(b), \lambda^*(c)\}.$$

If $b \in \Phi_\lambda^{\sim}(t)$, then we have $\lambda(0) \leq \lambda(b) < s = \lambda^*(b)$. Therefore, $\Phi_\lambda^{\sim*}$ is a hybrid Bd-subalgebra of B over E.

The following example shows that the converse of Theorem 3.9 is not true in general.

Example 3.10. Consider the Bd-algebra in Example 3.2. Let $\Phi_\lambda^{\sim}$ be a hybrid structure in B over $E = \{e_1, e_2, e_3, \ldots, e_9, e_{10}\}$ which is given by the following table:

Table 7. The hybrid structure $\Phi_\lambda^{\sim}$

B	**Φ**	**λ**
0	E	0,3
$\mathbf{b_1}$	$\{e_1, e_2, e_3, e_7, e_8\}$	0,5
$\mathbf{b_2}$	$\{e_1, e_4, e_6\}$	0,8
$\mathbf{b_3}$	$\{e_1, e_3\}$	0,8

For $\alpha = \{e_1, e_2, e_7\}$, we have $\Phi_\lambda^{\sim}(\alpha) = \{0, b_1\}$ and for $t = 0{,}6$, $\Phi_\lambda^{\sim}(t) = \{0, b_1\}$. Suppose that $\Phi_\lambda^{\sim*} \coloneqq (\Phi^{\sim*}, \lambda^*)$ is a hybrid structure in B over E defined by:

$$\Phi^{\sim*}: B \to P(E), b \mapsto \begin{cases} \Phi^{\sim}(b), & b \in \Phi_\lambda^{\sim}(\alpha) \\ \emptyset, & otherwise \end{cases}$$

and

$$\lambda^*: B \to I,\ b \mapsto \begin{cases} \lambda(b),\ b \in \Phi_\lambda^{\sim}(\alpha) \\ 0{,}9,\ otherwise \end{cases}.$$

More precisely, we define

$$\Phi^{\sim*}: B \to P(E), x \mapsto \begin{cases} E, & x = 0 \\ \{e_1, e_2, e_3, e_7, e_8\}, & x = b_1 \\ \emptyset, & x \in \{b_2, b_3\} \end{cases}$$

and

$$\lambda^*: B \to I,\ x \mapsto \begin{cases} 0{,}3, & x = 0 \\ 0{,}5, & x = b_1 \\ 0{,}9, & x \in \{b_2, b_3\} \end{cases}.$$

It is clearly that $\Phi_\lambda^{\sim*} \coloneqq (\Phi^{\sim*}, \lambda^*)$ is a hybrid Bd-subalgebra in B over E. But $\Phi_\lambda^{\sim}$ is not a Bd-subalgebra in B over E since $\Phi^{\sim}(0) \cap \Phi^{\sim}(b_2) = \{e_1, e_4, e_6\} \nsubseteq \{e_1, e_2, e_3, e_7, e_8\} = \Phi^{\sim}(b_1) = \Phi^{\sim}(0 * b_2)$.

Definition 3.11. Let $\theta: B \to C$ be a mapping from a set B to a set C. For a hybrid structure $\Phi_\lambda^{\sim}$ in B over E, consider a hybrid structure $\theta^{-1}(\Phi_\lambda^{\sim}) \coloneqq (\theta^{-1}(\Phi^{\sim}), \theta^{-1}(\lambda))$ in B over E, where $\theta^{-1}(\Phi^{\sim})(b) = \Phi^{\sim}\big(\theta(b)\big)$ and $\theta^{-1}(\lambda)(b) = \lambda\big(\theta(b)\big)$ for all $b \in B$. Then, $\theta^{-1}(\Phi_\lambda^{\sim})$ is called the hybrid preimage of $\Phi_\lambda^{\sim}$ under θ.

Theorem 3.12. Every homomorphic hybrid preimage of a hybrid Bd-subalgebra is a hybrid Bd-subalgebra.

Proof. Let $\theta: B \to C$ be a homomorphism of Bd-algebras. Assume that $\Phi_\lambda^{\sim}$ is a hybrid Bd-subalgebra of B over E and $b, c \in B$. Then, we get

$$\theta^{-1}(\Phi^{\sim})(0) = \Phi^{\sim}\big(\theta(0)\big) = \Phi^{\sim}(0) \supseteq \Phi^{\sim}\big(\theta(b)\big) = \theta^{-1}(\Phi^{\sim})(b)$$

and

$$\theta^{-1}(\Phi^{\sim})(b*c) = \Phi^{\sim}\big(\theta(b*c)\big) = \Phi^{\sim}\big(\theta(b)*\theta(c)\big) \supseteq \Phi^{\sim}\big(\theta(b)\big) \cap \Phi^{\sim}\big(\theta(c)\big)$$
$$= \theta^{-1}(\Phi^{\sim})(b) \cap \theta^{-1}(\Phi^{\sim})(c).$$

Also, we have

$$\theta^{-1}(\lambda)(0) = \lambda\big(\theta(0)\big) = \lambda(0) \leq \lambda\big(\theta(b)\big) = \theta^{-1}(\lambda)(b)$$

and

$$\theta^{-1}(\lambda)(b*c) = \lambda\big(\theta(b*c)\big) = \lambda\big(\theta(b)*\theta(c)\big) \leq \vee\{\lambda\big(\theta(b)\big), \lambda\big(\theta(c)\big)\}$$
$$= \vee\{\theta^{-1}(\lambda)(b), \theta^{-1}(\lambda)(c)\}.$$

Therefore, $\theta^{-1}(\Phi_{\lambda}^{\sim})$ is a hybrid Bd-subalgebra of B over E.

Remark 3.13. For an onto homomorphism $\theta: B \to C$ of Bd-algebras, let $\theta^{-1}(\Phi_{\lambda}^{\sim}) \coloneqq (\theta^{-1}(\Phi^{\sim}), \theta^{-1}(\lambda))$ be a hybrid Bd-subalgebra of B over E. Let $x, y \in C$. Since θ is onto, we get $\theta(b) = x$ and $\theta(c) = y$, for some $b, c \in B$. Thus,

$$\Phi^{\sim}(0) = \Phi^{\sim}\big(\theta(0)\big) = \theta^{-1}(\Phi^{\sim})(0) \supseteq \theta^{-1}(\Phi^{\sim})(b) = \Phi^{\sim}\big(\theta(b)\big) = \Phi^{\sim}(x)$$

and

$$\Phi^{\sim}(x*y) = \Phi^{\sim}\big(\theta(b)*\theta(c)\big) = \Phi^{\sim}\big(\theta(b*c)\big) = \theta^{-1}(\Phi^{\sim})(b*c)$$
$$\supseteq \theta^{-1}(\Phi^{\sim})(b) \cap \theta^{-1}(\Phi^{\sim})(c) = \Phi^{\sim}\big(\theta(b)\big) \cap \Phi^{\sim}\big(\theta(c)\big)$$
$$= \Phi^{\sim}(x) \cap \Phi^{\sim}(y).$$

Also, we have

$$\lambda(0) = \lambda\big(\theta(0)\big) = \theta^{-1}(\lambda)(0) \leq \vee\{\theta^{-1}(\lambda)(b), \theta^{-1}(\lambda)(c)\} = \vee\{\lambda\big(\theta(b)\big), \lambda\big(\theta(c)\big)\} = V\{\lambda(x), \lambda(y)\}.$$

Hence, we can write the following theorem.

Theorem 3.14. Let $\theta: B \to C$ be an onto homomorphism of Bd-algebras. For every hybrid structure $\Phi_{\lambda}^{\sim}$ in C over E, if the preimage $\theta^{-1}(\Phi_{\lambda}^{\sim})$ of $\Phi_{\lambda}^{\sim}$under θ is a hybrid Bd-subalgebra of C over E.

4. Conclusion

Hybrid structures provide a powerful theoretical framework by combining the strengths of fuzzy set theory and soft set theory. This integration allows for more flexible and nuanced modelling of uncertainty and imprecision within algebraic systems, overcoming some limitations inherent to each individual approach. By applying this hybrid approach to Bd-algebras, we open new avenues for capturing complex algebraic behaviours that are closer to real-world problems, especially in areas where uncertainty and gradation play a critical role. In this study, hybrid structures are applied to Bd-algebras. We present hybrid Bd-subalgebras, which are the first structure of hybrid structures of Bd-algebras. Nowadays, many researchers examine these properties of algebraic structures. These structures, especially the Bd-algebras examined in this article, are a generalization of MV-(multi-valued) algebras and have many applications in computer science. In future studies, this structure can be transferred to the ideals of Bd-algebras. It can also be examined for structures that are generalizations of Bd-algebras. We hope that this work will lead to many new studies investigating hybrid structures.

Author Contributions

The author read and approved the final version of the paper.

Conflict of Interest

The author declares no conflict of interest.

Ethical Review and Approval

No approval from the Board of Ethics is required.

References

[1] L. A. Zadeh, *Fuzzy sets*, Information and Control 8 (3) (1965) 338–353.

[2] D. A. Molodtsov, *Soft set theory–first results*, Computers and Mathematics with Applications 37 (4-5) (1999) 19–31.

[3] Y. B. Jun, S. Z. Song, G. Muhiuddin, *Hybrid structures and applications*, Annals of Communications in Mathematics 1 (1) (2018) 11–25.

[4] G. Muhiuddin, D. Al-Kadi, A. Mahboob, *Ideal theory of BCK/BCI-algebras based on hybrid structures*, Journal of Mathematics and Computer Science 23 (2) (2020) 136–144.

[5] Y. Imai, K. Iséki, *On axiom systems of propositional calculi*, I. Proceedings of the Japan Academy 41 (6) (1965) 436–439.

[6] K. Iséki, *An algebra related with a propositional calculus*, Proceedings of the Japan Academy 42 (1) (1966) 26–29.

[7] J. Neggers, H. S. Kim, *On d-algebras*, Mathematica Slovaca 49 (1) (1999) 19–26.

[8] J. Neggers, Y. B. Jun, H. S. Kim, *On d-ideals in d-algebras*, Mathematica Slovaca 49 (3) (1999) 243–251.

[9] J. Neggers, K. Sik, *On B-algebras*, Matematički Vesnik 54 (218) (2002) 21–29.

[10] H. S. Kim, H. G. Park, *On 0-commutative B-algebras*, Scientiae Mathematicae Japonicae 62 (1) (2005) 31–36.

[11] T. Bantaojai, C. Suanoom, J. Phuto, A. Iampan, *On Bd-algebras*, Computer Science 17 (2) (2022) 731–737.

[12] B. Elavarasan, G. Muhiuddin, K. Porselvi, Y. B. Jun, *On hybrid k-ideals in semirings*, Journal of Intelligent and Fuzzy Systems 44 (3) (2023) 4681–4691.

[13] V. Keerthika, G. Muhiuddin, Y. B. Jun, B. Elavarasan, *Hybrid ordered ideals in ordered semirings*, Journal of Intelligent and Fuzzy Systems 45 (1) (2023) 1397–1408.

[14] B. Elavarasan, G. Muhiuddin, K. Porselvi, Y. B. Jun, *Hybrid structures applied to ideals in near-rings*, Complex and Intelligent Systems 7 (2021) 1489–1498.

[15] B. Elavarasan, Y. B. Jun, *Regularity of semigroups in terms of hybrid ideals and hybrid bi-ideals*, Kragujevac Journal of Mathematics 46 (6) (2022) 857–864.

[16] K. Porselvi, G. Muhiuddin, B. Elavarasan, A. Assiry, *Hybrid nil radical of a ring*, Symmetry 14 (7) (2022) 1367.

[17] S. Meenakshi, G. Muhiuddin, D. Al-kadi, B. Elavarasan, *Hybrid bi-ideals in Near-Subtraction Semigroups*, Hacettepe Journal of Mathematics and Statistics 53 (5) (2024) 1250–1263.

[18] K. T. Kang, S. Z. Song, E. H. Roh, Y. B. Jun, *Hybrid ideals of BCK/BCI-algebras*, Axioms 9 (3) (2020) 85.

Journal of New Results in Science
dergipark.org.tr/tr/pub/jnrs
Open Access

ISSN: 1304-7981 | 14 (2) (2025) 82-99 | doi.org/10.54187/jnrs.1646665

On the Existence of C_n-Supermagic Labelings in Cycle-Based Graph Structures

Tarkan Öner[1]

Article Info
Received: 25 Feb 2025
Accepted: 13 Jun 2025
Published: 31 Aug 2025
Research Article

Abstract— In this paper, we prove the existence of C_n-supermagic labeling for the graph $G(n, n)$ formed by connecting a vertex of n copies of the C_n (n-edge cycle) graph to a vertex of a main C_n graph. Labeling functions enable the edges and the vertices of the graph to be labeled with subgraphs that resemble the structure of C_n. C_n-supermagic labeling requires the sum of the labels to be constant for each C_n-cover, and the labels must be uniquely distributed across the graph. The study examines different labelings of $G(n, n)$ based on the value of n modulo 4, demonstrating their validity through examples. The results show that such labelings are possible and can be applied consistently for specific values of n.

Keywords — *Graph labeling, C_n-supermagic labeling, circular graph, magic sum, H-cover*

1. Introduction

Graph labeling is a crucial area in graph theory that involves assigning labels (typically numerical values) to the elements of a graph, such as vertices, edges, or faces [1]. This process is vital in various applications, including cryptography, coding theory, communication networks, and even astronomy [2–8]. The labeling of graph elements often results in partial sums or weights, which are typically asymmetrically distributed. The diverse applications and the theoretical depth of graph labeling have led to a considerable increase in research in recent years.

In particular, graph labeling has become a significant focus in recent studies due to its numerous applications and its role in solving complex problems. Notable work in [9] explored antimagic labeling methods for the product of regular graphs. Furthermore, ELrokh et al. [10] introduced a new labeling technique combining permutation groups and cordiality concepts in graph theory. These contributions are a testament to the ongoing evolution of graph labeling techniques, which continue to shape both theoretical advancements and practical solutions in diverse fields.

Another important study is given by Ashari et al. [11] which investigates the forbidden subgraph properties of (K_2, H)-Sim-(Super)Magic graphs, offering a new perspective to better understand the structure of these graphs. This research marks a significant step toward understanding supermagic labeling and exploring restrictive subgraph structures in graph theory.

Recent studies on supermagic labelings [12–14] demonstrate continued interest in this area.

[1]tarkanoner@mu.edu.tr (Corresponding Author)
[1]Department of Mathematics, Faculty of Sciences, Muğla Sıtkı Koçman University, Muğla, Türkiye

This growing body of research highlights the complexity and diversity of graph labeling problems and their broad applicability. Understanding these developments in graph labeling is crucial for advancing both theoretical knowledge and real-world applications in areas such as computer science, network theory, and beyond.

In this paper, we explore the C_n-supermagic labeling of the graph $G(n,n)$, which is constructed by attaching n copies of the cycle graph C_n to a central C_n structure. The objective is to establish explicit labeling functions that ensure a constant magic sum across all C_n-subgraphs of $G(n,n)$. We systematically analyze the feasibility of such labelings based on the value of $n \mod 4$ and provide rigorous proofs for their existence.

The remainder of this paper is structured as follows: Section 2 provides the definition of H-supermagic labeling and introduces the $G(n,n)$ graph to be examined in this study. Section 3 presents the main theoretical results on C_n-supermagic labeling, proving its existence for different cases of n. Section 4 provides numerical examples illustrating these labelings with specific values of n. Finally, Section 5 summarizes our findings and discusses potential directions for future research.

2. Preliminaries

A graph $G(V,E)$ admits an H-covering if every edge belongs to a subgraph of G isomorphic to a simple graph H. A bijection $\lambda : V \cup E \to \{1,2,\ldots,|V|+|E|\}$ is called an H-magic labeling of G if there exists a constant $\mu(\lambda)$ (known as the magic sum) such that, for any subgraph $H' = (V', E')$ of G isomorphic to H:

$$\sum_{v \in H'} \lambda(v) + \sum_{e \in H'} \lambda(e) = \mu(\lambda).$$

A graph is H-magic if it satisfies this property. Furthermore, an H-magic labeling λ is considered H-supermagic if the labels assigned to the vertices of G cover the set $\{1,2,\ldots,|V|\}$ exactly [15].

Let $n \geq 3$ be given, where C_n is the cycle graph and n graphs of C_n are provided. The graph $G(n,n)$ is obtained by attaching the C_n graphs, denoted as G_i for $i = 1, \cdots, n$, to each vertex of the main C_n graph. This results in a graph with n^2+n edges and n^2 vertices. Let us denote these vertices and edges as follows:

$$V = \{v_i : i \in \{1,\ldots,n\}\} \cup \{v_{i,j} : i \in \{1,\ldots,n\},\ j \in \{1,\ldots,n-1\}\}$$

and

$$\begin{aligned} E = {} & \{e_i : i \in \{1,\ldots,n\}\} \cup \{e_{i,1} : e_{i,1} = v_i v_{i,1},\ i \in \{1,\ldots,n\}\} \\ & \cup \{e_{i,j} : e_{i,j} = v_{i,j-1}v_{i,j}, i \in \{1,\ldots,n\},\ j \in \{2,\ldots,n-1\}\} \\ & \cup \{e_{i,n} : e_{i,n} = v_{i,n-1}v_i,\ i \in \{1,\ldots,n\}\} \end{aligned}$$

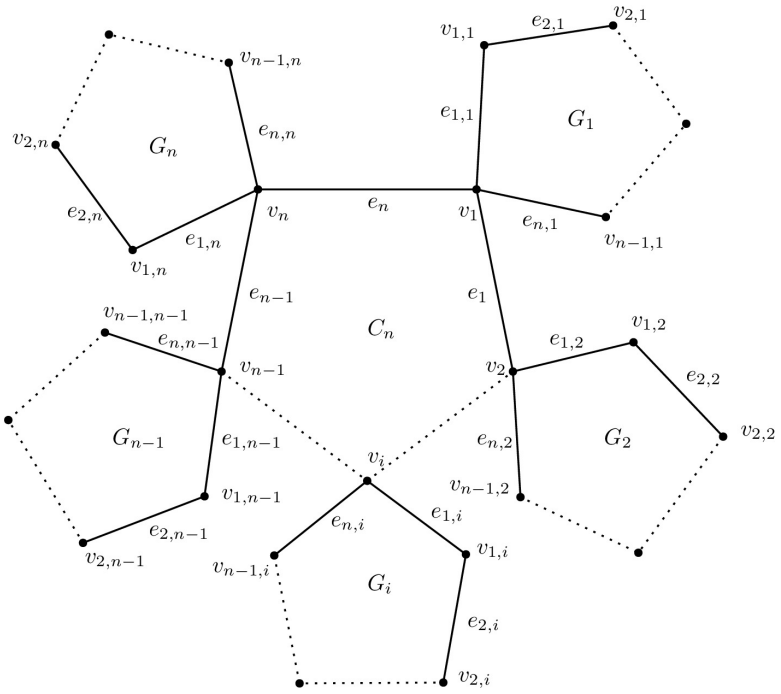

Figure 1. G(n,n)

There are $n+1$ subgraphs in $G(n,n)$ that are isomorphic to C_n. These subgraphs represent a C_n-structure for $G(n,n)$. Therefore, it can be questioned whether the graph $G(n,n)$ has a C_n- supermagic labeling.

3. Results

In this section, we examine the C_n-supermagic labeling of these graphs for different values of n.

Theorem 3.1. If $n \equiv 0 \pmod 4$, then the graph $G(n,n)$ has a C_n-supermagic labeling.

Proof. We define the labeling λ as follows:

$$\lambda(v_i) = \begin{cases} \frac{n}{2}n + 1 - i, & i \in \{1, \ldots, \frac{n}{2}\} \\ (\frac{n}{2}+1)n + 1 - i, & i \in \{\frac{n}{2}+1, \ldots, n\} \end{cases}$$

$$\lambda(v_{i,j}) = \begin{cases} (j-1)n + i, & j \in \{1,3,5,\ldots,\frac{n}{2}-1\}, i \in \{1,\ldots,n\} \\ jn + 1 - i, & j \in \{2,4,6,\ldots,\frac{n}{2}-2\}, i \in \{1,\ldots,n\} \\ (j+1)n + 1 - i, & j = \frac{n}{2}, i \in \{1,\ldots,\frac{n}{2}\} \\ jn + 1 - i, & j = \frac{n}{2}, i \in \{\frac{n}{2}+1,\ldots,n\} \\ jn + i, & j \in \{\frac{n}{2}+1, \frac{n}{2}+3, \frac{n}{2}+5, \ldots, n-1\}, i \in \{1,\ldots,n\} \\ (j+1)n + 1 - i, & j \in \{\frac{n}{2}+2, \frac{n}{2}+4, \frac{n}{2}+6, \ldots, n-2\}, i \in \{1,\ldots,n\} \end{cases}$$

$$\lambda(e_i) = n^2 + \frac{n}{2}n + i, \quad i \in \{1,\ldots,n\}$$

and

$$\lambda(e_{i,j}) = \begin{cases} n^2+(j-1)n+i, & j \in \{1,3,5,\ldots,\frac{n}{2}-1\}, i \in \{1,\ldots,n\} \\ n^2+jn+1-i, & j \in \{2,4,6,\ldots,\frac{n}{2}\}, i \in \{1,\ldots,n\} \\ n^2+jn+i, & j \in \{\frac{n}{2}+1,\frac{n}{2}+3,\frac{n}{2}+5,\ldots,n-1\}, i \in \{1,\ldots,n\} \\ n^2+(j+1)n+1-i, & j \in \{\frac{n}{2}+2,\frac{n}{2}+4,\frac{n}{2}+6,\ldots,n\}, i \in \{1,\ldots,n\} \end{cases}$$

For G_i where $i \in \{1,\ldots,n\}$:
Vertex Sum: Case 1: If $i \in \{1,\ldots,\frac{n}{2}\}$, then

$$\begin{aligned} \sum_{v\in G_i}\lambda(v) &= \sum_{j=1}^{n-1}\lambda(v_{i,j})+\lambda(v_i) \\ &= \sum_{j=1,3,5}^{\frac{n}{2}-1}\lambda(v_{i,j})+\sum_{j=2,4,6}^{\frac{n}{2}-2}\lambda(v_{i,j})+\lambda\left(v_{i,\frac{n}{2}}\right)+\sum_{j=\frac{n}{2}+1,\frac{n}{2}+3,\frac{n}{2}+5}^{n-1}\lambda(v_{i,j})+\sum_{j=\frac{n}{2}+2,\frac{n}{2}+4,\frac{n}{2}+6}^{n-2}\lambda(v_{i,j})+\lambda(v_i) \\ &= \sum_{j=1,3,5}^{\frac{n}{2}-1}((j-1)n+i)+\sum_{j=2,4,6}^{\frac{n}{2}-2}(jn+1-i)+((j+1)n+1-i) \\ &\quad +\sum_{j=\frac{n}{2}+1,\frac{n}{2}+3,\frac{n}{2}+5}^{n-1}(jn+i)+\sum_{j=\frac{n}{2}+2,\frac{n}{2}+4,\frac{n}{2}+6}^{n-2}((j+1)n+1-i))+\left(\frac{n}{2}n+1-i\right) \\ &= \frac{n^3+n}{2} \end{aligned}$$

Case 2: If $i \in \{\frac{n}{2}+1,\ldots,n\}$, then

$$\begin{aligned} \sum_{v\in G_i}\lambda(v) &= \sum_{j=1}^{n-1}\lambda(v_{i,j})+\lambda(v_i) \\ &= \sum_{j=1,3,5}^{\frac{n}{2}-1}\lambda(v_{i,j})+\sum_{j=2,4,6}^{\frac{n}{2}-2}\lambda(v_{i,j})+\lambda\left(v_{i,\frac{n}{2}}\right)+\sum_{j=\frac{n}{2}+1,\frac{n}{2}+3,\frac{n}{2}+5}^{n-1}\lambda(v_{i,j})+\sum_{j=\frac{n}{2}+2,\frac{n}{2}+4,\frac{n}{2}+6}^{n-2}\lambda(v_{i,j})+\lambda(v_i) \\ &= \sum_{j=1,3,5}^{\frac{n}{2}-1}((j-1)n+i)+\sum_{j=2,4,6}^{\frac{n}{2}-2}(jn+1-i)+(jn+1-i) \\ &\quad +\sum_{j=\frac{n}{2}+1,\frac{n}{2}+3,\frac{n}{2}+5}^{n-1}(jn+i)+\sum_{j=\frac{n}{2}+2,\frac{n}{2}+4,\frac{n}{2}+6}^{n-2}((j+1)n+1-i))+\left(\left(\frac{n}{2}+1\right)n+1-i\right) \\ &= \frac{n^3+n}{2} \end{aligned}$$

Edge Sum:

$$\sum_{e\in G_i}\lambda(e)=\sum_{j=1}^{n}\lambda(e_{i,j})$$

$$=\sum_{j=1,3,5}^{\frac{n}{2}-1}\lambda(e_{i,j})+\sum_{j=2,4,6}^{\frac{n}{2}}(e_{i,j})+\sum_{j=\frac{n}{2}+1,\frac{n}{2}+3,\frac{n}{2}+5}^{n-1}\lambda(e_{i,j})+\sum_{j=\frac{n}{2}+2,\frac{n}{2}+4,\frac{n}{2}+6}^{n}\lambda(e_{i,j})$$

$$=\sum_{j=1,3,5}^{\frac{n}{2}-1}\Big(n^2+(j-1)n+i\Big)+\sum_{j=2,4,6}^{\frac{n}{2}}\Big(n^2+jn+1-i\Big)+\sum_{j=\frac{n}{2}+1,\frac{n}{2}+3,\frac{n}{2}+5}^{n-1}\Big(n^2+jn+i\Big)$$

$$+\sum_{j=\frac{n}{2}+2,\frac{n}{2}+4,\frac{n}{2}+6}^{n}\Big(n^2+(j+1)n+1-i\Big)$$

$$=\frac{3n^3+n^2+n}{2}$$

Magic Sum:

$$\begin{aligned}\mu(\lambda)&=\sum_{v\in G_i}\lambda(v)+\sum_{e\in G_i}\lambda(e)\\&=\frac{n^3+n}{2}+\frac{3n^3+n^2+n}{2}\\&=2n^3+\frac{n^2}{2}+n\end{aligned}$$

For C_n:
Vertex Sum:

$$\begin{aligned}\sum_{v\in C_n}\lambda(v)&=\sum_{i=1}^{n}\lambda(v_i)=\sum_{i=1}^{\frac{n}{2}}\left(\frac{n}{2}n+1-i\right)+\sum_{i=\frac{n}{2}+1}^{n}\left(\left(\frac{n}{2}+1\right)n+1-i\right)\\&=\frac{n^3+n}{2}\end{aligned}$$

Edge Sum:

$$\begin{aligned}\sum_{e\in C_n}\lambda(e)&=\sum_{i=1}^{n}\lambda(e_i)=\sum_{i=1}^{n}\left(n^2+\frac{n}{2}n+i\right)\\&=\frac{3n^3+n^2+n}{2}\end{aligned}$$

Magic Sum:

$$\begin{aligned}\mu(\lambda)&=\sum_{v\in C_n}\lambda(v)+\sum_{e\in C_n}\lambda(e)\\&=\frac{n^3+n}{2}+\frac{3n^3+n^2+n}{2}\\&=2n^3+\frac{n^2}{2}+n\end{aligned}$$

□

Theorem 3.2. If $n \equiv 2 \pmod 4$, then the graph $G(n,n)$ has a C_n-supermagic labeling.

Proof. We define the labeling λ as follows:

$$\lambda(v_i) = \begin{cases} \frac{n}{2}n + i, & i \in \{1, \ldots, \frac{n}{2}\} \\ (\frac{n}{2} - 1)n + i, & i \in \{\frac{n}{2} + 1, \ldots, n\} \end{cases}$$

$$\lambda(v_{i,j}) = \begin{cases} (j-1)n + i, & j \in \{1, 3, 5, \ldots, \frac{n}{2} - 2\}, i \in \{1, \ldots, n\} \\ jn + 1 - i, & j \in \{2, 4, 6, \ldots, \frac{n}{2} - 1\}, i \in \{1, \ldots, n\} \\ (j-1)n + i, & j = \frac{n}{2}, i \in \{1, \ldots, \frac{n}{2}\} \\ jn + i, & j = \frac{n}{2}, i \in \{\frac{n}{2} + 1, \ldots, n\} \\ (j+1)n + 1 - i, & j \in \{\frac{n}{2} + 1, \frac{n}{2} + 3, \frac{n}{2} + 5, \ldots, n - 2\}, i \in \{1, \ldots, n\} \\ jn + i, & j \in \{\frac{n}{2} + 2, \frac{n}{2} + 4, \frac{n}{2} + 6, \ldots, n - 3\}, i \in \{1, \ldots, n\} \\ (j+1)n + 1 - i, & j = n - 1, \quad i \in \{1, \ldots, n\} \end{cases}$$

$$\lambda(e_i) = n^2 + \frac{n}{2}n + i, \quad i \in \{1, \ldots, n\}$$

and

$$\lambda(e_{i,j}) = \begin{cases} n^2 + (j-1)n + i, & j \in \{1, 3, 5, \ldots, \frac{n}{2}\}, i \in \{1, \ldots, n\} \\ n^2 + jn + 1 - i, & j \in \{2, 4, 6, \ldots, \frac{n}{2} - 1\}, i \in \{1, \ldots, n\} \\ n^2 + (j+1)n + 1 - i, & j \in \{\frac{n}{2} + 1, \frac{n}{2} + 3, \frac{n}{2} + 5, \ldots, n\}, i \in \{1, \ldots, n\} \\ n^2 + jn + i, & j \in \{\frac{n}{2} + 2, \frac{n}{2} + 4, \frac{n}{2} + 6, \ldots, n - 1\}, i \in \{1, \ldots, n\} \end{cases}$$

For G_i where $i \in \{1, \ldots, n\}$:
Vertex Sum: Case 1: If $i \in \{1, \ldots, \frac{n}{2}\}$, then

$$\sum_{v \in G_i} \lambda(v) = \sum_{j=1}^{n-1} \lambda(v_{i,j}) + \lambda(v_i)$$

$$= \sum_{j=1,3,5}^{\frac{n}{2}-2} \lambda(v_{i,j}) + \sum_{j=2,4,6}^{\frac{n}{2}-1} \lambda(v_{i,j}) + \lambda\left(v_{i,\frac{n}{2}}\right)$$

$$+ \sum_{j=\frac{n}{2}+1,\frac{n}{2}+3,\frac{n}{2}+5}^{n-2} \lambda(v_{i,j}) + \sum_{j=\frac{n}{2}+2,\frac{n}{2}+4,\frac{n}{2}+6}^{n-3} \lambda(v_{i,j}) + \lambda(v_{i,n-1}) + \lambda(v_i)$$

$$= \sum_{j=1,3,5}^{\frac{n}{2}-2} ((j-1)n + i) + \sum_{j=2,4,6}^{\frac{n}{2}-1} (jn + 1 - i) + \left(\left(\frac{n}{2} - 1\right)n + i\right)$$

$$+ \sum_{j=\frac{n}{2}+1,\frac{n}{2}+3,\frac{n}{2}+5}^{n-2} ((j+1)n + 1 - i) + \sum_{j=\frac{n}{2}+2,\frac{n}{2}+4,\frac{n}{2}+6}^{n-3} (jn + i) + \left(n^2 + 1 - i\right) + \left(\frac{n}{2}n + i\right)$$

$$= \frac{n^3 + n}{2}$$

Case 2: If $i \in \left\{\frac{n}{2}+1, \ldots, n\right\}$, then

$$\sum_{v\in G_i} \lambda(v) = \sum_{j=1}^{n-1} \lambda(v_{i,j}) + \lambda(v_i)$$

$$= \sum_{j=1,3,5}^{\frac{n}{2}-2} \lambda(v_{i,j}) + \sum_{j=2,4,6}^{\frac{n}{2}-1} \lambda(v_{i,j}) + \lambda\left(v_{i,\frac{n}{2}}\right)$$

$$+ \sum_{j=\frac{n}{2}+1,\frac{n}{2}+3,\frac{n}{2}+5}^{n-2} \lambda(v_{i,j}) + \sum_{j=\frac{n}{2}+2,\frac{n}{2}+4,\frac{n}{2}+6}^{n-3} \lambda(v_{i,j}) + \lambda(v_{i,n-1}) + \lambda(v_i)$$

$$= \sum_{j=1,3,5}^{\frac{n}{2}-2} ((j-1)n+i) + \sum_{j=2,4,6}^{\frac{n}{2}-1} (jn+1-i) + \left(\frac{n^2}{2}+i\right)$$

$$+ \sum_{j=\frac{n}{2}+1,\frac{n}{2}+3,\frac{n}{2}+5}^{n-2} ((j+1)n+1-i) + \sum_{j=\frac{n}{2}+2,\frac{n}{2}+4,\frac{n}{2}+6}^{n-3} (jn+i) + \left(n^2+1-i\right) + \left(\left(\frac{n}{2}-1\right)n+i\right)$$

$$= \frac{n^3+n}{2}$$

Edge Sum:

$$\sum_{e\in G_i} \lambda(e) = \sum_{j=1}^{n} \lambda(e_{i,j})$$

$$= \sum_{j=1,3,5}^{\frac{n}{2}} \lambda(e_{i,j}) + \sum_{j=2,4,6}^{\frac{n}{2}-1} (e_{i,j}) + \sum_{j=\frac{n}{2}+1,\frac{n}{2}+3,\frac{n}{2}+5}^{n} \lambda(e_{i,j}) + \sum_{j=\frac{n}{2}+2,\frac{n}{2}+4,\frac{n}{2}+6}^{n-1} \lambda(e_{i,j})$$

$$= \sum_{j=1,3,5}^{\frac{n}{2}} \left(n^2+(j-1)n+i\right) + \sum_{j=2,4,6}^{\frac{n}{2}-1} \left(n^2+jn+1-i\right) + \sum_{j=\frac{n}{2}+1,\frac{n}{2}+3,\frac{n}{2}+5}^{n} \left(n^2+(j+1)n+1-i\right)$$

$$+ \sum_{j=\frac{n}{2}+2,\frac{n}{2}+4,\frac{n}{2}+6}^{n-1} \left(n^2+jn+i\right)$$

$$= \frac{3n^3+n^2+n}{2}$$

Magic Sum:

$$\begin{aligned}\mu(\lambda) &= \sum_{v\in G_i} \lambda(v) + \sum_{e\in G_i} \lambda(e) \\ &= \frac{n^3+n}{2} + \frac{3n^3+n^2+n}{2} \\ &= 2n^3 + \frac{n^2}{2} + n\end{aligned}$$

For C_n:
Vertex Sum:

$$\begin{aligned}\sum_{v\in C_n}\lambda(v) &= \sum_{i=1}^{n}\lambda(v_i) = \sum_{i=1}^{\frac{n}{2}}\left(\frac{n}{2}n+i\right)+\sum_{i=\frac{n}{2}+1}^{n}\left(\left(\frac{n}{2}-1\right)n+i\right)\\ &= \frac{n^3+n}{2}\end{aligned}$$

Edge Sum:

$$\begin{aligned}\sum_{e\in C_n}\lambda(e) &= \sum_{i=1}^{n}\lambda(e_i) = \sum_{i=1}^{n}\left(n^2+\frac{n}{2}n+i\right)\\ &= \frac{3n^3+n^2+n}{2}\end{aligned}$$

Magic Sum:

$$\begin{aligned}\mu(\lambda) &= \sum_{v\in C_n}\lambda(v)+\sum_{e\in C_n}\lambda(e)\\ &= \frac{n^3+n}{2}+\frac{3n^3+n^2+n}{2}\\ &= 2n^3+\frac{n^2}{2}+n\end{aligned}$$

□

Theorem 3.3. If $n \equiv 1 \pmod 4$, then the graph $G(n,n)$ has a C_n-supermagic labeling.

Proof. We define the labeling λ as follows:

$$\lambda(v_i) = \begin{cases} \frac{n+1}{2}n+i, & i \in \left\{1,\ldots,\frac{n+1}{2}\right\}\\ (\frac{n+1}{2}-1)n+i, & i \in \left\{\frac{n+1}{2}+1,\ldots,n\right\}\end{cases}$$

$$\lambda(v_{i,j}) = \begin{cases} (j-1)n+i, & j \in \left\{1,3,5,\ldots,\frac{n+1}{2}-2\right\}, i \in \{1,\ldots,n\}\\ jn+1-i, & j \in \left\{2,4,6,\ldots,\frac{n+1}{2}-1\right\}, i \in \{1,\ldots,n\}\\ (j-1)n+i, & j = \frac{n+1}{2}, i \in \left\{1,\ldots,\frac{n+1}{2}\right\}\\ jn+i, & j = \frac{n+1}{2}, i \in \left\{\frac{n+1}{2}+1,\ldots,n\right\}\\ (j+1)n+1-i, & j \in \left\{\frac{n+1}{2}+1,\frac{n+1}{2}+3,\frac{n+1}{2}+5,\ldots,n-1\right\}, i \in \{1,\ldots,n\}\\ jn+i, & j \in \left\{\frac{n+1}{2}+2,\frac{n+1}{2}+4,\frac{n+1}{2}+6,\ldots,n-2\right\}, i \in \{1,\ldots,n\}\end{cases}$$

$$\lambda(e_i) = n^2+(\frac{n+1}{2}-1)n+i, \quad i \in \{1,\ldots,n\}$$

and

$$\lambda(e_{i,j}) = \begin{cases} n^2+jn+1-i, & j \in \left\{1,3,5,\ldots,\frac{n+1}{2}-2\right\}, i \in \{1,\ldots,n\}\\ n^2+(j-1)n+i, & j \in \left\{2,4,6,\ldots,\frac{n+1}{2}-1\right\}, i \in \{1,\ldots,n\}\\ n^2+(j+1)n+1-i, & j \in \left\{\frac{n+1}{2},\frac{n+1}{2}+2,\frac{n+1}{2}+4,\ldots,n\right\}, i \in \{1,\ldots,n\}\\ n^2+jn+i, & j \in \left\{\frac{n+1}{2}+1,\frac{n+1}{2}+3,\frac{n+1}{2}+5,\ldots,n-1\right\}, i \in \{1,\ldots,n\}\end{cases}$$

For G_i where $i \in \{1,\ldots,n\}$:

Vertex Sum: Case 1: If $i \in \left\{1, \ldots, \frac{n+1}{2}\right\}$, then

$$\sum_{v \in G_i} \lambda(v) = \sum_{j=1}^{n-1} \lambda(v_{i,j}) + \lambda(v_i)$$

$$= \sum_{j=1,3,5}^{\frac{n+1}{2}-2} \lambda(v_{i,j}) + \sum_{j=2,4,6}^{\frac{n+1}{2}-1} \lambda(v_{i,j}) + \lambda\left(v_{i,\frac{n+1}{2}}\right)$$

$$+ \sum_{j=\frac{n+1}{2}+1,\frac{n+1}{2}+3,\frac{n+1}{2}+5}^{n-1} \lambda(v_{i,j}) + \sum_{j=\frac{n+1}{2}+2,\frac{n+1}{2}+4,\frac{n+1}{2}+6}^{n-2} \lambda(v_{i,j}) + \lambda(v_i)$$

$$= \sum_{j=1,3,5}^{\frac{n+1}{2}-2} ((j-1)n+i) + \sum_{j=2,4,6}^{\frac{n+1}{2}-1} (jn+1-i) + \left((\frac{n+1}{2}-1)n+i\right)$$

$$+ \sum_{j=\frac{n+1}{2}+1,\frac{n+1}{2}+3,\frac{n+1}{2}+5}^{n-1} ((j+1)n+1-i) + \sum_{j=\frac{n+1}{2}+2,\frac{n+1}{2}+4,\frac{n+1}{2}+6}^{n-2} (jn+i) + \left(\frac{n+1}{2}n+i\right)$$

$$= \frac{n^3-1}{2} + i$$

Case 2: If $i \in \left\{\frac{n+1}{2}+1, \ldots, n\right\}$, then

$$\sum_{v \in G_i} \lambda(v) = \sum_{j=1}^{n-1} \lambda(v_{i,j}) + \lambda(v_i)$$

$$= \sum_{j=1,3,5}^{\frac{n+1}{2}-2} \lambda(v_{i,j}) + \sum_{j=2,4,6}^{\frac{n+1}{2}-1} \lambda(v_{i,j}) + \lambda\left(v_{i,\frac{n+1}{2}}\right)$$

$$+ \sum_{j=\frac{n+1}{2}+1,\frac{n+1}{2}+3,\frac{n+1}{2}+5}^{n-1} \lambda(v_{i,j}) + \sum_{j=\frac{n+1}{2}+2,\frac{n+1}{2}+4,\frac{n+1}{2}+6}^{n-2} \lambda(v_{i,j}) + \lambda(v_i)$$

$$= \sum_{j=1,3,5}^{\frac{n+1}{2}-2} ((j-1)n+i) + \sum_{j=2,4,6}^{\frac{n+1}{2}-1} (jn+1-i) + \left(\frac{n+1}{2}n+i\right)$$

$$+ \sum_{j=\frac{n+1}{2}+1,\frac{n+1}{2}+3,\frac{n+1}{2}+5}^{n-1} ((j+1)n+1-i) + \sum_{j=\frac{n+1}{2}+2,\frac{n+1}{2}+4,\frac{n+1}{2}+6}^{n-2} (jn+i) + \left(\left(\frac{n+1}{2}-1\right)n+i\right)$$

$$= \frac{n^3-1}{2} + i$$

Edge Sum:

$$\sum_{e\in G_i}\lambda(e)=\sum_{j=1}^{n}\lambda(e_{i,j})$$

$$=\sum_{j=1,3,5}^{\frac{n+1}{2}-2}\lambda(e_{i,j})+\sum_{j=2,4,6}^{\frac{n+1}{2}-1}(e_{i,j})+\sum_{j=\frac{n+1}{2},\frac{n+1}{2}+2,\frac{n+1}{2}+4}^{n}\lambda(e_{i,j})+\sum_{j=\frac{n}{2}+1,\frac{n}{2}+3,\frac{n}{2}+5}^{n-1}\lambda(e_{i,j})$$

$$=\sum_{j=1,3,5}^{\frac{n+1}{2}-2}\Big(n^2+jn+1-i\Big)+\sum_{j=2,4,6}^{\frac{n+1}{2}-1}\Big(n^2+(j-1)n+i\Big)+\sum_{j=\frac{n+1}{2},\frac{n+1}{2}+2,\frac{n+1}{2}+4}^{n}\Big(n^2+(j+1)n+1-i\Big)$$

$$+\sum_{j=\frac{n}{2}+1,\frac{n}{2}+3,\frac{n}{2}+5}^{n-1}\Big(n^2+jn+i\Big)$$

$$=\frac{3n^3+n^2+3n+1}{2}-i$$

Magic Sum:

$$\begin{aligned}\mu(\lambda)&=\sum_{v\in G_i}\lambda(v)+\sum_{e\in G_i}\lambda(e)\\&=\left(\frac{n^3-1}{2}+i\right)+\left(\frac{3n^3+n^2+3n+1}{2}-i\right)\\&=2n^3+\frac{n^2+3n}{2}\end{aligned}$$

For C_n:

Vertex Sum:

$$\begin{aligned}\sum_{v\in C_n}\lambda(v)=\sum_{i=1}^{n}\lambda(v_i)&=\sum_{i=1}^{\frac{n+1}{2}}\left(\frac{n+1}{2}n+i\right)+\sum_{i=\frac{n+1}{2}+1}^{n}\left(\left(\frac{n+1}{2}-1\right)n+i\right)\\&=\frac{n^3+n^2}{2}+n\end{aligned}$$

Edge Sum:

$$\begin{aligned}\sum_{e\in C_n}\lambda(e)=\sum_{i=1}^{n}\lambda(e_i)&=\sum_{i=1}^{n}\left(n^2+\left(\frac{n+1}{2}-1\right)n+i\right)\\&=\frac{3n^3+n}{2}\end{aligned}$$

Magic Sum:

$$\begin{aligned}\mu(\lambda)&=\sum_{v\in C_n}\lambda(v)+\sum_{e\in C_n}\lambda(e)\\&=\left(\frac{n^3+n^2}{2}+n\right)+\left(\frac{3n^3+n}{2}\right)\\&=2n^3+\frac{n^2+3n}{2}\end{aligned}$$

□

Theorem 3.4. If $n \equiv 3 \pmod 4$, then the graph $G(n,n)$ has a C_n-supermagic labeling.

Proof. We define the labeling λ as follows:

$$\lambda(v_i) = \begin{cases} \frac{n+1}{2}n + 1 - i, & i \in \left\{1, \ldots, \frac{n+1}{2} - 1\right\} \\ (\frac{n+1}{2} + 1)n + 1 - i, & i \in \left\{\frac{n+1}{2}, \ldots, n\right\} \end{cases}$$

$$\lambda(v_{i,j}) = \begin{cases} (j-1)n + i, & j \in \left\{1, 3, 5, \ldots, \frac{n+1}{2} - 1\right\}, i \in \{1, \ldots, n\} \\ jn + 1 - i, & j \in \left\{2, 4, 6, \ldots, \frac{n+1}{2} - 2\right\}, i \in \{1, \ldots, n\} \\ (j+1)n + 1 - i, & j = \frac{n+1}{2}, i \in \left\{1, \ldots, \frac{n-1}{2}\right\} \\ jn + 1 - i, & j = \frac{n+1}{2}, \quad i \in \left\{\frac{n-1}{2} + 1, \ldots, n\right\} \\ jn + i, & j \in \left\{\frac{n+1}{2} + 1, \frac{n+1}{2} + 3, \frac{n+1}{2} + 5, \ldots, n-2\right\}, i \in \{1, \ldots, n\} \\ (j+1)n + 1 - i, & j \in \left\{\frac{n+1}{2} + 2, \frac{n+1}{2} + 4, \frac{n+1}{2} + 6, \ldots, n-1\right\}, i \in \{1, \ldots, n\} \end{cases}$$

$$\lambda(e_i) = n^2 + (\frac{n+1}{2} - 1)n + i, \quad i \in \{1, \ldots, n\}$$

and

$$\lambda(e_{i,j}) = \begin{cases} n^2 + jn + 1 - i, & j \in \left\{1, 3, 5, \ldots, \frac{n+1}{2} - 1\right\}, i \in \{1, \ldots, n\} \\ n^2 + (j-1)n + i, & j \in \left\{2, 4, 6, \ldots, \frac{n+1}{2} - 2\right\}, i \in \{1, \ldots, n\} \\ n^2 + jn + i, & j \in \left\{\frac{n+1}{2}, \frac{n+1}{2} + 2, \frac{n+1}{2} + 4, \ldots, n-1\right\}, i \in \{1, \ldots, n\} \\ n^2 + (j+1)n + 1 - i, & j \in \left\{\frac{n+1}{2} + 1, \frac{n+1}{2} + 3, \frac{n+1}{2} + 5, \ldots, n-2\right\}, i \in \{1, \ldots, n\} \\ 2n^2 + i, & j = n, i \in \{1, \ldots, n\} \end{cases}$$

For G_i where $i \in \{1, \ldots, n\}$:
Vertex Sum: Case 1: If $i \in \left\{1, \ldots, \frac{n+1}{2} - 1\right\}$, then

$$\begin{aligned} \sum_{v \in G_i} \lambda(v) &= \sum_{j=1}^{n-1} \lambda(v_{i,j}) + \lambda(v_i) \\ &= \sum_{j=1,3,5}^{\frac{n+1}{2}-1} \lambda(v_{i,j}) + \sum_{j=2,4,6}^{\frac{n+1}{2}-2} \lambda(v_{i,j}) + \lambda\left(v_{i,\frac{n+1}{2}}\right) \\ &\quad + \sum_{j=\frac{n+1}{2}+1, \frac{n+1}{2}+3, \frac{n+1}{2}+5}^{n-2} \lambda(v_{i,j}) + \sum_{j=\frac{n+1}{2}+2, \frac{n+1}{2}+4, \frac{n+1}{2}+6}^{n-1} \lambda(v_{i,j}) + \lambda(v_i) \\ &= \sum_{j=1,3,5}^{\frac{n+1}{2}-1} ((j-1)n + i) + \sum_{j=2,4,6}^{\frac{n+1}{2}-2} (jn + 1 - i) + \left((\tfrac{n+1}{2} + 1)n + 1 - i\right) \\ &\quad + \sum_{j=\frac{n+1}{2}+1, \frac{n+1}{2}+3, \frac{n+1}{2}+5}^{n-2} (jn + i) + \sum_{j=\frac{n+1}{2}+2, \frac{n+1}{2}+4, \frac{n+1}{2}+6}^{n-1} ((j+1)n + 1 - i) + \left(\tfrac{n+1}{2}n + 1 - i\right) \\ &= \tfrac{n^3+2n+1}{2} - i \end{aligned}$$

Case 2: If $i \in \left\{\frac{n+1}{2}, \ldots, n\right\}$, then

$$\sum_{v\in G_i} \lambda(v) = \sum_{j=1}^{n-1} \lambda(v_{i,j}) + \lambda(v_i)$$

$$= \sum_{j=1,3,5}^{\frac{n+1}{2}-1} \lambda(v_{i,j}) + \sum_{j=2,4,6}^{\frac{n+1}{2}-2} \lambda(v_{i,j}) + \lambda\left(v_{i,\frac{n+1}{2}}\right)$$

$$+ \sum_{j=\frac{n+1}{2}+1,\frac{n+1}{2}+3,\frac{n+1}{2}+5}^{n-2} \lambda(v_{i,j}) + \sum_{j=\frac{n+1}{2}+2,\frac{n+1}{2}+4,\frac{n+1}{2}+6}^{n-1} \lambda(v_{i,j}) + \lambda(v_i)$$

$$= \sum_{j=1,3,5}^{\frac{n+1}{2}-1} ((j-1)n+i) + \sum_{j=2,4,6}^{\frac{n+1}{2}-2} (jn+1-i) + \left(\frac{n+1}{2}n+1-i\right)$$

$$+ \sum_{j=\frac{n+1}{2}+1,\frac{n+1}{2}+3,\frac{n+1}{2}+5}^{n-2} (jn+i) + \sum_{j=\frac{n+1}{2}+2,\frac{n+1}{2}+4,\frac{n+1}{2}+6}^{n-1} ((j+1)n+1-i) + \left((\frac{n+1}{2}+1)n+1-i\right)$$

$$= \frac{n^3+2n+1}{2} - i$$

Edge Sum:

$$\sum_{e\in G_i} \lambda(e) = \sum_{j=1}^{n} \lambda(e_{i,j})$$

$$= \sum_{j=1,3,5}^{\frac{n+1}{2}-1} \lambda(e_{i,j}) + \sum_{j=2,4,6}^{\frac{n+1}{2}-2} (e_{i,j}) + \sum_{j=\frac{n+1}{2},\frac{n+1}{2}+2,\frac{n+1}{2}+4}^{n-1} \lambda(e_{i,j}) + \sum_{j=\frac{n}{2}+1,\frac{n}{2}+3,\frac{n}{2}+5}^{n-2} \lambda(e_{i,j}) + \lambda(e_{i,n})$$

$$= \sum_{j=1,3,5}^{\frac{n+1}{2}-1} \left(n^2+jn+1-i\right) + \sum_{j=2,4,6}^{\frac{n+1}{2}-2} \left(n^2+(j-1)n+i\right) + \sum_{j=\frac{n+1}{2},\frac{n+1}{2}+2,\frac{n+1}{2}+4}^{n-1} \left(n^2+jn+i\right)$$

$$+ \sum_{j=\frac{n}{2}+1,\frac{n}{2}+3,\frac{n}{2}+5}^{n-2} \left(n^2+(j+1)n+1-i\right) + 2n^2 + i$$

$$= \frac{3n^3+n^2+n-1}{2} + i$$

Magic Sum:

$$\mu(\lambda) = \sum_{v\in G_i} \lambda(v) + \sum_{e\in G_i} \lambda(e)$$

$$= \left(\frac{n^3+2n+1}{2} - i\right) + \left(\frac{3n^3+n^2+n-1}{2} + i\right)$$

$$= 2n^3 + \frac{n^2+3n}{2}$$

For C_n:
Vertex Sum:

$$\sum_{v\in C_n}\lambda(v)=\sum_{i=1}^{n}\lambda(v_i)=\sum_{i=1}^{\frac{n+1}{2}-1}\left(\frac{n+1}{2}n+1-i\right)+\sum_{i=\frac{n+1}{2}}^{n}\left(\left(\frac{n+1}{2}+1\right)n+1-i\right)$$
$$=\frac{n^3+n^2}{2}+n$$

Edge Sum:

$$\sum_{e\in C_n}\lambda(e)=\sum_{i=1}^{n}\lambda(e_i)=\sum_{i=1}^{n}\left(n^2+\left(\frac{n+1}{2}-1\right)n+i\right)$$
$$=\frac{3n^3+n}{2}$$

Magic Sum:

$$\mu(\lambda)=\sum_{v\in C_n}\lambda(v)+\sum_{e\in C_n}\lambda(e)$$
$$=\left(\frac{n^3+n^2}{2}+n\right)+\left(\frac{3n^3+n}{2}\right)$$
$$=2n^3+\frac{n^2+3n}{2}$$

□

The following corollary directly follows from the preceding theorems and provides an immediate consequence of our main findings.

Corollary 3.5. $G(n,n)$ has a C_n-supermagic labeling.

4. Examples

To illustrate the theoretical results established in the previous sections, we present specific examples of C_n-supermagic labeling for different values of n. The following cases demonstrate how the labeling functions ensure a constant magic sum across all C_n-subgraphs in the graph $G(n,n)$.

We consider examples where $n\equiv 0,1,2,3 \pmod 4$, showing that our labeling method holds for various values of n. The tables provided detail the assigned labels for vertices and edges, verifying the correctness of our constructions. Additionally, graphical representations illustrate the labeled structures for better visualization.

These examples not only validate the theoretical framework but also serve as a guide for extending C_n-supermagic labeling to larger and more complex graph families.

Example 4.1. Consider the graph $G(8,8)$. By Theorem 3.1, $\mu(\lambda)=1064$ and C_8-supermagic labeling of $G(8,8)$ is illustrated in Figure 2 and detailed in Table 1.

Table 1. Labeling for the vertices and edges of $G(8,8)$

G_i graphs																	
	v_i	$v_{i,1}$	$v_{i,2}$	$v_{i,3}$	$v_{i,4}$	$v_{i,5}$	$v_{i,6}$	$v_{i,7}$	$e_{i,1}$	$e_{i,2}$	$e_{i,3}$	$e_{i,4}$	$e_{i,5}$	$e_{i,6}$	$e_{i,7}$	$e_{i,8}$	$\mu(\lambda)$
G_1	32	1	16	17	40	41	56	57	65	80	81	96	105	120	121	136	1064
G_2	31	2	15	18	39	42	55	58	66	79	82	95	106	119	122	135	1064
G_3	30	3	14	19	38	43	54	59	67	78	83	94	107	118	123	134	1064
G_4	29	4	13	20	37	44	53	60	68	77	84	93	108	117	124	133	1064
G_5	36	5	12	21	28	45	52	61	69	76	85	92	109	116	125	132	1064
G_6	35	6	11	22	27	46	51	62	70	75	86	91	110	115	126	131	1064
G_7	34	7	10	23	26	47	50	63	71	74	87	90	111	114	127	130	1064
G_8	33	8	9	24	25	48	49	64	72	73	88	89	112	113	128	129	1064
C_8 graph																	
	v_1	v_2	v_3	v_4	v_5	v_6	v_7	v_8	e_1	e_2	e_3	e_4	e_5	e_6	e_7	e_8	$\mu(\lambda)$
C_4	32	31	30	29	36	35	34	33	97	98	99	100	101	102	103	104	1064

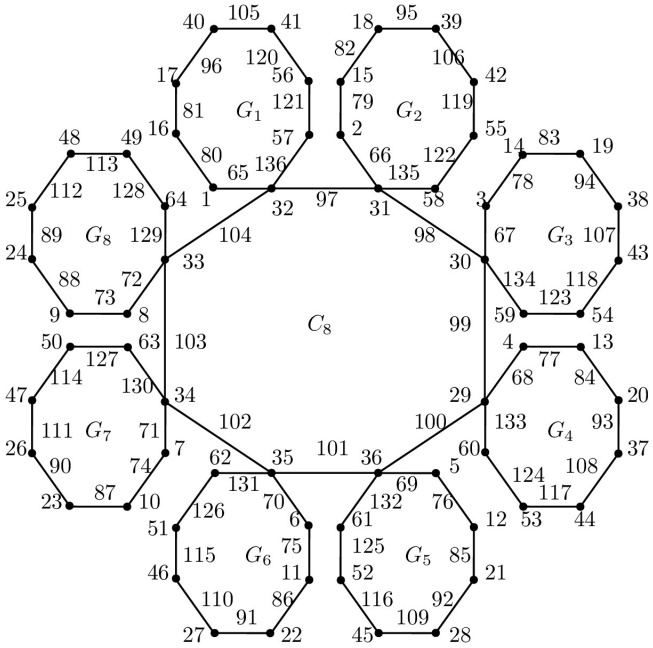

Figure 2. C_8-supermagic labeling of $G(8,8)$

Example 4.2. Consider the graph $G(6,6)$. By Theorem 3.2, $\mu(\lambda) = 456$ and C_6-supermagic labeling of $G(6,6)$ is illustrated in Figure 3 and detailed in Table 2.

Table 2. Labeling for the vertices and edges of $G(6,6)$

G_i graphs												
	v_i	$v_{i,1}$	$v_{i,2}$	$v_{i,3}$	$v_{i,4}$	$v_{i,5}$	$e_{i,1}$	$e_{i,2}$	$e_{i,3}$	$e_{i,4}$	$e_{i,5}$	$e_{i,6}$	$\mu(\lambda)$
G_1	19	1	12	13	30	36	37	48	49	66	67	78	456
G_2	20	2	11	14	29	35	38	47	50	65	68	77	456
G_3	21	3	10	15	28	34	39	46	51	64	69	76	456
G_4	16	4	9	22	27	33	40	45	52	63	70	75	456
G_5	17	5	8	23	26	32	41	44	53	62	71	74	456
G_6	18	6	7	24	25	31	42	43	54	61	72	73	456
C_6 graph													
	v_1	v_2	v_3	v_4	v_5	v_6	e_1	e_2	e_3	e_4	e_5	e_6	$\mu(\lambda)$
C_6	19	20	21	16	17	18	55	56	57	58	59	60	456

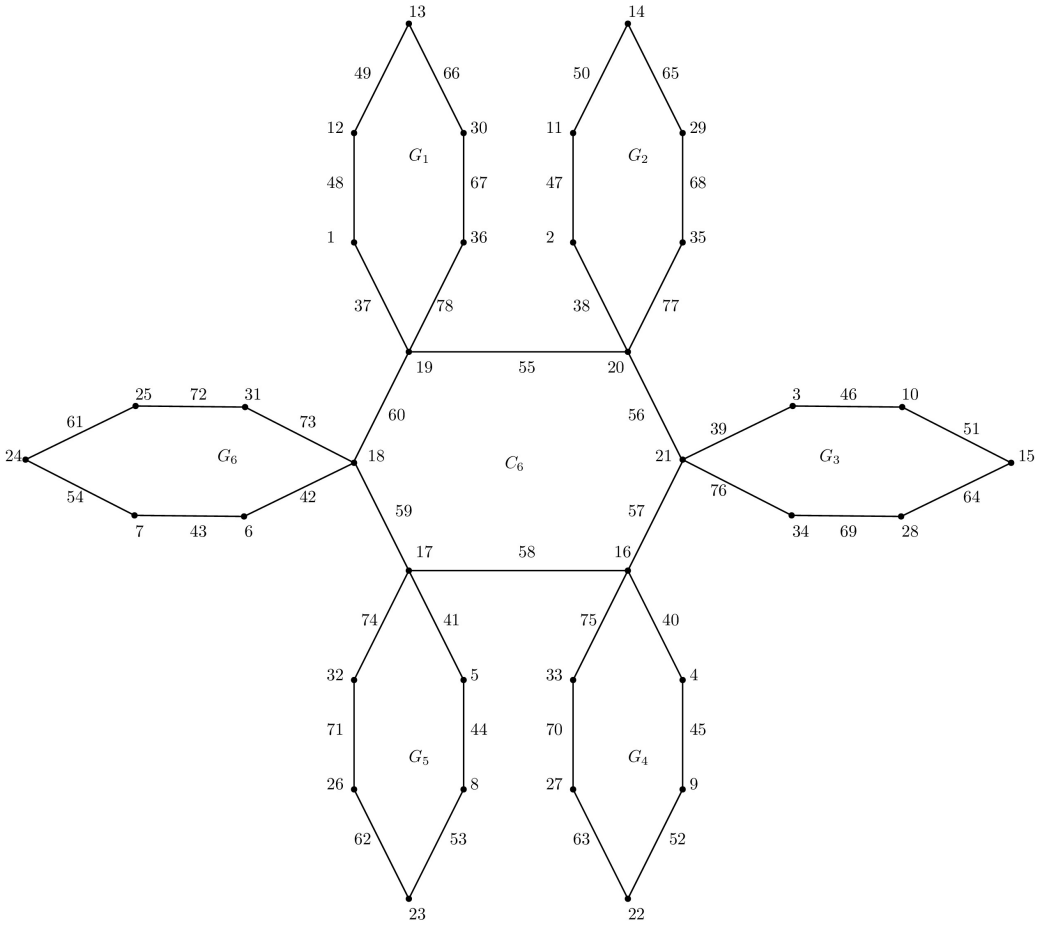

Figure 3. C_6-supermagic labeling of $G(6,6)$

Example 4.3. Consider the graph $G(5,5)$. By Theorem 3.3, $\mu(\lambda) = 270$ and C_5-supermagic labeling of $G(5,5)$ is illustrated in Figure 4 and detailed in Table 3.

Table 3. Labeling for the vertices and edges of $G(5,5)$

G_i graphs											
	v_i	$v_{i,1}$	$v_{i,2}$	$v_{i,3}$	$v_{i,4}$	$e_{i,1}$	$e_{i,2}$	$e_{i,3}$	$e_{i,4}$	$e_{i,5}$	$\mu(\lambda)$
G_1	16	1	10	11	25	30	31	45	46	55	270
G_2	17	2	9	12	24	29	32	44	47	54	270
G_3	18	3	8	13	23	28	33	43	48	53	270
G_4	14	4	7	19	22	27	34	42	49	52	270
G_5	15	5	6	20	21	26	35	41	50	51	270
C_5 graph											
	v_1	v_2	v_3	v_4	v_5	e_1	e_2	e_3	e_4	e_5	$\mu(\lambda)$
C_5	16	17	18	14	15	36	37	38	39	40	270

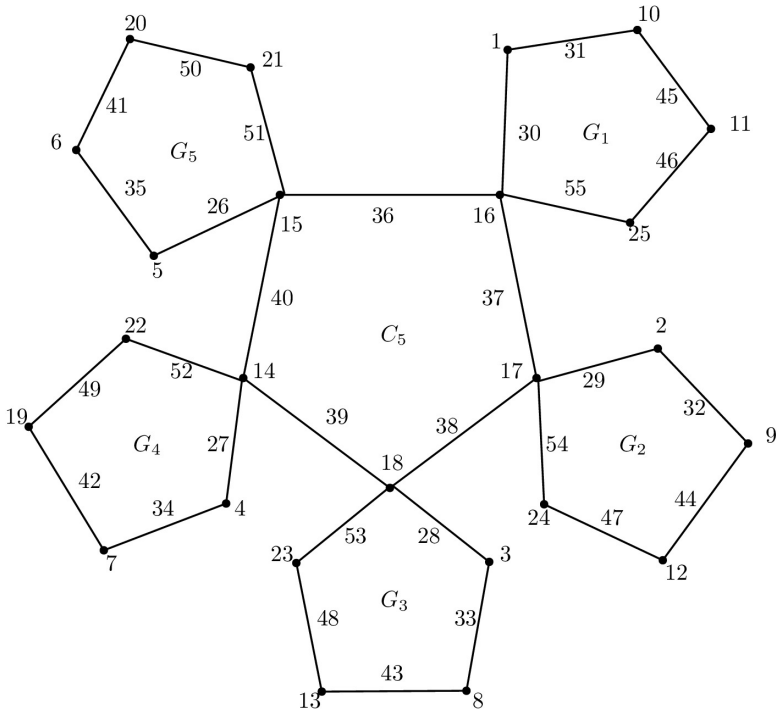

Figure 4. C_5-supermagic labeling of $G(5,5)$

Example 4.4. Consider the graph $G(7,7)$. By Theorem 3.4, $\mu(\lambda) = 721$ and C_7-supermagic labeling of $G(7,7)$ is illustrated in Figure 5 and detailed in Table 4.

Table 4. Labeling for the vertices and edges of $G(7,7)$

G_i graphs															
	v_i	$v_{i,1}$	$v_{i,2}$	$v_{i,3}$	$v_{i,4}$	$v_{i,5}$	$v_{i,6}$	$e_{i,1}$	$e_{i,2}$	$e_{i,3}$	$e_{i,4}$	$e_{i,5}$	$e_{i,6}$	$e_{i,7}$	$\mu(\lambda)$
G_1	28	1	14	15	35	36	49	56	57	70	78	91	92	99	721
G_2	27	2	13	16	34	37	48	55	58	69	79	90	93	100	721
G_3	26	3	12	17	33	38	47	54	59	68	80	89	94	101	721
G_4	32	4	11	18	25	39	46	53	60	67	81	88	95	102	721
G_5	31	5	10	19	24	40	45	52	61	66	82	87	96	103	721
G_6	30	6	9	20	23	41	44	51	62	65	83	86	97	104	721
G_7	29	7	8	21	22	42	43	50	63	64	84	85	98	105	721
C_7 graph															
	v_1	v_2	v_3	v_4	v_5	v_6	v_7	e_1	e_2	e_3	e_4	e_5	e_6	e_7	$\mu(\lambda)$
C_7	28	27	26	32	31	30	29	71	72	73	74	75	76	77	721

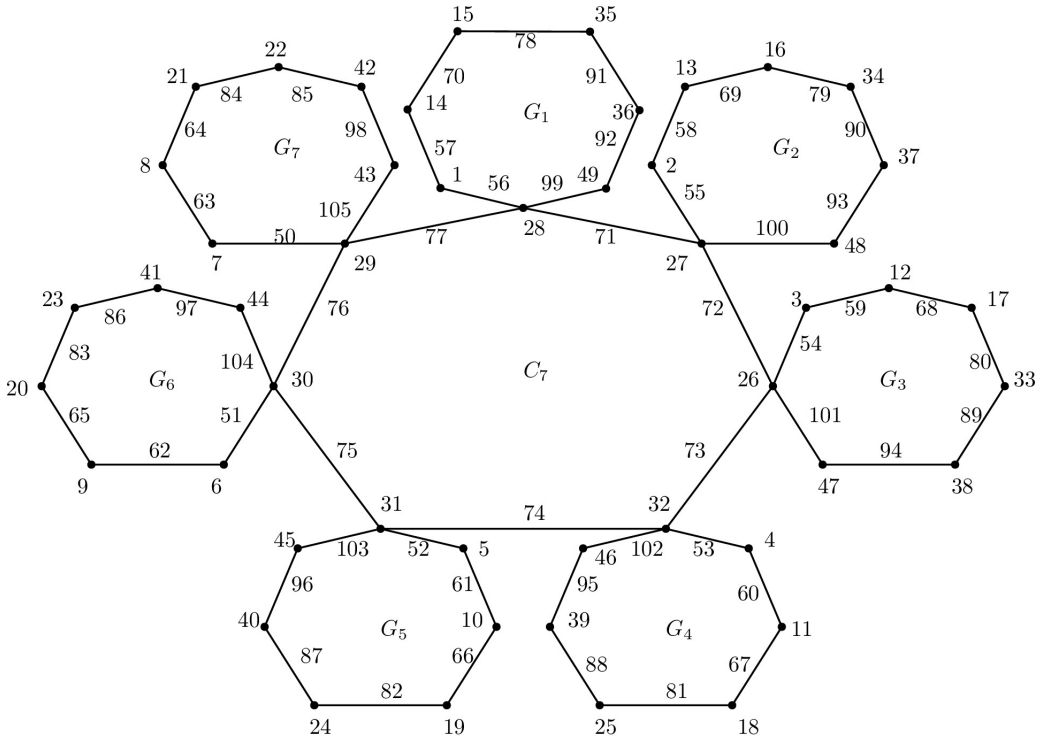

Figure 5. C_7-supermagic labeling of $G(7,7)$

5. Conclusion

In this study, we investigated the C_n-supermagic labeling of the $G(n,n)$ graph, which is constructed by connecting multiple C_n cycle graphs to a central C_n graph. We established necessary conditions and explicit labeling functions that ensure C_n-supermagic properties based on different values of $n \mod 4$.

Our results demonstrate that $G(n,n)$ graphs admit C_n-supermagic labeling for all $n \equiv 0,1,2,3 \pmod 4$. The explicit formulas for vertex and edge labeling guarantee a constant magic sum for each C_n-subgraph, proving the feasibility of such labelings. Furthermore, we provided concrete examples for $n = 5, 6, 7$, and 8, confirming the validity of our theoretical findings.

This research contributes to the broader field of graph labeling, offering insights into magic and supermagic properties of structured graphs. Future work could explore extending supermagic labeling to more complex graph families, such as bipartite cycle graphs, higher-dimensional structures, or graphs with varying connectivity patterns. Additionally, investigating the applications of these labeling techniques in cryptography, network security, and combinatorial optimization could provide practical insights. Further research might also focus on developing efficient algorithms for generating supermagic labelings in larger graphs and exploring the relationship between graph labeling and other graph-theoretical properties, such as graph coloring or decomposition.

Author Contributions

The author read and approved the final version of the paper.

Conflicts of Interest

The author declares no conflict of interest.

Ethical Review and Approval

No approval from the Board of Ethics is required.

References

[1] A. Rosa, *On certain valuations of the vertices of a graph*, in: P. Rosenstiehl (Ed.), Theory of Graphs, International Symposium, Rome, İtay, 1966, pp. 349–355.

[2] D. K. Gurjar, A. Krishnaa, *Labeled paths in cryptography*, International Journal of Mathematics, Game Theory and Algebra 30 (4) (2021) 173–194.

[3] A. U. Maheswari, A.S. Purnalakshimi, *Graph labelling and chaldean numerology in cryptography*, Res Militaris 13 (2) (2023) 6564–6571.

[4] R. Jegan, P. Vijayakumar, V. D. Ambethkumar, P. Vijay, E. M. Onyema, *Encryption and decryption of a word into weighted graph using super-edge anti-magic total labeling of bi-star graph*, Journal of Discrete Mathematical Sciences and Cryptography 26 (5) (2023) 1355–1365.

[5] H. R. Medini, S. D'Souza, D. Nayak, P. G. Bhat, *Encoding and decoding of messages using graph labeling and complement of a graph*, Global and Stochastic Analysis 11 (1) (2024) 1–13.

[6] H. R. Medini, S. D'Souza, D. Nayak, P. G. Bhat, *Multifaceted coding of messages using the concepts of graph theory*, IAENG International Journal of Computer Science 51 (2) (2024) 143–153.

[7] S. Pirzada, A. Dharwadker, *Applications of graph theory*, Journal of the Korean Society for Industrial and Applied Mathematics 11 (4) (2007) 19–38.

[8] L. H. Hsu, C. K. Lin, Graph theory and interconnection networks, 1st Edition, CRC Press, 2008.

[9] V. Latchoumanane, M. Varadhan, *Antimagic labeling for product of regular graphs*, Symmetry 14 (6) (2022) 1235.

[10] A. ELrokh, M. M. A. Al-Shamiri, M. M. A. Almazah, A. A. El-hay, *A novel problem for solving permuted cordial labeling of graphs*, Symmetry 15 (4) (2023) 825.

[11] Y. F. Ashari, A. N. M. Salman, R. Simanjuntak, *On forbidden subgraphs of (K2, H)-sim-(super)magic graphs*, Symmetry 13 (8) (2021) 1346.

[12] Y. F. Ashari, A. N. M. Salman, R. Simanjuntak, A. Semaničová-Feňovčíková, M. Baca, *On (F, H)-sim-magic labelings of graphs*, Electronic Journal of Graph Theory and Applications 11 (1) (2023) 49–64.

[13] M. Azeem, *Cycle-super magic labeling of polyomino linear and zig-zag chains*, Journal of Operations Intelligence 1 (1) (2023) 67–81.

[14] K. Iyappan, A. Loganathan, D. Kumar, *H-E-Supermagic labelings of some families of graphs*, Nonlinear Studies 31 (3) (2024) 957–963.

[15] A. Gutiérrez, A. Llado, *Magic covering*, Journal of Combinatorial Mathematics and Combinatorial Computing 55 (2005) 43–56.

Journal of New Results in Science
dergipark.org.tr/en/pub/jnrs
Open Access

ISSN: 1304-7981 14 (2) (2025) 100-114 doi.org/10.54187/jnrs.1651291

Synthesis of Novel Asymmetric Bis-Hydrazone Compounds Containing Indenoquinoxaline and Phenolic Moieties and Colorimetric Investigation of Chemosensing Properties for Various Ions

Fatma Aydın[1]

Article Info
Received: 04 Mar 2025
Accepted: 08 Aug 2025
Published: 31 Aug 2025
Research Article

Abstract −Novel three asymmetric bis-hydrazone compounds, 2-((11*H*-indeno[1,2-b] quinoxaline-11-ylidene)hydrazone)methyl-phenol, 4-((11*H*-indeno[1,2-b]quinoxalin-11-ylidene)hydrazone) methyl-benzene-1,3-diol, 1-((11*H*-indeno[1,2-b]quinoxalin-11-yidene)hydrazone)methyl-naphthalen-2-ol, containing indenoquinoxaline and phenolic moieties as sensors (5a-c), were designed and synthesized in high yield (82-87%). Their structures were characterized by FT-IR, ^{1}HNMR, ^{13}C NMR, and MS spectroscopic methods. Their colorimetric sensor properties were investigated, and changes in the absorption of the UV-vis spectrum when interacting with some anions and cations in aqueous acetonitrile solution, as well as a well-defined color change detectable with the naked eye, were observed. While no change was observed with the addition of anions such as Cl^-, Br^-, I^-, SCN^-, OCl^-, HSO_4^-, $H_2PO_4^-$, HPO_4^{2-} and PO_4^{3-} to the host solution (5a-c), the addition of the F^-, CN^-, OH^-, and OAc^- anions was resulted with a red shift of the charge-transfer absorbance band accompanied by a color change from light yellow to purple-blue. In addition, the sensing behavior of receptors for different metal ions, such as Cu^{2+}, Ni^{2+}, Zn^{2+}, Co^{2+}, Mn^{2+}, Pb^{2+}, Fe^{2+}, Fe^{3+}, Hg^{+2}, Ag^+, and Sn^{2+} in aqueous acetonitrile solution was investigated, and they showed receptor properties against Cu^{2+}, Ni^{2+}, Co^{2+}, and Zn^{2+} ions among them.

Keywords − *Indenoquinoxaline, asymmetric bis-hydrazones, ion sensors, UV-vis spectrum, naked eye*

1. Introduction

Anions play an essential role in the daily life of humans and animals as well as in the growth of plants. Several anions have a significant role in chemical reactions, biological metabolisms, pharmaceutical processes, and many other processes [1,2]. However, the scarcity and excess of biologically important ions such as fluoride, acetate, and phosphate lead to various metabolic disorders. Detection of fluoride anions among halogen anions is a significant research area in both the detection of diseases such as fluorosis, kidney disease, bone and skeletal cancer due to the excess of fluoride ions, and beneficial effects such as prevention of dental caries and treatment of osteoporosis [3,4]. Phosphate (PO_4^{3-}) is one of the main nutrients plants require for proper growth [5]. It is also an anion found naturally in all living organisms in soils and aquatic environments [6,7]. Acetate ions (OAc^-) are more important in living organisms as acetyl coenzyme [8]. Although cyanide ions are beneficially applied in the gold mining, electroplating, and metal plating industries, cyanide ions are known to play a frightening role as toxins in the environmental and biological fields [9,10]. Additionally, humans and animals can absorb cyanide from consuming vegetables that contain cyanogenic glycoside derivatives, such as amygdalin [11]. Metal ions are essential elements in the lives of humans, animals, and plants. Furthermore,

[1]faydin@comu.edu.tr (Corresponding Author)
[1]Department of Chemistry, Sciences Faculty, Çanakkale Onsekiz Mart University, Çanakkale, Türkiye

metal ions play significant roles in numerous fields, including chemical, biochemical, geochemical, industry, and material science [12]. However, their toxic effects should also be considered [13]. Both copper (Cu) and Zinc (Zn) are metals required in protein production for the growth of plants, and they play essential roles in ethylene sensing and oxidative stress production [14]. Cobalt (Co) creates a toxic effect on plants in high concentrations and causes pale-colored leaves and loss of leaves [15]. The element nickel (Ni) is a crucial plant micronutrient because it activates the urease enzyme [16].

Even if instrumental analysis is used for ion analysis, it has some negative features, such as difficulty in portability to the field, the need for skilled technicians, and expensive and complex instrumentation. Recently, to ensure practicality, the synthesis of new compounds has been focused on by designing colorimetric sensors that can be easily observed with the naked eye [17–20].

Indenoquinoxaline derivatives, an important group of aza-polycyclic compounds, are important compounds of N-heterocycles, a large conjugation tetracyclic structure [21–23]. They form useful intermediates in organic compound synthesis, such as spiro indenoquinoxaline pyrrolizidines [24] and spirolactonnes [25]. Their spiro compounds are also used as α-glucosidase inhibitors [26], anticancer [27], and antibacterial agents [28]. Of these, 11H-indeno[1,2-b]quinoxalin-11-one is a ketone compound, and its hydrazone derivative can be formed with hydrazine hydrate [29], and this derivative is used in various reactions [30,31]. Similarly, indeno-1-one [2,3-b]quinoxaline is an effective inhibitor for the corrosion of mild steel [32].

In the current work, asymmetric bis-hydrazone compounds featuring an indenoquinoxaline moiety (5a-5c) were synthesized utilizing phenolic aldehydes (Scheme 1). The structures of these compounds were subsequently characterized through various spectroscopic techniques. Besides, their colorimetric sensor properties for both various anions and cations were investigated by their spectral responses changed in the UV-vis absorption spectrum. The anion recognition properties of these compounds toward F^-, CN^-, OH^-, OAc^- in the presence of other anions, such as Cl^-, Br^-, I^-, SCN^-, OCl^-, HSO_4^-, $H_2PO_4^-$, HPO_4^{2-} and PO_4^{3-} in acetonitrile-water solution were explored using the UV-vis molecular absorption spectroscopy and also by naked-eye detection. Besides, by examining the receptor detection behaviors against different metal ions (Cu^{2+}, Ni^{2+}, Zn^{2+}, Co^{2+}, Mn^{2+}, Pb^{2+}, Fe^{2+}, Fe^{3+}, Hg^{2+}, Ag^+, and Sn^{2+}), in aqueous acetonitrile solution, their interactions with the UV-vis spectroscopic method and a naked eye detector were investigated. Among them, it was observed that the new title compounds (5a-c) were selected for Cu^{2+}, Ni^{2+}, Zn^{2+}, and Co^{2+} transition metal ions.

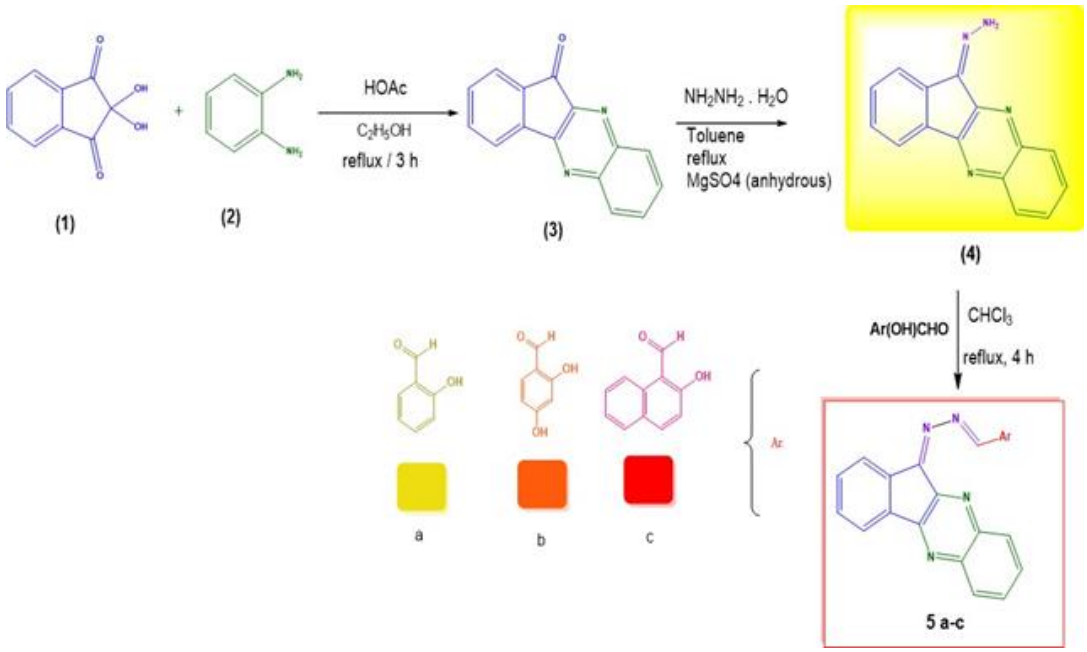

Scheme 1. The synthesis of the novel asymmetric bis-hydrazone compounds, **(5a-c)**

2. Experimental Section

2.1. Reagents and Techniques

All chemicals, such as ninhydrin, o-phenylenediamine, hydrazine hydrate, salicylaldehyde 2,4-dihydroxybenzaldehyde, 2-hydroxy-1-naphthaldehyde, were purchased from Sigma-Aldrich, Merck Chemical Companies, and ethyl acetate, tetrahydrofuran, ethanol, chloroform, and acetonitrile were used as solvents without further purification. In the titration experiments, all the anions and cations were added in the form of tetra-n-butyl ammonium salts (TBAX, X: F, Cl, Br, I, SCN, OCl, HSO_4, PO_4, HPO_4, H_2PO_4, CN, OAc, OH), which were purchased from Argos, Sigma-Aldrich Chemical, and stored in a vacuum desiccator before use. The stock solutions of different metal ions were made from acetate salts and chloride salts. Reactions during the synthesis of the title compound were monitored by thin-layer chromatography (TLC) on silica-gel 60 F254 plates (Merck) and a UV lamp. Using a capillary tube, the melting point was measured with an Electrothermal IA 9100 apparatus. Elemental analysis was conducted on a LECO-932 CHNS analyzer. FT-IR analysis was performed using a Perkin Elmer Spectrum 100 FT-IR instrument with an ATR apparatus of 4000-650 cm^{-1}. The UV-vis spectra were measured using a Perkin Elmer 25 spectrometer. ^{1}H NMR and ^{13}C NMR spectra were recorded on a JEOL ECX- 400 NMR spectrometer operating at 400 and 100 MHz, respectively, using DMSO-d6 as solvent. MS analyses were performed with a Shimadzu LC-MS/MS 8040 liquid chromatograph mass spectrometer with an electrospray ionization source.

2.2. General Procedure for Synthesis of the Novel Asymmetric Bis-hydrazone Compounds (5a-c)

Novel compounds (5a-c) were synthesized according to the steps outlined in Scheme 1. Firstly, the starting material 11H-indeno[1,2-b]-11-one (3) was prepared through the reaction of ninhydrin (1) with 1,2-diaminobenzene (2) according to the procedure reported in the literature [33]. m.p. 107-108 °C, FT-IR, cm^{-1}: 1726 (C=O), 1608, 1506 (C=C_{arom}), 1189 (C=N), 863, 771, 734 (C-C_{arom}).

Secondly, in a round bottom flask, 11H-indeno[1,2-*b*]-11-one (3) (0.23 g, 1.02 mmol) was dissolved in 20 mL of toluene. Hydrazine hydrate (0.840 mL, 17.2 mmol) was dropped slowly into the stirred solution. After adding anhydrous $MgSO_4$ (ca. 2 g), the mixture was refluxed for 6 h. The reaction mixture was cooled and filtered, and the residue was washed with petroleum spirit (40-60 °C fraction). The filtrate and the washings were combined. After that, the obtained lemon-yellow color solid 11-hydrazone-11H-indeno[1,2-b]quinoxaline (4) was filtered, dried, and recrystallized from chloroform. m.p. 107-108 °C, FT-IR, cm-1: 3411, 3310 (N-NH_2), 1608 (C=N), 1506 (C=C_{arom}), 1189 (C=N_{arom}), 863, 771, 734 (C-C_{arom}).

To a solution of 11-hydrazone-11H-indeno[1,2-b]quinoxaline (4), (0.06275 g, 0.25 mmol) in chloroform (10 mL) was added the solution of various aromatic hydroxy aldehydes, 5a-c (0.25 mmol) in chloroform (10 mL) at room temperature and refluxed by stirring. The progress of the reaction was monitored by thin-layer chromatography (TLC) analysis. After the reaction, the mixture was cooled, and the precipitate was collected by filtration, washed with cold ethanol, and dried overnight under a vacuum. The crystallization of these crude products from tetrahydrofuran yielded new pure products (5a-c) with different colors. The physical parameters were determined, and spectroscopic methods were used to characterize the structures.

2-((11H-indeno[1,2-b] quinoxaline-11-ylidene)hydrazono)methyl)-phenol (5a)

Orange-yellow needles, yield: 0.0762 g (87%), mp: 212 °C; UV-vis λ_{max}: 394 and 289 nm in CH_3CN. $C_{22}H_{14}N_4O$; elemental analysis calcd. (found) %: C, 75.42 (75.37); H, 4.03 (4.06); N, 15.99 (15.97); O, 4.57 (4.61). FT-IR, (cm^{-1}): 3230 (O-H), 3143, 3058, 3013 (C_{arom} _H), 2944 (-NC-H), 1627 (CH=N-), 1531 (C_{arom}=N), 1227 (C=C), 1023 (C-O), 745 (C=C). ^{1}H-NMR (400. MHz; DMSO-d6; δ ppm): 12.42 (s, 1H, –OH), 8.90 (s, 1H, –CH=N), 8.35 - 6.94 (m, 12H, Ar–H). ^{13}C-NMR (100 MHz, DMSO-d6, δ ppm): 167.4

(C_{ipso}=N), 160.8 (C_{arom}-O), 156.8 (-CH=N), 154.7, 147.0, 142.1, 141.8 (C_{arom}=N), 137.8-117.7 (C_{arom}); ESI: m/z 351 (M^+).

4-((11H-indeno[1,2-b] quinoxalin-11-ylidene)hydrazono)methyl)benzene-1,3-diol (5b)

Brick red solid, yield: 0.0752 g (82%), mp: 292 °C; UV-vis λ_{max}: 411 and 286 nm in CH_3CN. $C_{22}H_{14}N_4O_2$; elemental analysis calcd. (found) %: C, 72.22 (72.06); H, 3.85 (3.89); N, 15.29 (15.25); O, 8.73 (8.79). FT-IR, (υ, cm^{-1}): 3340 (O-H), 3225 (O-H), 3061 (C_{arom}—H), 2931 (-NC-H), 1629 (-CH=N-), 1528, 1505 (C_{arom}=N), 1224 (C=C), 1025 (C-O), 755 (C=C). ^{1}H-NMR (400 MHz; DMSO-d6; δ ppm): 12.46 (s, 1H, –OH), 10.43 (s, 1H, –OH), 8.90 (s, 1H, –CH=N), 7.98 - 6.37 (11H, Ar–H). ^{13}C-NMR (100 MHz, DMSO-d6, δ ppm): 167.9 (C_{ipso}=N), 164.1 (C_{arom}-O), 163.0 (C_{arom}-O), 154.8, (-CH=N), 154.6, 141.8, 141.5, 138.6 (C_{arom}=N), 137.2-103.4 (C_{arom}); ESI: m/z 367 (M^+).

1-((11H-indeno[1,2-b] quinoxalin-11-ylidene)hydrazono)methyl-naphthalen-2-ol (5c)

Red solid, yield: 0.0841 g (84%), mp: 281 °C; UV-vis λ_{max}: 444, 289 nm in CH_3CN. $C_{26}H_{16}N_4O$; elemental analysis calcd. (found) %: C, 77.99 (77.92); H, 4.03 (4.11); N, 13.99 (13.93); O, 4.00 (4.05). FT-IR, (cm^{-1}): 3371 (O-H), 3123, 3057 (C_{arom} —H), 3007 (NC-H), 1619 (CH=N), 1526 (C_{arom}=N), 1288 (C=C), 1024 (C-O), 769 (C=C). ^{1}H-NMR (400 MHz; DMSO-d6; δ ppm): 14.00 (s, 1H, –OH), 10.00 (s, 1H, –CH=N), 8.52 – 7.32 (m, 14H, Ar–H). ^{13}C-NMR (100 MHz, DMSO-d6, δ ppm): 164.1 (C_{ipso}=N), 163.3 (C_{arom}-O), 162.4 (-CH=N), 157.8, 154.9, 154.6, 146.9 (C_{arom}=N), 137.5-108.9 (C_{arom}); ESI: m/z 401 (M^+).

3. Results and Discussion

3.1. Spectral Characterization

The structure of novel title compounds 5a-c was characterized by FT-IR, ^{1}H-NMR, ^{13}C-NMR, and MS spectra. In the FT-IR spectra of the title compounds 5a-c, the sharp peaks observed at 1627, 1629, and 1619 cm^{-1}, respectively, belong to the CH=N stretching vibrations, confirming the formation of the hydrazomethine units [34]. Aromatic C-H stretching vibrations located at 3013, 3061, and 3057 cm^{-1}, respectively, confirm the presence of indeno-quinoxaline units, respectively. Moreover, the peaks observed at 1227 and 1023 cm^{-1}, 1224 and 1025 cm^{-1}, and 1288 and 1024 cm^{-1} belong to the aromatic C=C and C-O stretching vibrations of title compounds 5a-c, respectively, and highlight phenolic units (Figure S1-S3).

UV-vis spectral measurements of the title compounds (5a-c) were studied in aqueous acetonitrile solution. The absorption spectra of the title compounds 5a-c in CH_3CN-H_2O were characterized by a UV-vis spectrophotometer (Figure 1). Compounds 5a and 5b exhibit the two strong absorbance bands at 394 and 289 nm and 411 and 286 nm due to the contribution to internal-charge transfer (ICT) of the indenoquinoxaline and the phenolic moiety as mono-hydroxy and di-hydroxy units, respectively. The compound 5c exhibits the three strong absorbance bands at 444, 289, and 230 nm due to different conjugations of the mono-hydroxy naphthyl moiety (Figure S4).

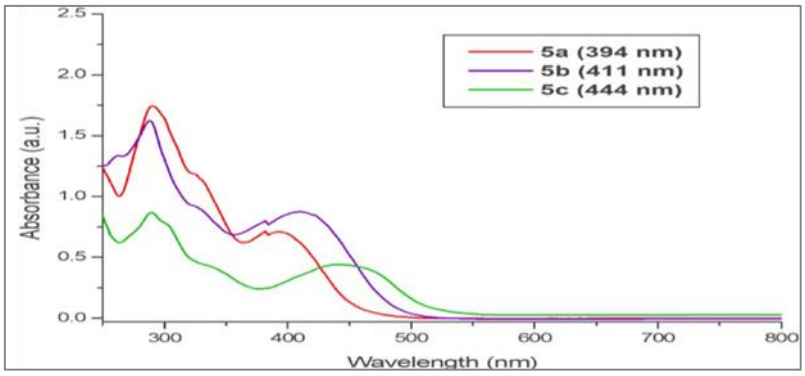

Figure 1. The UV-vis spectrum of the title compounds **(5a-c)**

^{1}H and ^{13}C NMR spectra of the title compounds, 5a-c were obtained in DMSO-d6 (Figure 2-7). In the ^{1}H-NMR spectra peaks belonging to the protons of phenolic hydroxyl groups (-OH) were seen at δ 12.42 ppm, 12.46, 10.43 ppm, and 14.00 ppm for the title compounds 5a-c, respectively, due to intermolecular interactions of the –OH proton with the polar aprotic solvent like DMSO-d6. The single peaks observed at δ 8.90, 8.90, and 10.00 ppm verified the formation of the –CH=N functional groups of the title compounds 5a-c, respectively. Multiple aromatic protons observed around 8.90-6.37 ppm supported that asymmetric bis-aromatic hydrazone compounds (5a-c) were synthesized. (Figure 2-4).

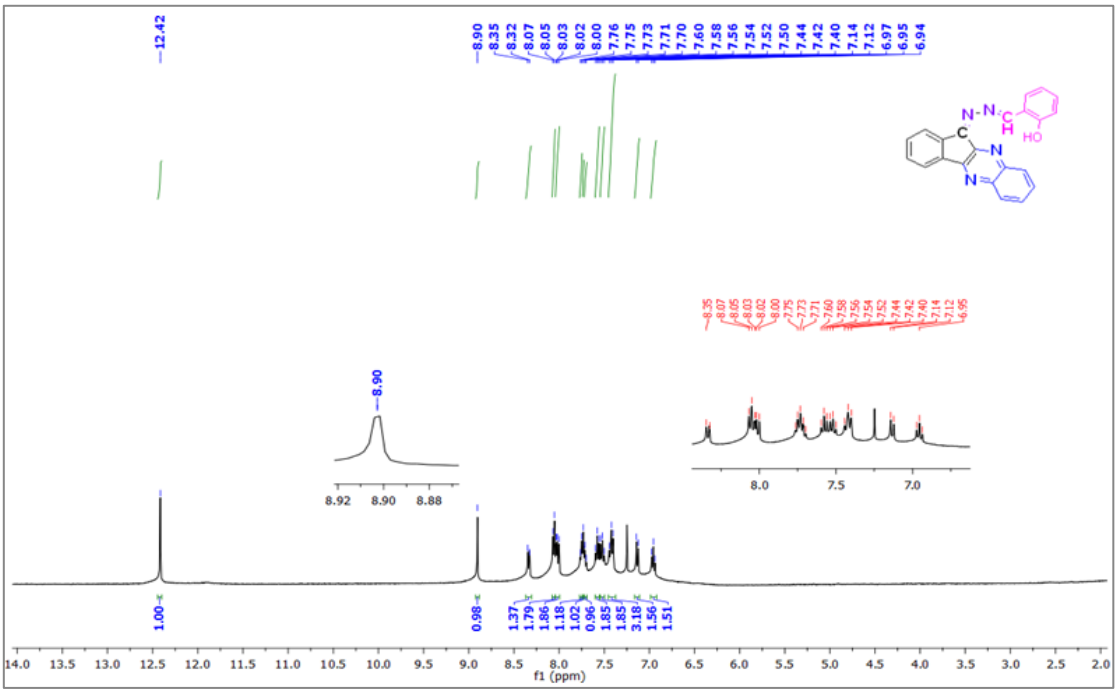

Figure 2. The ^{1}H-NMR spectrum of the 2-((11H-indeno[1,2-b] quinoxalin-11-ylidene)hydrazono)methyl-phenol (**5a**)

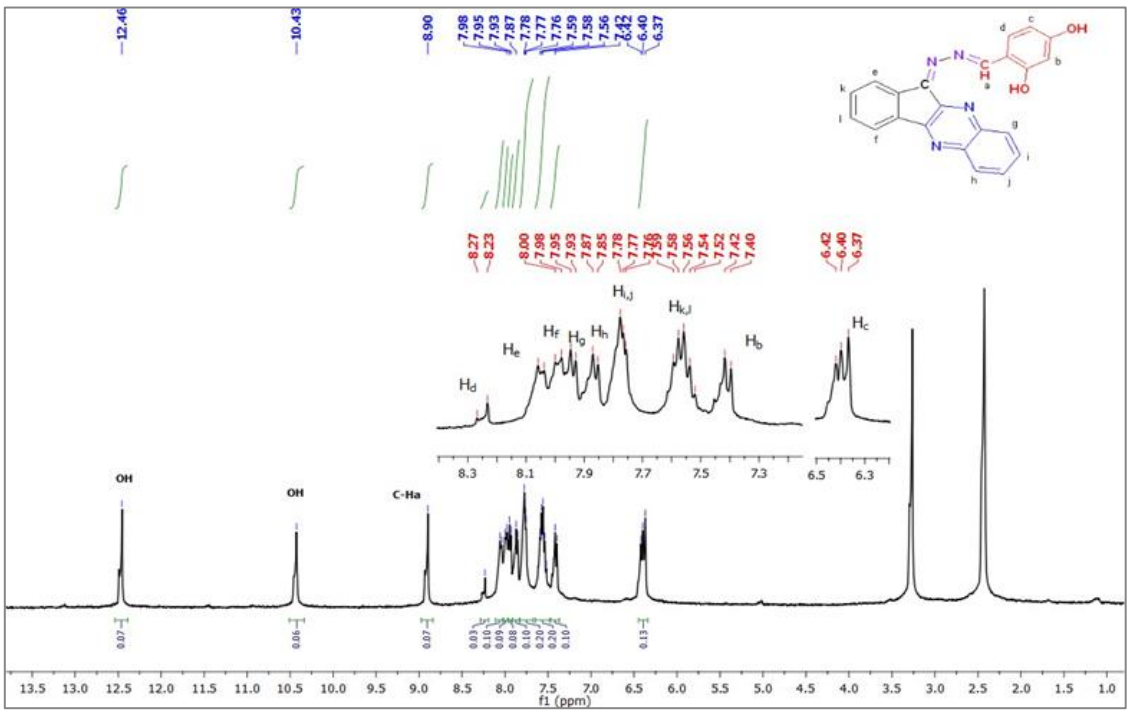

Figure 3. The ^{1}H-NMR spectrum of the 4-((11H-indeno[1,2-b] quinoxalin-11-ylidene)hydrazono)methyl-benzene-1,3-diol **(5b)**

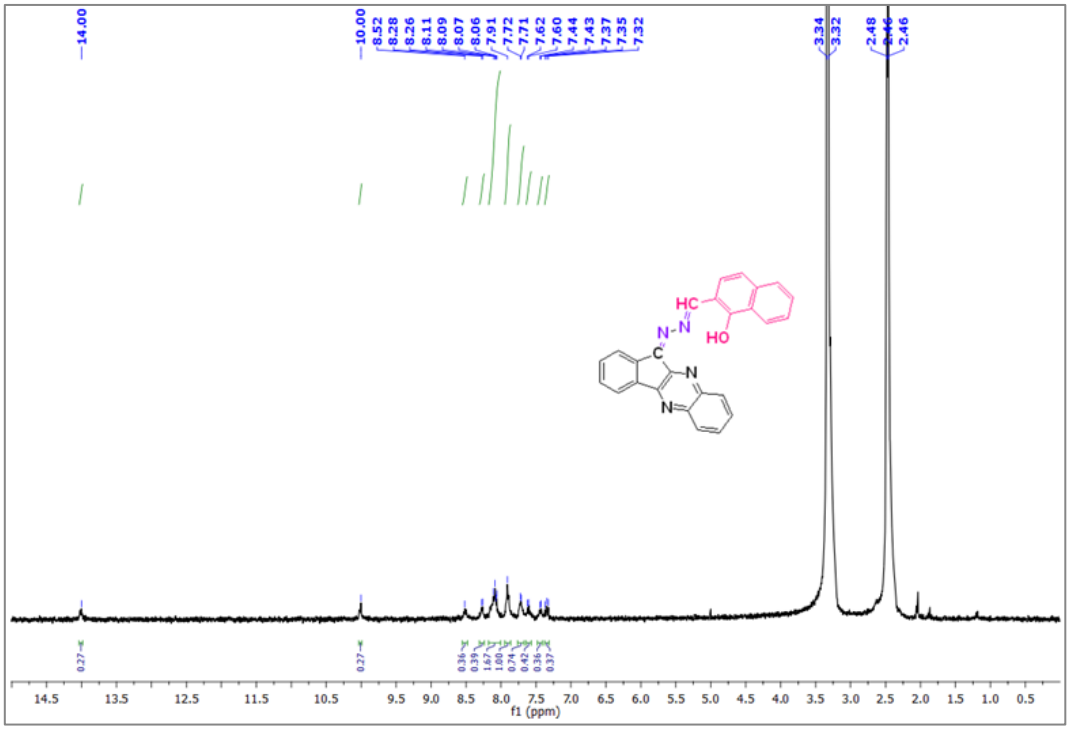

Figure 4. The ^{1}H-NMR spectrum of the 1-((11H-indeno[1,2-b] quinoxalin-11-ylidene)hydrazono)methyl-naphthalen-2-ol **(5c)**

In the ^{13}C-NMR spectra, the carbon atom signals of the C=N and CH=N groups were observed at 167.4 and 156.8 ppm, 167.9 and 154.8 ppm, 164.1 and 162.4 ppm for the 5a-c, respectively. In addition to multiple aromatic carbon peaks, the peaks of the phenolic carbons were observed at around 160 ppm. (Figure 5-7).

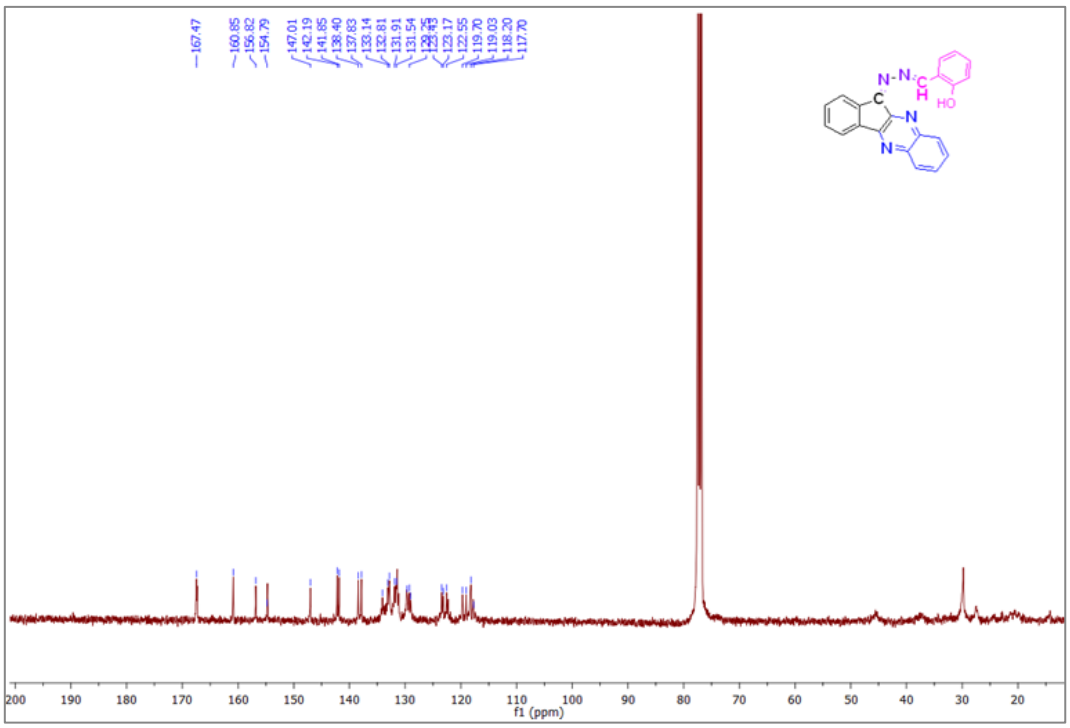

Figure 5. The ^{13}C-NMR spectrum of the 2-((11H-indeno[1,2-b] quinoxalin-11-ylidene)hydrazono)methyl-phenol **(5a)**

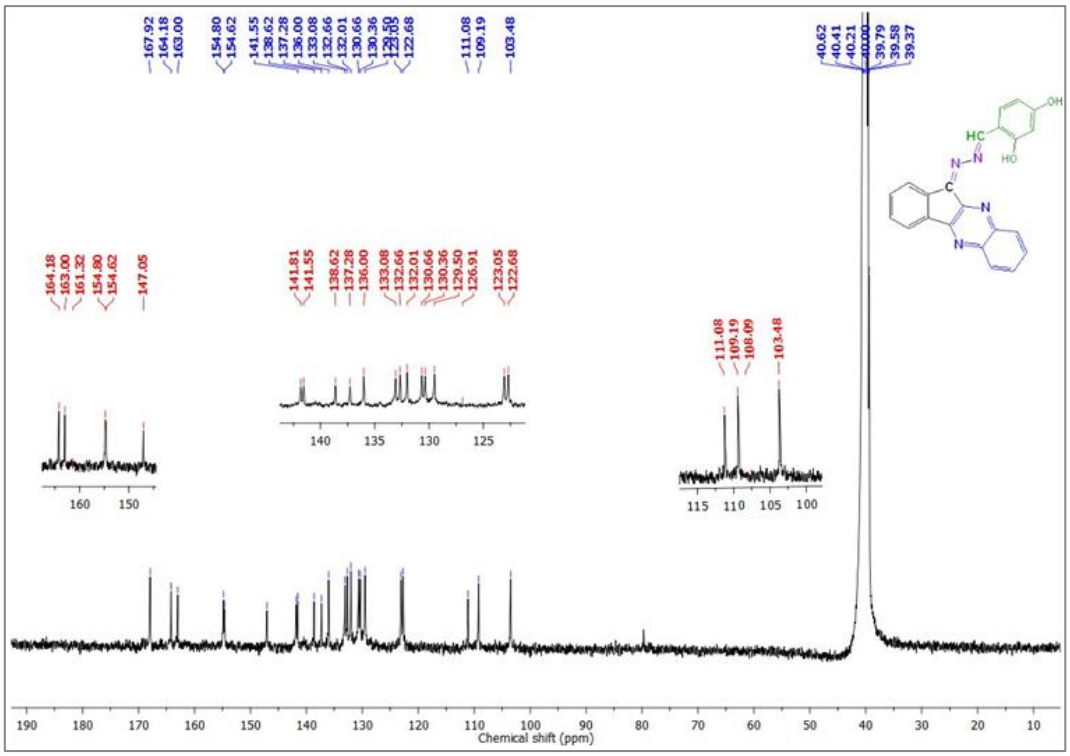

Figure 6. The ^{13}C-NMR spectrums of the 4-((11H-indeno[1,2-b] quinoxalin-11-ylidene)hydrazono)methyl-benzene-1,3-diol **(5b)**

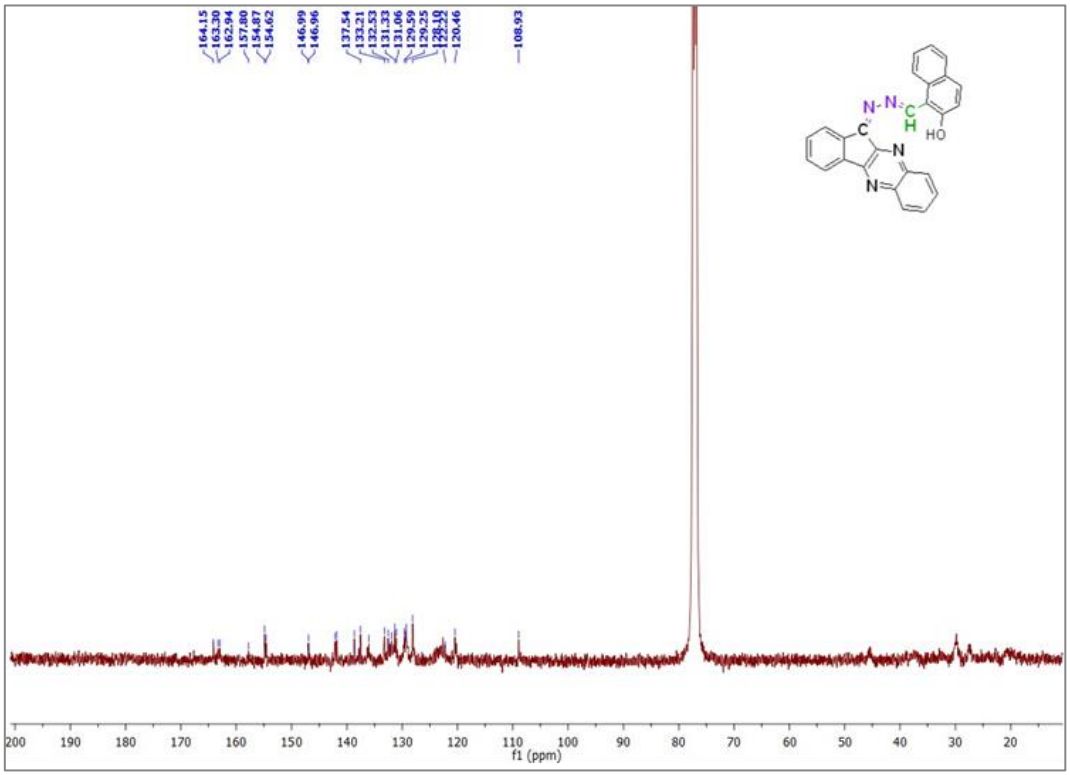

Figure 7. The ^{13}C-NMR spectrums of the 1-((11H-indeno[1,2-b] quinoxalin-11-ylidene)hydrazono)methyl-naphthalen-2-ol **(5c)**

The mass spectrums of title compounds (5a-c) showed molecular ion peaks at m/z 351, 367, and 401 corresponding to the formula $C_{22}H_{14}N_4O$, $C_{22}H_{14}N_4O_2$, and $C_{26}H_{16}N_4O$, respectively, and the synthesis of them also was confirmed (Figure S5-S7).

3.2. Colorimetric Sensing Studies

3.2.1. Interaction of Anions with Title Compounds (5a-c) as UV-vis Spectroscopic Studies

Various anions and cations are fundamental for maintaining the life span of plants, animals, and humans, positively or negatively. Therefore, their qualitative and quantitative analysis are important. The newly synthesized compounds (5a-c), which were structurally characterized, also have potential anion binding sites due to the phenolic proton and hydrazomethine units. Considering the hydrogen binding properties due to different hydroxyl groups and indenoquinoxaline units, the interaction of the title compounds with several anions was investigated. To visualize the qualitative recognition events of selected anions of these synthesized compounds, the UV-vis spectroscopic methods and practical photographic techniques were used. Due to their insolvency in the water of the title compounds (5a-c), studying the interaction of anions in the acetonitrile-water (V/V; 9:1) mixture method was considered.

The changes in the UV-vis absorption spectra as well as the colors of the complexes upon interaction with thirteen anions as their TBA salts (X: F^-, Cl^-, Br^-, I^-, OCl^-, SCN^-, HSO_4^-, $H_2PO_4^-$, HPO_4^{2-}, PO_4^{3-}, OAc^-, CN^-, and OH^-) are displayed in Figure 6. Among the studied anions F^-, CN^-, OH^-, and partly OAc^- induce charge, albeit to different extents, due to the differences in their basic capacity. The title compounds (5a-c) displayed absorbance in the 350-450 nm region. To determine and visualize the recognition events of the selected anions, solutions were added to each sample solution in equal amounts (5a-c), and their absorbance values were measured by using a UV-vis spectrophotometer. A shift in the maximum absorbance of the UV-vis spectrum of each title compound (5a-b) from approximately 400 nm to 536-638 nm was observed for F^-, CN^-, and OH^- anions, while no change was observed for the other anions. At the same time, an immediate color change was observed from yellow to different colors such as purple, dark purple, light blue, and dark blue for F^-, CN^-, and OH^- anions, respectively. Addition of other anions (PO_4^{3-}, HPO_4^{2-}, $H_2PO_4^-$, OAc^-, OCl^-, SCN^-, HSO_4^-, Cl^-, Br^-, and I^-) to the solutions of the title compounds did not cause any change in the sample color (Figure 8 (5a-c)). In compound 5b, absorption and color change were observed due to interaction with F^-, CN^-, and OH^- anions, as well as OAc^- anion due to a second hydroxyl functional group (Figure 8 (5b)). These color changes, which are easy to observe with the naked eye and provide practical convenience, were also photographed under natural light and UV lamp (365 nm).

Unlike the interactions of F^- and OH^- anions, different absorption and color formation were observed as a result of the nucleophilic reaction of cyanide anion to the carbon atom of the hydrazone group and the subsequent transfer of the phenolic proton to the neighboring nitrogen anion via an intramolecular hydrogen bond [35,36]. As shown in Figure 6, on results of the interaction of fluoride, cyanide, and hydroxyl anions with receptors (5a-c), new absorbance peaks were observed to appear in the range of 530-640 nm maximum, with the original peak disappearance of the original peak at 394, 411, and 444 nm, respectively. At the same time, as indicated in the photograph, the marked change in colors also allowed F^-, CN^-, and OH^- anions to be detected with the naked eye. In compound 5b, absorption and color change were observed due to interaction with OAc^- anion, due to a second hydroxyl functional group (Table 1).

Table 1. Changes in the wavelength (nm) of the absorption maximum (λ_{max}) of the title compounds (5a-c) in acetonitrile for F^-, CN^-, OH^- and OAc^- anions

Sample/anions λ_{max} (nm)	**Free**	**F^-**	**CN^-**	**OH^-**	**OAc^-**
5a	394	536	618	558	
5b	411	558	612	568	545
5c	444	602	638	602	

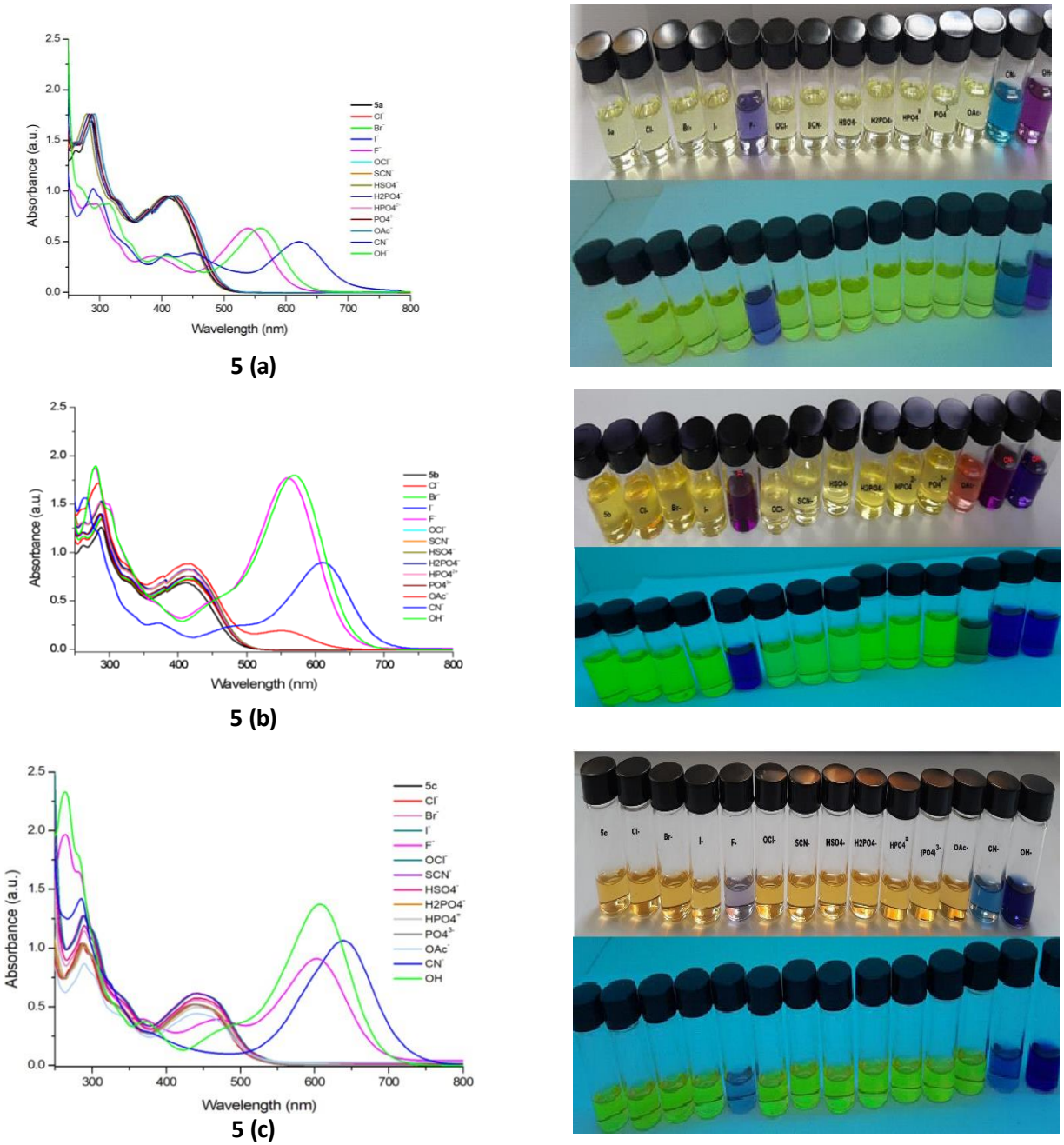

Figure 8. Changes in the UV-vis absorption spectra and color changes observed with naked-eye under a natural light (up-right row) and UV lamp-365 nm (down-right row) upon addition of equivalent amount of various anions ($[Bu_4N]X$: X: Cl, Br, I, F, OCl, SCN, HSO_4, H_2PO_4, HPO_4, PO_4, OAc, CN, and OH) to the solution of the title compounds **(5a-c)** (1 x 10^{-5} M) in (CH_3CN: H_2O, 9:1, V/V) at room temperature

The more acidic phenolic proton would deprotonate upon exposure to more basic OH^- and F ions, and therefore, the intramolecular proton transfer occurs to the keto-hydrazine form (Figure 9 (i)). The cyanide ion (CN^-), which has nucleophilic properties, bounds to the carbon atom of an electron-deficient hydrazone group. As a result of the hydrazo-azo tautomerism that will occur, rapid proton transfer occurs through an intramolecular hydrogen bond from the phenol hydrogen to the quinoxaline's nitrogen anion. Then, hydrogen bonding of the cyano group occurs via the enolate resonance (Figure 9 (ii)).

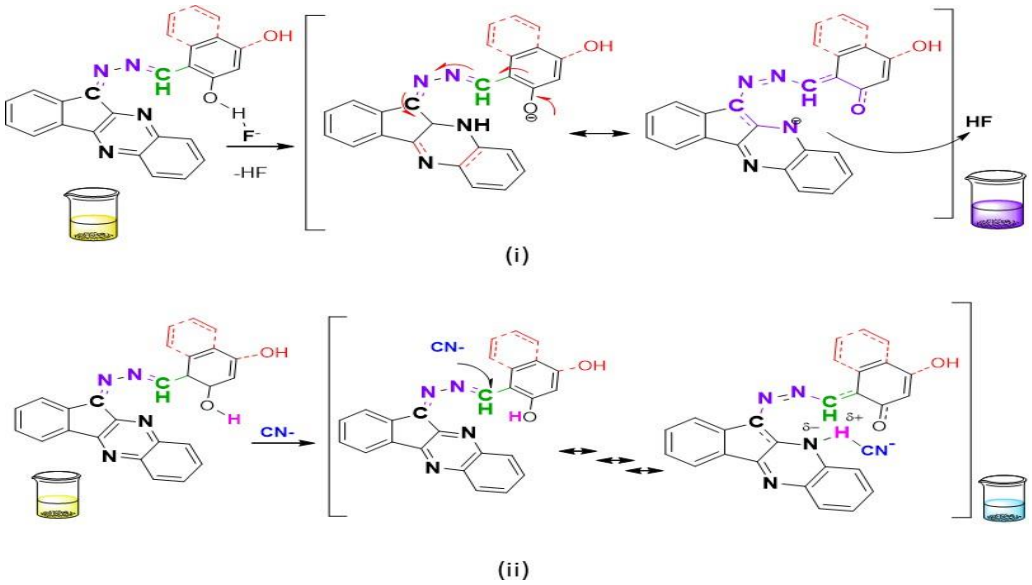

Figure 9. The proposed sensing mechanism of the title compounds **(5a-c)** for **(i)** F^- and OH^-, **(ii)** CN^- anions in CH_3CN solution.

3.2.2. Interaction of Metal Ions with New Compounds (5a-c) as UV-vis Spectroscopic Studies

Due to the molecular structure of the synthesized compounds, the title compounds also have potential metal ion binding sites due to the phenolic oxygen atom and nitrogen atoms of hydrazo and indenoquinoxaline units. [37,38]. Due to their functional groups, the receptor properties of the synthesized compounds (5a-c) towards cations were investigated. For this purpose, the UV-vis absorption spectra of the title compounds (5a-c) solutions ($1x10^{-5}$ M) in CH_3CN: H_2O (9:1, V:V) were recorded between 250 and 800 nm range at room temperature. The UV-vis spectrum of free 5a-c exhibited two broad bands centered at 289, 394 nm, 286, 411 nm, and 289, 444 nm, respectively. The chemosensor behavior of the title compounds 5a-c ($1x10^{-5}$ M) was investigated by monitoring the UV-vis absorption spectral behavior upon addition of various metal ions prepared from acetate salts such as Cu^{2+}, Ni^{2+}, Zn^{2+}, Co^{2+}, Mn^{2+}, Pb^{2+}, Fe^{2+}, Fe^{3+}, Hg^{2+}, Ag^{+}, and Sn^{2+} in CH_3CN: H_2O (9:1, V:V) solution. While no absorbance change was observed on addition the equivalent amount of each metal ions such as Mn^{2+}, Pb^{2+}, Fe^{2+}, Fe^{3+}, Hg^{+2}, Ag^{+} and Sn^{2+} into sample solutions, it was observed that a new absorbance maximum appeared starting from 400-450 nm and ranging from 500-650 nm with the addition of Cu^{2+}, Ni^{2+}, Zn^{2+}, and Co^{2+} ions (Figure 10, Table 2). The additions of Mn^{2+}, Pb^{2+}, Fe^{2+}, Fe^{3+}, Hg^{2+}, Ag^{+}, and Sn^{2+} ions did not show any significant color changes. As soon as the Cu^{2+}, Zn^{2+}, and Co^{2+} solution was added, the light-yellow color of receptor solutions (5a-c) changed to a different color for Cu^{2+} (pink), Zn^{2+} (red), and Co^{2+} (greenish). While the color and spectral changes occurred immediately for Cu^{2+}, Zn^{2+}, and Co^{2+} ions, these changes were observed after 5 minutes with the addition of Ni^{2+} ions. It was observed for Ni^{2+} (violet). According to Irving-Williams' theory, copper (II) complexes are thermodynamically more stable than the corresponding nickel (II) complexes [39,40].

Table 2. Changes in the wavelength (nm) of the absorption maximum (λ_{max}) of the title compounds (5a-c) in CH_3CN: H_2O (9:1, V:V) for Cu^{2+}, Ni^{2+}, Zn^{2+}, Co^{2+} cations

Sample/cations λmax (nm)	Free	Cu^{2+}	Ni^{2+}	Co^{2+}	Zn^{2+}
5a	394	518	542	604	521
5b	411	550	554	624	524
5c	444	523	582	608	566

The existence of a distinct color change in the qualitative recognition of the Cu^{2+}, Co^{2+}, $Zn^{2+,}$ and Ni^{2+} ions and the fact that the color change was clearly visible to the naked eye indicate that the synthesized new bis-hydrazo compounds (5a-c) may have a good selectivity towards metal ions (Cu^{2+}, Co^{2+}, $Zn^{2+,}$ and Ni^{2+}) over other competitive cations (Mn^{2+}, Pb^{2+}, Fe^{2+}, Fe^{3+}, Hg^{2+}, Ag^{+} and Sn^{2+}) (Figure 11). Based on this observation, they can be used in future studies in the potential chemosensor field.

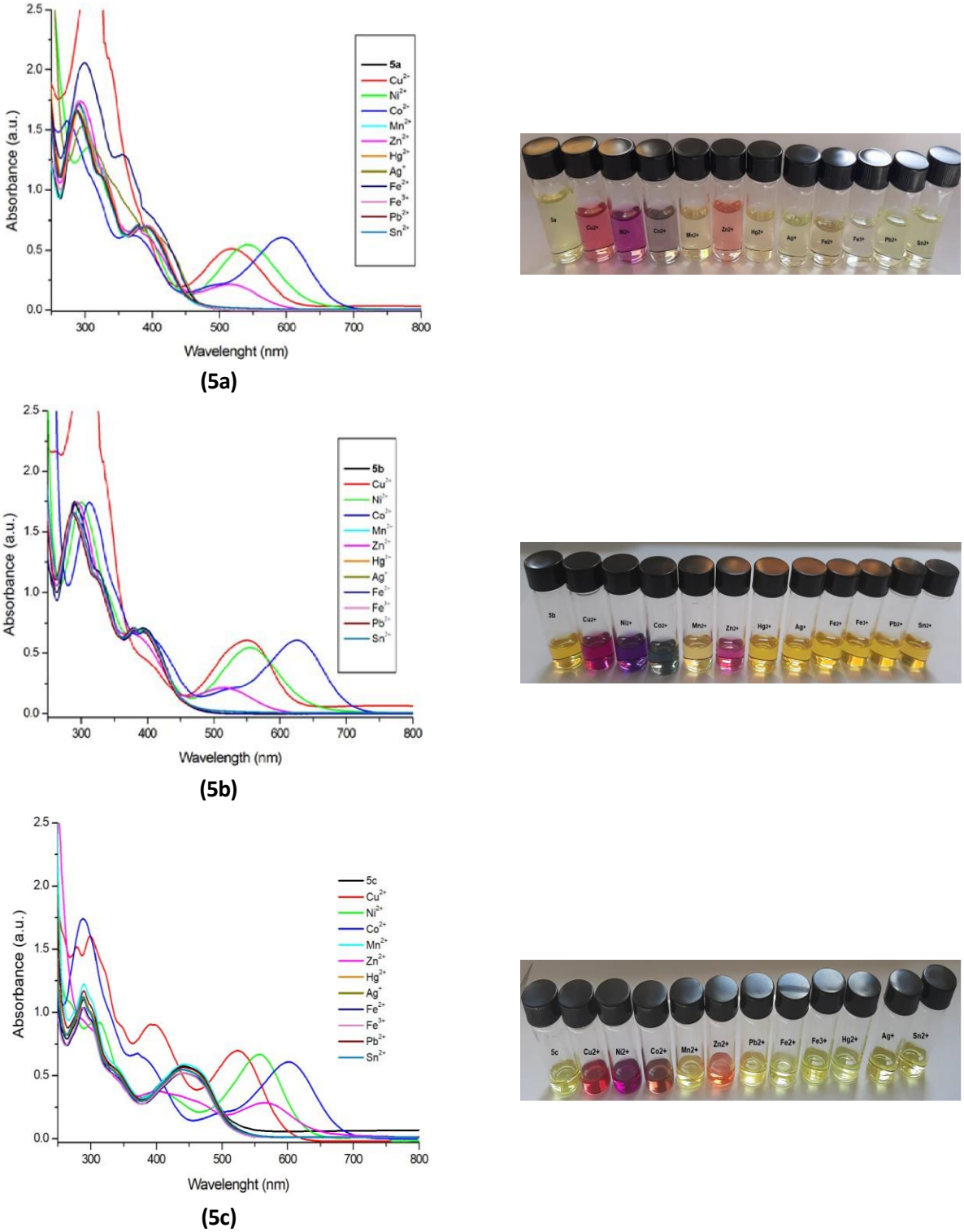

Figure 10. Changes in the UV-vis absorption spectra and color changes observed with naked-eye under a natural light (right row) upon the addition of equivalent amount of metal ion solutions (Cu^{2+}, Ni^{2+}, Zn^{2+}, Co^{2+}, Mn^{2+}, Pb^{2+}, Fe^{2+}, Fe^{3+}, Hg^{+2}, Ag^{+}, and Sn^{2+}) to the solution of the title compounds **(5a-c)** ($1x10^{-5}$ M) in CH_3CN: H_2O (9:1, V:V) at room temperature

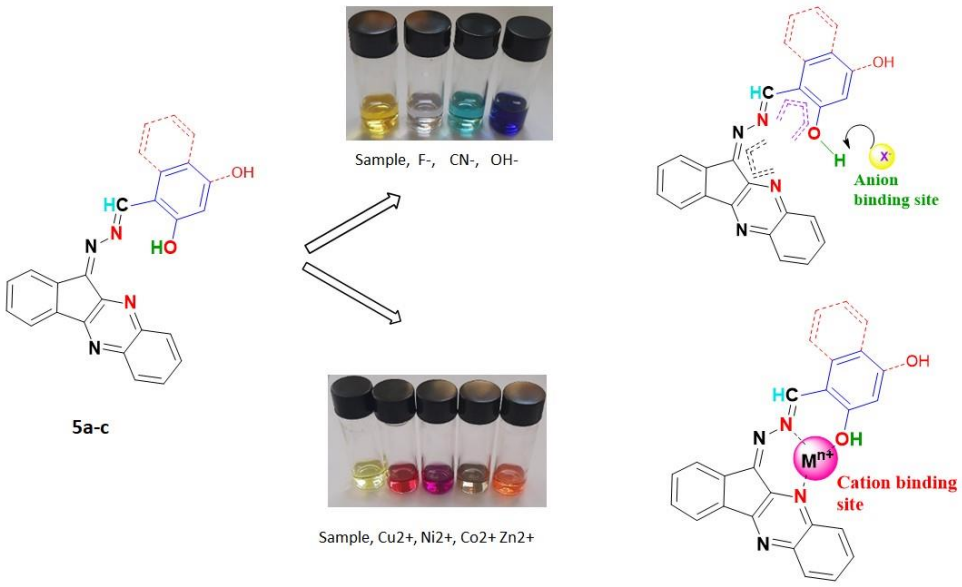

Figure 11. Identification of binding moiety and visually observable color changes of the title compounds **(5a–c)** with solutions of the various ions (F–, CN–, OH–, Cu^{2+}, Ni^{2+}, Zn^{2+} and Co^{2+})

4. Conclusion

Three novel asymmetric bis-hydrazone compounds containing indenoquinoxaline and phenolic units were synthesized, and the structures of the title compounds (5a-c) were confirmed by spectral data. UV-vis spectra and naked-eye observation investigated their colorimetric chemosensors for some anions and metal cations. The title compounds, as chemosensors, showed sensitivity to F^-, CN^-, and OH^- anions among various anions. Although there was only a subtle structural difference in the three chemosensors, distinctions were found for anions in their recognition behavior. Compounds 5a and 5c contain only one hydroxy unit, while compound 5b contains two hydroxyl units. This difference also caused a difference in the detection of the acetate anion (OAc^-) for the title compound 5b. However, since the lattice unit as a ligand in interaction with metal cations is the same in the title compounds, the interaction of cations was the same. Although they showed sensitivity for Cu^{2+}, Ni^{2+}, Zn^{2+}, and Co^{2+} cations, the difference in their ion diameter and nuclear charge caused the difference in both color and absorption changes.

These synthesized asymmetric bis-hydrozone compounds may prove useful in developing multi-analyte sensor arrays. These results have been determined to be structures that can display colorimetric sensor properties for a method that can be used qualitatively by monitoring the color changes. This will allow the detection of some anions and cations in a sample without a complex method. In the development of the test kit for selective detection of some cations and anions, and practicality needs to be visible with the naked eye at the scene, in addition to the UV-vis spectroscopic method. It is hoped that these synthesized bis-hydrazo compounds will be used as sensors in the case of the development of the test kit.

Author Contributions

The author read and approved the final version of the paper.

Conflict of Interest

The author declares no conflict of interest.

Ethical Review and Approval

No approval from the Board of Ethics is required.

Supplementary Material

https://dergipark.org.tr/en/download/journal-file/34959

Acknowledgment

This research was supported by the Scientific Research Coordination Unit of Çanakkale Onsekiz Mart University, Grant number: FYL-2022-3834.

References

[1] J. L. Sessler, P. A. Gale, W.S. Cho, Anion receptor chemistry, Royal Society of Chemistry, 2006.

[2] P. A. Gale, T. Gunnlaugsson, *Preface: Supramolecular chemistry of anionic species themed issue*, Chemical Society Reviews 39 (2010) 3595–4008.

[3] S. Ahmad, R. Singh, T. Arfin, K. Neeti, *Fluoride contamination, consequences and removal techniques in water: A review*, Environmental Science: Advances 1 (5) (2022) 620–661.

[4] A. Singh, J. Singh, *Effects on human health due to fluoride*, in: M.H. Dehghani, R. Karri, E. Lima (Eds.), Green Technologies for the Defluorination of Water, Elsevier, 2021, Ch. 1, pp. 1–16.

[5] P. D. Johan, O. H. Ahmed, L. Omar, N. A. Hasbullah, *Phosphorus transformation in soils following co-application of charcoal and wood ash*, Agronomy 11 (10) (2021) 2010.

[6] S.G. Assuero, A. Mollier, S. Pellerin, *The decrease in growth of phosphorus-deficient maize leaves is related to a lower cell production*, Plant, Cell & Environment 27 (7) (2004) 887–895.

[7] M. Razaq, P. Zhang, H. Shen, Salahuddin, *Influence of nitrogen and phosphorous on the growth and root morphology of Acer mono*, PLoS One 12 (2) (2017) e0171321.

[8] Y. Qiao, H. Lin, J. Shao, H. Lin, *A highly selective naked-eye colorimetric sensor for acetate ion based on 1, 10-phenanthroline-2, 9-dicarboxyaldehyde-di-(p-substitutedphenyl-hydrazone)*, Spectrochimica Acta Part A: Molecular and Biomolecular Spectroscopy 72 (2) (2009) 378–381.

[9] T.I. Logsdon, M.J. Hagelstein, K. Mudder, The Management of Cyanide in Gold Extraction, ICME Publications, Ottawa, 1999.

[10] D. Medina, C.G. Anderson, *A review of the cyanidation treatment of copper-gold ores and concentrates*, Metals 10 (7) (2020) 897.

[11] I.F. Bolarinwa, M.O. Oke, S.A. Olaniyan, A.S. *A review of cyanogenic glycosides in edible plants*, in: S. Soloneski, M.L. Larramendy (Eds.), Toxicology - New Aspects to This Scientific Conundrum, InTech Open Book, 2016, Ch. 8, pp. 179–191.

[12] M. Moustakas, *The role of metal ions in biology, biochemistry and medicine*, Materials 14 (3) (2021) 549.

[13] M. Jaishankar, T. Tseten, N. Anbalagan, B.B. Mathew, K.N. Beeregowda, *Toxicity, mechanism and health effects of some heavy metals*, Interdisciplinary Toxicology 7 (2) (2014) 60–72.

[14] M.A. Abau Seeda, E.A.A. Abou El-Nour, A.A. Yassen, M. Gad Mervat, S.M. Zaghloul, *Interaction of Copper, Zinc, and their importance in plant physiology*: *Review*, Acquisition and Transport, Middle East Journal of Applied Sciences 10 (03) (2020) 407–434.

[15] X. Hu, X. Wei, J. Ling, J. Chen, *Cobalt: An essential micronutrient for plant growth?*, Frontiers in plant science 12 (2021) 768523.

[16] A. Mustafiz, A. Ghosh, A.K. Tripathi, C. Kaur, A.K. Ganguly, N.S. Bhavesh, J.K. Tripathi, A. Pareek, S.K. Sopory, S.L. Singla-Pareek, *A unique Ni^{2+} -dependent and methylglyoxal-inducible rice glyoxalase I possesses a single active site and functions in abiotic stress response*, The Plant Journal 78 (6) (2014) 951–963.

[17] P.A. Gale, *Anion and ion-pair receptor chemistry: highlights from 2000 and 2001*, Coordination Chemistry Reviews 240 (1-2) (2003) 191–221.

[18] K.N. Farrugia, D. Makuc, A. Podborska, K. Szaciłowski, J. Plavec, D.C. Magri, *Colorimetric naphthalene-based thiosemicarbazide anion chemosensors with an internal charge transfer mechanism,* European Journal of Organic Chemistry 2016 (25) (2016) 4415–4422.

[19] F. Aydın, *Synthesis and recognition properties of colorimetric anion chemosensor bearing 2,4-dinitrophenylhydrazone and indene-1,3-dione moieties*, European Journal of Chemistry 5 (2) (2014) 370–373.

[20] X. He, J. Zhang, X. Liu, L. Dong, D. Li, H. Qiu, S. Yin, *A novel BODIPY-based colorimetric and fluorometric dual-mode chemosensor for Hg2+ and Cu2+*, Sensors and Actuators B: Chemical 192 (2014) 29–35.

[21] G. Balamurugan, S. Velmathi, *Quinoxaline based redox relay receptor for iodide ions and its application towards real sample analysis and logic gate function*, Sensors and Actuators B: Chemical 256 (2018) 126–134.

[22] G. Balamurugan, S. Velmathi, *Ninhydrin-based chemosensor for the selective detection and scavenging of mercury (II) ions in aqueous solution,* ChemistrySelect 2 (33) (2017) 10946–10950.

[23] R. Kumari, M. Singh, *Photocatalytic reduction of fluorescent dyes in sunlight by newly synthesized spiroindenoquinoxaline pyrrolizidines,* ACS Omega 5 (2020) 23201–23218.

[24] A.V. Velikorodov, N.N. Stepkina, E.A. Shustova, V.A. Ionova, *Synthesis of new spiro compounds proceeding from 11H-Indeno[1,2-b]quinoxalin-2-one,* Russian Journal of Organic Chemistry 51 (5) (2015) 674–679.

[25] J. Azizian, M. Shaabanzadeh, F. Hatamjafari, M.R. Mohammadizadeh, *One-pot rapid and efficient synthesis of new spiro derivatives of 11H-indeno[1,2-b]quinoxalin-11-one, 6H-indeno[1,2-b]pyrido[3,2-e]pyrazin-6-one and isatin-based 2-pyrazolines*, Arkivoc 11 (2006) 47–58.

[26] M.S. Khan, M.A. Munawar, M. Ashraf, U. Alam, A. Ata, A.M. Asiri, S. Kousar, M.A. Khan, *Synthesis of novel indenoquinoxaline derivatives as potent α-glucosidase inhibitors,* Bioorganic & Medicinal Chemistry 22 (3) (2014) 1195–1200.

[27] C. Tseng, Y. Chen, C. Tzeng, W. Liu, C. Chou, C. Chiu, Y. Chen, *Discovery of indeno[1,2-b]quinoxaline derivatives as potential anticancer agents*, European Journal of Medicinal Chemistry 108 (2016) 258–273.

[28] S. Hameed, K.M. Khan, U. Salar, M. Özil, N. Baltaş, F. Saleem, U. Qureshi, M. Taha, Z. Ul-Haq, *Hydrazinyl thiazole linked indenoquinoxaline hybrids: Potential leads to treat hyperglycemia and oxidative stress, multistep synthesis, α-amylase, α-glucosidase inhibitory and antioxidant activities*, International Journal of Biological Macromolecules 221 (2022) 1294–1312.

[29] F. Abd Elghany El-Samahy, E.A. Ahmed Ezet Eldeken, E. Mostafa Zayed, F. Hassan Osman, G. Elgemeie, *A novel phosphonates synthesized from Schiff's base indenoquinoxaline derivatives and its biological activity*, ChemistrySelect 8 (2023) 1–10.

[30] M.A.-M. Gomaa, M.H. El-Katatny, H.A. Ali, *Synthesis and characterization of N' -(11 H-indeno[1,2-b]quinoxalin-11-ylidene)benzohydrazonamides as potential antimicrobial agents,* Synthetic Communications 50 (18) (2020) 2819–2829.

[31] A.R. Kovrizhina, E.I. Samorodova, A.I. Khlebnikov, *11H-Indeno[1,2-b]quinoxalin-11-one 2-(4-ethylbenzylidene)hydrazone*, Molbank 2021 (4) (2021) M1299.

[32] I.B. Obot, N.O. Obi-Egbedi, *Indeno-1-one [2,3-b]quinoxaline as an effective inhibitor for the corrosion of mild steel in 0.5M H_2SO_4 solution,* Materials Chemistry and Physics 122 (2-3) (2010) 325–328.

[33] L.W. Deady, J. Desneves, A.C. Ross, *Synthesis of some 11H-indeno[1,2-b]quinoxalin-11-ones*, Tetrahedron 49 (43) (1993) 9823–9828.

[34] F.H. Suydam, *The C=N Stretching Frequency in Azomethines,* Analytical Chemistry 35 (1963) 193–195.

[35] Ö. Şahin, U.Ö. Özdemir, N. Seferoğlu, B. Aydıner, M. Sarı, T. Tunç, Z. Seferoğlu, *A highly selective and sensitive chemosensor derived coumarin-thiazole for colorimetric and fluorimetric detection of CN^- ion in DMSO and aqueous solution: synthesis, sensing ability, Pd(II)/Pt(II) complexes and theoretical studies*, Tetrahedron 72 (39) (2016) 5843–5852.

[36] S. Tadesse, Y. Bingöl Alpaslan, M. Yıldız, H. Ünver, K. Aslan, *Synthesis, characterization and applications of (E)-3-((5-bromo-2-hydroxy-3-methoxycyclohexa-1,3-dienyl) methyleneamino)-6-(hydroxymethyl)-tetrahydro-2H-pyran-2,4,5-triol*, Nano Biomedicine and Engineering 8 (2) (2016) 72–81.

[37] S. Çınar, *Synthesis of hydrazone based ion sensor and photophysical characterization,* Hacettepe Journal of Biology and Chemistry 53 (1) (2025) 13–18.

[38] L. C. da Silva, V. G. Machado, F. G. Menezes, *Quinoxaline-based chromogenic and fluorogenic chemosensors for the detection of metal cation*s, Chemical Papers 75 (2021) 1775–1793.

[39] H. Irving, R.J.P. Williams, *637.The stability of transition-metal complexes,* Journal of the Chemical Society (0) (1953) 3192–3210.

[40] S. Busse, H. Elias, J. Fischer, M. Poggemann, K. J. Wannowius, R. Boca, *Kinetics and mechanism of metal substitution and the Irving-Williams series: anion-catalyzed substitution of nickel for copper in Cu(amben) [=(N, N'-Ethylenebis (2-aminobenaldiminato))copper(II)]*, Inorganic Chemistry 37 (16) (1998) 3999–4005.

Journal of New Result in Science
dergipark.org.tr/en/pub/jnrs
Open Access

ISSN: 1304-7981 14 (2) (2025) 115-123 doi.org/10.54187/jnrs.1667993

Theoretical Evaluation of Electrical Resistivity with Bloch-Gruneisen Function

Melek Gökbulut[1], Elif Somuncu[2]

Article Info

Received: 29 Mar 2025
Accepted: 13 Aug 2025
Published: 31 Aug 2025
Research Article

Abstract − In this study, a simple and efficient analytical formula is presented to calculate the generalized Bloch-Gruneisen function. The proposed analytical formula for the generalized Bloch-Gruneisen function is corrected for non-integer and integer values of parameter m. Note that the Bloch-Gruneisen function is preferred to calculate thermal conductivity and electrical resistivity of solid materials. It has been demonstrated that the offered analytical formula gives very correct results of semiconductor and superconductivity for a wide range of temperatures. As an example, the Bloch-Gruneisen function of MgB_2 material, which is envisioned as an alternative superconducting wire for advanced fusion reactors, has been calculated and compared with theoretical calculations and experimental data. The results obtained for $m = 3.5$ were found to be in excellent agreement with the experimental data, with a maximum deviation of approximately 1.26%. The results demonstrated that the analytical formula can be satisfactorily used for solid materials.

Keywords − *Bloch-Gruneisen function, debye temperature, electrical resistivity, magnesium diboride, superconductivity*

1. Introduction

The study of electrical transport, which yields significant insights into electronic phase transitions in *m*etals, semiconductors, and superconductors, is basic to condensed matter systems [1,2]. Specifically, agnetoresistance (MR) at higher magnetic fields, in spintronic technology such as magnetic field sensors and magnetic memory devices [3], and transition metal dichalcogenide (TMDC) systems are important. Therefore, many experimental and theoretical studies have been conducted to explore electrical resistivity in these systems [3-5]. One of the theoretical methods is the Bloch-Gruneisen function that controls phonon resistivity. Ansari has proposed a numerical solution for the Bloch-Gruneisen function to show the electron-phonon interaction in the MgB_2 superconductor [6-8]. Poddar et al. [9] calculated the electrical resistivity and thermal conductivity of MgB_2 using the Bloch-Gruneisen function. Mamedov and Askerov [10] presented the generalized Bloch-Gruneisen function and calculated the electrical resistivity of MgB_2. Hu et al. [11] have investigated electrical resistivity of some Weyl semimetals and Dirac semimetals using Bloch-Gruneisen function. Therefore, Bloch-Gruneisen functions are significant and influential numerical methods of thermophysical properties of condensed matter systems [12,13]. These functions enable the efficient investigation of thermophysical properties of condensed matter systems.

In this study, an effective and simple analytical formula is proposed for calculating the electrical resistivity of the Magnesium diboride (MgB_2) compound using Bloch-Gruneisen functions for integer and non-integer

[1]melek.kgb@gmail.com (Corresponding Author); [2]elf_smnc@hotmail.com
[1]Department of Optician Program, Erbaa Vocational School, Tokat Gaziosmanpaşa University, Tokat, Türkiye
[2]Department of Optician Program, Ulubey Vocational School, Uşak University, Uşak, Türkiye

values of the parameter n. The MgB_2 is a remarkable material predicted to be superconducting at a critical temperature of approximately 39 K [14, 15]. The simple crystal structure, high critical current densities and fields, and transparency to current flow of MgB_2 have made it promising for large-scale applications in electronic devices [16, 17]. The effective use of MgB_2 and MgB_2-based superconductors at liquid hydrogen temperatures has allowed for the application of these materials as components in various devices, including magnets, magnetic bearings, fault current limiters, electric motors, generators, and magnetic resonance imaging (MRI) systems [18-20].

In addition to all of these, the high critical temperature MgB_2 superconductor possesses advantages such as high magnetic field resistance and low neutron activation. Nuclear fusion power is one of the most promising energy source candidates for solving global energy problems in terms of both safety and environmental health protection compared to other energy sources. In the world-standard International Thermonuclear Experimental Reactor (ITER) fusion energy project, a high magnetic field is needed to confine the deuterium (D)-tritium (T) plasma and to sustain the fusion reaction. The selection of superconducting materials for nuclear fusion reactors plays a critical role in both effective confinement of the magnetic field and long-term stability. As a result, MgB_2 has been considered as an alternative to Nb-based superconducting wires for use in advanced fusion reactors [21]. Based on this, studies have been presented suggesting that MgB_2's superior properties could enhance long-term operational reliability and optimize maintenance processes in fusion reactors [22, 23]. In addition, the state-of-the-art MgB_2 material has been evaluated as a potential material for the poloidal field (PF) coils of a future fusion reactor because of its high critical temperature and low material cost [24, 25]. The design and analysis of a Helium-Cooled MgB_2-Based superconducting current feeder system for tokamak application was carried out. In this context, a gas helium-cooled HTS/MgB_2 based hybrid superconducting current feeder system is reported to have potential benefits for superconducting tokamaks and accelerators in terms of improved temperature margin and cryo-stability [26-30].

The aim of this paper is to present an efficient and simple analytical formula for the calculation of electrical resistivity with Bloch-Gruneisen functions for non-integer and integer values of the parameter n. It is to show that the proposed method is an accurate and usable method for the calculation of Bloch-Gruneisen functions of condensed matter systems by applying it to the MgB_2 material during critical case analytical evaluations.

The rest of the paper is organized as follows: Section 2 includes the steps used for the analytical solution of the Bloch-Gruneisen function and the theoretical calculations including the definition of electrical resistivity according to the Bloch-Gruneisen function. In Section 3, the numerical results obtained for the Bloch-Gruneisen function using the developed analytical formula and the numerical results obtained for the electrical resistivity of MgB_2 material for certain temperature values are presented and their comparison with some theoretical studies in the literature is given. Section 4 includes the conclusions that can be drawn from the study.

2. Materials and Methods

2.1. Theory and Basic Formula

The generalized Bloch-Gruneisen function is written following form:

$$J_m\left(\frac{T}{\theta_D}\right) = \int_0^{\theta_D/T} \frac{x^m}{(e^x - 1)(1 - e^{-x})} dx \tag{2.1}$$

where θ_D is Debye temperature, T is the absolute temperature and m takes integer and non-integer values [4]. To evaluate analytical formula from (2.1), used binomial expansion series theorem. Binomial expansion series theorem is expressed as [31]:

$$(x \pm y)^n = \sum_{m=0}^{\infty} (\pm 1)^m F_m(n) x^{n-m}\, y^m \tag{2.2}$$

where $F_m(n)$

$$F_m(n) = \begin{cases} n!/m!\,(n-m)! & \text{for integer } n \\ \dfrac{(-1)^m \Gamma(m-n)}{m!\,\Gamma(-n)} & \text{for noninteger } n \end{cases} \tag{2.3}$$

Considering from (2.2) and (2.1), the analytical formula for the generalized Bloch-Gruneisen functions is taken as follows

$$J_m\left(\frac{T}{\theta_D}\right) = \left(\frac{\theta_D}{T}\right)^{m+1} \lim_{N\to\infty} \sum_{n=0}^{N} (-1)^n\, F_m(-2)_1F_1\,[m+1; m+2; -(1+n)\theta_D/T] \tag{2.4}$$

where N is the upper limit of summation and 1F1 is Kummer confluent hypergeometric function [31]. The Kummer confluent hypergeometric function is a fundamental special function in the solution of differential equations and plays a critical role in analytic approaches to problems in quantum mechanics, chemistry, and engineering [32].

2.2. Definition of Electrical Resistivity According to Bloch-Gruneisen Functions

The electrical resistivity is written with Bloch-Gruneisen function following as:

$$\rho(T) = \rho_0 + (m-1)\rho' \theta_D \left(\frac{T}{\theta_D}\right)^m J_m\left(\frac{T}{\theta_D}\right) \tag{2.5}$$

For bulk resistivity determined by electron-phonon scattering, it is expressed as follows:

$$\rho(T) = \rho_0 + CT^5 J_5\left(\frac{T}{\theta_D}\right) \tag{2.6}$$

Here, ρ_0 is the temperature-independent residual resistivity, ρ' is the temperature coefficient of resistivity, and C is a constant that is evaluated from the bulk room temperature resistivity [6, 33, 34, 35]. From (2.5), ρ_0 = 228.2 $\mu\Omega cm$, ρ' = 0.9 $\mu\Omega cm\ K{-}1$ and $\theta_D = 1016$ [33]. From (2.5), $m = 2$ defines the electron-electron interaction, $m = 3$ defines the electron-magnon or $s - d$ interband electron scattering, and $m = 5$ defines the electron-phonon interaction [8]. Therefore, m values give important information on the electronic phase transitions. By performing the substitution from (2.4) into (2.5), we get the analytical formula for the electrical resistivity.

3. Results and Discussion

In this work, a simple and efficient analytical formula is presented for the direct assessment of the Bloch Gruneisen function for a wide range of temperatures. The analytical expression has been evaluated by the solution from (2.1), which is computed easily and fast by using the binomial series expansion theorem. For the calculation of the Bloch-Gruneisen function using the given analytical formula, the Mathematica 7.0 program was used. The accuracy and validity of the method defined above are demonstrated by the numerical results presented in Tables 1-3.

Table 1. The comparison of Bloch-Gruneisen function with Ref. [10] for $m = 5$ and $N = 700$

T	θ_D	Equation (2.4)	Ref. [10] Equation (8)	Ref. [10] Equation (10)
45	285	7.713407079974676E+01	7.71340707997467E+01	7.71340707998706E+01
15	128	1.067761167806964E+02	1.067761167480696E+02	1.06776116780820E+02
8	54	8.435004623272282 E+01	8.435004623272282E+01	8.43500462328467E+01
65	24	4.611546135472945E-03	4.61151099836592E−03	4.61154626152632E−03
55	424	9.810032305020188 E+01	9.810032305020188E+01	9.81003230503257E+01
72.3	675.4	1.1285488199685302 E+02	1.1285488199685294E+02	1.12854881961971E+02
85.7	446.5	5.473342182310225 E+01	5.473342182310225E+01	5.47334218232861E+01
118	118	2.366158791152123 E-01	2.366158791152123E−01	2.36615879239556E−01
118	1280	1.195010848419946 E+02	1.195010848419946E+02	1.19501084842119E+02
125	1400	1.204384359081927 E+02	1.204384359081927E+02	1.20438435908317E+02
140	750	5.783799227117943 E+01	5.78379922711794E+01	5.78379922713033E+01
180	2400	1.233960539405156 E+02	1.2339605394051516E+02	1.23396053940639E+0

Table 2. The comparison of Bloch-Gruneisen function with Ref. [8] for $m = 6$ and $N = 800$

T	θ_D	Equation (4)	Ref. (8)
35	180	1.976810544330356 E+02	1.97681054433016E+02
170	1420	5.364815894141548 E+02	5.36481589414526E+02
20	154	4.794345649493133 E+02	4.79434564949680E+02
18	107	2.889752193806172 E+02	2.88975219380716E+02
95	56	1.394433525605535 E-02	1.39443352569230E-02
70.8	520.5	4.453005445450895 E+02	4.45300544545428E+02
52	21	2127648839680634 E+02	2.12764884053156E-03
55.3	354.6	343.0906991827409 E+02	3.43090699182929E+02
112	112	1.885436027559607 E-01	1.88543602757016E-01
117	1180	6.425971231507819 E+02	6.42597123150886E+02

Table 3. The comparison of Bloch-Gruneisen function with Ref. [10] for $N = 700$

T	θ_D	m	Equation (4)	Ref. [10]
25.2	124	3	5.545509412217248	5.54550941221725
35.6	336	4.5	5.189028578843398E+01	5.18902857884338E+01
126.5	126.5	6.8	1.6214159806815917E-01	1.62141598068159E−01
42.3	312.6	5.6	2.3709937031836674E+02	2.37099370318367E+02
64.2	431.2	8.56	2.467496260270341 E+04	2.46749626027034E+04
76.4	843.1	12.8	8.864635449361584 E+08	8.86557523688933E+08
87.6	1084.3	18.3	6.323998747333172 E+14	6.32399874733316E+14
108.7	1500.4	8.8	2.0744014455065216 E+05	2.07440144552222E+05
128.2	2500	13.6	2.6886549604272587 E+10	2.68865496042726E+10
252	1250	9	1.143160656624750 E+04	1.14316065662475E+04
352	875	12	1.343285492575711 E+03	1.34328549257573E+03
435	2875	16	1.086584296086333 E+10	1.08658429608633E+10
543	3287.5	20	4.0945494743327056 E+12	4.09454947433271E+12
273	1328	24	5.796195653441484 E+13	5.79619565344143E+13

The analytical formula of the Bloch–Grüneisen function proposed in this study is valid for both integer and non-integer values of the parameter m. In Tables 1-3, the accuracy of the obtained analytical formula is shown through comparison with other studies. As seen in Tables 1-3, the results from the analytical formula are in good agreement with literature data [8, 10], indicating that the convergence properties from (2.4) vary widely. To demonstrate the accuracy of the proposed analytical formula, electrical resistivity was calculated for MgB_2 as an example, and the results are presented in Table 4. In Table 4, the accuracy and precision of the analytical formula for electrical resistivity are shown through the comparison of results from experimental data [9] for $m = 3$, $m = 3.5$, and $m = 5$ values. The calculations were performed using a Debye temperature of $\theta_D = 1016$ K.

Table 4. Electrical resistivity of MgB_2 for $\theta_D = 1016$ K

T	$m = 3$	$m = 3.5$	$m = 5$	Experimental [9]
60.8	231.027	229.77	228.549	231.82267768300028
70.1	232.531	230.783	228.909	233.70418020778328
80.5	234.753	232.385	229.602	233.6186573657477
90.5	237.49	234.477	230.672	235.44810250842215
100.9	241.014	237.308	232.323	237.98404069399925
110.1	244.733	240.414	234.329	240.25225520016062
120.8	249.779	244.769	237.382	242.87371622777334
130.6	255.069	249.461	240.902	247.99021321216355
140.2	260.845	254.696	245.033	253.32609487829725
150.2	267.448	260.786	250.046	259.9782846348918
160.1	274.527	370.716	353.961	268.1438568570727
170.5	282.487	274.961	262.313	274.2308521793451
180.6	290.673	282.804	269.359	281.0578060044472
190.4	298.994	290.844	276.723	287.3939330839537
200.2	307.637	299.253	284.549	296.9910833141217
210.2	316.743	308.166	292.957	306.3911591691642
220.2	326.096	317.366	301.736	317.35295648746535
230.2	335.656	326.811	310.837	323.83410055998866
240.6	345.782	336.851	320.593	333.840273078153
250.2	355.266	346.283	329.823	343.9468419760982
260.1	365.159	356.146	339.532	354.4215309332401
270.1	375.245	366.224	349.502	364.65452490202057
280.2	385.507	376.497	359.71	374.11781329248066
290.4	395.931	386.948	370.135	384.77842147143906
300.7	406.501	397.561	380.756	393.9665494136108

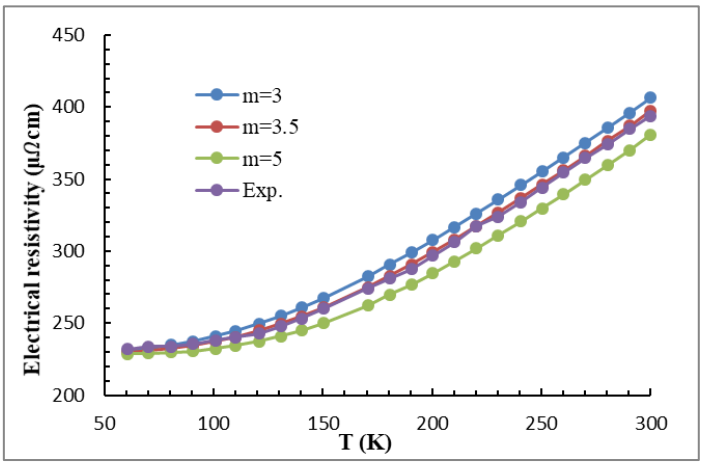

Figure 1. Variation of electrical resistivity values calculated of MgB_2 for $m = 3$, $m = 3.5$ and $m = 5$ values and experimental data against temperature.

The temperature dependence graph of the calculations from Table 4 and the available experimental data for MgB_2 is shown in Figure 1. As seen in Figure 1, the calculated electrical resistivity values for MgB_2 at $m = 3.5$ show good agreement with the experimental data, especially compared to the values calculated for $m = 3$ and $m = 5$. The largest difference is at $T = 70.1\ K$, and is approximately 1.26%. In some studies [36, 37], it has been reported that the values obtained at $m = 3$ can be explained by the existence of scattering events due to both electron-phonon ($m = 5$) and possible electron-electron ($m = 2$) dependencies. The fact that the calculated values for $m = 3.5$ provide a better fit with the experimental data indicates that, in addition to the primary electron-electron and electron-phonon interactions considered for $m = 3$, the contributions of other scattering mechanisms such as electron-magnon [38, 39] and electron-paramagnon may also be significant. This situation suggests that the material under investigation may have a more complex electronic and magnetic structure.

4. Conclusion

In this study, a simple, effective analytical formula has been derived for the evaluation of the Block-Gruneisen function. Considering the obtained results [see Table 1-4], it is demonstrated that the proposed method can lead to a much more efficient algorithm for the accurate and precise estimation of the Bloch-Gruneisen function and electrical resistivity. In conclusion, the analytical formula demonstrates sufficiently accurate results for the Bloch-Gruneisen function, applicable across a wide parameter range. The analytical formula is a confident approach to calculating the electrical resistivity of materials, and it provides great advantages according to its computational impact and its suitability. Considering that the Bloch-Gruneisen function is used to calculate the electrical resistivity of materials, the electrical resistivity of the MgB_2 material, which is planned to be used as a superconducting wire in advanced nuclear fusion reactors, was calculated. In this regard, it was concluded that all the computational results derived would be useful for diverse areas of technology and industry. The analytical approach presented in this study provides a promising basis for further investigation into the electrical resistivity of various solid-state systems. Future studies may focus on extending the proposed formula to other superconducting or thermoelectric materials with different Debye temperatures and electron-phonon coupling strengths. Additionally, this method can be integrated into numerical simulation tools to enhance the efficiency of modelling thermophysical properties in applied superconducting technologies. This work could provide a theoretical basis for other materials that will be used under non-ambient conditions, such as high magnetic fields or extreme pressures, which are particularly important for fusion energy applications. Furthermore, upcoming research could evaluate the formula's applicability to transport phenomena in Dirac or Weyl semimetals. Finally, by incorporating additional scattering mechanisms or coupling effects, the approach may be refined to provide more accurate predictions for anisotropic or strongly correlated systems.

Author Contributions

All the authors equally contributed to this work.

Conflict of Interest

All the authors declare no conflict of interest.

Ethical Review and Approval

No approval from the Board of Ethics is required.

References

[1] A. Grünebohm, A. Hütten, A. E. Böhmer, J. Frenzel, I. Eremin, R. Drautz, I. Ennen, L. Caron, T. Kuschel, F. Lechermann, D. Anselmetti, T. Dahm, F. Weber, K. Rossnagel, G. Schierning, *A unifying perspective of common motifs that occur across disparate classes of materials harboring displacive phase transitions*, Advanced Energy Materials 13 (30) (2023) 2300754.

[2] H. Zhang, W. Zhong, X. Yu, B. Yue, F. Hong, *Electronic phase transitions and superconductivity in ferroelectric S n_2 P_2 Se_6 under pressure*, Physical Review B 109 (2024) 214517.

[3] N. S. Piro, A. S. Mohammed, S. M. Hamad, *Electrical resistivity measurement, piezo resistivity behaviour and compressive strength of concrete: a comprehensive review*, Materials Today Communications 36 (2023) 106573.

[4] R. Singh, M. Ahmad, A. Caceres, R. Eybel, M. Medraj, *The influence of defects on hydrogen-induced electrical resistivity changes in Fe-based systems: A first-principles study*, International Journal of Hydrogen Energy 126 (2025) 429-438.

[5] E. Eser, H. Koç, *Investigations of temperature dependences of electrical resistivity and specific heat capacity of metals*, Physica B: Condensed Matter 492 (2016) 7–10.

[6] I. A. Ansari, *Numerical solution of Bloch–Gruneisen function to determine the contribution of electron–phonon interaction in polycrystalline MgB_2 superconductor*, Physica C: Superconductivity 470 (11-12) (2010) 508–510.

[7] I. A. Ansari, *The Analytical Solution of Incomplete Gamma Function to Determine the Electrical Resistivity at Normal State for MgB_2 Superconductor*, Journal of Physics: Conference Series 1172 (2019) 012028.

[8] I. A. Ansari, C. Rao, *Evaluation of Bloch–Gruneisen Function to Determine the Electrical Resistivity for Pure Nano-MgB_2, Superconductor* Materials Research Proceedings 22 (2022) 13-17.

[9] A. Poddar, B. Bandyopadhyay, P. Mandal, D. Bhattacharya, P. Choudhury, U. Sinha, B. Ghosh, *Studies of transport properties of MgB_2 superconductor*, Physica C: Superconductivity 390 (2003) 191–196.

[10] B. Mamedov, I. Askerov, *A new algorithm for accurate evaluation of the generalized Bloch–Gruneisen function and its applications to MgB_2 superconductor*, Physics Letters A 362 (2007) 324–326.

[11] Z. Hu, J. Deng, H. Li, M. Ogunbunmi, X. Tong, Q. Wang, D. Graf, *Robust three-dimensional type-II Dirac semimetal state in SrAgBi*. Npj Quantum Materials 8 (2023) 20.

[12] Z. Dogan, T. Mehmetoglu, *An approach to improve energy performance of electric vehicle: Theoretical evaluation of electric motor winding heat capacity and electrical resistivity using Debye and Bloch-Gruneisen approximations*, International Journal of Hydrogen Energy 41 (42) (2016) 19265-19268.

[13] Z. Dogan, T. Mehmetoglu, *An analytical evaluation method of the temperature dependence of resistive losses in electric motors*, Journal of Power Technologies 103 (2) (2023) 118-122.

[14] C. Buzea, T. Yamashita, *Review of the superconducting properties of MgB_2*, Superconductor Science and Technology 14 (11) (2001) R15.

[15] J. Nagamatsu, N. Nakagawa, T. Muranaka, Y. Zenitani, J. Akimitsu, *Superconductivity at 39 K in magnesium diboride*, Nature 410 (2001) 63.

[16] S. Giannelli, G. Montenero, A. Ballarino, *Investigation of Splice Resistances of High-Current MgB_2 Cables Operated in Liquid and Helium Gas*, IEEE Transactions on Applied Superconductivity, 27 (4) (2017) 4802505.

[17] C. Guo, H. Wang, X. Cai, W. Luo, Z. Huang, Y. Zhang, Q. Feng, Z. Gan, High performance superconducting joint for MgB_2 films, Physica C: Superconductivity and its applications 584 (2021) 1353863.

[18] D. Patel, A. Matsumoto, H. Kumakura, M. Maeda, S.H. Kim, M. S. A. Hossain, S. Choib, J. H. Kim, *MgB_2 for MRI application: Dual sintering induced performance variation in in situ and IMD processed MgB_2 conductors*, Journal of Materials Chemistry C (7) (2020) 2507-2516.

[19] D. Matera, M. Bonura, R. Cerny, S. M. Walker, F. Buta, D. LeBoeuf, X. Chaud, E. Giannini, C. Senatore, *High-field superconductivity in C-doped MgB_2 bulk samples prepared by a rapid synthesis route*, Scientific Reports 10 (2020) 17656.

[20] T. Prikhna, V. Sokolovsky, V. Moshchil, *Bulk MgB_2 Superconducting materials: technology, properties, and applications* Materials 17 (11) (2024) 2787.

[21] Y. Hishinuma, A. Kikuchi, Y. Iijima, Y. Yoshida, T. Takeuchi, A. Nishimura, *Fabrication of MgB_2 superconducting wires as low activation superconducting materials for an advanced fusion reactor application*, Fusion Engineering and Design 81 (20-22) (2006) 2467–2471.

[22] Q. Cai, Q. Guo, Y. Liu, Z. Ma, H. Li, W. Qiu, D. Patel, H. Jie, J.H. Kim, M. Somer, E. Yanmaz, A. Devred, V. Luzin, A. Fatehmulla, W. A. Farooq, D. Gajda, Y. Bando, Y. Yamauchi, S. Pradhan, S.A. Hossain, Doping-induced isotopic Mg11B2 bulk superconductor for fusion application, Energies 10 (3) (2017) 409.

[23] F. Cheng, Y. Liu, Z. Ma, M. S. Al Hossain, M. Somer, *Improved superconducting properties in the $Mg^{11}B_2$ low activation superconductor prepared by low-temperature sintering*, Scientific Reports 6 (2016) 25498.

[24] P. Gao, Y.X. He, H.J. Ma, V.A. Anvar, J.F. Huang, X.F. Pan, C. Zhou, A. Nijhuis, J.G. Li, J.G. Qin, W. J. Wang, M. Yu, H. Jin, *DC performance and AC loss of sub-size MgB_2 CICC conductor for fusion magnet application*, Nuclear Fusion 62 (5) (2022) 056014.

[25] W. Wang, Y. Wu, Y. He, P. Gao, A. Nijhuis ve J. Qin, *Heat Transfer Analysis of MgB_2 Coil in Heat Treatment Process for Future Fusion Reactor*, IEEE Transactions on Applied Superconductivity, 33 (5) (2023) 4200605.

[26] K. Konstantopoulou, J. Hurte, J. Fleiter, A. Ballarino, *Electro-Magnetic Performance of MgB_2 Cables for the High Current Transmission Lines at CERN*, IEEE Transactions on Applied Superconductivity 29 (5) (2019) 4802205.

[27] N. Bairagi, V. L. Tanna, D. Raju, *Preliminary design and analysis of 20 K helium cooled MgB_2 based superconducting current feeder system for tokamak application*, IEEE Transactions on Applied Superconductivity 32 (6) (2022) 4802305.

[28] N. Bairagi , D. Sonara, H. Nivamat , V. L. Tanna, U. Prasad, D. Raju, *Copper electroplating technique for development of HTS current leads bottom joints using MgB_2 wires*, Physica C: Superconductivity and its Applications 601 (2022) 1354108.

[29] N. Bairagi, V. L. Tanna, H. Nimavat, D. Sonara, R. Panchal, A. Garg, *Test results of a prototype HTS current lead with MgB_2 and NbTi superconducting joints*, IEEE Transactions on Applied Superconductivity 33 (4) (2023) 4801408.

[30] N. Bairagi, V. L. Tanna, H. Nimavat, D. Sonara, A. Garg, R. Panchal, *Feasibility study of HTS current leads with MgB_2 shunt for tokamak application*, IEEE Transactions on Applied Superconductivity 34 (5) (2024) 4800804.

[31] I. Gradshteyn, I. Ryzhik, Tables of Integrals, Series and Products, in: A. Jeffery, D.Zwillinger (Eds.), 7th Edition, Elsevier Academic Press, New York, 1980.

[32] M. N. Mathews, M. A. Esrick, Z. Y. Teoh, J. K. Freericks, *A Physicist's Guide to the solution of Kummer's Equation and Confluent Hypergeometric Functions*, Condensed Matter Physics 25 (3) (2022) 33203.

[33] Y. Kong, O. Dolgov, O. Jepsen, O. Anderson, *Electron-phonon interaction in the normal and superconducting states of MgB_2*, Physical Review B 64 (2) (2001) 020501.

[34] A. Bharathi, S.J. Balaselvi, S. Kalavathi, G.L.N. Reddy, V. Sankar Sastra, Y. Hariharan, T.S. Radhakrishnan, *Carbon solubility and superconductivity in MgB_2*, Physica C: Superconductivity 370 (4) (2002) 211–218.

[35] C. Adelmann, *On the extraction of resistivity and area of nanoscale interconnect lines by temperature-dependent resistance measurements*, Solid State Electronics 152 (2019) 72–80.

[36] V.A. Gasparov, N.S. Sidorov, I.I. Zverkova, S.S. Khassanov, M.P. Kulakov, *Electron Transport, Penetration Depth, and the Upper Critical Magnetic Field in ZrB_{12} and MgB_2*, Journal of Experimental and Theoretical Physics 101 (1) (2005) 98–106.

[37] M. Susner, M. Bhatia, M. Sumption, E. Collings, *Electrical resistivity, Debye temperature, and connectivity in heavily doped bulk MgB_2 superconductors*, Journal of Applied Physics 105 (2009) 103916.

[38] M. C. T. D. Müller, S. Blügel, C. Friedrich, *Electron-magnon scattering in elementary ferromagnets from first principles: Lifetime broadening and band anomalies*. Physical Review B 100 (2019) 045130.

[39] P. K. G. Bedi, *Superconducting critical temperature and isotope effect in the presence of electron-phonon,electron-paramagnon, and electron-electron interactions in rhodium*. Physica C: Superconductivity and its applications 596 (2022) 1354049.

Journal of New Result in Science
dergipark.org.tr/en/pub/jnrs
Open Access

ISSN: 1304-7981 14 (2) (2025) 124-137 doi.org/10.54187/jnrs.1671939

Fixed Point Approach for Fractional Order Differential Equation Systems

Lale Cona[1], Alperen Hasan Kocağ[2]

Article Info

Received: 08 Apr 2025

Accepted: 19 Jun 2025

Published: 31 Aug 2025

Research Article

Abstract − This paper examines the existence and uniqueness of solutions to a nonlinear system of fractional differential equations involving the Atangana–Baleanu fractional derivative. The system under consideration is analyzed through a fixed-point approach by means of the Perov sense. The Atangana–Baleanu fractional derivative, characterized by a non-local and non-singular kernel, provides a more suitable framework for modeling various physical phenomena. The main results are illustrated through an example, which demonstrates the applicability and reliability of the proposed approach.

Keywords − *Atangana-Baleanu Caputo fraction order derivative, initial value problem, fraction order differential equation systems, fixed point theorem*

1. Introduction

Newton and Leibniz introduced differential and integral calculus in the late 17th century, and their calculations were used in many fields such as engineering, physics, chemistry, and economics. In the same period, Leibniz worked on the existence and meaning of the 1/2-order derivative, but his studies did not progress sufficiently due to the limited application areas of fractional derivatives. Liouville's work defining fractional integration can be considered as the first systematic research of that time. In the following period, researchers such as [1–4] published studies on linear and nonlinear fractional differential equations. Despite the introduction of various definitions of fractional-order derivatives—such as those by Grünwald-Letnikov, Riemann-Liouville, Caputo, Hadamard, Marchaud, Riesz, Riesz–Miller, Miller–Ross, Weyl, and Erdélyi–Kober—the Caputo and Riemann-Liouville types remain the most widely applied in current research. Even though these definitions are widely used, there are some weaknesses inherent in their formulations. While several definitions of fractional-order derivatives exist in the literature, no single definition is universally superior. Each has its own analytical and physical interpretations, depending on the specific context of application [5]. Recently, in order to eliminate the weaknesses of these derivatives, Caputo and Fabrizio introduced new derivative definitions in 2015 [6], and Atangana and Baleanu followed with another in 2016 [7]. Atangana and Baleanu proposed a generalized form of fractional-order derivative by modifying the kernel structure in the Caputo-Fabrizio definition, thereby enhancing its analytical flexibility and applicability.

Over the past few decades, fractional calculus has gained prominence as an effective mathematical framework for describing complex systems with memory and hereditary characteristics, which traditional integer-order differential equations often fail to model accurately. This nonlocal characteristic of fractional derivatives enables more accurate descriptions of various processes in physics, biology, control theory, and engineering.

[1]lalecona@gumushane.edu.tr (Corresponding Author); [2]matematikce.alperenhk@gmail.com
[1]Department of Mathematical Engineering, Faculty of Engineering and Natural Sciences, Gumushane University, Türkiye
[2]Mathematics Engineering, Graduate Education Institute, Gumushane University, Türkiye

For instance, fractional-order models have been successfully applied in rheology field [8], complex dynamical systems [9], biological sciences [10], linear time-invariant systems of any order with point delays [11,12], diffusion equations [13], epidemic modeling [14], finance [15], outbreak control [16], chous control [17], image diagnosis [18], delay-dependent systems [19,20], data fitting [21], blood flow [22], fluid mechanics [23], capacitor theory [24], aerodynamics [25]. Furthermore, in the context of data prediction and model validation, fractional-order models have proven useful [26, 27]. These studies demonstrate that fractional calculus has become a widely used framework, both in theoretical investigations and practical applications across various scientific fields.

With this expanding applicability comes an increasing need for rigorous mathematical analysis of fractional-order systems, particularly regarding the existence and uniqueness of solutions to such models. The well-posedness of these systems ensures that the physical models they represent are mathematically consistent and reliable for simulation and prediction. A wide range of studies has focused on the theoretical and practical aspects of fractional-order differential equations, including the investigation of existence and uniqueness of solutions, stability, periodic behavior, asymptotic properties, and both analytical and numerical solution techniques. These include two-point, three-point, multi-point, and nonlocal boundary value problems. Compared to prior works relying on Caputo or Riemann–Liouville derivatives [28–36], the adoption of the Atangana–Baleanu operator provides a more generalized and physically relevant model formulation. Its non-singular and non-local kernel structure facilitates more accurate descriptions of memory-dependent processes without imposing singularity-related limitations, which are often encountered in traditional definitions. In this context, substantial effort has been devoted to developing fixed-point theorems, topological methods, and functional analysis tools tailored for fractional differential equations.

Motivated by these developments, this study aims to investigate the existence and uniqueness of solutions for a class of fractional differential equation systems using advanced techniques in fractional calculus and nonlinear analysis. Fractional-order models, particularly those involving Atangana–Baleanu derivatives with non-singular and non-local kernels, have proven effective in capturing such phenomena. However, their analysis, especially in nonlinear and high-dimensional settings, remains mathematically demanding. To address these challenges, we employ advanced tools from fractional calculus and nonlinear analysis, specifically a fixed point approach adapted to the Perov mean. This study, unlike previous works that mainly utilize classical Caputo or Riemann–Liouville derivatives, addresses non-singular and non-local kernel structures, providing a novel theoretical framework with wider applicability for models with memory effects. The results not only contribute to the theoretical foundations of fractional-order systems but also enhance their applicability across various scientific and engineering domains. The organization of the paper is as follows. Section 2 outlines the fundamental concepts essential for the analysis. Section 3 is devoted to examining the existence and uniqueness of solutions to a nonlinear system of fractional differential equations, utilizing a fixed point approach based on in the sense of Perov

$$\begin{cases} {}^{ABC}D^{\alpha}_{0,t}x(t) + T\big(x(t),y(t)\big) = \phi\big(t,x(t),y(t)\big) \\ {}^{ABC}D^{\beta}_{0,t}y(t) + S\big(x(t),y(t)\big) = \psi\big(t,x(t),y(t)\big) \\ t \in [0,b] \ , \quad 0 < \alpha,\beta < 1 \\ x(0) = x_0 \ , \ y(0) = y_0 \end{cases} \tag{1.1}$$

where the ${}^{ABC}D^{\alpha}$ and ${}^{ABC}D^{\beta}$ $\alpha,\beta \in (0,1)$ are Atangana-Baleanu Caputo fractional derivatives, also here $T,S: K \times K \to \mathbb{R} \times \mathbb{R}$ and $f,g: R \times R \to \mathbb{R} \times \mathbb{R}$, $f(t,x,y) = \phi(t,x,y) - T(x,y)$, $g(t,x,y) = \psi(t,x,y) - S(x,y)$, $x_0, y_0 \in \mathbb{R}$ for $J = [0,b]$, $K = \{x,y \in \mathbb{R}: |x - x_0| < \delta, |y - y_0| < \delta\}$ and $R = J \times K \times K$.

2. Preliminaries

In this section, basic information about the Gamma function, Beta function, Mittag-Leffler function, Riemann–Liouville fractional derivative, and Caputo fractional derivative is provided, and the Atangana–Baleanu derivative in the Caputo sense, which will be used in our study, is introduced.

Definition 2.1. [37] Let $p \in [1,\infty)$ and (a,b) be an open subset of $\mathbb{R}$, the Sobolev space $H^p(a,b)$ defined by

$$H^p(a,b) = \{f \in L^2(a,b) : \ D^\beta f \in L^2, \ |\beta| < p\}$$

Definition 2.2. [7] The one-dimensional Sobolev space in the interval (a,b) is defined by $H^1(a,b) = \{f | f \text{absolutely continuous and} f' \in L^2(a,b)\}$.

Definition 2.3. [38] Let (X,d) be a metric space and $T : X \to X$ be an operator. T is called a Lipschitzian mapping, if there is a number $\alpha > 0$ such that

$$d(Tx,Ty) \leq \alpha d(x,y)$$

for all $x, y \in X$. If there is at least one real number $\alpha \in (0,1)$, T is called a contraction mapping.

Now, let's state the Banach fixed point theorem [39].

Theorem (Banach fixed point theorem) 2.4. Let (X,d) be a complete metric space and $A: X \to X$ be a contraction operator. In this case,

i. A has one and only one fixed point $x \in X$

ii. For any $x_0 \in X$, iteration sequence $(A^n x_0)$ (i.e. iteration sequence (x_n) defined by $x_n = Ax_{n-1}$ for all $n \in \mathbb{N}$) converges to the unique fixed point of A

Definition 2.5 [34] A real square matrix M is said to be convergent to zero if and only if $M^n \to 0$ as $n \to \infty$.

Lemma 2.6. [40] Let $M \in \mathcal{M}_{m,m}(\mathbb{R}_+)$. The following conditions are mutually equivalent:

i. M is a matrix that convergent to zero

ii. All eigenvalues of M lie strictly within the open unit disk centered at the origin; that is, $|\mu| < 1$ for every $\mu \in \mathbb{C}$ satisfying $det(M - \mu I) = 0$

iii. The matrix $I - M$ is nonsingular and $(I - M)^{-1} = I + M + \cdots + M^n + \cdots$

iv. The matrix $I - M$ is nonsingular and $(I - M)^{-1}$ has nonnegative elements

v. $M^n q \to 0$ and $M^n q \ \to 0$ as $n \to \infty$, for any $q \in \mathbb{R}^m$

Example 2.7. The first three examples given below are matrices converging to zero. But the fourth example does not converge to zero

i. $M = \begin{pmatrix} \alpha & \beta \\ \alpha & \beta \end{pmatrix}$ where $\alpha, \beta \in \mathbb{R}_+$ and $\alpha + \beta < 1$

ii. $M = \begin{pmatrix} \alpha & \alpha \\ \beta & \beta \end{pmatrix}$ where $\alpha, \beta \in \mathbb{R}_+$ and $\alpha + \beta < 1$

iii. $M = \begin{pmatrix} \alpha & \beta \\ 0 & \gamma \end{pmatrix}$ where $\alpha, \beta, \gamma \in \mathbb{R}_+$ and $max\{\alpha, \gamma\} < 1$

iv. $M = \begin{pmatrix} \alpha & \beta \\ \gamma & \lambda \end{pmatrix}$ where $\alpha, \beta, \gamma, \lambda \in \mathbb{R}_+$ and $\alpha + \beta \geq 1$, $\gamma + \lambda \geq 1$

Definition 2.8. [41] Let (X, d) be a generalized metric space. An operator $A: X \to X$ is called a contraction if there exists a matrix M that convergent to zero such that

$$d\big(A(x), A(y)\big) \leq Md(x, y) \text{ for all } x, y \in X$$

If there is a convergent M matrix, A is defined as a contraction operator and M is defined as Lipschitz matrix.

The following theorem extends the Banach fixed-point theorem to generalized metric spaces within the framework of the Perov sense [42, 43].

Theorem (Fixed point theorem in the Perov sense) 2.9. Let (X, d) be a complete generalized metric space and let $A: X \to X$ be a contractive operator associated with Lipschitz matrix M. Then, A admits a unique fixed point $x^* \in X$, and for every initial point $x_0 \in X$, the following holds:

$$d\big(A^k(x_0), x^*\big) \leq M^k(I - M)^{-1} d\big(x_0, A(x_0)\big)$$

for all $k \in \mathbb{N}$.

Definition (Gamma Function) 2.10. [4] The gamma function, which generalizes the factorial of a non-negative integer n and makes it possible to use n as a non-integer, is one of the main functions of fractional analysis. The definition of this function is as follows

$$\Gamma: \mathbb{R}\backslash\{\mathbb{Z}^-, 0\} \to \mathbb{R} \ , \ \Gamma(x) = \int_0^\infty e^{-t} t^{x-1} dt$$

This function defined by the generalized integral is called gamma function.

Definition (Beta Function) 2.11. [1] The beta function is closely related to the gamma function, and for positive values of x and y the function is defined by the integral β as follows

$$\beta(x, y) = \int_0^1 t^{x-1}(1 - t)^{y-1} dt \ , \ x, y > 0$$

Regarding the relationship between beta and gamma functions

$$\beta(x, y) = \frac{\Gamma(x)\Gamma(y)}{\Gamma(x + y)}$$

where the β function for non-positive values of x and y is defined.

Definition 2.12. [44,45] The special function

$$E_\alpha(z) = \sum_{i=0}^{\infty} \frac{z^i}{\Gamma(1 + \alpha i)} \ , \alpha \in \mathbb{C}, R(\alpha) > 0, z \in \mathbb{C}$$

and its general form for $\alpha, \beta \in \mathbb{C}, R(\alpha) > 0, R(\beta) > 0, z \in \mathbb{C}$

$$E_{\alpha,\beta}(z) = \sum_{i=0}^{\infty} \frac{z^i}{\Gamma(\beta + \alpha i)}$$

with $\mathbb{C}$ being the set of complex numbers are called Mittag-Leffler functions.

We recall the next useful lemma [46].

Lemma 2.13. Mittag-Leffler function $E_{\alpha,\beta}(-x)$ is completely monotonic when $0 < \alpha \leq 1$ and $\beta \geq \alpha$. For $\forall n \in \mathbb{N}$ it yields that

$$(-1)^n \frac{d^n}{dx^n} E_{\alpha,\beta}(-x) \geq 0$$

and then

$$0 \leq E_{\alpha,\beta}(-x) \leq \frac{1}{\Gamma(\beta)}$$

where $x > 0$ and $0 < \alpha \leq 1$.

Definition 2.14. [47] Let $n \in \mathbb{R}_+$, *n-th* order Riemann-Liouville fractional integral, for $a \leq x \leq b$ is defined as following

$$I_a^n f(x) = \frac{1}{\Gamma(n)} \int_a^x (x-t)^{n-1} f(t) dt$$

If $n = 0$, $I_a^n := I$ is the unit operator. When $n \in \mathbb{N}$ is taken, the Riemann-Liouville fractional integral and the classical integral are the same, except that the domain is expanded from Riemann integrable functions to Lebesgue integrable functions.

Definition 2.15. [47] Let $n \in \mathbb{R}_+$ and $m = \lceil n \rceil$. The operator

$$D_a^n f = D^m \frac{1}{\Gamma(m-n)} \int_a^x (x-t)^{m-n-1} f(t) dt$$

is called the n-th order Riemann-Liouville fractional derivative operator. $D_a^0 f = I$ is unit operator for $n = 0$.

Among the solution techniques for fractional order differential equations, the Caputo derivative provides the most suitable formulation for incorporating initial conditions in a physically meaningful way. Its primary advantage is that the initial conditions for the Caputo's fractional derivative are expressed in the same form as those in integer-order differential equations.

Definition 2.16. [47] *Let* $n \geq 0$ and $m = \lceil n \rceil$, Caputo fractional derivative is defined as follows

$${}_a^C D_x^n f(x) = \frac{1}{\Gamma(m-n)} \int_a^x \frac{f^{(m)}(t)}{(x-t)^{n+1-m}} dt$$

Definition 2.17. [7] Let $f \in H^1(a,b), b > a$ and $\alpha \in [0,1]$. Caputo sense of Atangana-Baleanu derivative is defined as follows

$${}^{ABC}_b D_t^\alpha \big(f(t)\big) = \frac{B(\alpha)}{1-\alpha} \int_b^t f'(x) E_\alpha \left[-\alpha \frac{(t-x)^\alpha}{1-\alpha}\right] dx$$

where $B(\alpha)$ is a normalization function that satisfies the condition $B(0) = B(1) = 1$.

3. Main Results

First, we state some results related to the initial value problem given from (3.1) below, which are included in the work [48] and will assist in solving the problem we address in this study.

$$\begin{cases} {}^{ABC}D_{0,t}^\alpha y(t) + N\big(y(t)\big) = g\big(t, y(t)\big) \\ 0 < \alpha < 1, \;\; y(0) = y_0 \end{cases} \tag{3.1}$$

where $N\big(y(t)\big)$ is a nonlinear function.

Theorem 3.1. [48] Let $J=[0,b]$, $C=\{y\in\mathbb{R}:\ |y-y_0|\le\delta\}$, $D=J\times C$ and $f(t,y)=g(t,y)-N(y)$. And assume that $f:D\to\mathbb{R}$, $g:D\to\mathbb{R}$ and $N:C\to\mathbb{R}$ are functions that satisfy the following conditions:

i. $\|f\|_\infty\le\left(\delta B(\alpha)/(1-\alpha)\right)$

ii. $g(t,y)$ and $N(y)$ are continuous functions

In this case, there is a function $y:[0,b^*]\to\mathbb{R}$ which is the solution to problem (3.1) where

$$b^*=min\left\{b;\ \left((B(\alpha)\Gamma(\alpha+1)/\alpha)\right)\left((\delta/\|f\|_\infty)-\left(1-\alpha/B(\alpha)\right)\right)^{\frac{1}{\alpha}}\right\}$$

Let us give theorems expressing the one-dimensional and global local existence and uniqueness of the solution of problem (3.1).

Theorem 3.2. [48] Let $a=\left(B(\alpha)/(1-\alpha)\right)$ and $b=\alpha/(1-\alpha)$. In this case, the solution to problem (3.1) is

$$y(t)=\frac{1}{a}f\big(t,y(t)\big)+y(0)E_{\alpha,1}(-bt^\alpha)-\int_0^t y(s)E'_{\alpha,1}(-b(t-s)^\alpha)ds \tag{3.2}$$

where $f(t)=g(t,y)-N(y)$.

Theorem 3.3. [48] Let $J=[0,b]$, $C=\{y\in\mathbb{R}:|y-y_0|\le\delta\}$, $D=J\times C$ and $f(t,y)=g(t,y)-N(y)$. Assume that $f:D\to\mathbb{R}$, $g:D\to\mathbb{R}$ and $N:C\to\mathbb{R}$ are functions that satisfy the following conditions.

i. For $\forall y,\bar{y}\in C$ and $\forall t\in J\ |g(t,y)-g(t,\bar{y})|\le L_1|y-\bar{y}|$ there is a number $L_1\ge 0$

ii. For $\forall y,\bar{y}\in C\ |N(y)-N(\bar{y})|\le L_2|y-\bar{y}|$ there is a number $L_2\ge 0$

iii. $L_1+L_2<a$

In this case, problem (3.1) has one and only one solution $y:[0,b]\to\mathbb{R}$.

Now, the theorem giving the global existence and uniqueness of problem (1.1) will be stated and proved. Let $\alpha,\beta\in(0,1)$, $J=[0,b]$, $K=\{x,y\in\mathbb{R}:\ |x-x_0|<\delta$ and $|y-y_0|<\delta\}$, $R=J\times K\times K$ and $f(t,x,y)=\phi(t,x,y)-T(x,y)$, $g(t,x,y)=\psi(t,x,y)-S(x,y)$. We consider the problem (1.1) given with the Atangana-Baleanu Caputo fractional derivative of ${}^{ABC}D^\alpha$ and ${}^{ABC}D^\beta$, where $x_0,y_0\in\mathbb{R}$. Then, $(x,y)\in C[0,b]\times C[0,b]$ is a solution to the problem (1.1) if and only if $a_1=\left(B(\alpha)/(1-\alpha)\right)$, $a_2=\left(B(\beta)/(1-\beta)\right)$ and for $t\in[0,b]$ and

$$\begin{cases} x(t)=\dfrac{1}{a_1}f\big(t,x(t),y(t)\big)+x_0E_{\alpha,1}(-bt^\alpha)-\displaystyle\int_0^t x(s)E'_{\alpha,1}(-b(t-s)^\alpha)ds \\ y(t)=\dfrac{1}{a_2}g\big(t,x(t),y(t)\big)+y_0E_{\beta,1}\big(-bt^\beta\big)-\displaystyle\int_0^t y(s)E'_{\beta,1}\big(-b(t-s)^\beta\big)ds \end{cases} \tag{3.3}$$

Theorem 3.4. Let $J=[0,b]$, $K=\{x,y\in\mathbb{R}:|x-x_0|<\delta,|y-y_0|<\delta\}$, $R=J\times K\times K$; $f,g:R\times R\to\mathbb{R}\times\mathbb{R}$; $T,S:K\times K\to\mathbb{R}\times\mathbb{R}$ and $f(t,x,y)=\phi(t,x,y)-T(x,y)$, $g(t,x,y)=\psi(t,x,y)-S(x,y)$, $x_0,y_0\in\mathbb{R}$ and $\alpha,\beta\in(0,1)$, and assume that it satisfies the following conditions.

i. ϕ,ψ,T,S are continuous functions

ii. $\|f(t,x,y)\|\le a_1$, $\|g(t,x,y)\|\le a_2$

iii. For $\forall x, y, \bar{x}, \bar{y} \in K$ the numbers $L_1, L_2, L_3, L_4 > 0$ exist such that

$$|\phi(t,x,y) - \phi(t,\bar{x},\bar{y})| \leq \frac{L_1}{\Gamma(\alpha)}|x-\bar{x}| + \frac{L_2}{\Gamma(\alpha)}|y-\bar{y}|$$

$$|T(x,y) - T(\bar{x},\bar{y})| \leq \frac{L_3}{\Gamma(\alpha)}|x-\bar{x}| + \frac{L_4}{\Gamma(\alpha)}|y-\bar{y}|$$

iv. For $\forall x, y, \bar{x}, \bar{y} \in K$ the numbers $N_1, N_2, N_3, N_4 > 0$ exist such that

$$|\psi(t,x,y) - \psi(t,\bar{x},\bar{y})| \leq \frac{N_1}{\Gamma(\beta)}|x-\bar{x}| + \frac{N_2}{\Gamma(\beta)}|y-\bar{y}|$$

$$|S(x,y) - S(\bar{x},\bar{y})| \leq \frac{N_3}{\Gamma(\beta)}|x-\bar{x}| + \frac{N_4}{\Gamma(\beta)}|y-\bar{y}|$$

v. $L_1 + L_2 < a_1$ and $L_3 + L_4 < a_1$. Also, $N_1 + N_2 < a_2$ and $N_3 + N_4 < a_2$

vi. $\frac{1}{\Gamma(\alpha)} + \frac{1}{\Gamma(\beta)} < 1$

In this case, problem (1.1) has one and only one solution.

PROOF. We introduce the set $G = \{(x,y) \in C[0,b] \times C[0,b] : |x - x_0| \leq \delta, |y - y_0| \leq \delta\}$ where G is a nonempty closed subset of the Banach space $C[0,b] \times C[0,b]$. Then, under the conditions of Theorem 3.4, we transform from (1.1) into a fixed point problem with the operator A on G by $A(x,y) = \big(A_1(x,y),\ A_2(x,y)\big)$ where

$$\begin{cases} A_1(x,y)(t) = \dfrac{1}{a_1} f\big(t, x(t), y(t)\big) + x_0 E_{\alpha,1}(-bt^\alpha) - \displaystyle\int_0^t x(s) E'_{\alpha,1}(-b(t-s)^\alpha) ds \\ A_2(x,y)(t) = \dfrac{1}{a_2} g\big(t, x(t), y(t)\big) + y_0 E_{\beta,1}\big(-bt^\beta\big) - \displaystyle\int_0^t y(s) E'_{\beta,1}\big(-b(t-s)^\beta\big) ds \end{cases}$$

Firstly, it will be shown that the operator A is well-defined. $(x,y) \in G$ and for $t \in [0,b]$

$$A_1(x,y)(t) = \frac{1}{a_1} f\big(t, x(t), y(t)\big) + x_0 E_{\alpha,1}(-bt^\alpha) - \int_0^t x(s) E'_{\alpha,1}(-b(t-s)^\alpha) ds$$

$$A_1(x,y)(t) = \frac{1}{a_1} f\big(t, x(t), y(t)\big) + x_0 E_{\alpha,1}(-bt^\alpha) - \left\{ [x(s) \cdot E(-b(t-s)^\alpha)]_{s=0}^{s=t} - \int_0^t x'(s) E_{\alpha,1}(-b(t-s)^\alpha) ds \right\}$$

$$A_1(x,y)(t) = \frac{1}{a_1} f\big(t, x(t), y(t)\big) + 2x_0 E_{\alpha,1}(-bt^\alpha) - x(t) + \int_0^t x'(s) E_{\alpha,1}(-b(t-s)^\alpha) ds$$

For the solution $\big(x(t), y(t)\big)$ of the problem (1.1) we have $A_1(x,y)(t) = x(t)$ and multiplying both sides of the above equation we write

$$2a_1 A_1(x,y)(t) = f\big(t, x(t), y(t)\big) + 2a_1 x_0 E_{\alpha,1}(-bt^\alpha) + a_1 \int_0^t x'(s) E_{\alpha,1}(-b(t-s)^\alpha) ds$$

$$\Rightarrow A_1(x,y)(t) = \frac{1}{2a_1} f\big(t,x(t),y(t)\big) + x_0 E_{\alpha,1}(-bt^\alpha) + \frac{1}{2}\int_0^t x'(s)E_{\alpha,1}(-b(t-s)^\alpha)ds$$

$$\Rightarrow \|A_1(x,y)\| \le \frac{1}{2a_1}\big\|f\big(t,x(t),y(t)\big)\big\| + |x_0|\underbrace{\big\|E_{\alpha,1}(-bt^\alpha)\big\|}_{\le 1} + \frac{1}{2}\left\|\int_0^t x'(s)E_{\alpha,1}(-b(t-s)^\alpha)ds\right\|$$

$$\le \frac{1}{2a_1}\big\|f\big(t,x(t),y(t)\big)\big\| + |x_0| + \frac{1}{2}\underbrace{\big\|E_{\alpha,1}(-b(t-s)^\alpha)\big\|}_{\le 1}\left\|\int_0^t x'(s)ds\right\|$$

$$\le \frac{1}{2a_1}\big\|f\big(t,x(t),y(t)\big)\big\| + |x_0| + \left(\frac{1}{2}|x(s)|_0^t\right)$$

$$\le \frac{1}{2a_1}a_1 + \frac{1}{2}\|x\| + \frac{1}{2}|x_0|$$

$$= \frac{1}{2}(1 + \|x\| + |x_0|)$$

Similarly,

$$\|A_2(x,y)\| \le \frac{1}{2}(1 + \|y\| + |y_0|)$$

Thus, the operator A is well defined. Clearly, the fixed points of the operator A are solutions to problem (1.1). Now let's show that A is a contraction operator. For $\forall (x,y),(\bar{x},\bar{y}) \in G$

$$|A_1(x,y)(t) - A_1(\bar{x},\bar{y})(t)| = \left|\frac{1}{2a_1}f\big(t,x(t),y(t)\big) + x_0E_{\alpha,1}(-bt^\alpha) + \frac{1}{2}\int_0^t x'(s)E_{\alpha,1}(-b(t-s)^\alpha)ds\right.$$

$$\left. - \frac{1}{2a_1}f\big(t,\bar{x}(t),\bar{y}(t)\big) - \bar{x}_0E_{\alpha,1}(-bt^\alpha) - \frac{1}{2}\int_0^t \bar{x}'(s)E_{\alpha,1}(-b(t-s)^\alpha)ds\right|$$

$$\le \frac{1}{2a_1}\big|f\big(t,x(t),y(t)\big) - f\big(t,\bar{x}(t),\bar{y}(t)\big)\big| + \big|(x_0-\bar{x}_0)E_{\alpha,1}(-bt^\alpha)\big|$$

$$+\frac{1}{2}\left|\int_0^t \big(x'(s)-\bar{x}'(s)\big)E_{\alpha,1}(-b(t-s)^\alpha)ds\right|$$

If the norms of both sides of the inequality are taken we have

$$|A_1(x,y)(t) - A_1(\bar{x},\bar{y})(t)| \le \frac{1}{2\Gamma(\alpha)}(\|x-\bar{x}\| + \|y-\bar{y}\|) + \|x_0-\bar{x}_0\|\underbrace{\big\|E_{\alpha,1}(-bt^\alpha)\big\|}_{\le 1}$$

$$+\frac{1}{2}\big\|E_{\alpha,1}(-b(t-s)^\alpha)\big\|\left|\int_0^t \big(x'(s)-\bar{x}'(s)\big)ds\right|$$

$$\le \frac{1}{2\Gamma(\alpha)}(\|x-\bar{x}\| + \|y-\bar{y}\|) + \|x_0-\bar{x}_0\| + \frac{1}{2}\|x-\bar{x}\|$$

$$\le \frac{1}{2\Gamma(\alpha)}(\|x-\bar{x}\| + \|y-\bar{y}\|) + \frac{1}{2}\|x-\bar{x}\|$$

$$\leq \frac{1}{2\Gamma(\alpha)}(\|x-\bar{x}\|+\|y-\bar{y}\|)+\frac{1}{2\Gamma(\alpha)}\|x-\bar{x}\|+\frac{1}{2\Gamma(\alpha)}\|y-\bar{y}\|$$

$$=\frac{1}{\Gamma(\alpha)}(\|x-\bar{x}\|+\|y-\bar{y}\|)$$

and similarly we have

$$|A_2(x,y)(t)-A_2(\bar{x},\bar{y})(t)| \leq \frac{1}{\Gamma(\beta)}(\|x-\bar{x}\|+\|y-\bar{y}\|)$$

We obtain,

$$\|A(x,y)-A(\bar{x},\bar{y})\| \leq M\begin{pmatrix}\|x-\bar{x}\|\\ \|y-\bar{y}\|\end{pmatrix}$$

where,

$$M=\begin{pmatrix}\frac{1}{\Gamma(\alpha)} & \frac{1}{\Gamma(\alpha)}\\ \frac{1}{\Gamma(\beta)} & \frac{1}{\Gamma(\beta)}\end{pmatrix} \in \mathcal{M}_{2\times 2}(\mathbb{R}^2)$$

A is a contraction operator since the matrix M is convergent to zero. Therefore, according to Theorem 2.9 the operator A has a unique fixed point, which is the solution of problem (1.1).

The following example is given to explain Theorem 3.4 stated above and to explain the application process of the proposed method.

Example 3.2. Consider the problem:

$$\begin{cases} {}^{ABC}D_{0,t}^{0,4}x(t)+x^2-y = e^{-t}x+siny \\ {}^{ABC}D_{0,t}^{0,5}y(t)+y^2-x = cosx+ty \\ t\in[0,2]\ , \quad 0<\alpha,\beta<1 \\ x(0)=1\ ,\ y(0)=2 \end{cases} \tag{3.4}$$

$J=[0,2]$, $K=\{x,y\in\mathbb{R}:|x-x_0|<\delta,|y-y_0|<\delta\}$ where $x_0=1, y_0=2$, $\delta=1$ meaning $K=(0,2)\times(1,3)$ also, $\alpha=0.4$, $\beta=0.5$ and $a_1=2$, $a_2=3$. Let is define the continuous functions as follows.

$$\phi(t,x,y)=e^{-t}x+siny\ ,\ \psi(t,x,y)=cosx+ty$$

$$T(x,y)=x^2-y\ ,\ S(x,y)=y^2-x$$

Thus, we have

$$f(t,x,y)=e^{-t}x+siny-(x^2-y)$$

$$g(t,x,y)=cosx+ty-(y^2-x)$$

Now, we determine the Lipschitz constants:

$$L_1=\frac{1}{\Gamma(0.4)}\ ,\quad L_2=\frac{1}{\Gamma(0.4)}$$

$$N_1=\frac{1}{\Gamma(0.5)}\ ,\quad N_2=\frac{1}{\Gamma(0.5)}$$

$$L_3=\frac{1}{\Gamma(0.4)}\ ,\quad L_4=\frac{1}{\Gamma(0.4)}$$

$$N_3 = \frac{1}{\Gamma(0.5)}, \quad N_4 = \frac{1}{\Gamma(0.5)}$$

Here, we verify the conditions:

$$L_1 + L_2 < a_1, \quad L_3 + L_4 < a_1$$
$$N_1 + N_2 < a_2, \quad N_3 + N_4 < a_2$$

and

$$\frac{1}{\Gamma(0.4)} + \frac{1}{\Gamma(0.5)} < 1$$

Since all the conditions of Theorem 3.4 are satisfied, it follows that problem (3.4) has a unique solution.

4. Conclusion

In this study, we addressed the initial value problem for a nonlinear system of fractional differential equations involving the Atangana–Baleanu derivative in the Caputo sense. By utilizing a fixed point theorem in the Perov framework, we rigorously established sufficient conditions for the existence and uniqueness of solutions. The fixed point approach employed herein not only generalizes classical Banach-type results but also offers a robust mathematical foundation tailored to fractional systems with nonlocal and nonsingular kernels.

The presented theoretical framework was validated through an illustrative example, where all conditions of the main theorem were satisfied explicitly. This example demonstrated the practical applicability of the proposed method and confirmed the contraction nature of the associated operator via a Lipschitz matrix that converges to zero. The successful application to this example highlights the consistency and effectiveness of the Perov-type fixed point technique in handling nonlinear coupled systems.

The main contributions of this work can be summarized as follows:

- We adapted the Perov fixed point theorem to a class of nonlinear fractional systems with Atangana–Baleanu dynamics.
- We demonstrated the applicability of this approach to coupled differential equations, offering a new path for analytical treatment of such models.
- We provided verifiable criteria involving Lipschitz conditions and matrix convergence, which can guide future analytical and numerical investigations.

Future studies may explore several directions based on this framework. These include:

- Extending the analysis to systems involving variable-order or distributed-order derivatives.
- Applying the method to partial fractional differential equations arising in physics, biology, or engineering.
- Integrating the approach with numerical approximation methods for simulations involving real-world data.
- Investigating stability, controllability, and asymptotic behavior of such fractional systems under various boundary or delay conditions.

We believe that this work lays a solid foundation for further development in both the theory and applications of fractional-order differential equations governed by generalized derivative operators.

Author Contributions

All authors contributed equally to the preparation of this work. The paper is based on the second author's master's thesis, conducted under the supervision of the first author. All authors have read and approved the final version of the manuscript.

Conflict of Interest

The authors declare that there is no conflict of interest regarding the publication of this paper.

Ethical Review and Approval

This study did not require approval from an institutional ethics committee.

Acknowledgment

I would like to thank the referees who contributed to this article with their comments and suggestions.

References

[1] K. B. Oldham, J. Spanier, The fractional calculus – Theory and applications of differentiation and integration to arbitrary order, Vol. 111 of Mathematics in Science and Engineering, 1st Edition, Elseiver Science, New York, 1974.

[2] J. Padovan, *Computational algorithms for FE formulations involving fractional operators*, Computational Mechanics 2 (4) (1987) 271–287.

[3] K. S. Miller, B. Ross, An introduction to the fractional calculus and fractional differential equations, John Wiley & Sons, New York, 1993.

[4] I. Podlubny, Fractional differential equations – An introduction to fractional derivatives, fractional differential equations, to methods of their solution and some of their applications, Vol. 198 of Mathematics in Science and Engineering, 1st Edition, Academic Press, San Diego, 1999.

[5] H. Bilgil, S. Yüksel, *Comparision of conformable and Caputo fractional grey models*, Journal of Computational and Applied Mathematics 463 (2025) 116500.

[6] M. Caputo, M. Fabrizio, *A new definition of fractional derivative without singular kernel*, Progress in Fractional Differentiation and Applications 1 (2) (2015) 73–85.

[7] A. Atangana, B. Dumitru, *New fractional derivatiands with nonlocal and non-singular kernel: Theroy and aplicaion to heat transfer model*, Thermal Sciences 20 (2) (2016) 763–769.

[8] A. Chidouh, A. Guezane-Lakoud, R. Bebbouchi, *Positive solutions of the fractional relaxation equation using lower and upper solutions*, Vietnam Journal of Mathematics 44 (4) (2016) 739–748.

[9] M. ur Rahman, M. Arfan, D. Baleanu, *Piecewise fractional analysis of the migration effect in plant-pathogen-herbivore interactions*, Bulletin of Biomathematics 1 (1) (2023) 1–23.

[10] N. A. Shah, D. Vieru, C. Fetecau, *Effects of the fractional order and magnetic field on the blood flow in cylindrical domains*, Journal of Magnetism and Magnetic Materials 409 (2016) 10–19.

[11] Z. Ali, S. N. Nia, F. Rabiei, K. Shah, M. K. Tan, *A semi-analytical approach for the solution of time-fractional Navier-Stokes equation*, Advances in Mathematical Physics 2021 (2021) 5547804.

[12] V. Tripathi, S. Das, *Time-optimal feedback control of nonlocal Hilfer fractional state-dependent delay inclusion with Clarke's subdifferential*, Mathematical Methods in the Applied Sciences 47 (9) (2024) 7637–7657.

[13] M. Hajipour, A. Jajarmi, D. Baleanu, H. Sun, *On an accurate discretization of a variable-order fractional reaction-diffusion equation*, Communications in Nonlinear Science and Numerical Simulation 69 (2019) 119–133.

[14] U. B. Odionyenma, N. Ikenna, B. Bolaji, *Analysis of a model to controlthe co-dynamics of Chlamydia and Gonorrhea using Caputo fractional derivative*, Mathematical Modelling and Numerical Simulation with Applications 3 (2) (2023) 111–140.

[15] A. Jajarmi, M. Hajipour, D. Baleanu, *New aspects of the adaptive synchronization and hyperchaos suppression of a financial model*, Chaos, Solitons & Fractals 99 (2017) 285–296.

[16] H. Joshi, B. K. Jha, M. Yavuz, *Modelling and analysis of fractional-order vaccination model for control of COVID-19 outbreak using real data*, Mathematical Biosciences and Engineering 20 (1) (2023) 213-240.

[17] M. Hajipour, A. Jajarmi, D. Baleanu, *An efficient nonstandard finite difference scheme for a class of fractional chaotic systems*, Journal of Computational and Nonlinear Dynamics 13 (2) (2018) 021013.

[18] M. Wang, S. Wang, X. Ju, Y. Wang, *Image denoising method relying on iterative adaptive weight-mean filtering*, Symmetry 15 (2023) 1181.

[19] M. Hashemi, E. Ashpazzadeh, M. Moharrami, M. Lakestani, *Fractional order Alpert multiwavelets for discretizing delay fractional differential equation of pantograph type*, Applied Numerical Mathematics 170 (2021) 1–13.

[20] D. Baleanua, M. Hajipourc, A. Jajarmid, *An accurate finite difference formula for the numerical solution of delay-dependent fractional optimal control problems*, An International Journal of Optimization and Control: Theories & Applications 14 (3) (2024) 183–192.

[21] N. H. Can, H. Jafari, M. N. Ncube, *Fractional calculus in data fitting*, Alexandria Engineering Journal 59 (2020) 3269–3274.

[22] N. A. Shah, D. Vieru, C. Fetecau, *Effects of the fractional order and magnetic field on the blood flow in cylindrical domains*, Journal of Magnetism and Magnetic Materials 409 (2016) 10‑19.

[23] Z. Ali, S. N. Nia, F. Rabiei, K. Shah, M. K. Tan, *A semi-analytical approach for the solution of time-fractional Navier-Stokes equation*, Advances in Mathematical Physics 2021 (2021) 5547804.

[24] Y. Jiang, B. Zhang, X. Shu, Z. Wei, *Fractional-order autonomous circuits with order larger than one*, Journal of Advanced Research 25 (2020) 217‑225.

[25] O. W. Abdulwahhab, N. H. Abbas, *A new method to tune a fractional-order PID controller for a twin rotor aerodynamic system*, Arabian Journal for Science and Engineering 42 (2017) 5179–5189.

[26] H. Gu, *Forecasting carbon dioxide emission regional difference in China by damping fractional grey model*, Fractal and Fractional 8 (2024) 597.

[27] H. Bilgil, Ü. Erdinç, *China total energy consumption forecast with optimized continuous conformable fractional grey model*, Alphanumeric Journal 12 (2024) 157–168.

[28] Y. Zhou, *Existence and uniqueness of solitions for a system of fractional differential equations*, Fractional Calculus and Applied Analysis 12 (2) (2009) 195–204.

[29] B. Ahmad, J. J. Nieto, A. Alsaedi, *Existence and uniqueness of solutions for nonlinear fractional differential equations with non-separated type integral boundary conditions*, Acta Mathematica Scientia 31 (6) (2011) 2122–2130.

[30] B. Ahmad, S. K. Ntouyas, *Fractional differential inclusions with fractional separated boundary conditions*, Fractional Calculus and Applied Analysis 15 (2012) 362–382.

[31] X. Liu, Z. Liu, *Separated boundary value problem for fractional differential equations depending on lower-order derivative*, Advances in Difference Equations (2013) 78.

[32] N. I. Mahmudov, A. Al-Khateeb, *Stability, existence and uniqueness of boundary value problems for a coupled system of fractional differential equations*, Mathematics 7 (2019) 1–14.

[33] D. Chergui, T. E. Oussaeif, M. Ahcene, *Existence and uniqueness of solutions for nonlinear fractional differential equations depending on lower-order derivative with non-separated type integral boundary conditions*, AIMS Mathematics 4 (1) (2019) 112–133.

[34] C. Guendouz, J. E. Lazreg, J. J. Nieto, A. Ouahab, *Existence and compactness results for a system of fractional differential equations*, Journal of Function Spaces (2020) 5735140.

[35] A. Y. Madani, M. N. A. Rabih, F. A. Alqarni, Z. Ali, K. A. Aldwoah, M. Hleili, *Existence, uniqueness, and stability of a nonlinear tripled Fractional Order Differential System*, Fractal and Fractional 8 (416) (2024) 1–19.

[36] A. Ashyralyev, Y. A. Sharifov, *Existence and uniqueness of solutions for the system of nonlinear fractional differential equations with nonlocal and integral boundary conditions*, Abstract and Applied Analysis (2012) 594802.

[37] M. I. Syam, M. Al-Refai, *Fractional differential equations with Atangana–Baleanu fractional derivatiand: Analysis and applications*, Chaos, Solitons & Fractals:X 2 (2019) 100013.

[38] V. Berinde, Iterative approximation of fixed points, Vol. 1912 of Lecture Notes in Mathematics, 2nd Edition, Springer Berlin, Heidelberg, 2007.

[39] S. Banach, *Sur les opérations dans les ensembles abstraits et leur application aux équations intégrales*, Fundamenta Mathematicae 3 (1) (1922) 133–181.

[40] R. S. Varga, Matrix iteratiand analysis, Vol. 27 of Springer Series in Computational Mathematics, 2nd Edition, Springer Berlin, Heidelberg, 2000.

[41] I. A. Rus, Generalized contractions and applications, Cluj University Press, Cluj-Napoca, 2001.

[42] A. I. Perov, *On the Cauchy problem for a system of ordinary differential equations*, Približ. Metod. Rešen. Differencial. Uravnen. 2 (1964) 115–134.

[43] J. R. Graef, J. Henderson, A. Ouahab, Topological methods for differential equations and inclusions, Monographs and Research Notes in Mathematics, 1st Edition, Chapman & Hall/CRC Press, 2018.

[44] G. M. Mittag-Leffler, *Sur la nouandlle fonction* $E_\alpha(x)$, Comptes Rendus de l'Academie des Sciences Paris 137 (2) (1903) 554–558.

[45] A. Wiman, *Über die nullstellun der funktionen* $E_\alpha(x)$, Acta Mathematica 29 (1905) 217–234.

[46] W. R. Schineider, *Completely monotone generalized Mittag-Leffler functions*, Expositiones Mathematicae 14 (1996) 3–16.

[47] K. Diethelm, *The analysis of fractional differential equations: An application-oriented exposition using differential operators of Caputo type*, in: J. -M. Morel, F. Takens, B. Teissier (Eds.), Vol. 2004 of Lecture Notes in Mathematics, Springer-Verlag Berlin Heidelberg, 2010.

[48] M. Hassouna, E. H. El Kinani, A. Ouhadan, *Global existence and uniqueness of solution of Atangana–Baleanu Caputo fractional differential equation with nonlinear term and approximate solutions*, International Journal of Differential Equations 2021 (2021) 1–11.

Journal of New Results in Science
dergipark.org.tr/tr/pub/jnrs
Open Access

ISSN: 1304-7981 14 (2) (2025) 138-151 doi.org/10.54187/jnrs.1671958

An Extension of Maddox's Paranormed Sequence Spaces with Narayana Numbers

Hacer Bilgin Ellidokuzoğlu[1], Serkan Demiriz[2]

Article Info
Received: 08 Apr 2025
Accepted: 23 Jul 2025
Published: 31 Aug 2025
Research Article

Abstract— This study focuses on constructing an extended version of Maddox's paranormed sequence spaces, denoted by $c_0(N,p)$, $c(N,p)$, $\ell_\infty(N,p)$, and $\ell(N,p)$. The study aims to define and investigate the characteristics of these sequence spaces, along with their paranormed extensions. In particular, it develops a theoretical framework for Narayana sequence spaces, establishing their topological, algebraic, and matrix transformation properties. The Schauder basis for these spaces is introduced, laying the foundation for further functional analysis. The research also examines the α-, β-, and γ-duals of these spaces and investigates the conditions under which matrix transformations preserve their structural properties. The findings highlight the equivalences between these spaces and classical sequence spaces such as ℓ_1, c, and ℓ_∞.

Keywords — *Narayana numbers, Maddox's paranormed sequence spaces, Schauder basis, topological properties, paranormed sequence spaces*

1. Introduction

In the 14th century, Narayana investigated a problem concerning a herd of cows and calves, which is analogous to the well-known Fibonacci rabbit problem [1, 2]. In this problem, each cow gives birth to one calf annually, and starting from its fourth year, each calf also begins to reproduce every year. The primary question posed is: How many calves are present after 20 years? This situation can be modeled similarly to the Fibonacci sequence as

$$n_{s+3} = n_{s+2} + n_s, \quad \text{with } s \geq 0,\ n_0 = 0,\ n_1 = 1,\ n_2 = 1.$$

The resulting sequence is:

$$0, 1, 1, 1, 2, 3, 4, 6, 9, 13, 19, 28, \ldots$$

This sequence is known as the Narayana sequence, or sometimes the Fibonacci–Narayana sequence, and has drawn significant attention in contemporary mathematical literature [3–8].

In recent years, integer sequences such as Fibonacci, Lucas, Padovan, Catalan, Bell, Schröder, and Narayana have been extensively examined in the field of sequence space theory. In 2023, Bilgin Ellidokuzoğlu introduced a new regular matrix constructed via Narayana numbers, which facilitated the formulation of novel sequence spaces. Paranormed spaces, which generalize normed spaces by

[1]hacer.bilgin@erdogan.edu.tr(Corresponding Author); [2]serkandemiriz@gmail.com
[1]Department of Mathematics, Faculty of Arts and Sciences, Recep Tayyip Erdoğan University, Rize, Türkiye
[2]Department of Mathematics, Faculty of Arts and Sciences, Tokat Gaziosmanpaşa University, Tokat, Türkiye

relaxing some of their constraints, constitute the principal focus of this study. This work extends the sequence spaces initially introduced by Bilgin Ellidokuzoğlu [9].

The rest of the paper is organized as follows: Section 2 provides a detailed definition and characterization of the extended paranormed sequence spaces, including their foundational properties and key theorems. Section 3 presents the theoretical framework for Narayana sequence spaces, focusing on their topological and algebraic structures. Section 4 discusses the duals of these spaces, specifically the α-, β-, and γ-duals, and explores the conditions under which matrix transformations maintain their properties. Section 5 concludes with a summary of the results and potential areas for further research.

2. Preliminaries

Let ω denote the set of all real or complex sequences. A sequence space is defined as a vector subspace of ω, with classical examples including c_0, c, ℓ_p, and ℓ_∞. These spaces possess well-established topological structures and are foundational in functional analysis.

c_0: the space of all sequences converging to zero.
c: the space of all convergent sequences.
ℓ_p: the space of sequences whose p-th power of absolute values is summable, for $1 \leq p < \infty$.
ℓ_∞: the space of all bounded sequences.

Each of these is a Banach space, meaning it is complete with respect to the corresponding norm, and thus plays a central role in analysis.

In the context of functional analysis, a real or complex linear space Z is often equipped with a function $\rho : Z \to \mathbb{R}$ satisfying certain axioms. The pair (Z, ρ) is referred to as a *paranormed space* if ρ satisfies the following properties for all $z, h \in Z$ and scalars α:

i. $\rho(z) \geq 0$ and $\rho(z) = 0$ if and only if $z = 0$ (positivity and definiteness).

ii. $\rho(\alpha z) = |\alpha|\rho(z)$ (absolute homogeneity).

iii. $\rho(z + h) \leq \rho(z) + \rho(h)$ (triangle inequality).

iv. $|\alpha_n - \alpha| \to 0$ and $\rho(z_n - z) \to 0$ imply $\rho(\alpha_n z_n - \alpha z) \to 0$ (continuity of scalar multiplication).

These conditions generalize the concept of normed spaces, especially in infinite-dimensional contexts.

Maddox [10], Simons [11], and Nakano [12] developed generalized sequence spaces $c_0(p)$, $c(p)$, $\ell_\infty(p)$, and $\ell(p)$, defined as follows:

$$\begin{aligned} c_0(p) &= \{z = (z_r) \in \omega : \lim_{r\to\infty} |z_r|^{p_r} = 0\}, \\ c(p) &= \{z = (z_r) \in \omega : \lim_{r\to\infty} |z_r - \lambda|^{p_r} = 0 \text{ for some } \lambda \in \mathbb{R}\}, \\ \ell_\infty(p) &= \{z = (z_r) \in \omega : \sup_{r\in\mathbb{N}} |z_r|^{p_r} < \infty\}, \\ \ell(p) &= \left\{z = (z_r) \in \omega : \sum_r |z_r|^{p_r} < \infty\right\}. \end{aligned}$$

To demonstrate that each of the spaces $c_0(p)$, $c(p)$, $\ell(p)$, and $\ell_\infty(p)$ forms a linear space under pointwise addition and scalar multiplication, we define the following paranorms:

$$\rho_1(z) = \sup_{r\in\mathbb{N}} |z_r|^{p_r/L}, \quad \rho_2(z) = \left(\sum_r |z_r|^{p_r}\right)^{1/L},$$

where $p = (p_r)$ is a bounded sequence of positive real numbers, $M = \sup_r p_r$, and $L = \max\{1, M\}$.

It has been shown that $c_0(p)$ and $c(p)$ are complete paranormed spaces with respect to ρ_1, provided $p \in \ell_\infty$ [13]. According to [14], the inclusion $c_0(p) \subset c(p)$ holds if and only if $\liminf q_r/p_r > 0$. Similarly, $\ell_\infty(p)$ is complete under ρ_1 when $\inf p_r > 0$. The space $\ell(p)$ is also a linear space under coordinatewise operations and is complete with respect to the paranorm ρ_2.

Let Λ and Ω be sequence spaces, and let $\mathcal{T} = (t_{rs})$ be an infinite matrix with entries in $\mathbb{R}$ or $\mathbb{C}$, where $r, s \in \mathbb{N}$. The matrix $\mathcal{T}$ defines a transformation $\mathcal{T} : \Lambda \to \Omega$ if, for every $z = (z_s) \in \Lambda$, the sequence $\mathcal{T}z = \{(\mathcal{T}z)_r\}$ belongs to Ω, with

$$(\mathcal{T}z)_r = \sum_s t_{rs} z_s, \quad (r \in \mathbb{N}).$$

The collection of all such matrices is denoted by $(\Lambda : \Omega)$, meaning that $\mathcal{T} \in (\Lambda : \Omega)$ if the series on the right converges for each $r \in \mathbb{N}$ and $\mathcal{T}z \in \Omega$ for all $z \in \Lambda$.

The domain of the matrix $\mathcal{T}$ in a sequence space Z is defined by

$$Z_{\mathcal{T}} = \{z \in \omega : \mathcal{T}z \in Z\}. \tag{2.1}$$

Historically, the study of paranormed sequence spaces as domains of special triangular matrices has yielded significant insights, particularly within the spaces $\ell(p)$, $c_0(p)$, $c(p)$, and $\ell_\infty(p)$. Ahmad and Mursaleen [15] investigated the forward difference matrix Δ, defining the associated sequence spaces by

$$X(\Delta, p) = \{z \in \omega : \Delta z \in X(p)\},$$

where $X \in \{c_0, c, \ell_\infty\}$.

More recently, numerous researchers have constructed new paranormed sequence spaces by using matrix domains derived from various summability methods. For relevant studies, see [16–40].

3. Paranormed Narayana Sequence Spaces

This section introduces the Narayana sequence spaces, their definitions, and characteristics, along with the paranormed sequence spaces derived from the Narayana matrix.

The Narayana matrix $N = (n_{rs})$ is defined as follows:

$$n_{rs} = \begin{cases} \frac{n_s}{n_{r+3}-1}, & 1 \leqslant s \leqslant r, \\ 0, & s > r, \end{cases}$$

for all $r, s \in \mathbb{N}$. The inverse of N, denoted by $N^{-1} = (n_{rs}^{-1})$, is given by:

$$n_{rs}^{-1} = \begin{cases} (-1)^{r-s} \dfrac{n_{s+3} - 1}{n_r}, & r \leqslant s \leqslant r+1, \\ 0, & s > r, \end{cases}$$

for all $r, s \in \mathbb{N}$.

In a recent publication, Bilgin Ellidokuzoğlu [9] defined the following spaces using the Narayana matrix:

$$
\begin{aligned}
c_0(N) &= \left\{ z=(z_s)\in\omega : \lim_{r\to\infty}\sum_{s=1}^{r}\frac{n_s}{n_{r+3}-1}z_s=0 \right\},\\
c(N) &= \left\{ z=(z_s)\in\omega : \lim_{r\to\infty}\sum_{s=1}^{r}\frac{n_s}{n_{r+3}-1}z_s \text{ exists} \right\},\\
\ell_p(N) &= \left\{ z=(z_s)\in\omega : \sum_{r=1}^{\infty}\left|\sum_{s=1}^{r}\frac{n_s}{n_{r+3}-1}z_s\right|^p<\infty \right\},\\
\ell_\infty(N) &= \left\{ z=(z_s)\in\omega : \sup_{r\in\mathbb{N}}\left|\sum_{s=1}^{r}\frac{n_s}{n_{r+3}-1}z_s\right|<\infty \right\}.
\end{aligned}
$$

Bilgin Ellidokuzoğlu's work focuses on the development of these sequence spaces based on Narayana sequences, demonstrating their algebraic and topological properties. Her study highlights the connections between these new spaces and classical sequence spaces, significantly contributing to the understanding and application of Narayana sequences in various mathematical contexts.

In this paper, we introduce a class of paranormed sequence spaces derived from the Narayana matrix N. The spaces considered are $c_0(N,p)$, $c(N,p)$, $\ell_\infty(N,p)$, and $\ell(N,p)$, defined as follows:

$$
\begin{aligned}
c_0(N,p) &= \left\{ z=(z_s)\in w : \lim_{r\to\infty}\left|\sum_{s=1}^{r}\frac{n_s}{n_{r+3}-1}z_s\right|^{p_r}=0 \right\},\\
c(N,p) &= \left\{ z=(z_s)\in w : \lim_{r\to\infty}\left|\sum_{s=1}^{r}\frac{n_s}{n_{r+3}-1}z_s-\lambda\right|^{p_r}=0, \exists\lambda\in\mathbb{R} \right\},\\
\ell_\infty(N,p) &= \left\{ z=(z_s)\in\omega : \sup_{r\in\mathbb{N}}\left|\sum_{s=1}^{r}\frac{n_s}{n_{r+3}-1}z_s\right|^{p_r}<\infty \right\},\\
\ell(N,p) &= \left\{ z=(z_s)\in\omega : \sum_{r=1}^{\infty}\left|\sum_{s=1}^{r}\frac{n_s}{n_{r+3}-1}z_s\right|^{p_r}<\infty \right\}.
\end{aligned}
$$

These spaces generalize classical sequence spaces by incorporating the Narayana matrix N and the parameter p. In subsequent sections, we investigate their topological and algebraic properties, exploring the relationships between them.

The representation of the sequence spaces $c_0(N,p)$, $c(N,p)$, $\ell_\infty(N,p)$, and $\ell(N,p)$ can be denoted using the notation (2.1) as follows:

$$
\begin{aligned}
c_0(N,p) &= [c_0(p)]_N, c(N,p)=[c(p)]_N,\\
\ell_\infty(N,p) &= [\ell_\infty(p)]_N \text{ and } \ell(N,p)=[\ell(p)]_N.
\end{aligned}
$$

When $p=(p_s)=1$, the above sequence spaces are reduced to $c_0(N)$, $c(N)$, $\ell_\infty(N)$, and $\ell_p(N)$, respectively, which were initially introduced by Bilgin Ellidokuzoğlu [9].

In the following section, we will focus on exploring the topological properties of these spaces. Specifically, we will examine aspects such as completeness, convergence, and continuity of the transformations defined by the Narayana matrix N. Our aim is to develop a deeper understanding of how these new paranormed Narayana sequence spaces relate to classical sequence spaces. This will help us gain insights into their mathematical structure and their potential uses in various fields.

The sequence $h=(h_r)$ can be obtained by applying the N-transform to the sequence $z=(z_r)$, with the following expression:

$$h_r = \sum_{s=1}^{r} \frac{n_s}{n_{r+3} - 1} z_s, \quad \text{for all } r \in \mathbb{N}.$$

Conversely, the sequence $z = (z_r)$ can be expressed in terms of $h = (h_r)$ as follows:

$$z_r = \sum_{s=r-1}^{r} (-1)^{r-s} \frac{n_{s+3} - 1}{n_r} h_s, \quad \text{for all } r \in \mathbb{N}. \tag{3.1}$$

Let us proceed to the next important theorem in our study.

Theorem 3.1. The sequence spaces $c_0(N, p)$, $c(N, p)$ and $\ell_\infty(N, p)$ are each complete linear metric spaces, with the paranorm given by

$$f(z) = \sup_{r \in \mathbb{N}} \left| \sum_{s=1}^{r} \frac{n_s}{n_{r+3} - 1} z_s \right|^{p_r/L}. \tag{3.2}$$

Proof. We present the proof for the $c(N, p)$ space here, and the other cases can be proven similarly. First, assume that $f(\theta) = 0$, and for all $z \in c(N, p)$, we have $f(-z) = f(z)$. For $z, t \in c(N, p)$ and scalars $\alpha_1, \alpha_2 \in \mathbb{R}$, we obtain the following expression:

$$f(\alpha_1 z + \alpha_2 t) = \sup_{r} \left| \sum_{s=1}^{r} \frac{n_s}{n_{r+3} - 1} (\alpha_1 z_s + \alpha_2 t_s) \right|^{p_r/L}.$$

Using the properties of the supremum and absolute values, we can separate the sum into two terms:

$$f(\alpha_1 z + \alpha_2 t) \leq \max\{1, |\alpha_1|\} f(z) + \max\{1, |\alpha_2|\} f(t).$$

This shows that the function is linear with respect to scalar multiplication and coordinatewise addition. Thus, we have proven that the space $c(N, p)$ is a linear space. Assume that $\{z^r\}$ is a sequence of points $z^r \in c(N, p)$ such that $f(z^r - z) \to 0$, and (α_r) is a sequence of scalars with $\alpha_r \to \alpha$. By the subadditivity of f, the following inequality holds:

$$f(z^r) \leq f(z) + f(z^r - z),$$

which shows that the sequence $\{f(z^r)\}$ is bounded. Consequently, we obtain the following inequality:

$$f(\alpha_r z^r - \alpha z) = \sup_{r \in \mathbb{N}} \left| \sum_{s=1}^{r} \frac{n_s}{n_{r+3} - 1} (\alpha_r z_s^r - \alpha z_s) \right|^{p_r/L},$$

and it can be bounded as:

$$\leq |\alpha_r - \alpha|^{p_r/L} f(z^r) + |\alpha|^{p_r/L} f(z^r - z),$$

which tends to zero as $r \to \infty$. This shows that scalar multiplication is continuous. Therefore, f is a paranorm on the space $c(N, p)$.

Next, we need to prove that the space $c(N, p)$ is complete. Let $\{z^r\}$ be any Cauchy sequence in the space $c(N, p)$, where

$$z^r = \{z_0^{(r)}, z_1^{(r)}, z_2^{(r)}, \ldots\}.$$

For a given $\varepsilon > 0$, there exists $n_0(\varepsilon)$ such that for all $r, s > n_0(\varepsilon)$,

$$f(z^r - z^s) < \frac{\varepsilon}{2}.$$

For each fixed $k \in \mathbb{N}$, using the definition of f, we can write the following inequality:

$$|(Nz^r)_k - (Nz^s)_k|^{p_k/L} \leq \sup_{k\in\mathbb{N}} |(Nz^r)_k - (Nz^s)_k|^{p_k/L} < \frac{\varepsilon}{2}, \tag{3.3}$$

for all $s, r > n_0(\varepsilon)$. As a result, for each fixed $k \in \mathbb{N}$, $\{(Nz^r)_k\}$ is a Cauchy sequence of real numbers. Since $\mathbb{R}$ is complete, the sequence converges, meaning that

$$(Nz^r)_k \to (Nz)_k \text{ as } k \to \infty.$$

Now we define the sequence $\{(Nz)_0, (Nz)_1, \ldots\}$ using these infinitely many limits $(Nz)_0, (Nz)_1, \ldots$. For every fixed $k \in \mathbb{N}$, we have

$$|(Nz^r)_k - (Nz)_k|^{p_k/L} \leq \frac{\varepsilon}{2} \ (r > n_0(\varepsilon)), \tag{3.4}$$

from (3.3) with $s \to \infty$. Since $z^r = \{z_k^{(r)}\} \in c(N,p)$ for each $k \in \mathbb{N}$,

$$|(Nz^r)_k|^{p_k/L} < \frac{\varepsilon}{2}, \tag{3.5}$$

for every $r \geq n_0(\varepsilon)$ and for each fixed $k \in \mathbb{N}$. For this reason, assuming a constant $r > n_0(\varepsilon)$ we derive by (3.4) and (3.5) that

$$|(Nz)_k|^{p_k/L} \leq |(Nz)_k - (Nz^r)_k|^{p_k/L} + |(Nz^r)_k|^{p_k/L} < \varepsilon,$$

for every $s > s_0(\varepsilon)$. This demonstrates that $v \in c(N,p)$. The space $c(N,p)$ is complete, and this closes the proof because $\{z^r\}$ was an arbitrary Cauchy sequence. □

Theorem 3.2. The sequence space $\ell(N,p)$ is a complete linear metric spaces with the paranorm:

$$f_2(z) = \left(\sum_{r=0}^{\infty} \left| \sum_{s=1}^{r} \frac{n_s}{n_{r+3}-1} z_s \right|^{p_r} \right)^{1/L}. \tag{3.6}$$

Theorem 3.3. The sequence spaces $c_0(N,p)$, $c(N,p)$, $\ell_\infty(N,p)$, and $\ell(N,p)$ are linearly isomorphic to the classical sequence spaces $c_0(p)$, $c(p)$, $\ell_\infty(p)$, and $\ell(p)$, respectively, under the condition that $0 < p_s \leq H < \infty$.

Proof. To avoid redundancy, we will only prove that the space $c(N,p)$ is linearly bijective to $c(p)$. Define the linear transformation $T : c(N,p) \to c(p)$ by $z \mapsto f = Tz$, where f is expressed as in (3.1). The linearity of T is straightforward since it follows directly from the definition of T. Additionally, T is injective because if $Tz = \theta$, then $z = \theta$.

Conside $f \in c(p)$, with its representation given in (3.1):

$$f(u) = \sup_r \left| \sum_{s=1}^{r} \frac{n_s}{n_{r+3}-1} z_s \right|^{p_r/L}.$$

Substituting $z_s = \sum_{i=s-1}^{s} (-1)^{s-i} \frac{n_{i+3}-1}{n_s} h_i$, we obtain:

$$f(u) = \sup_r \left| \sum_{s=1}^{r} \frac{n_s}{n_{r+3}-1} \sum_{i=s-1}^{s} (-1)^{s-i} \frac{n_{i+3}-1}{n_s} h_i \right|^{p_r/L}.$$

This simplifies to:

$$f(u) = \sup_r \left| \sum_{s=0}^{r} \delta_{rs} h_s \right|^{p_r/L},$$

where

$$\delta_{rs} = \begin{cases} 1, & \text{if } s = r, \\ 0, & \text{if } s \neq r. \end{cases}$$

Further simplification gives:

$$f(u) = \sup_r |h_r|^{p_r/L}.$$

Since $f \in c(p)$, it follows that $h \in c(N,p)$, establishing that T is a surjective. As T is both injective and surjective, it is a linear bijection. Therefore, the spaces $c(N,p)$ and $c(p)$ are linearly isomorphic. □

In conclusion, we present the Schauder basis for the spaces $c_0(N,p)$, $c(N,p)$, and $\ell(N,p)$. To begin, the concept of the Schauder basis is analyzed. Let (X,g) represent a paranormed space. A sequence of scalars (α_s) satisfies

$$g\left(v - \sum_{s=0}^{r} \alpha_s \beta_s\right) \to 0 \quad \text{as } r \to \infty,$$

if and only if the sequence (β_s) of elements in X forms a basis for X.

Suppose X is a sequence space and $\mathcal{T}$ a triangle. Based on the observation (see [41, Remark 2.4]) that $X_{\mathcal{T}}$ possesses a basis whenever X has one, the following theorem is derived.

Theorem 3.4. Let $X_s = (Nz)_s$ for all $s \in \mathbb{N}$, where $0 < p_s \leq L < \infty$. Define the sequence $t^{(s)} = \{t^{(s)}\}_{s\in\mathbb{N}}$, consisting of elements from the spaces $c_0(N,p)$, $c(N,p)$, and $\ell(N,p)$, as follows:

$$t_r^{(s)} = \begin{cases} (-1)^{r-s} \dfrac{n_{s+3} - 1}{n_r}, & \text{if } r - 1 \leq s < r, \\ 0, & \text{otherwise} \end{cases}$$

for any fixed $s \in \mathbb{N}$. Then:

i. The sequence $\{t^{(s)}\}_{s\in\mathbb{N}}$ forms a basis for the spaces $c_0(N,p)$ and $\ell(N,p)$. Furthermore, any $z \in c_0(N,p)$ or $z \in \ell(N,p)$ can be uniquely expressed as:

$$z = \sum_s X_s t^{(s)}.$$

ii. The set $\{e, t^{(s)}\}_{s\in\mathbb{N}}$ forms a basis for the space $c(N,p)$. Moreover, any $z \in c(N,p)$ admits a unique representation of the form:

$$z = \tau e + \sum_s [X_s - \tau]\, t^{(s)},$$

where $\tau = \lim_{s\to\infty}(Nz)_s$.

4. The Duals of the New Sequence Spaces

In this section, we present and prove the main theorems that establish the α-, β-, and γ-duals for the newly defined paranormed sequence spaces. We assume that $p^\star$ represents the conjugate of p, i.e., $\frac{1}{p} + \frac{1}{p^\star} = 1$, and denote the collection of all finite subsets of $\mathbb{N}$ by $\mathcal{N}$.

The α-, β-, and γ-duals of the sequence space D are denoted by D^α, D^β, and D^γ, respectively, and are defined as follows:

$$\begin{aligned} D^{\alpha} &= \{z=(z_s)\in\omega : wz=(w_s z_s)\in \ell_1, \forall w=(w_s)\in D\}, \\ D^{\beta} &= \{z=(z_s)\in\omega : wz=(w_s z_s)\in cs, \forall w=(w_s)\in D\}, \\ D^{\gamma} &= \{z=(z_s)\in\omega : wz=(w_s z_s)\in bs, \forall w=(w_s)\in D\}. \end{aligned}$$

To derive the α-, β-, and γ-duals of the spaces $c_0(N,p)$, $c(N,p)$, $\ell_\infty(N,p)$, and $\ell(N,p)$, we will rely on the following lemma.

Lemma 4.1. [42, $t_r=1$] For an infinite matrix $\mathcal{T}=(t_{rs})$, the following conditions hold:

i. $\mathcal{T}\in(c_0(p):\ell(t))$ if and only if

$$\exists M>1 \text{ such that } \sup_{K\in\mathcal{N}}\sum_r\left|\sum_{s\in K} t_{rs}M^{-1/p_s}\right|^{t_r}<\infty \quad \text{for all} \quad t_r\geq 1. \tag{4.1}$$

ii. $\mathcal{T}\in(c(p):\ell(t))$ if and only if condition (4.1) holds, and

$$\sum_r\left|\sum_s t_{rs}\right|^{t_r}<\infty. \tag{4.2}$$

iii. $\mathcal{T}\in(c_0(p):c(t))$ if and only if

$$\exists M>1 \text{ such that } \sup_r\sum_s |t_{rs}|M^{-1/p_s}<\infty, \tag{4.3}$$

$$\exists(\alpha_s) \text{ such that } \lim_r |t_{rs}-\alpha_s|^{t_r}=0, \tag{4.4}$$

$$\forall L, \exists M>1 \text{ and } \exists(\alpha_s) \text{ such that } \sup_r L^{1/t_r}\sum_s |t_{rs}-\alpha_s|\,M^{-1/p_s}<\infty. \tag{4.5}$$

iv. $\mathcal{T}\in(c(p):c(t))$ if and only if conditions (4.3), (4.4), and (4.5) hold, and

$$\exists\alpha \text{ such that } \lim_r\left|\sum_s t_{rs}-\alpha\right|^{t_r}=0. \tag{4.6}$$

v. $\mathcal{T}\in(c_0(p):\ell_\infty(t))$ if and only if

$$\exists M, \sup_r\left(\sum_s |t_{rs}|M^{-1/p_s}\right)^{t_r}<\infty. \tag{4.7}$$

vi. $\mathcal{T}\in(c(p):\ell_\infty(t))$ if and only if condition (4.7) holds, and

$$\sup_r\left|\sum_s t_{rs}\right|^{t_r}<\infty. \tag{4.8}$$

Theorem 4.2. Let $K \in \mathcal{F}$. Consider the sets $\mathcal{S}_1, \mathcal{S}_2, \mathcal{S}_3, \mathcal{S}_4, \mathcal{S}_5, \mathcal{S}_6, \mathcal{S}_7, \mathcal{S}_8$ defined as follows:

$$\mathcal{S}_1 = \bigcup_{M>1} \left\{ a = (a_s) \in w : \sup_K \sum_r \left| \sum_{s \in K} (-1)^{r-s} \frac{n_{s+3} - 1}{n_r} a_r M^{-1/p_s} \right| < \infty \right\},$$

$$\mathcal{S}_2 = \left\{ a = (a_s) \in w : \sum_r \left| \sum_s (-1)^{r-s} \frac{n_{s+3} - 1}{n_r} a_r \right| < \infty \right\},$$

$$\mathcal{S}_3 = \bigcup_{M>1} \left\{ a = (a_s) \in w : \sup_r \sum_s \left| \sum_{i=s}^{r} (-1)^{s-i} \frac{n_{i+3} - 1}{n_s} d_i \right| M^{-1/p_s} < \infty \right\},$$

$$\mathcal{S}_4 = \left\{ a = (a_s) \in w : \exists (\alpha_s) \subset \mathbb{R} \text{ such that } \lim_r \left| \sum_{i=s}^{r} (-1)^{s-i} \frac{n_{i+3} - 1}{n_s} d_i - \alpha_s \right| = 0 \right\},$$

$$\mathcal{S}_5 = \bigcup_{M>1} \left\{ a = (a_s) \in w : \exists (\alpha_s) \subset \mathbb{R} \text{ such that } \sum_s \left| \sum_{i=s}^{r} (-1)^{s-i} \frac{n_{i+3} - 1}{n_s} d_i - \alpha_s \right| M^{-1/p_s} < \infty \right\},$$

$$\mathcal{S}_6 = \left\{ a = (a_s) \in w : \exists (\alpha_s) \subset \mathbb{R} \text{ such that } \lim_r \left| \sum_s \sum_{i=s}^{r} (-1)^{s-i} \frac{n_{i+3} - 1}{n_s} d_i - \alpha_s \right| < \infty \right\},$$

$$\mathcal{S}_7 = \bigcup_{M>1} \left\{ a = (a_s) \in w : \sup_r \left(\sum_s \left| \sum_{i=s}^{r} (-1)^{s-i} \frac{n_{i+3} - 1}{n_s} d_i \right| M^{-1/p_s} \right) < \infty \right\},$$

$$\mathcal{S}_8 = \left\{ a = (a_s) \in w : \sup_r \left| \sum_s \sum_{i=s}^{r} (-1)^{s-i} \frac{n_{i+3} - 1}{n_s} d_i \right| < \infty \right\}.$$

It follows that

$$[\mathcal{S}_0(N,p)]^\alpha = \mathcal{S}_1, \qquad [\mathcal{S}(N,p)]^\alpha = \mathcal{S}_1 \cap \mathcal{S}_2,$$
$$[\mathcal{S}_0(N,p)]^\beta = \mathcal{S}_3 \cap \mathcal{S}_4 \cap \mathcal{S}_5, \qquad [\mathcal{S}(N,p)]^\beta = \mathcal{S}_3 \cap \mathcal{S}_4 \cap \mathcal{S}_5 \cap \mathcal{S}_6,$$
$$[\mathcal{S}_0(N,p)]^\gamma = \mathcal{S}_7, \qquad [\mathcal{S}(N,p)]^\gamma = \mathcal{S}_8.$$

Proof. For proving the α-dual, let $t = (t_r) \in w$ and $v = (v_r) \in c_0(p)$ be given. Define $u = (u_r)$ as in (3.1). Then,

$$t_r u_r = \sum_{s=r-1}^{r} (-1)^{r-s} \frac{n_{s+3} - 1}{n_r} t_r v_s = (Tv)_r, \quad r \in \mathbb{N}, \tag{4.9}$$

where the matrix $T = (t_{rs})$ is defined by

$$t_{rs} = \begin{cases} (-1)^{r-s} \frac{n_{s+3}-1}{n_r} a_r, & \text{if } r-1 \le s \le r, \\ 0, & \text{otherwise.} \end{cases}$$

From equation (4.9), it can be concluded that $tu = (t_r u_r) \in \ell_1$ for every $v \in c_0(p)$ if and only if $Tv \in \ell_1$. This means that $t = (t_r) \in [c_0(N,p)]^\alpha$ if and only if $T \in (c_0(p) : \ell_1)$. By substituting $t_r = 1$ for all $r \in \mathbb{N}$ into equation (4.1), we get the result that $[c_0(N,p)]^\alpha = \mathcal{S}_1$.

Similarly, using (4.1), (4.2), and (4.9), we can prove that $[c(N,p)]^\alpha = \mathcal{S}_1 \cap \mathcal{S}_2$.

Next, consider the equation:

$$\begin{aligned} \sum_{s=1}^{r} d_s v_s &= \sum_{s=1}^{r} \left[\sum_{i=0}^{s} (-1)^{s-i} \frac{n_{i+3} - 1}{n_s} v_i \right] d_s \\ &= \sum_{s=1}^{r} \left[\sum_{i=s}^{r} (-1)^{s-i} \frac{n_{i+3} - 1}{n_s} d_i \right] v_s = (Dv)_r, \end{aligned} \tag{4.10}$$

where $D = (d_{rs})$ is the matrix defined by

$$d_{rs} = \begin{cases} \sum_{i=s}^{r} (-1)^{s-i} \frac{n_{i+3}-1}{n_s} d_i, & \text{if } 0 \leq s \leq r, \\ 0, & \text{if } s > r. \end{cases}$$

Thus, it follows from (4.10) that $dv = (d_s v_s) \in cs$ whenever $v = (v_s) \in c_0(p)$ if and only if $Dv \in c_0$. This implies that $d = (d_s) \in [c_0(N,p)]^\beta$ if and only if $D \in (c_0(p) : c)$.

Therefore, by using (4.3), (4.4), (4.5), and (4.10), we conclude that $[c_0(N,p)]^\beta = \mathcal{S}_3 \cap \mathcal{S}_4 \cap \mathcal{S}_5$. Similarly, by incorporating (4.6), the proof of $[c(N,p)]^\beta = \mathcal{S}_3 \cap \mathcal{S}_4 \cap \mathcal{S}_5 \cap \mathcal{S}_6$ can be completed in a similar manner.

The proof of the γ-dual follows similarly to the β-dual and is left to the reader. □

5. Matrix Transformations on the New Paranormed Sequence Spaces

In this section, we examine the matrix transformations related to the newly defined paranormed sequence spaces as well as the classical spaces $c_0(N,p)$, $c(N,p)$, $\ell_\infty(N,p)$, and $\ell(N,p)$. Our focus is twofold: first, to identify the conditions under which a matrix maps elements between paranormed sequence spaces while preserving their structural properties; and second, to explore the equivalence of the following conditions in the context of these spaces:

$$v \in H_{\mathcal{T}} \quad \text{for every triangular matrix } \mathcal{T} \text{ and any sequence space } H$$
$$\text{if and only if } f = \mathcal{T}v \in H.$$

This equivalence is justified by the fact that $H_{\mathcal{T}} \cong H$.

Theorem 5.1. Let $H \in \{\ell_\infty, c, \ell_1\}$. Then:

i. The matrix $\mathcal{T} = (t_{rs}) \in (c_0(N,p) : H)$ holds if and only if:

$$\mathcal{T}_r \in \{c_0(N,p)\}^\beta \quad \text{for all } r \in \mathbb{N}, \tag{5.1}$$
$$B \in (c_0 : H), \tag{5.2}$$

where $B = (b_{rs})$ with

$$b_{rs} = \sum_{i=s}^{\infty} (-1)^{s-i} \frac{n_{i+3}-1}{n_s} a_{ri}, \quad \text{for all } r, s \in \mathbb{N},$$

and $\mathcal{T}_r$ denotes the r-th row of the infinite matrix $\mathcal{T}$, where n_s and a_{ri} are sequences appropriately defined in relation to the elements of $\mathcal{T}$.

ii. The matrix $\mathcal{T} = (t_{rs}) \in (c(N,p) : H)$ holds if and only if:

$$\mathcal{T}_r \in \{c(N,p)\}^\beta \quad \text{for all } r \in \mathbb{N}, \tag{5.3}$$
$$B \in (c : H). \tag{5.4}$$

Proof. We will demonstrate only part (i). Assume that $\mathcal{T} = (t_{rs}) \in (c_0(N,p) : H)$ and let $v \in c_0(N,p)$ be an arbitrary sequence. By assumption, $\mathcal{T}_r \in \{c_0(N,p)\}^\beta$ holds for every $r \in \mathbb{N}$. Define $f = Nv$. From the condition $\mathcal{T}_r \in \{c_0(N,p)\}^\beta$, it follows that:

$$(\mathcal{T}v)_r = (Bf)_r \quad \text{for all } r \in \mathbb{N}. \tag{5.5}$$

Thus, $Bf \in H$ for every $f \in c_0$, implying that $B \in (c_0 : H)$.

Next, consider the relationship $Ef = \mathcal{T}v$, leading to the conclusion that $E \in (c_0(p) : \mu)$. Now, suppose conditions (5.1) and (5.2) are satisfied. Then, (5.5) remains valid, indicating that $\mathcal{T}v \in H$ for all

$v \in c_0(N,p)$. □

Corollary 5.2. Let $\mathcal{T} = (t_{rs})$ be an infinite matrix. The following hold:

i. $\mathcal{T} \in (c_0(N,p) : \ell(t))$ if and only if $\{t_{rs}\}_{s\in\mathbb{N}} \in \{c_0(N,p)\}^\beta$ for all $r \in \mathbb{N}$ and equation (4.1) holds with b_{rs} instead of t_{rs} and $t = 1$.

ii. $\mathcal{T} \in (c_0(N,p) : c(t))$ if and only if $\{t_{rs}\}_{s\in\mathbb{N}} \in \{c_0(N,p)\}^\beta$ for all $r \in \mathbb{N}$, and conditions (4.3), (4.4), and (4.5) hold with b_{rs} instead of t_{rs} and $t = 1$.

iii. $\mathcal{T} \in (c_0(N,p) : \ell_\infty(t))$ if and only if $\{t_{rs}\}_{s\in\mathbb{N}} \in \{c_0(N,p)\}^\beta$ for all $r \in \mathbb{N}$, and condition (4.7) holds with b_{rs} instead of t_{rs} and $t = 1$.

Corollary 5.3. Let $\mathcal{T} = (t_{rs})$ be an infinite matrix. The following statements hold:

i. $\mathcal{T} \in (c(N,p) : \ell(t))$ if and only if $\{t_{rs}\}_{s\in\mathbb{N}} \in \{c(N,p)\}^\beta$ for all $r \in \mathbb{N}$, and conditions (4.1) and (4.2) hold with b_{rs} instead of t_{rs} and $t = 1$.

ii. $\mathcal{T} \in (c(N,p) : c(t))$ if and only if $\{t_{rs}\}_{s\in\mathbb{N}} \in \{c(N,p)\}^\beta$ for all $r \in \mathbb{N}$, and conditions (4.3), (4.4), (4.5), and (4.6) hold with b_{rs} instead of t_{rs} and $t = 1$.

iii. $\mathcal{T} \in (c(N,p) : \ell_\infty(t))$ if and only if $\{t_{rs}\}_{s\in\mathbb{N}} \in \{c(N,p)\}^\beta$ for all $r \in \mathbb{N}$, and condition (4.8) holds with b_{rs} instead of t_{rs} and $t = 1$.

6. Conclusions

This study has expanded upon previous research on sequence spaces formed by combinatorial sequences such as Fibonacci, Lucas, Padovan, Catalan, Bell, Schröder, and Narayana numbers. Building upon earlier research involving the construction of sequence spaces using Narayana numbers, we have developed new paranormed sequence spaces, thereby broadening the understanding of combinatorial sequences in the context of functional analysis.

Our findings contribute to advancements in additive theory and provide a foundation for future investigations. Key areas for further exploration include:

- Exploring Narayana difference sequence spaces
- Investigating the measure of compactness in the $\ell_p(N)$ space

These results open up new avenues for research at the intersection of combinatorial mathematics and functional analysis. Future studies may explore the properties and applications of these newly defined sequence spaces, potentially leading to novel insights in both fields. Furthermore, this work may have implications for related areas such as operator theory, spectral analysis, and the study of infinite-dimensional spaces. By continuing to investigate the connections between combinatorial sequences and functional analysis, researchers may uncover new mathematical structures and relationships with applications in various branches of mathematics and theoretical physics.

Author Contributions

All the authors equally contributed to this work. They all read and approved the final version of the paper.

Conflict of Interest

All the authors declare no conflict of interest.

Ethical Review and Approval

No approval from the Board of Ethics is required.

References

[1] J. Allouche, T. Johnson, *Narayana's cows and delayed morphisms*, Journées d'Informatique Musicale (1996) hal-02986050.

[2] A. N. Singh, *On the use of series in Hindu mathematics*, Osiris 1 (1936) 606–628.

[3] G. Bilgici, *The generalized order-k Narayana's cows numbers*, Mathematica Slovaca 66 (4) (2016) 795–802.

[4] C. Flaut, V. Shpakivskyi, *On generalized Fibonacci quaternions and Fibonacci-Narayana quaternions*, Advances in Applied Clifford Algebras 23 (3) (2013) 673–688

[5] T. Goy, *On identities with multinomial coefficients for Fibonacci-Narayana sequence*, in: Annales Mathematicae et Informaticae 49 (2018) 75–84.

[6] J. L. Ramírez, V. F. Sirvent, *A note on the k-Narayana sequence*, Annales mathematicae et informaticae 45 (2015) 91–105.

[7] R. Zatorsky, T. Goy, *Parapermanents of triangular matrices and some general theorems on number sequences.*, Journal of Integer Sequences 19 (2) (2016) 16.2.2

[8] Y. Soykan, *On generalized Narayana numbers*, International Journal of Advances in Applied Mathematics and Mechanics 7 (3) (2020) 43–56.

[9] H. Bilgin Ellidokuzoğlu, *On some new normed Narayana sequence spaces*, Journal of New Theory 46 (2024) 40–50.

[10] I. Maddox, *Paranormed sequence spaces generated by infinite matrices*, Mathematical Proceedings of the Cambridge Philosophical Society 64 (2) (1968) 335–340.

[11] S. Simons, *The sequence spaces $\ell(p_v)$ and $m(p_v)$*, Proceedings of the London Mathematical Society s3-15 (3) (1965) 422–436.

[12] H. Nakano, *Modulared sequence spaces*, Proceedings of the Japan Academy 27 (9) (1951) 508–512.

[13] I. Maddox, *Some properties of paranormed sequence spaces*, Journal of the London Mathematical Society s2-1 (1) (1969) 316–322.

[14] I. Maddox, *Some analogues of Knopp's core theorem*, International Journal of Mathematics and Mathematical Sciences 2 (4) (1979) 605–614.

[15] Z.U. Ahmad, Mursaleen, *Köthe-Toeplitz duals of some new sequence spaces and their matrix maps*, Publications de l'Institut Mathématique 42 (56) (1987) 57–61.

[16] M. İlkhan, S. Demiriz, E. E. Kara, *A new paranormed sequence space defined by Euler totient matrix*, Karaelmas Science and Engineering Journal 9 (2) (2019) 277–282.

[17] M. C. Dağlı, T. Yaying, *Some new paranormed sequence spaces derived by regular Tribonacci matrix*, The Journal of Analysis 31 (1) (2023) 109–127.

[18] P. Zengin Alp, *A new paranormed sequence space defined by Catalan conservative matrix*, Mathematical Methods in the Applied Sciences 44 (9) (2021) 7651–7658.

[19] M. C. Dağlı, *On the paranormed sequence space arising from Catalan-Motzkin matrix*, Advances in Operator Theory 8 (2) (2023) 33.

[20] E. Savaş, *On new paranormed sequence spaces.*, Palestine Journal of Mathematics 12 (1) (2023) 300–305.

[21] T. Yaying, *On the paranormed Nörlund difference sequence space of fractional order and geometric properties*, Mathematica Slovaca 71 (1) (2021) 155–170.

[22] M. Candan, A. Güneş, *Paranormed sequence space of non-absolute type founded using generalized difference matrix*, Proceedings of the National Academy of Sciences, India Section A: Physical Sciences 85 (2) (2015) 269–276.

[23] M. Candan, *A new sequence space isomorphic to the space $\ell(p)$ and compact operators*, Journal of Mathematical and Computational Science 4 (2) (2014) 306–334.

[24] F. Gökçe, M. A. Sarıgöl, *Generalization of the space $\ell(p)$ derived by absolute Euler summability and matrix operators*, Journal of Inequalities and Applications 2018 (2018) 133.

[25] T. Yaying, B. Hazarika, *On sequence spaces defined by the domain of a regular tribonacci matrix*, Mathematica Slovaca 70 (3) (2020) 697–706.

[26] T. Yaying, M. Ilkhan, *On sequence spaces defined by the domain of tribonacci matrix in c'' and c*, Korean Journal of Mathematics 29 (1) (2021) 25–40.

[27] T. Yaying, Paranormed Riesz difference sequence spaces of fractional order, Kragujevac Journal of Mathematics 46 (2) (2022) 175–191.

[28] T. Yaying, *A study of novel telephone sequence spaces and some geometric properties*, Journal of Inequalities and Applications 2024 (2024) 141.

[29] T. Yaying, F. Başar, *A study on some paranormed sequence spaces due to Lambda-Pascal matrix*, Acta Scientiarum Mathematicarum 91 (2025) 161–180.

[30] S. Erdem, S. Demiriz, H. Bilgin Ellidokuzoğlu, *Paranormed Motzkin sequence spaces*, Dera Natung Government College Research Journal 9 (1) (2024) 36–51.

[31] M. Karakaş, M.C. Dağlı, *A New Paranormed Sequence Space Defined by Regular Bell Matrix*, Dera Natung Government College Research Journal 8 (1) (2023) 30–45.

[32] E. E. Kara, *Some topological and geometrical properties of new Banach sequence spaces*, Journal of Inequalities and Applications 2013 (2013) 38.

[33] M. Candan, E. E. Kara, *A study of topological and geometrical characteristics of new Banach sequence spaces*, Gulf Journal of Mathematics 3 (4) (2015) 67–84.

[34] E. E. Kara, M. Ilkhan, *Some properties of generalized Fibonacci sequence spaces*, Linear and Multilinear Algebra 64 (11) (2016) 2208–2223.

[35] M. Karakaş, A. M. Karakaş, *New Banach sequence spaces that is defined by the aid of Lucas numbers*, Iğdır University Journal of the Institute of Science and Technology 7 (4) (2017) 103–111.

[36] M. Karakaş, A. M. Karakaş, *A study on Lucas difference sequence spaces $\ell_p(\hat{E}(r,s))$ and $\ell_\infty(\hat{E}(r,s))$*, Maejo International Journal of Science and Technology 12 (01) (2018) 70–78.

[37] T. Yaying, B. Hazarika, S. A. Mohiuddine, *On difference sequence spaces of fractional-order involving Padovan numbers*, Asian-European Journal of Mathematics 14 (06) (2021) 2150095.

[38] M. İ. Kara, E. E. Kara, *Matrix transformations and compact operators on Catalan sequence spaces*, Journal of Mathematical Analysis and Applications 498 (1) (2021) 124925.

[39] M. Karakaş, *On the sequence spaces involving Bell numbers*, Linear and Multilinear Algebra 71 (14) (2022) 2298–2309.

[40] M. C. Dağli, *A new almost convergent sequence space defined by Schröder matrix*, Linear and Multilinear Algebra 71(11) (2023) 1863-1874.

[41] A. Jarrah, E. Malkowsky, *BK spaces, bases and linear operators*, Rendiconti del Circolo Matematico di Palermo Series II 52 (1990) 177–191.

[42] K.-G. Grosseerdmann, *Matrix transformations between the sequence spaces of Maddox*, Journal of Mathematical Analysis and Applications 180 (1) (1993) 223–238.

Journal of New Results in Science
dergipark.org.tr/en/pub/jnrs
Open Access

ISSN: 1304-7981 14 (2) (2025) 152-165 doi.org/10.54187/jnrs.1675428

In Silico Analyzing 37 kDa Salivary Protein D7 and Discovering Vaccine Candidate and Diagnostic Epitopes to Develop a Transmission-blocking Multi-epitope Vector Vaccine Against *Aedes* Species (*A. aegypti* and *A. albopictus*) Transmitting Several Arboviral Pathogens

Ahmet Efe Köseoğlu[1], Buminhan Özgültekin[2], Yusuf Şeflekçi[3]

Article Info

Received: 13 Apr 2025

Accepted: 04 Aug 2025

Published: 31 Aug 2025

Research Article

Abstract − *Aedes* mosquitoes, primarily *Aedes aegypti* and *Aedes albopictus*, are significant vectors of arboviral diseases, including dengue, chikungunya, Zika, and yellow fever. With expanding geographical distributions due to climate change and urbanization, these species increasingly threaten public health. Current vector control strategies rely heavily on insecticides, which face challenges due to increased resistance. An alternative approach involves developing transmission-blocking vaccines targeting mosquito vector proteins rather than individual pathogens. This study performed an in-silico analysis of the 37 kDa salivary protein D7, a highly conserved and abundantly secreted protein in Aedes saliva, to identify potential vaccine and diagnostic epitopes. Through sequence comparison, structural modeling, and immunoinformatics approaches, B-cell, MHC-I, and MHC-II epitopes with high antigenicity, non-allergenicity, and non-toxicity were predicted. Selected epitopes were incorporated into multi-epitope vaccine constructs against *A. aegypti* and *A. albopictus* vectors, which were subsequently modeled, validated, and simulated to induce IgM, IgG, and IFN-g. The present study's findings suggest that the 37 kDa salivary protein D7 is a promising candidate for a transmission-blocking vector vaccine targeting *Aedes* mosquitoes, offering a novel strategy for controlling mosquito-borne diseases. Further experimental validation is necessary to confirm the immunogenicity and protective potential of the identified epitopes.

Keywords − *Aedes, salivary protein D7, epitope, vaccine, in silico*

1. Introduction

Mosquitoes are the deadliest pathogen vectors, and mosquito-borne diseases have impacted human history from ancient to modern times [1,2]. These diseases infect more than 700 million people annually, causing over 1 million deaths worldwide, with an estimated 50% of the global population at risk [3]. Among them, malaria remains the most severe, causing over 600,000 deaths each year, mostly among children, and is transmitted by *Anopheles* mosquitoes, as discovered in the late 19th century [4,5].

Other major mosquito-borne diseases include several arboviral infections such as dengue, chikungunya, Zika, yellow fever, and West Nile virus. These are primarily transmitted by *Culex pipiens* and *Aedes aegypti*

[1]ahmetefekoseoglu@gmail.com (Corresponding Author); [2]buminhanozgultekin@gmail.com; [3]yseflekci@biruni.edu.tr
[1]COMED Therapeutics, Malta Life Sciences Park, San Gwann, Malta
[2]Acıbadem University, Faculty of Engineering and Natural Sciences, Department of Biomedical Engineering, Istanbul, Türkiye
[3]Biruni University, Faculty of Engineering and Natural Sciences, Department of Molecular Biology and Genetics, Istanbul, Türkiye

mosquitoes [2,3]. Among them, *Aedes* mosquitoes can transmit all these arboviral disease pathogens, including West Nile virus, to humans [6].

The two primary arboviral vectors, *A. aegypti* (the yellow fever mosquito) and *A. albopictus* (Asian tiger mosquito), have increased in number in newly emerged water-based environments driven by anthropogenic alterations and urbanization. Also, global trade and transportation have contributed to their spread beyond native regions. [6–8]. Additionally, climate change is altering their geographic distribution and the dynamics of virus transmission by bringing mosquitoes into closer contact with human populations and wildlife reservoirs [7, 9, 10].

Both *A. aegypti* and *A. albopictus* are capable of transmitting multiple arboviruses, including yellow fever virus (YFV), dengue virus (DENV), chikungunya virus (CHIKV), and Zika virus (ZIKAV). Notably, *A. albopictus* is particularly well-adapted to colder climates and exhibits aggressive daytime biting behavior. This makes it a key vector in regions where *A. aegypti* is absent or present at low density [6, 11, 12].

The transcriptomic analyses performed to characterize proteins in the mosquito saliva revealed that *A. aegypti* has more than 120 (estimated 100–200) salivary proteins, most of which are associated with the increased pathogen transmissibility, and 30–40% belong to previously uncharacterized protein families [2, 3, 13]. Moreover, similar to the A. aegypti transcriptome, A. albopictus has 69 putative salivary proteins with immunogenic properties that are classified within the same main protein families [11]. 37 kDa salivary protein D7 is the most abundantly secreted protein in the salivary glands of female dipterans, including mosquitoes, and is distantly related to the odorant-binding family [14]. It facilitates the blood-feeding process and pathogen transmission with adaptive properties, including anti-hemostatic activity, antagonizing vasoconstriction, and platelet aggregation at the biting site [11, 14]. Interestingly, the individuals frequently exposed to *A. aegypti* saliva in the endemic areas have naturally specific antibody responses against 37 kDa salivary protein D7 compared to healthy non-exposed individuals [14].

Regarding current vector prevention and control strategies, insecticides are still used against arthropod vectors, including mosquitoes, but increased genetic resistance to insecticides occurs [15-17]. Alternatively, vector monitoring and control by reducing the contact between the mosquito vectors and human hosts has become another current strategy to prevent vector-borne diseases [6]. On the other hand, instead of individual pathogens, transmission-blocking antigen-based vector vaccines are becoming increasingly popular, focusing on tick and *Anopheles* mosquito proteins, transmitting tick-borne pathogens and *Plasmodium* species, respectively [18, 19]. Although there are vaccines against individual arboviral pathogens transmitted by *Aedes* mosquito vectors [6, 20], there is still no FDA-approved safe and effective multi-epitope-based vector vaccine against both *A. aegypti* and *A. albopictus* transmitting arboviral pathogens.

Therefore, this study aims to analyze 37 kDa salivary protein D7, which is the most abundantly secreted protein in the saliva with anti-hemostatic activity, and discover conserved vaccine candidate epitopes to develop a multi-epitope-based vector vaccine against both *Aedes* species (*A. aegypti* and *A. albopictus*) transmitting several arboviral pathogens like yellow fever virus (YFV), dengue virus (DENV), chikungunya virus (CHIKV), and Zika virus (ZIKAV).

2. Materials and Methods

Protein Sequence Data Retrieval: 37 kDa salivary protein D7 sequences representing *A. aegypti* and *A. albopictus* were retrieved from the NCBI database with accession numbers as follows: XP_001657778.1 and XP_029727655.1, respectively.

Pairwise Sequence Alignment: 37 kDa salivary proteins D7 sequences were aligned by Clustal Omega [21].

Phylogenetic Analysis: The phylogenetic tree for *A. aegypti* and *A. albopictus* 37 kDa salivary proteins D7 sequences were reconstructed by Molecular Evolutionary Genetics Analysis (MEGA) 11.0 [22] using the

Maximum Likelihood Method with Whelan and Goldman (WAG) model with gamma distribution (G) and 1000 Bootstrap replications after the model test. *Armigeres subalbatus* (XP_062552429.1) and *Ochlerotatus camptorhynchus* (XP_065077893.1) were used as outgroups in the phylogenetic analysis. The outgroup selection criterion was based on the closest species to *Aedes* species with available 37 kDa salivary protein D7 sequences deposited in the NCBI database.

3D (tertiary) Protein Modeling, Refinement and Validation: 3D protein models of 37 kDa salivary proteins D7 sequences were predicted by I-TASSER [23]. 3D protein models were visualized by UCSF Chimera 1.14 [24]. Modeled proteins were refined by the GalaxyRefine server [25]. Then, the refined models were evaluated by different validation tools to determine the optimal model and assess its overall quality. The tools utilized for structural validation include PROCHECK, the ERRAT server [26], and the PROSA web tool [27].

2D (secondary) Protein Structure Prediction: The secondary structures were predicted by GOR IV [28].

Prediction of Physicochemical and Immunoinformatics Parameters: For 37 kDa salivary proteins D7 of the analyzed *Aedes* species, physicochemical properties such as aliphatic index, molecular weight, stability, half-life, and hydrophilicity were estimated by Expasy ProtParam [29]. Antigenicity for each antigen was predicted by Vaxijen v2.0 (model: parasite, threshold: 0.5) [30]. Solubility was predicted by SolPro. Subcellular localization was predicted by Euk-mPLoc 2.0 [31]. The number of transmembrane helices was predicted by TMHMM Server v. 2.0 [32]. Signal-BLAST was used to predict the signal peptide [33]. Algpred was used to estimate allergenicity based on IgE epitopes and MEME/MAST motif [34]. Similarity to the host proteome was predicted by BlastP.

Posttranslational Modification (PTM) Prediction: Among posttranslational modifications, N-Glycosylation and O-Glycosylation were predicted by NetNGlyc1.0 and NetOGlyc4.0, respectively. Phosphorylation was predicted by NetPhos3.1. Also, NetSurfP 2.0 was used to predict the surface accessibility of posttranslational modification positions for the analyzed proteins.

Prediction of B Cell Epitopes: B-cell epitopes were predicted by Bcepred and Bepipred Linear Epitope Prediction 2.0, and overlapped epitopes were selected [35, 36]. Finally, antigenicity of predicted B cell epitopes was estimated by Vaxijen 2.0, while allergenicity and toxicity were predicted by AllerTOP v2.1 and ToxinPred, respectively [30, 37, 38]. B-cell epitopes showing a high "IC50" value (more than or equal to 50), non-antigenicity, allergenicity, and toxicity were discarded from the analyses.

Prediction of MHC-I and MHC-II Epitopes: Predictions of MHC-I and MHC-II epitopes for all *Aedes* 37 kDa salivary protein D7 sequences were performed by IEDB [36]. ANN 4.0 method and twelve alleles (A01.01, A02.01, A03.01, A24.02, A26.01, B07.02, B08.01, B15.01, B27.05, B39.01, B40.01, and B58.01) were selected for the MHC-I epitope prediction while NetMHCIIpan 4.3 BA method with seven alleles (DRB1.03.01, DRB1.07.01, DRB1.15.01, DRB3.01.01, DRB3.02.02, DRB4.01.01, and DRB5.01.01) were selected for the MHC-II epitope prediction [39]. Similarly, antigenicity, allergenicity, and toxicity were predicted by Vaxijen 2.0, AllerTOP v2.1, and ToxinPred, respectively [30, 37, 38]. MHC-I/II epitopes showing high "IC50" value (more than or equal to 50), non-antigenicity, allergenicity, and toxicity were discarded from the analyses.

The Design and Modeling of Multi-Epitope Vector Vaccine Constructs for *A. aegypti* and *A. albopictus*: The multi-epitope vaccine construct designed for *A. aegypti* and *A. albopictus* starts a 45 amino acid adjuvant (GIINTLQKYYCRVRGGRCAVLSCLPKEEQIGKCSTRGRKCCRRKK) at the N-terminal end. It includes prominently selected B-cell, MHC-I, and MHC-II epitopes for each Aedes species, connected by linkers (EAAAK, GPGPG, and AAY) [40-42]. Then, vaccine constructs were tested for antigenicity and allergenicity by Vaxijen 2.0 AllerTOP v2.1, respectively [30, 38]. 3D protein models of vaccine constructs were predicted by I-TASSER [23]. 3D protein models were visualized by UCSF Chimera 1.14 [24]. Modeled vaccine constructs were refined by the GalaxyRefine server [25].

Immune Simulation of Multi-Epitope Vector Vaccine Designs: *In silico* immune simulations were run by the C-ImmSim 10.1 server, which selected the parameters as default to predict whether the designed vaccines' immunological potential stimulated the adaptive immune system [43].

3. Results

3.1. Sequence Comparison

After comparison by pairwise sequence alignment, 37 kDa salivary protein D7 sequences for *A. aegypti* and *A. albopictus* were similar, with a 67% (224/332) amino acid identity (Figure 1).

```
CLUSTAL O(1.2.4) multiple sequence alignment


Aedes_aegypti_XP_001657778.1        MFPPRKFLLSSFILAALHVTAAPLWDAKDPEQLRFITSRCMEDWYPKAKNPKAALQNWLG      60
Aedes_albopictus_XP_029727655.1     MHSPKSFLLLAVAFVALRVTAAPLWNAKNPEQLQFIAARCMEEWSPKAKDPKAALKNWME      60
                                    *. *:.*** :. :.**:*******:**:****:**::****:* ****:*****:**:

Aedes_aegypti_XP_001657778.1        WKLEPSDDQATQCYTKCVLEKIGFYEPGEKRFKGVRVMQQWETFHKYLNADREKVHDLTS      120
Aedes_albopictus_XP_029727655.1     WRLQPSTEEATQCYTKCMLENIGFYEPVEKRLKGVRVMQQWETFNRYQSADREKVHDLTD      120
                                    *:*:** ::********:**:****** ***:*************:* .**********.

Aedes_aegypti_XP_001657778.1        TFDFIPPLKSSSCSEVFEAFKKVNGKHSETIRAILFGKGESSKKYYQEKGVKIKQKEQSL      180
Aedes_albopictus_XP_029727655.1     TFDFIRPLKSSSCSDVFNAYKDVHAKHLETIKAILFCDGKSAEKYYKDKGKNIKQKGQSI      180
                                    ***** ********:**:*:*.*:.** ***:**** .*:*::***::** :**** **:

Aedes_aegypti_XP_001657778.1        FMHCEALNYPKGSPQRKDLCGIRKYQMGSGIVFERHMECIFKGLRYMTSKNELDVDEIAR      240
Aedes_albopictus_XP_029727655.1     VVHCEEIHYPVGSQQRKELCKVRKYEMGTGKPFENLMECIFKGVRYFNDKNELNIDEIAR      240
                                    .:*** ::** ** ***:** :***:**:*  **. *******:**:..****::*****

Aedes_aegypti_XP_001657778.1        DFIVVKKKPDAMKAMMKTCKANLKEKNPGKIAVHYYKCLMNDSKVTNDFKEAFDYREVRS      300
Aedes_albopictus_XP_029727655.1     DFTQVGKKPDAVKATMQNCKSKTKETDPGKKAVEYYKCLLADPKLKKDFMEAFDYREIRS      300
                                    **  * *****:** *:.**:: **.:*** **.*****: * *:.:** *******:**

Aedes_aegypti_XP_001657778.1        KDYFAALTGKLKPYSRSDVRKQVDDIDKIQCS   332
Aedes_albopictus_XP_029727655.1     KDYYAQITGKLKPYSASDVRKEVDDIDSKQCV   332
                                    ***:* :******** *****:*****. **
```

Figure 1. The sequence comparison of 37 kDa salivary protein D7 for *A. aegypti* and *A. albopictus*. The asterisks show the identical amino acid positions

3.2. 3D (Tertiary) Structures and Phylogenetic Relationship

In the phylogenetic tree based on 37 kDa salivary protein D7 sequences, *A. aegypti* and *A. albopictus* were grouped in a cluster, while *A. subalbatus* and *O. camptorhynchus* were more distantly diverged as outgroups, respectively. Moreover, 3D protein structures were highly similar, with minor differences in alpha helices and coils and no beta sheets (Figure 2). Refined tertiary structures of the two vaccine constructs (*A. aegypti* (upper) and *A. albopictus* (lower)) by the GalaxyRefine server. Adjuvant, B-cell, MHC-I, and MHC-II epitopes were given in green, red, yellow, and purple colors. Residue distribution in Ramachandran plots generated by the PROCHECK program. *A. aegypti*: 69.3% in the favored region (red), 18.7% in the allowed region (yellow), and 9.3% in the disallowed region (white). *A. albopictus*: 76.6% in the favored region (red), 19.5% in the allowed region (yellow), and 2.6% in the disallowed region (white). Z-score plot generated by the ProSA-Web program, indicating Z-scores of -3.57 and -3.83 for *A. aegypti* and *A. albopictus*, respectively. The ERRAT overall quality factor was calculated as 76.543 and 85.915 for *A. aegypti* and *A. albopictus*, respectively (Figure 3).

Figure 2. The phylogenetic relationship, 3D structures, and discovered epitopes of 37 kDa salivary protein D7 for *A. aegypti* and *A. albopictus*. For each species, the most antigenic B-cell, MHC-I, and MHC-II epitopes are given in red, green, and yellow colors, respectively. The overlapped epitope region is shown in an underlined orange color. The figure was prepared using silhouette images of *Aedes* mosquitoes from PhyloPic

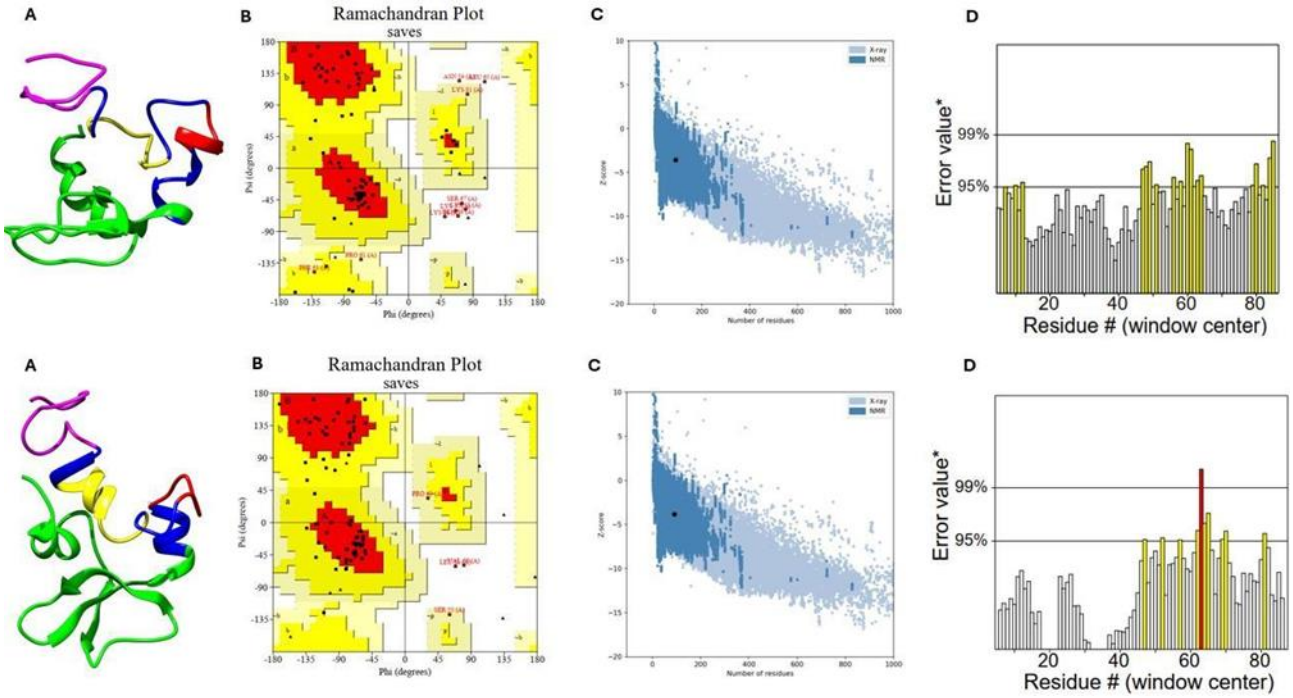

Figure 3. The vaccine constructs generated for *A. aegypti* (upper) and *A. albopictus* (lower) **(A)** Refined tertiary structures of the two vaccine constructs (*A. aegypti* (upper) and *A. albopictus* (lower)) by GalaxyRefine server. Adjuvant, B-cell, MHC-I, and MHC-II epitopes were given in green, red, yellow, and purple colors. **(B)** Residue distribution in Ramachandran plots generated by the PROCHECK program. **(C)** Z-score plot generated by the ProSA-Web program. **(D)** The ERRAT overall quality factor was calculated

3.3. 2D (Secondary) Structures

According to 2D (secondary) structure analyses of 37 kDa salivary protein D7 by GOR IV, alpha helices, extended strands, and random coils were predicted 30.72%, 21.99%, and 47.29% for *A. aegypti*, while they were predicted 38.86%, 15.06%, and 46.08% for *A. albopictus*, respectively (Table 1).

Table 1. Secondary structures

Species	Alpha helix (%)	Extended strand (%)	Random coil (%)
A. aegypti	30.72	21.99	47.29
A. albopictus	38.86	15.06	46.08

3.4. Physico-Chemical Parameters

Among physicochemical parameters, the number of amino acids and the estimated half-life (h) of 37 kDa salivary protein D7 sequences predicted the same for both *A. aegypti* and *A. albopictus*. 37 kDa salivary protein D7 of *A. aegypti* was predicted with a higher molecular weight, theoretical pI, and GRAVY, while it was predicted with a lower aliphatic index compared with 37 kDa salivary protein D7 of *A. albopictus*. The total number of positively charged residues (Arg+Lys) was predicted to be higher in 37 kDa salivary protein D7 of A. aegypti, while the total number of negatively charged residues (Asp+Glu) was predicted to be higher in 37 kDa salivary protein D7 of *A. albopictus*. Although 37 kDa salivary protein D7 sequences were predicted as stable according to instability index (II), 37 kDa salivary protein D7 of *A. albopictus* was predicted to be more stable than 37 kDa salivary protein D7 of *A. aegypti* (Table 2).

Table 2. Physicochemical parameters

Species	Number of amino acids	Molecular weight	Theoretical pI	Total number of negatively charged residues (Asp+Glu)	Total number of positively charged residues (Arg+Lys)	The estimated half-life (hour)	The instability index (II)	Aliphatic index	GRAVY (Grand average of hydropathicity)
A. aegypti	332	38627.77	9.32	43	61	30	33.04/stable	65.81	-0.649
A. albopictus	332	38565.37	8.95	48	59	30	39.35/stable	66.11	-0.714

3.5. Antigenicity, Solubility, Subcellular Localization, and Transmembrane Helix

Although both 37 kDa salivary protein D7 sequences were predicted as non-antigenic, they were predicted as soluble and extracellular. No transmembrane helix was predicted in 37 kDa salivary protein D7 sequences of *A. aegypti* and *A. albopictus* (Table 3).

Table 3. Antigenicity, solubility, subcellular localization, and transmembrane helices

Species	Antigenicity (Vaxijen v2.0) (Threshold: 0.5)	Solubility (SolPro)	Subcellular Localization (Euk-mPLoc 2.0)	Transmembrane Helices (TMHMM Server v.2.0)
A. aegypti	0.3382 (Non-antigen)	Soluble	Extracellular	0
A. albopictus	0.4489 (Non-antigen)	Soluble	Extracellular	0

3.6. Signal Peptide

37 kDa salivary protein D7 sequences of *A. aegypti* and *A. albopictus* were predicted to have signal peptides according to three parameters of Signal-BLAST without one parameter (Table 4).

Table 4. Signal peptides

Species	Sensitivity	Specificity	Balanced prediction	Cleavage site
A. aegypti	Yes	No	Yes	Yes
A. albopictus	Yes	No	Yes	Yes

3.7. Allergenicity and Similarity with Host Proteome

37 kDa salivary protein D7 sequences of *A. aegypti* and *A. albopictus* were predicted to be non-allergenic regarding the IgE epitope and MEME/MAST motif. Furthermore, no similarity to the host proteome (*Homo sapiens*) was detected for 37 kDa salivary protein D7 sequences of *A. aegypti* and *A. albopictus* by BLASTp (Table 5).

Table 5. Allergenicity and host proteome similarity

Species	Allergenicity (AlgPred)		Similarity to host proteome (*Homo sapiens*) (BLASTp)
	IgE epitope	MEME/MAST motif	
A. aegypti	No allergen	No allergen	No significant similarity
A. albopictus	No allergen	No allergen	No significant similarity

3.8. Posttranslational Modifications (PTMs)

Based on posttranslational modification (PTM) predictions of 37 kDa salivary protein D7 sequences, no N-glycosylation position was detected for *A. aegypti* and *A. albopictus*. 3 O-glycosylation positions (2 on the exposed surface) were predicted for A. aegypti, while 3 O-glycosylation positions (all on the exposed surface) were predicted for *A. albopictus*. In terms of phosphorylation, 29 positions (18 of them on the exposed surface) and 31 positions (21 of them on the exposed surface) were predicted for *A. aegypti* and *A. albopictus*, respectively (Table 6).

Table 6. Prediction of posttranslational modifications

Species	Number of N glycosylation positions	Number of N glycosylation positions located in exposed surface	Number of O glycosylation positions	Number of O glycosylation positions in exposed surface	Number of phosphorylation positions	Number of phosphorylation positions in exposed surface
A. aegypti	0	0	3	2	29	18
A. albopictus	0	0	3	3	31	21

3.9. B Cell, MHC-I, and MHC-II Epitopes

8 B-cells, 3 MHC-I, and 23 epitopes were predicted for 37 kDa salivary protein D7 of *A. aegypti*, while 5 B-cells, 3 MHC-I, and 24 epitopes were predicted for 37 kDa salivary protein D7 of *A. albopictus* with antigenic, non-allergenic, and non-toxic properties (Tables 7-9). In terms of transmission-blocking antigen usage as well as vaccine candidate and diagnostic purposes, the most antigenic B-cell, MHC-I, and MHC-II epitopes were selected as KEKNPGK, FLLSSFILAA, and KYYQEKGVKIKQKEQ for *A. aegypti*, while they were selected as CDGKSAEK, FLLLAVAFVA, and AEKYYKDKGKNIKQK for *A. albopictus*, respectively (Figures 2 and 4). For the codes and scripts for producing Figure 4, see [44].

Table 7. B-cell epitopes

Species	B-cell epitopes	Antigenicity
A. aegypti	GKGESSKKY	1.3088 (Antigen)
	KGESSKKY	1.0726 (Antigen)
	KGESSKKYYQEKG	1.0078 (Antigen)
	KIKQKE	1.3478 (Antigen)
	KGSPQR	1.1756 (Antigen)
	KGSPQRKD	0.9164 (Antigen)
	KEKNPGK	2.0478 (Antigen)
	REVRSKD	1.6861 (Antigen)
A. albopictus	SPKAKD	0.9416 (Antigen)
	CDGKSAEK	1.6364 (Antigen)
	YKDKGKN	1.1538 (Antigen)
	KSAEKYYKDKGKNIKQKG	1.3369 (Antigen)
	SKTKETDPGKK	1.0145 (Antigen)

Only antigenic, non-toxic, and non-allergenic epitopes predicted are given in the table. The most antigenic epitope was given in bold for each Aedes species

Table 8. MHC-I epitopes

Species	MHC-I							Antigenicity
	Allele	Start	Stop	Length	Epitope	IC50	Percentile Rank	
A. aegypti	HLA-A*02:01	7	16	10	**FLLSSFILAA**	12.97	0.11	2.0289
A. albopictus	HLA-A*02:01	6	15	10	KFLLSSFILA	32.86	0.29	1.9397
	HLA-B*15:01	128	137	10	LKSSSCSEVF	35.06	0.18	0.6327
	HLA-A*02:01	6	15	10	SFLLLAVAFV	19.71	0.18	1.012
	HLA-A*02:01	7	16	10	**FLLLAVAFVA**	32.86	0.29	1.2349
	HLA-A*02:01	8	17	10	LLLAVAFVAL	48.11	0.44	1.0565

Only antigenic, non-toxic, and non-allergenic epitopes predicted are given in the table. The most antigenic epitope was given in bold for each Aedes species

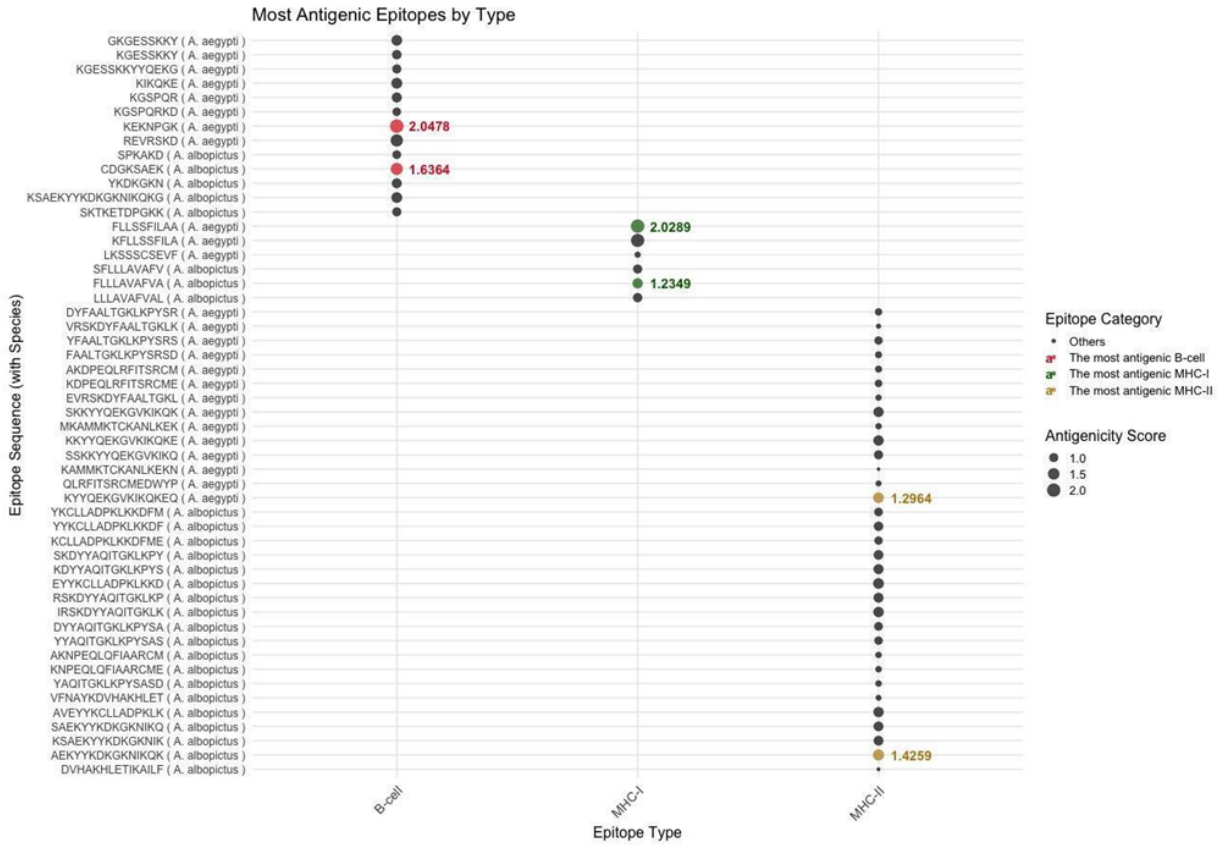

Figure 4. The B-cell, MHC-I, and MHC-II epitopes predicted with the highest antigenicities and selected for the design of vaccine constructs

Table 9. MHC-II epitopes

Species	MHC-II								Antigenicity
	Allele	Start	Stop	Length	Core sequence	Epitope	IC50	Percentile Rank	
A. aegypti	HLA-DRB5*01:01	302	316	15	FAALTGKLK	DYFAALTGKLKPYSR	4.16	0.06	0.7539
	HLA-DRB5*01:01	298	312	15	FAALTGKLK	VRSKDYFAALTGKLK	4.45	0.06	0.5672
	HLA-DRB5*01:01	303	317	15	FAALTGKLK	YFAALTGKLKPYSRS	4.65	0.06	0.8734
	HLA-DRB5*01:01	304	318	15	TGKLKPYSR	FAALTGKLKPYSRSD	9.33	0.58	0.7083
	HLA-DRB1*07:01	27	41	15	LRFITSRCM	AKDPEQLRFITSRCM	12.16	0.65	0.7145
	HLA-DRB1*07:01	28	42	15	LRFITSRCM	KDPEQLRFITSRCME	13.3	0.8	0.7815
	HLA-DRB1*07:01	298	312	15	YFAALTGKL	VRSKDYFAALTGKLK	14.25	0.9	0.5672
	HLA-DRB1*07:01	297	311	15	YFAALTGKL	EVRSKDYFAALTGKL	15.04	1	0.6459
	HLA-DRB5*01:01	162	176	15	YYQEKGVKI	SKKYYQEKGVKIKQK	16.38	1.8	1.2074
	HLA-DRB5*01:01	252	266	15	MKTCKANLK	MKAMMKTCKANLKEK	17.98	1.9	0.6522
	HLA-DRB5*01:01	163	177	15	YYQEKGVKI	KKYYQEKGVKIKQKE	20.83	2.3	1.2366
	HLA-DRB5*01:01	161	175	15	YYQEKGVKI	SSKKYYQEKGVKIKQ	21.99	2.5	0.9991
	HLA-DRB5*01:01	28	42	15	LRFITSRCM	KDPEQLRFITSRCME	24.25	2.8	0.7815
	HLA-DRB5*01:01	253	267	15	MKTCKANLK	KAMMKTCKANLKEKN	26.77	3.3	0.5233
	HLA-DRB1*07:01	32	46	15	FITSRCMED	QLRFITSRCMEDWYP	27.9	2.5	0.6206
	HLA-DRB1*15:01	28	42	15	LRFITSRCM	KDPEQLRFITSRCME	28.26	1.3	0.7815
	HLA-DRB1*07:01	302	316	15	YFAALTGKL	DYFAALTGKLKPYSR	37.75	3.5	0.7539
	HLA-DRB5*01:01	164	178	15	YYQEKGVKI	**KYYQEKGVKIKQKEQ**	40.2	5.1	1.2964
	HLA-DRB5*01:01	297	311	15	YFAALTGKL	EVRSKDYFAALTGKL	43.45	5.5	0.6459
	HLA-DRB1*07:01	162	176	15	YYQEKGVKI	SKKYYQEKGVKIKQK	43.54	4.2	1.2074
	HLA-DRB5*01:01	32	46	15	FITSRCMED	QLRFITSRCMEDWYP	44.09	5.6	0.6206
	HLA-DRB5*01:01	27	41	15	LRFITSRCM	AKDPEQLRFITSRCM	44.45	5.6	0.7145
	HLA-DRB1*07:01	161	175	15	YYQEKGVKI	SSKKYYQEKGVKIKQ	45.78	4.4	0.9991
A. albopictus	HLA-DRB1*03:01	276	290	15	LLADPKLKK	YKCLLADPKLKKDFM	5.44	0.01	0.9447
	HLA-DRB1*03:01	275	289	15	LLADPKLKK	YYKCLLADPKLKKDF	5.96	0.01	1.0621
	HLA-DRB1*03:01	277	291	15	LLADPKLKK	KCLLADPKLKKDFME	6.55	0.01	0.8827
	HLA-DRB5*01:01	300	314	15	YAQITGKLK	SKDYYAQITGKLKPY	6.62	0.24	1.1164
	HLA-DRB5*01:01	301	315	15	YAQITGKLK	KDYYAQITGKLKPYS	6.8	0.25	1.1843
	HLA-DRB1*03:01	274	288	15	LLADPKLKK	EYYKCLLADPKLKKD	7.27	0.01	1.3232
	HLA-DRB5*01:01	299	313	15	YAQITGKLK	RSKDYYAQITGKLKP	7.58	0.34	1.1429
	HLA-DRB5*01:01	298	312	15	YAQITGKLK	IRSKDYYAQITGKLK	8.48	0.46	1.255
	HLA-DRB5*01:01	302	316	15	YAQITGKLK	DYYAQITGKLKPYSA	8.64	0.47	0.9466
	HLA-DRB5*01:01	303	317	15	YAQITGKLK	YYAQITGKLKPYSAS	9.49	0.61	0.8969
	HLA-DRB5*01:01	275	289	15	YKCLLADPK	YYKCLLADPKLKKDF	16.26	1.7	1.0621
	HLA-DRB5*01:01	274	288	15	YKCLLADPK	EYYKCLLADPKLKKD	18.36	2	1.3232
	HLA-DRB5*01:01	276	290	15	LLADPKLKK	YKCLLADPKLKKDFM	23.71	2.7	0.9447
	HLA-DRB1*07:01	27	41	15	LQFIAARCM	AKNPEQLQFIAARCM	25.12	2.1	0.6511
	HLA-DRB1*07:01	28	42	15	LQFIAARCM	KNPEQLQFIAARCME	27.1	2.4	0.6649
	HLA-DRB5*01:01	304	318	15	YAQITGKLK	YAQITGKLKPYSASD	29.34	3.6	0.6568
	HLA-DRB1*07:01	136	150	15	YKDVHAKHL	VFNAYKDVHAKHLET	38.7	3.6	0.6131
	HLA-DRB5*01:01	272	286	15	YKCLLADPK	AVEYYKCLLADPKLK	38.75	5	1.2339
	HLA-DRB3*01:01	161	175	15	YYKDKGKNI	SAEKYYKDKGKNIKQ	45.26	1.5	1.1354
	HLA-DRB3*01:01	160	174	15	YYKDKGKNI	KSAEKYYKDKGKNIK	45.56	1.5	1.1278
	HLA-DRB3*01:01	162	176	15	YYKDKGKNI	**AEKYYKDKGKNIKQK**	46.13	1.5	1.4259
	HLA-DRB5*01:01	28	42	15	LQFIAARCM	KNPEQLQFIAARCME	47.66	6	0.6649
	HLA-DRB1*07:01	142	156	15	LETIKAILF	DVHAKHLETIKAILF	48.42	4.7	0.526
	HLA-DRB5*01:01	277	291	15	LLADPKLKK	KCLLADPKLKKDFME	49.16	6.2	0.8827

Only antigenic, non-toxic, and non-allergenic epitopes predicted are given in the table. The most antigenic epitope was given in bold for each Aedes species

3.10. Antigenicity, Allergenicity, and Immune Simulation of Vaccine Constructs

The designed multi-epitope vaccine constructs for *A. aegypti* and *A. albopictus* were predicted antigenic with antigenicity scores of 0.7719 and 0.8883, respectively. Moreover, both vaccine constructs were estimated as non-allergenic. After *in silico* immune simulation, multi-epitope vaccine constructs against *A. aegypti* and *A. albopictus* were estimated to induce IFN-g, IgM, and IgG levels (Figure 5).

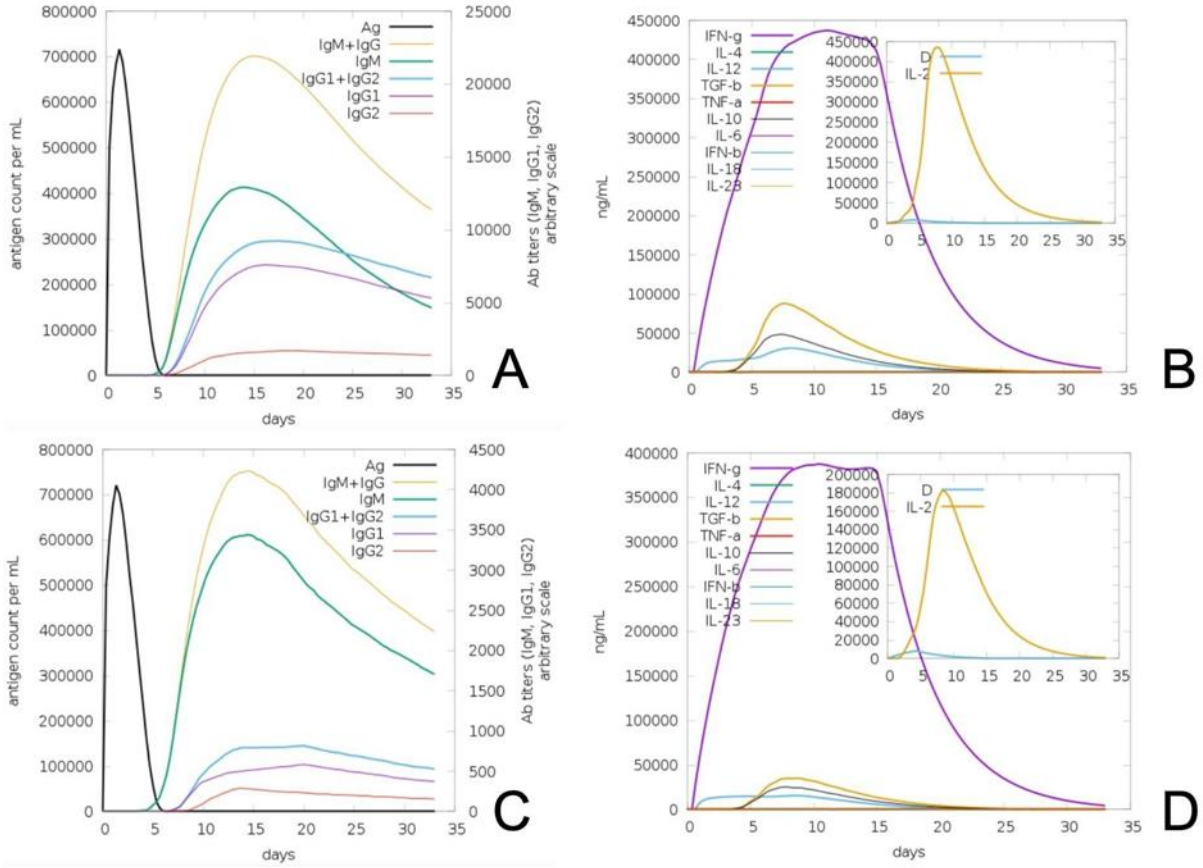

Figure 5. The immune simulations for vaccine constructs. IgM + IgG level for *A. aegypti* vaccine construct **(A)**. IFN-g level for *A. aegypti* vaccine construct **(B)**. IgM + IgG level for *A. albopictus* vaccine construct **(C)**. IFN-g level for *A. albopictus* vaccine construct **(D)**

4. Discussion

Arthropod vector-borne diseases, particularly those transmitted by mosquitoes, are rising as emerging and re-emerging zoonotic threats, placing nearly 3.5 billion people at risk globally and creating substantial public health burdens, especially in tropical regions [18, 45]. Although insecticides and acaricides control arthropod diseases, including tick-borne, flea-borne, and mosquito-borne diseases, genetic resistance has significantly evolved [15-17]. Alternatively, vaccine studies against vector-borne pathogens have been performed for several pathogens using *in silico* epitope discovery approaches [46-49].

However, in recent years, transmission-blocking antigens that target arthropod vectors, rather than the pathogens themselves, have gained prominence in vaccine research, offering a novel approach to combating vector-borne diseases [5, 18]. For instance, several transmission-blocking vaccines targeting vector-derived antigens, such as BM86, SUB, Salp25D, and HAA86, which are secretory and surface proteins identified in ticks like *Ixodes scapularis*, *Hyalomma anatolicum*, and *Rhipicephalus microplus*, have shown promise in reducing both tick infestations and the transmission of pathogens, including *Anaplasma phagocytophilum*, *Anaplasma marginale*, *Borrelia burgdorferi*, *Babesia bigemina*, and *Theileria annulata* [18]. For mosquito-

borne pathogens, fibrinogen-like (FBG) domain of the fibrinogen-related protein 1 (FREP1) located in the mosquito midgut, which facilitates the transmission of *Plasmodium falciparum*, was found to be conserved with a similarity rate of more than 90 percent among *Anopheles* mosquitoes in different parts of the world, and anti-FBG antibodies against malaria have been found to block the transmission in all *Anopheles* species [19].

Similarly, in the present study, 37 kDa salivary protein D7 of *Aedes* species (*A. aegypti* and *A. albopictus*) was predicted to be highly conserved in sequence and structural levels as well as phylogenetic relationship (Figures 1-3). Moreover, as a good transmission-blocking antigen, it was predicted with suitable physicochemical and immunogenic properties, including solubility, globular structure, negative GRAVY value, no transmembrane helix, no-host similarity, highly random coils, non-allergenicity, negative GRAVY value, signal peptide, and low posttranslational modifications, for both *A. aegypti* and *A. albopictus* [39, 42, 50, 51] (Table 1-6).

Furthermore, B-cell, MHC-I, and MHC-II epitopes showing high antigenicity, no allergenicity, and no toxicity were discovered by *in silico* approaches (Tables 7-9). Among them, KEKNPGK, FLLSSFILAA, and KYYQEKGVKIKQKEQ epitopes were selected for *A. aegypti*, while CDGKSAEK, FLLLAVAFVA, and AEKYYKDKGKNIKQK were selected for *A. albopictus* as prominent epitopes to design multi-epitope vaccine constructs which were predicted to be antigenic and non-allergenic (Tables 7-9; Figures 2 and 4). According to immune simulations, it was shown that multi-epitope vaccine constructs designed against *A. aegypti* and *A. albopictus* stimulate the production of IgM, IgG, and IFN-g (Figure 5).

5. Conclusion

Based on the analyses of 37 kDa salivary protein D7, prominent epitopes with the designed transmission-blocking multi-epitope vector vaccine can potentially be used in experimental vaccine development studies against *A. aegypti* and *A. albopictus*. Therefore, preliminary results in the present study will bring new perspectives for future veterinary and human medicine studies, especially in preventing and reducing *Aedes* mosquito-borne diseases. The discovered *Aedes* epitopes in the present study have the potential to be compared with other mosquito 37 kDa salivary protein D7 sequences, including *Culex* species, and multi-species conserved epitope discovery and universal vaccine design might be performed for many mosquito species. In future studies, it is thought that *in vitro* investigations on the discovery and synthesis of new peptides are needed in addition to *in silico* analyses in order to develop new vaccines and diagnostic tests against mosquito vector species carrying zoonotic pathogens.

Author Contributions

The first author: Conceptualization, methodology, formal analysis and investigation, writing-original draft preparation, supervision. The second author: Formal analysis and investigation, writing-review and editing. The third author: Formal analysis and investigation, writing-review and editing, supervision. They all read and approved the final version of the paper.

Conflict of Interest

All the authors declare no conflict of interest.

Ethical Review and Approval

No approval from the Board of Ethics is required.

References

[1] A. Nebbak, L. Almeras, P. Parola, I. Bitam, *Mosquito vectors (Diptera: Culicidae) and mosquito-borne diseases in North Africa*, Insects 13 (10) (2022) 962.

[2] S. Liu, X. Xia, E. Calvo, Z. H. Zhou, *Native structure of mosquito salivary protein uncovers domains relevant to pathogen transmission*, Nature Communications 14 (2023) 899.

[3] E. Gavor, Y. K. Choong, Y. Liu, J. Pompon, E. E. Ooi, Y. K. Mok, H. Liu, R. M. Kini, J. Sivaraman, *Identification of Aedes aegypti salivary gland proteins interacting with human immune receptor proteins*, PLoS Neglected Tropical Diseases 16 (9) (2022) e0010743.

[4] D. C. Rinker, R. J. Pitts, L. J. Zwiebel, *Disease vectors in the era of next generation sequencing*, Genome Biology 17 (1) (2016) 95.

[5] C. H. Coelho, R. Rappuoli, P. J. Hotez, P. E. Duffy, *Transmission-blocking vaccines for malaria: time to talk about vaccine introduction*, Trends in Parasitology 35 (7) (2019) 483–486.

[6] S. Buezo Montero, P. Gabrieli, A. Poinsignon, B. Z. H. Zamble, F. Lombardo, F. Remoue, B. Arcà, *Human IgG responses to the Aedes albopictus 34k2 salivary protein: Analyses in Reunion Island and Bolivia confirm its suitability as marker of host exposure to the tiger mosquito*, Parasites and Vectors 15 (1) (2022) 260.

[7] B. R. Egid, M. Coulibaly, S. K. Dadzie, B. Kamgang, P. J. McCall, L. Sedda, K. H. Toe, A. L. Wilson, *Review of the ecology and behaviour of Aedes aegypti and Aedes albopictus in Western Africa and implications for vector control*, Current Research in Parasitology and Vector-Borne Diseases 2 (2022) 100074.

[8] L. Braack, A. P. Gouveia de Almeida, A. J. Cornel, R. Swanepoel, C. De Jager, *Mosquito-borne arboviruses of African origin: review of key viruses and vectors*, Parasites and Vectors 11 (2018) 29.

[9] S. J. Ryan, C. J. Carlson, E. A. Mordecai, L. R. Johnson, *Global expansion and redistribution of Aedes-borne virus transmission risk with climate change*, PLoS Neglected Tropical Diseases 13 (3) (2019) e0007213.

[10] N. Vasilakis, J. Cardosa, K. A. Hanley, E. C. Holmes, S. C. Weaver, *Fever from the forest: prospects for the continued emergence of sylvatic dengue virus and its impact on public health*, Nature Reviews Microbiology 9 (7) (2011) 532–541.

[11] I. Martin-Martin, L. B. Smith, A. C. Chagas, A. Sá-Nunes, G. Shrivastava, P. C. Valenzuela-Leon, E. Calvo, *Aedes albopictus D7 salivary protein prevents host hemostasis and inflammation*, Biomolecules 10 (10) (2020) 1372.

[12] Z. Li, C. Ji, J. Cheng, M. Åbrink, T. Shen, X. Kuang, Z. Shang, J. Wu, *Aedes albopictus salivary proteins adenosine deaminase and 34k2 interact with human mast cell specific proteases tryptase and chymase*, Bioengineered 13 (5) (2022) 13752–13766.

[13] M. K. McCracken, R. C. Christofferson, B. J. Grasperge, E. Calvo, D. M. Chisenhall, C. N. Mores, *Aedes aegypti salivary protein "aegyptin" co-inoculation modulates dengue virus infection in the vertebrate host*, Virology 468-470 (2014) 133–139.

[14] R. Oktarianti, K. Senjarini, T. Hayano, F. Fatchiyah, Aulanni'am, *Proteomic analysis of immunogenic proteins from salivary glands of Aedes aegypti*, Journal of Infection and Public Health 8 (6) (2015) 575–582.

[15] W. R. Shaw, F. Catteruccia, *Vector biology meets disease control: using basic research to fight vector-borne diseases*, Nature Microbiology 4 (1) (2019) 20–34.

[16] S. Erkunt Alak, A. E. Köseoğlu, Ç. Kandemir, T. Taşkın, S. Demir, M. Döşkaya, C. Ün, H. Can, *High frequency of knockdown resistance mutations in the para gene of cat flea (Ctenocephalides felis) samples collected from goats*, Parasitology Research 119 (7) (2020) 2067–2073.

[17] J. G. van Oosterwijk, S. K. Wikel, *Resistance to ticks and the path to anti-tick and transmission blocking vaccines*, Vaccines 9 (7) (2021) 725.

[18] O. Merino, P. Alberdi, J. M. Pérez de la Lastra, J. de la Fuente, *Tick vaccines and the control of tick-borne pathogens*, Frontiers in Cellular and Infection Microbiology 3 (2013) 30.

[19] G. Niu, A. C. Franca, G. Zhang, W. Roobsoong, W. Nguitragool, X. Wang, J. Prachumsri, N. S. Butler, J. Li, *The fibrinogen-like domain of FREP1 protein is a broad-spectrum malaria transmission-blocking vaccine antigen*, Journal of Biological Chemistry 292 (28) (2017) 11960–11969.

[20] J. E. Manning, T. Cantaert, *Time to micromanage the pathogen-host-vector interface: considerations for vaccine development*, Vaccines 7 (1) (2019) 10.

[21] F. Sievers, D. G. Higgins, *Clustal omega*, Current Protocols in Bioinformatics 48 (1) (2014) 3.13.1-3.13.16.

[22] K. Tamura, G. Stecher, S. Kumar, *MEGA11: molecular evolutionary genetics analysis version 11*, Molecular Biology and Evolution 38 (7) (2021) 3022–3027.

[23] J. Yang, Y. Zhang, *I-TASSER server: new development for protein structure and function predictions*, Nucleic Acids Research 43 (W1) (2015) W174–W181.

[24] E. F. Pettersen, T. D. Goddard, C. C. Huang, G. S. Couch, D. M. Greenblatt, E. C. Meng, T. E. Ferrin, *UCSF Chimera—a visualization system for exploratory research and analysis*, Journal of Computational Chemistry 25 (13) (2004) 1605–1612.

[25] J. Ko, H. Park, L. Heo, C. Seok, *GalaxyWEB server for protein structure prediction and refinement*, Nucleic Acids Research 40 (W1) (2012) W294–W297.

[26] C. Colovos, T. O. Yeates, *Verification of protein structures: patterns of nonbonded atomic interactions*, Protein Science 2 (9) (1993) 1511–1519.

[27] M. Wiederstein, M. J. Sippl, *ProSA-web: interactive web service for the recognition of errors in three-dimensional structures of proteins*, Nucleic Acids Research 35 (W2) (2007) W407–W410.

[28] J. Garnier, J. F. Gibrat, B. Robson, *GOR method for predicting protein secondary structure from amino acid sequence*, Methods in Enzymology 266 (1996) 540–553.

[29] E. Gasteiger, C. Hoogland, A. Gattiker, S. Duvaud, M. R. Wilkins, R. D. Appel, A. Bairoch, *Protein identification and analysis tools on the ExPASy server*, in: J. M. Walker (Eds.) The Proteomics Protocols Handbook, Springer Protocols Handbooks, Humana Press Inc., Totowa, NJ, 2005, pp. 571-607.

[30] I. A. Doytchinova, D. R. Flower, *VaxiJen: a server for prediction of protective antigens, tumour antigens and subunit vaccines*, BMC Bioinformatics 8 (2007) 4.

[31] K. C. Chou, H. B. Shen, *A new method for predicting the subcellular localization of eukaryotic proteins with both single and multiple sites: Euk-mPLoc 2.0*, PLoS One 5 (4) (2010) e9931.

[32] A. Krogh, B. Larsson, G. Von Heijne, E. L. Sonnhammer, *Predicting transmembrane protein topology with a hidden Markov model: application to complete genomes*, Journal of Molecular Biology 305 (3) (2001) 567–580.

[33] K. Frank, M. J. Sippl, *High-performance signal peptide prediction based on sequence alignment techniques*, Bioinformatics 24 (19) (2008) 2172–2176.

[34] S. Saha, G. P. S. Raghava, *AlgPred: prediction of allergenic proteins and mapping of IgE epitopes*, Nucleic Acids Research 34 (W2) (2006) W202–W209.

[35] S. Saha, G. P. S. Raghava, *BcePred: prediction of continuous B-cell epitopes in antigenic sequences using physico-chemical properties*, in: G. Nicosia, V. Cutello, P. J. Bentley, J. Timmis (Eds.), International Conference on Artificial Immune Systems, ICARIS 2004, Lecture Notes in Computer Science, Vol. 3239, Springer, Berlin, 2004, pp. 197–204.

[36] R. Vita, S. Mahajan, J. A. Overton, S. K. Dhanda, S. Martini, J. R. Cantrell, D. K. Wheeler, A. Sette, B. Peters, *The immune epitope database (IEDB): 2018 update*, Nucleic Acids Research 47 (D1) (2019) D339–D343.

[37] S. Gupta, P. Kapoor, K. Chaudhary, A. Gautam, R. Kumar, Open Source Drug Discovery Consortium, G. P. Raghava, *In silico approach for predicting toxicity of peptides and proteins*, PLoS One 8 (9) (2013) e73957.

[38] I. Dimitrov, I. Bangov, D. R. Flower, I. Doytchinova, *AllerTOP v. 2—a server for in silico prediction of allergens*, Journal of Molecular Modeling 20 (6) (2014) 2278.

[39] H. Can, S. Erkunt Alak, A. E. Köseoğlu, M. Döşkaya, C. Ün, *Do Toxoplasma gondii apicoplast proteins have antigenic potential? An in silico study*, Computational Biology and Chemistry 84 (2020) 107158.

[40] M. Ali, R. K. Pandey, N. Khatoon, A. Narula, A. Mishra, V. K. Prajapati, *Exploring dengue genome to construct a multi-epitope based subunit vaccine by utilizing immunoinformatics approach to battle against dengue infection*, Scientific Reports 7 (1) (2017) 9232.

[41] P. Kalita, A. K. Padhi, K. Y. Zhang, T. Tripathi, *Design of a peptide-based subunit vaccine against novel coronavirus SARS-CoV-2*, Microbial Pathogenesis 145 (2020) 104236.

[42] A. E. Köseoğlu, F. Özgül, E. N. Işıksal, Y. Şeflekçi, D. Tülümen, B. Özgültekin, G. Deniz Köseoğlu, S. Özyiğit, M. Ihlamur, Y. Ekenoğlu Merdan, *In silico discovery of diagnostic/vaccine candidate antigenic epitopes and a multi-epitope peptide vaccine (NaeVac) design for the brain-eating amoeba Naegleria fowleri causing human meningitis*, Gene 902 (2024) 148192.

[43] N. Rapin, O. Lund, M. Bernaschi, F. Castiglione, *Computational immunology meets bioinformatics: the use of prediction tools for molecular binding in the simulation of the immune system*, PLoS One 5 (4) (2010) e9862.

[44] A. E. Köseoğlu, GitHub (2025), https://github.com/drahmetefe/aedes/blob/main/dot_plot_for_top_antigenic_epitopes, Accessed 06 Mar 2025.

[45] B. Londono-Renteria, A. Troupin, T. M. Colpitts, *Arbovirosis and potential transmission blocking vaccines*, Parasites and Vectors 9 (1) (2016) 516.

[46] S. Arumugam, P. Varamballi, *In-silico design of envelope based multi-epitope vaccine candidate against Kyasanur forest disease virus*, Scientific Reports 11 (1) (2021) 17118.

[47] S. Aiman, A. Ahmad, A. A. Khan, A. M. Alanazi, A. Samad, S. L. Ali, C. Li, Z. Ren, A. Khan, S. Khattak, *Vaccinomics-based next-generation multi-epitope chimeric vaccine models prediction against Leishmania tropica-a hierarchical subtractive proteomics and immunoinformatics approach*, Frontiers in Immunology 14 (2023) 1259612.

[48] A. E. Köseoğlu, H. Can, M. Güvendi, S. Erkunt Alak, A. Değirmenci Döşkaya, M. Karakavuk, M. Döşkaya, C. Ün, *Molecular characterization of Anaplasma ovis Msp4 protein in strains isolated from ticks in Turkey: A multi-epitope synthetic vaccine antigen design against Anaplasma ovis using immunoinformatic tools*, Biologicals 85 (2024) 101749.

[49] O. Saha, A. Razzak, N. Sarker, N. Rahman, A. bin Zahid, A. Sultana, T. A. Shishir, N. M. Bahadur, M. M. Rahaman, F. Hossen, M. R. Amin, M. S. Akter, *In silico design and evaluation of multi-epitope dengue virus vaccines: A promising approach to combat global dengue burden*, Discover Applied Sciences 6 (2024) 210.

[50] R. A. Shey, S. M. Ghogomu, K. K. Esoh, N. D. Nebangwa, C. M. Shintouo, N. F. Nongley, B. F. Asa, F. N. Ngale, L. Vanhamme, J. Souopgui, *In-silico design of a multi-epitope vaccine candidate against onchocerciasis and related filarial diseases*, Scientific Reports 9 (1) (2019) 4409.

[51] H. Can, A. E. Köseoğlu, S. Erkunt Alak, M. Güvendi, M. Döşkaya, M. Karakavuk, A. Y. Gürüz, C. Ün, *In silico discovery of antigenic proteins and epitopes of SARS-CoV-2 for the development of a vaccine or a diagnostic approach for COVID-19*, Scientific Reports 10 (1) (2020) 22387.

Journal of New Results in Science
dergipark.org.tr/en/pub/jnrs
Open Access

ISSN: 1304-7981 14 (2) (2025) 166-180 doi.org/10.54187/jnrs.1698629

Green Synthesis of Zinc Oxide Nanoparticles from *Malus domestica*, *Tilia cordata*, and its Biological Activities

Nilgün Güler[1], Halime Güzin Aslan[2], Ercan Karaköse[3], Mithat Güllü[4]

Article Info
Received: 17 May 2025
Accepted: 25 Aug 2025
Published: 31 Aug 2025
Research Article

Abstract − This study aimed to evaluate the anticancer and antibacterial drug status of biomass, including zinc oxide (ZnO) nanoparticles (NPs) synthesized from two plant extracts according to the results of Topoisomerase-I enzyme inhibition, DNA cleavage, DNA binding, and antibacterial activity tests. The *Malus domestica* (apple) and *Tilia cordata* (linden) plants were dried and powdered, and their extracts were prepared in pure water. X-Ray Diffraction (XRD), Scanning Electron Microscopy (SEM), and Fourier Transform Infrared (FTIR) analyses were applied for the characterization of the light-yellow powder ZnO NPs. Additionally, Topoisomerase-I enzyme inhibition, DNA cleavage, and DNA binding analyses were performed by agarose gel electrophoresis method. Powder ZnO NPs (biomass) were analyzed by the agar well diffusion method by using two gram-positive and two gram-negative bacteria. According to the XRD analysis results, the peaks obtained show that there is no foreign matter or secondary diffraction peak other than the hexagonal ZnO structure. It was observed that ZnO NPs from *Tilia cordata* extract are effective against *Klebsiella pneumoniae*. ZnO NPs from *Malus domestica* extract have the potential to be an effective human Topoisomerase-I enzyme inhibitor. There was poor DNA cleavage activity in all samples. In ZnO NPs from linden extract, there was an interaction at a 1mg/mL concentration of CT-DNA.

Keywords − *Enzyme inhibition, green synthesis, inorganic drug, anti-bacterial activity, ZnO NPs*

1. Introduction

Nanoparticles are particles that range in size from 1 to 100 nm. Due to their small size and large surface area, they exhibit unique properties such as enhanced catalytic reactivity, biological activity, thermal conductivity, nonlinear optical performance, and chemical stability. As a result, nanoparticles are widely applied in various fields, including healthcare, food, feed, aviation, chemistry, cosmetics, and agriculture [1-3].

Nanoparticles can be synthesized using either physical or chemical methods. Physical processes are often lengthy and difficult to carry out, whereas chemical processes typically involve reagents and procedures that may be harmful to the environment. To overcome these limitations, alternative approaches such as green synthesis have been developed. This environmentally friendly method, which relies on biomaterials, is also referred to as green chemistry and has gained increasing attention in recent years.

There are several studies in the literature on nano ZnO synthesized through green methods. The ability of organisms and organic compounds to reduce metal ions and stabilize them as nanoparticles (NPs) forms the

[1]nilgunkusculu@kayseri.edu.tr (Corresponding Author); [2]guzina@erciyes.edu.tr; [3]ekarakose@kayseri.edu.tr; [4]mgullu@erciyes.edu.tr
[1]Department of Chemistry Technology, Mustafa Çıkrıkçıoğlu Vocational School, Kayseri University, Kayseri, Türkiye
[2]Department of Chemistry, Faculty of Science, Erciyes University, Kayseri, Türkiye
[3]Department of Basic Sciences, Faculty of Engineering, Kayseri University, Kayseri, Türkiye
[4]Department of Biology, Faculty of Science, Erciyes University, Kayseri, Türkiye

basis of green synthesis. In particular, secondary metabolites present in plant extracts, such as flavonoids and other phytochemicals, play a key role in the reduction process [4,5]. For example, a study reported the synthesis of ZnO NPs using extracts derived from Hibiscus leaves [6]. This work is noteworthy as it represents an initial step toward the treatment of diabetes mellitus, one of the most common diseases of our time.

In the literature, the majority of green synthesis research has focused on the preparation of NPs containing silver and gold, as well as the evaluation of their biological activities [7–14]. In addition, studies have also explored the synthesis of NPs containing copper, palladium, and platinum using plant extracts through green synthesis methods [15–19].

There are also publications investigating the antioxidant, antifungal, antibacterial, photodegradative, and cytotoxic properties of ZnO NPs synthesized via green methods [20–26]. In addition, studies in the literature have reported nanosynthesis of the quercetin–iron complex as well as various complexes of copper (II) [27,28]. In some cases, High-Performance Liquid Chromatography–Fourier Transform Infrared Spectroscopy (HPLC–FTIR) analyses were performed to identify which phytochemical secondary metabolites, such as flavonoids, tannins, saponins, and terpenoids, acted as reducing agents in the extracts [29,30].

The co-conjugation of these nanoparticles with secondary metabolites further expands their applicability in industrial biotechnology. Nanoparticle-mediated delivery of therapeutically important flavonoids and other biomolecules can enhance their pharmacological efficacy. For instance, hesperetin-conjugated gold NPs have been explored as a potential drug delivery system to reduce the dosage of chemotherapeutic agents, thereby improving the treatment of hepatocellular carcinoma while minimizing adverse side effects [31].

More recently, several reports have highlighted the potential risks of NPs to both human health and the environment. This underscores the need for reliable detection methods in food and biological samples. A standardized, rapid, and straightforward flavonoid-assisted green synthesis method has been developed for the extraction and detection of Titanium dioxide nanoparticles (TiO2 NPs) from food samples [32]. Moreover, this method can be extended to detect flavonoid residues in biological samples, such as urine and blood [33].

Given its efficiency, low cost, and eco-friendly characteristics, green synthesis represents an important alternative to conventional nanoparticle production methods. To date, NPs have been synthesized from a variety of metal ions using numerous plant extracts; however, ZnO NPs derived from apple and linden extracts have not yet been reported. In the present study, we focused on the interaction of ZnO NPs produced via this method with biomolecules, owing to their environmentally friendly and non-toxic nature. Specifically, this work aimed to investigate the binding of ZnO NPs with DNA molecules, their potential to induce separation within the DNA helix, their interaction with the replication enzyme Topoisomerase-I, and their antibacterial activity. To date, although numerous plant extracts have been employed for the synthesis of zinc oxide nanoparticles (ZnO NPs), no reports exist on the use of apple or linden. The present study aims to investigate the biological interactions of ZnO NPs synthesized by green methods from these sources, with a particular focus on DNA binding, cleavage activity, Topoisomerase-I inhibition, and antibacterial properties.

2. Materials

Plant materials were obtained from local vendors in the Yahyalı district and the Kayseri city center. Apple (S1) and linden (S2) were selected as sources for the green synthesis of ZnO NPs. Zinc nitrate hexahydrate ($Zn(NO3)_2 \cdot 6H_2O$) (Sigma-Aldrich) was employed as the zinc precursor in the synthesis process.

3. Methods

3.1. Preparation of Extracts from Plants

The process began with the cleaning and crushing of apples and linden to obtain their extracts. For each plant, 25 g of material was used and mixed with 100 mL of distilled H2O using a magnetic stirrer for 1 hour at 95 °C. The resulting extract was then cooled to 25 °C and filtered twice through filter paper to remove large particles. The prepared extracts were subsequently stored at 4 °C for use in further experiments [34].

3.2. Green Synthesis of ZnO NPs

The synthesis of zinc oxide nanoparticles was carried out through a simple procedure. Briefly, 5 g of Zn(NO3)2·6H2O and a small amount of distilled water were added to 50 mL of plant extract, and the mixture was magnetically stirred at 100 °C until the ZnO structure was formed. The resulting mixture was then annealed in an oven at 400 °C for 120 minutes, yielding ZnO-NPs in powder form. The light yellow powder thus obtained was used for subsequent biological studies. For characterization, Field Emission Scanning Electron Microscopy (FE-SEM), X-ray Diffraction (XRD), and Fourier Transform Infrared Spectroscopy (FT-IR) analyses were performed on ZnO-NPs synthesized from both plant sources [34].

3.2.1. Explanation of Synthesis Reaction

Figure 1 illustrates the possible reaction pathway for the production of zinc oxide nanoparticles using apple and linden extracts. Volatile phytochemicals such as quercetin-3-glucosides, monomeric and oligomeric compounds, kaempferol, quercetin, cinnamic acid, caffeic acid, rosmarinic acid, and other flavonoid molecules can undergo nucleation with Zn^{2+} ions to form zinc–flavonoid complex molecules. Upon heat treatment (annealing), these complexes are transformed into ZnO-NPs [35].

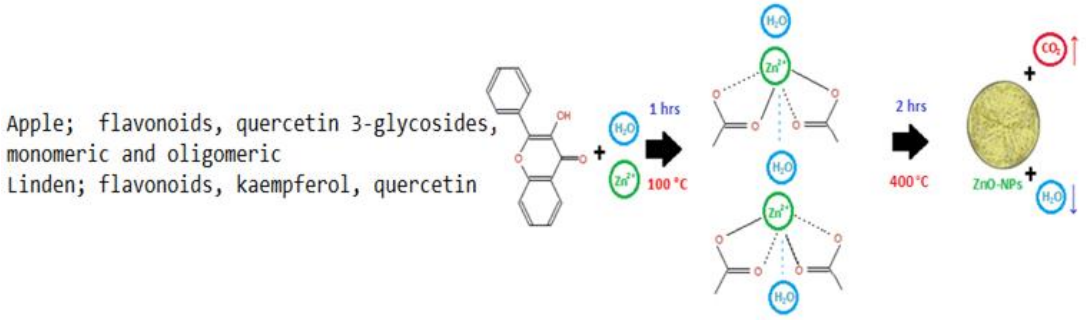

Figure 1. Possible reaction mechanism for ZnO-NPs

However, the proposed reaction mechanism remains unclear and requires further investigation to be fully understood. During the synthesis process, water vapor (H2O(g)) and carbon dioxide (CO2(g)) are released as by-products. Consequently, this ZnO-NP synthesis method is considered environmentally friendly.

3.3. SEM, XRD, and FT-IR Analysis

Structural analyses of zinc oxide nanoparticles were performed using Scanning Electron Microscopy (SEM), X-ray Diffraction (XRD), and Fourier Transform Infrared Spectroscopy (FT-IR). ZnO NPs in dry powder form were directly analyzed with an FEI Quanta SEM, providing image resolutions of up to 1 nm. XRD measurements were carried out on powdered samples using a Panalytical Empyrean diffractometer.

In addition, FT-IR analyses were conducted with a Perkin Elmer Model 400 FT-IR/FT-FIR Spectrometer equipped with a Spotlight 400 Imaging System. This technique was used to determine the presence of

functional groups, evaluate bond characteristics, and identify the binding sites within the structure, as well as to distinguish whether the organic components were aromatic or aliphatic in nature [36].

3.4. Antimicrobial Studies

3.4.1. Microorganism Samples

In this study, four bacterial strains were used to evaluate the antimicrobial activity of zinc oxide nanoparticles synthesized from extracts of two different plant sources. The names of the microorganisms and their corresponding culture collection codes are presented in Table 1.

Table 1. Organism names and culture code

Microorganisms	Organism Code
Bacillus cereus	NRLL B-3008
Escherichia coli	ATCC 25922
Klebsiella pneumonia	ATCC 13883
Staphylococcus epidermidis	ATCC 12228

- *Bacillus cereus:* It is a gram-positive, rod-shaped, endospore-forming, facultative aerobic bacterium, 1x3-4 μm in size. Bacillus cereus, a soil bacterium, can cause food poisoning by affecting many types of food by secreting emetic and enterotoxin [37].
- *Escherichia coli:* It is a gram-negative bacillus with an average length of 2-6 μm and a width of 1-1.5 μm. It is mobile thanks to its peritrich cilia. There are also sleeping species. Some strains have capsules or microcapsules. They do not form spores and are facultative anaerobes [38].
- *Klebsiella pneumonia:* It is a gram-negative bacterium that can cause many diseases. Pneumonia, blood infections, wound or surgical site infections, and meningitis are some of these diseases [39].
- *Staphylococcus epidermidis:* Staphylococcus epidermidis is a type of bacteria among the staphylococci whose seeds are found in clusters. It is gram-positive, catalase-positive, and coagulase-negative. It is naturally found in the person's upper respiratory tract. They are resistant to a wide range of antibiotics, including penicillin and methicillin [40].

3.4.2. Culture Medium Information

- Müller Hinton Agar Medium (gr/lt): 2.0 g meat extract, 17.5 g casein hydrolyzate, 1.5 g starch, 17.0 g agar were all taken into a bottle and sterilized by autoclaving at 121ºC for 15 minutes.
- Müller Hinton Liquid Medium (gr/lt): 2.0 g meat extract, 17.5 g casein hydrolyzate, and 1.5 g starch were all taken into a bottle and sterilized by autoclaving at 121ºC for 15 minutes.

3.4.3. Antimicrobial Activity Study

Antimicrobial activity of the two zinc oxide nanoparticles synthesized from plant extracts was evaluated using the agar well diffusion method. Two Gram-positive and two Gram-negative bacterial strains were employed in the study (Table 1). Bacteria from stock cultures were first grown in Mueller–Hinton broth at 37 °C for 24 hours. Each culture was then reinoculated at 1% (v/v) into fresh broth and incubated for 18 hours until reaching the exponential growth phase. The bacterial suspensions were subsequently adjusted to the standard McFarland density [41].

From each standardized culture, 100 µL was spread onto Mueller–Hinton agar plates using the spread plate technique, after which 6 mm diameter wells were aseptically punched into the agar. A volume of 100 µL of ZnO NPs, dissolved in dimethylformamide (DMF), was introduced into each well, and the plates were incubated under standard conditions. Antimicrobial effects were assessed by measuring the diameters of the inhibition zones around the wells after incubation [42].

3.5. DNA and Enzyme Experiments

3.5.1. Chemicals

Agarose (Isolab), dimethyl sulfoxide (DMSO), double-distilled water (DDW), bromophenol blue, calf thymus deoxyribonucleic acid (CT-DNA), ethylenediaminetetraacetic acid (EDTA), dimethylformamide (DMF), sodium dodecyl sulfate (SDS), Tris base, glycerol, loading dye, ethidium bromide (EtBr), and irinotecan were used in this study. Supercoiled pBR322 plasmid DNA was obtained from Thermo Scientific, while the human topoisomerase I assay kit was purchased from TopoGEN.

3.5.2. DNA Cleavage Experiment

Agarose gel electrophoresis was employed to investigate the effects of zinc oxide (ZnO) nanoparticles synthesized from apple and linden extracts on the double-stranded helical structure of pBR322 plasmid DNA.

3.5.3. DNA Binding Experiment

ZnO NPs obtained from two plants were separately dissolved in dimethylformamide (DMF) to prepare 100 µM stock solutions. Agarose gel electrophoresis was performed to evaluate the interaction of the compounds with calf thymus DNA (CT-DNA). In this study, CT-DNA 2–1 (mg/mL) was prepared in Tris(hydroxymethyl) aminomethane hydrochloride (Tris-HCl) buffer, while the concentrations of the two ZnO NP samples in DMF were fixed at 3% (mg/µL). The mixtures were adjusted to a final volume of 25 µL with buffer in PCR tubes and incubated at 37 °C for 24 hours. After incubation, the samples were loaded onto a 1% agarose gel containing ethidium bromide in Tris-acetate-EDTA (TAE) buffer [43].

The inhibitory effect of the two ZnO NPs on human topoisomerase I (Topo I) was also investigated by assessing their ability to relax supercoiled pBR322 plasmid DNA (100 µg) in the absence and presence of ZnO NP samples. They were used at concentrations ranging from 3% to 0.75% in 10× TGS buffer. Each reaction mixture was incubated at 37 °C for 1 hour. It was terminated by adding 4 µL of 5× loading buffer containing 4.5% sodium dodecyl sulfate (SDS), 0.25% bromophenol blue, and 45% glycerol. Electrophoresis was then performed on 1% agarose gels in 1× TAE buffer at 80 V for 60 minutes [44].

4. Results and Discussion

4.1. SEM and XRD Analysis Results of Apple (S1), Linden (S2) Samples

Figure 2(a) shows that zinc oxide nanoparticles (ZnO NPs) synthesized using apple extract consist of porous structures. At higher magnification (Figure 2(b)), these structures were observed to be composed of dot-shaped ZnO particles with sizes ranging from 10 to 30 nm. Figures 2(c–d) present ZnO NPs produced from linden extract; in the scanning electron microscopy (SEM) images, red blood cell-like ZnO nanostructures were detected. At higher magnification (Figure 2(d)), these nanostructures were further resolved as dot-shaped ZnO particles with dimensions of 10–20 nm.

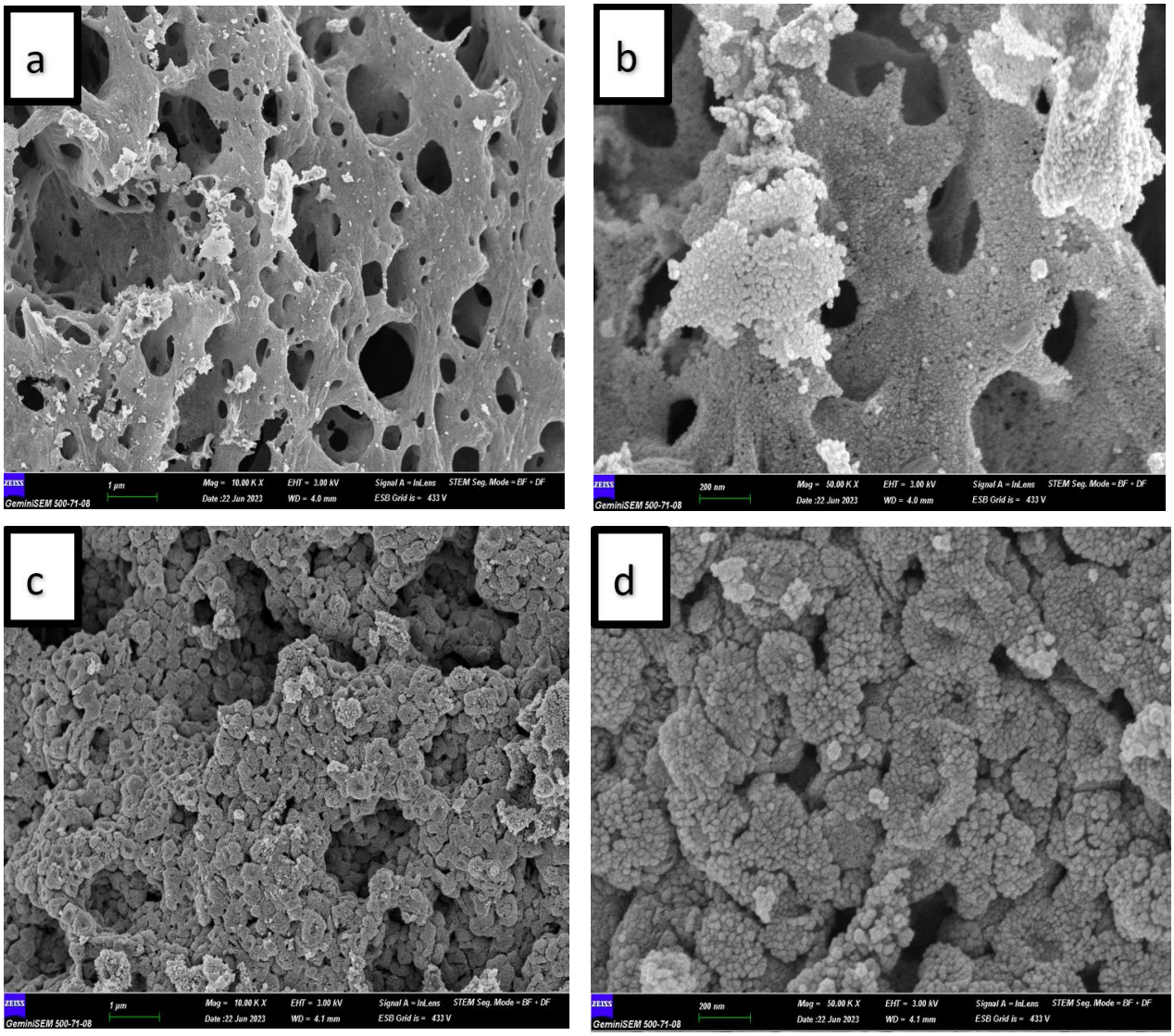

Figure 2. SEM images of ZnO NP's produced from **(a)-(b)** apple (S1) and **(c)-(d)** linden (S2) extract; Photographs at **(a)-(c)** 10,000, and **(b)-(d)** 50,000 times magnification

Similar dot-shaped ZnO nanostructures of varying sizes have been reported in several studies. For example, Joulaee et al. [45] synthesized ZnO nanoparticles (NPs), nickel oxide nanoparticles (NiO NPs), ZnO/NiO nanocomposites (NCs), and ZnO/NiO/graphene quantum dot nanocomposites (ZnO/NiO/GQDs NCs) via a novel green co-deposition and hydrothermal approach, reporting ZnO dots with diameters of 74 nm. Tshangana et al. [46] investigated the photocatalytic and antimicrobial activities of ZnO nanohybrids (ZnO-NFs@GQDs and ZnO-NRs@GQDs) and determined the average ZnO dot radius to be 23.5 nm. Similarly, Camacho et al. [47] synthesized ZnO nanoparticles using Ipomoea stans leaf extracts. Their characterization confirmed the presence of active functional groups and Zn–O bonds, while photocatalytic tests demonstrated more than 91% degradation efficiency against methyl orange, methylene blue, and rhodamine B dyes, with particle sizes ranging from 10.16 to 30.78 nm.

X-ray diffraction analysis revealed diffraction peaks at 2θ = 31.90°, 34.57°, 36.41°, 47.70°, 56.76°, 62.97°, 66.58°, 68.07°, 69.21°, 72.75°, 76.98°, and 81.51°, which correspond to the (100), (002), (101), (102), (110), (103), (200), (112), (201), (004), (202) and (104) planes, respectively. These reflections are characteristic of the wurtzite (hexagonal) crystal structure of ZnO. Furthermore, the XRD pattern shown in Figure 3 indicates the absence of any impurity or secondary diffraction peaks, confirming the purity of the hexagonal ZnO structure. The obtained diffraction peaks are in good agreement with previously reported studies [48,49].

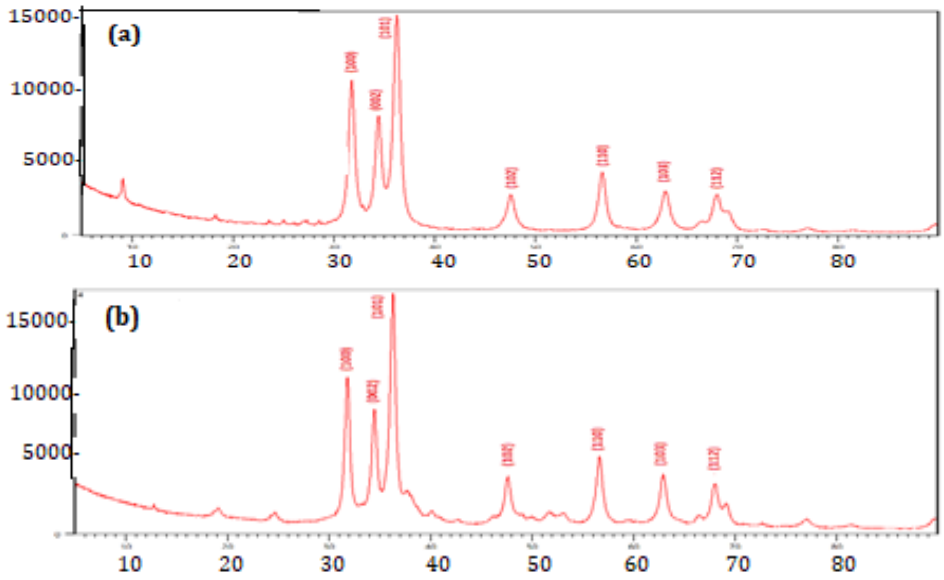

Figure 3. XRD analysis results of ZnO NPs produced from plant extract: **(a)** apple (S1), and **(b)** linden (S2)

The average crystallite size of the ZnO NP samples was estimated using the Debye–Scherrer equation:

$$D = \frac{K\lambda}{\beta Cos\theta} \tag{4.1}$$

From (4.1), D represents the average crystallite size, K is the Scherrer constant (≈0.9), λ is the wavelength of the X-rays (CuKα, 1.542 Å), β is the full width at half maximum (FWHM) of the diffraction peak, and θ is the Bragg diffraction angle. Based on this calculation, the average crystallite sizes of the ZnO NPs were determined to be 27 nm for the apple extract and 36 nm for the linden extract. These values are consistent with those reported for ZnO NPs synthesized from Hibiscus, Azolla, and Ipomoea leaf extracts [6,7,47].

4.2. FTIR Analysis Results of Apple (S1), Linden (S2) Samples

Fourier Transform Infrared Spectroscopy was employed to analyze the chemical structures of the synthesized ZnO nanoparticles. The positions of the absorption bands and the number of peaks observed are influenced by the crystal structure, type of chemical bonding, and morphology of the material. The characteristic FTIR peaks and corresponding band assignments of ZnO NPs are presented in Table 2 and Figure 4, respectively.

Table 2. FTIR band analysis results of ZnO NPs from plants

Peaks	ZnO (cm^{-1})	Assignments	References
1	526.96–551.04	Stretching of (Zn–O) bond	[17], [19]
2	813.74	C–H vibration	[18], [20]
3	1067.0–1069.1	C–H vibration; C–O stretching	[18]
4	1322.4–1376.6	C–H vibration	[18]
5	1661.4	C=O stretching vibration	
6	2142.2	C=O stretching	[18]
7	2353.4–2357.8	C=O stretching	[18]
8	2918.1	C–H stretching vibration	[18], [20]

A broad absorption band observed in the range of 2700–3500 cm-¹, together with a peak at 1092 cm-¹, corresponds to the O–H stretching vibration of polymeric H2O molecules associated with the Zn–O lattice. The absorption peak between 2344 and 2352 cm-¹ is attributed to atmospheric CO2. Since measurements were conducted at room temperature under ambient air conditions, contributions from moisture (H2O) and CO2 absorption were unavoidable. Notably, the absence of peaks just above 3000 cm-¹ indicates that the S1 and S2 samples do not contain aromatic flavonoid or phenolic chromophore structures.

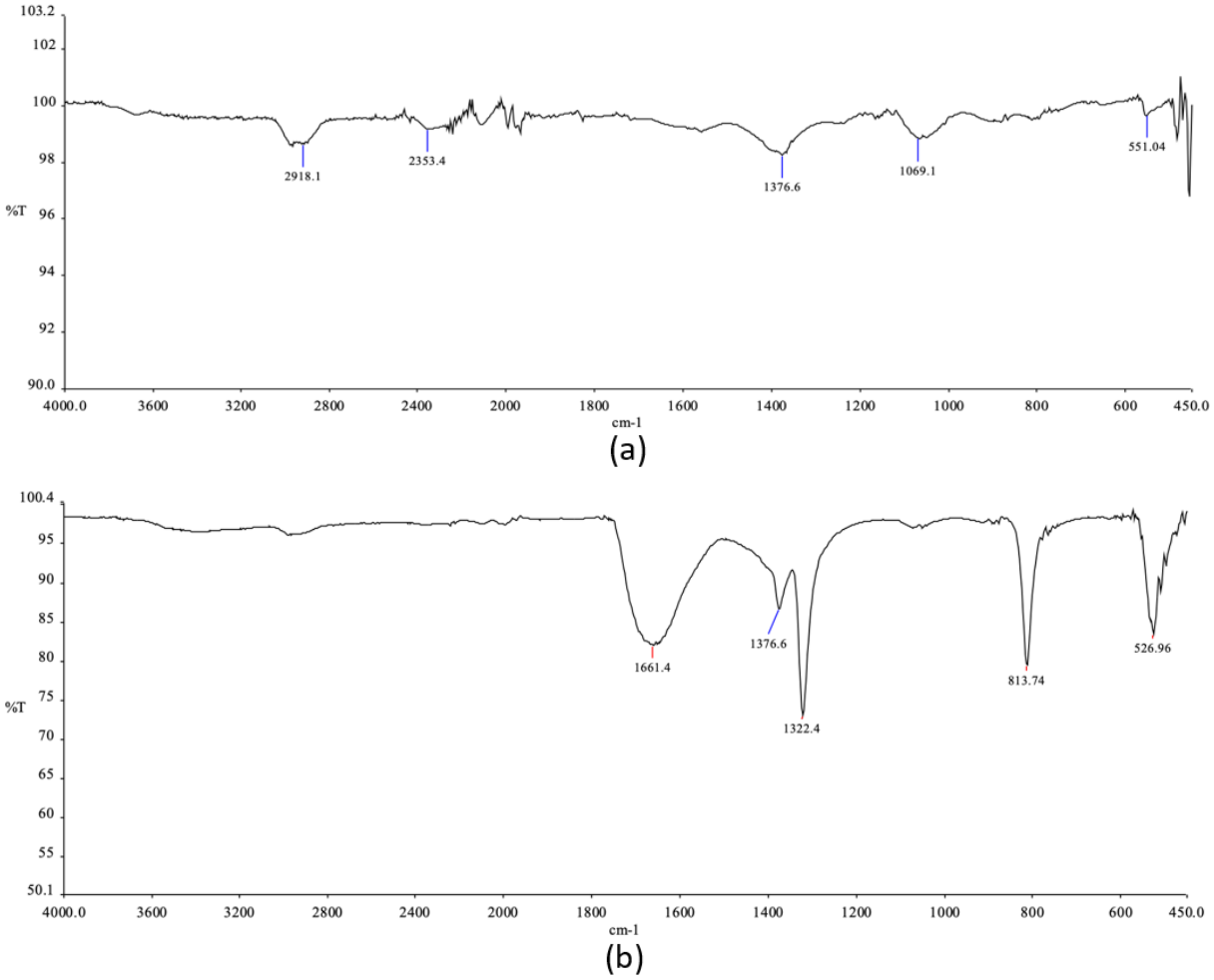

Figure 4. FTIR analysis results of ZnO NPs produced from plant extract: **(a)** apple (S1), and **(b)** linden (S2)

4.3. Samples CT-DNA Binding Experiment of Apple (S1), Linden (S2) Samples

The binding interactions of zinc oxide nanoparticles from two plants with calf thymus DNA (CT-DNA) were evaluated by agarose gel electrophoresis. Results are presented in Figure 5. In this assay, the concentrations of all nanoparticle samples were fixed at 100 μM, while the CT-DNA concentration was gradually decreased from 2 mg/mL to 1 mg/mL.

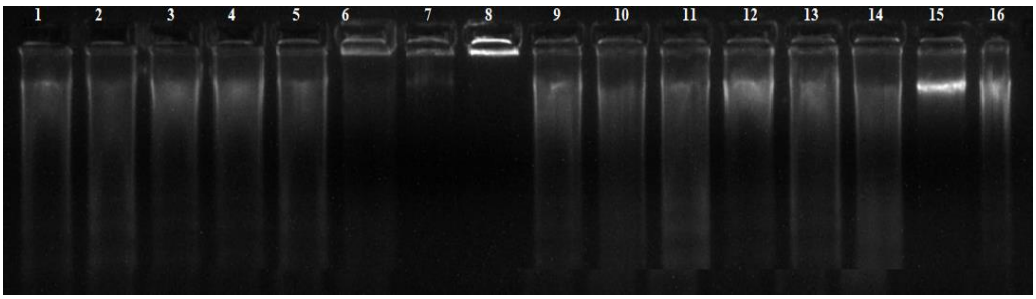

Figure 5. Agarose gel electrophoresis of S1, S2 samples. Ingredients of lines. Line1,5, 9,13: CT-DNA (2mg/mL) in buffer (pH=7), Line2-4: CT-DNA (2-0.5mg/mL) +buffer+sample S1 (%3), Line 14-16: CT-DNA (2-0.5mg/mL)+ buffer+sample S2 (%3)

The electrophoretic bands were assessed relative to the brightness and quenching of the control lanes containing CT-DNA alone (lanes 1, 5, 9, and 13). No DNA binding or interaction was observed at any concentration for sample S1. In contrast, sample S2 exhibited interaction with CT-DNA at the concentration of 1 mg/mL, indicating partial binding under these conditions.

4.4. Result of the DNA Cleavage Experiment of Apple (S1), Linden (S2) Samples

As shown in Figure 6(a–b), partial DNA cleavage was observed in lanes 1 and 5, which was attributed to the effect of water on pBR322 DNA. In the remaining lanes containing the nanoparticle samples, a reduction in the degree of DNA separation was detected. Since this phenomenon was observed in both samples, the overall DNA cleavage activity of the ZnO NPs was determined to be weak.

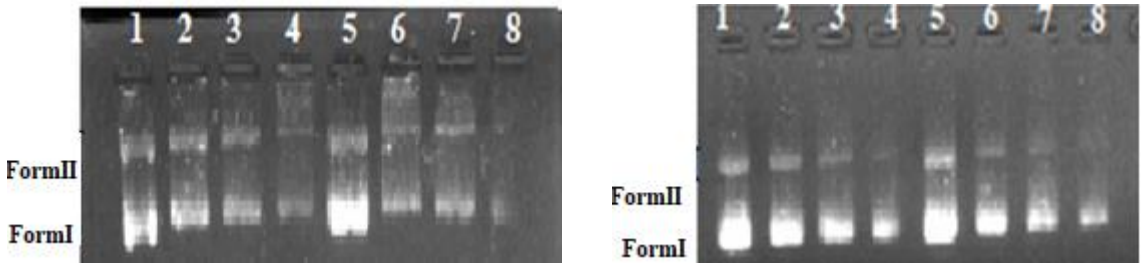

(a) **(b)**

Figure 6. Agarose gel electrophoresis of S1, S2 samples. Ingredients of lines **(a)**: Line1,5: pBR322DNA in dw, Line2-4: pBR322DNA in dw+ sample S1 (%3-%0.75), **(b)** Line1,5: pBR322DNA in dw, Line6-8: pBR322DNA in dw+ sample S2 (%3-%0.75)

4.5. Result of Human Topoisomerase -I Experiment of Apple (S1), Linden (S2) Samples

As shown in Figure 7, lane 1 demonstrates that the topoisomerase enzyme is active, as it successfully relaxes supercoiled DNA. In contrast, lane 5, containing irinotecan as a positive control, shows no relaxation, thereby confirming its inhibitory effect. In lanes 6 and 7, corresponding to sample S1, the inhibition of topoisomerase activity is evident, as DNA relaxation and the formation of Form II are prevented. Conversely, in lanes 12 and 13, partial DNA relaxation is observed for sample S2, indicating that it does not exhibit strong inhibitory activity. These results suggest that only sample S1 has the potential to act as an effective human topoisomerase I inhibitor, while sample S2 does not demonstrate significant inhibitory properties.

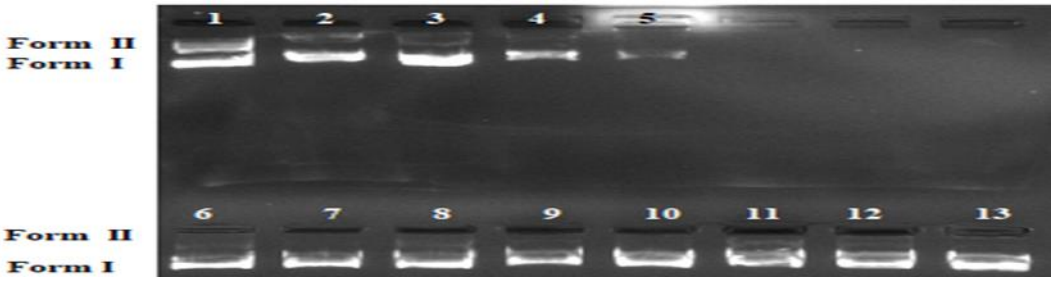

Figure 7. The inhibitory effects against the S1 and S2 samples. Lane 1: pBR322DNA +1 Unit Topo-I; Lane 2: pBR322DNA in buffer (TGS); Lane 3: pBR322DNA st human topoisomerase I of Control; Lane 4: pBR322DNA + 1 Unit Topo I + buffer (TGS); Lane 5: pBR322DNA + 1 Unit Topo I + buffer (TGS)+ irinotecan (3%); Line 6-7: pBR322DNA + 1 Unit Topo I + buffer (TGS)+ S1 (3-1.5%); Lane 12-13: pBR322DNA + 1 Unit Topo I + buffer (TGS)+ S2 (3-1.5%)

4.6. Antimicrobial Activity Results of Apple (S1), Linden (S2) Samples

4.6.1. Agar Diffusion Method

Zinc oxide nanoparticles synthesized from the extracts of two plant sources were dissolved in dimethylformamide (DMF). Their antimicrobial activity was evaluated against two kinds of Gram-positive bacteria, such as Staphylococcus epidermidis ATCC 12228, Bacillus cereus NRRL B-3008, and two kinds of

Gram-negative bacteria, such as Escherichia coli ATCC 25922 and Klebsiella pneumoniae ATCC 13883. Antimicrobial effects were assessed using the agar well diffusion method at a concentration of 100 ppm.

The results demonstrated that ZnO NPs (S1 and S2), synthesized by the green synthesis (biomethod) from apple and linden extracts, had inhibitory activity against all four bacterial strains. Detailed results of the inhibition zone diameters are presented in Table 3.

Table 3. Antimicrobial effects of ZnO NPs synthesized from different plants

Microorganisms	S1 Sample	S2 Sample
Bacillus cereus	18mm	16mm
Escherichia coli	17mm	20mm
Klebsiella pneumonia	16mm	21mm
Staphylococcus epidermidis	12mm	16mm

**The inhibition zones include a hole diameter of 6 mm*

It was observed that the ZnO NPs synthesized from linden extract (Sample S2) exhibited the strongest antimicrobial effect, with the largest inhibition zone diameter (21 mm) recorded against *Klebsiella pneumoniae.*

4.6.2. Images of Individual Inhibition Zones of Samples in a Petri Dish

These findings indicate that the antimicrobial activity of zinc oxide nanoparticles (ZnO NPs) synthesized from different plant sources varies in effectiveness against different microorganisms. The corresponding results are presented in Figure 8(a–d).

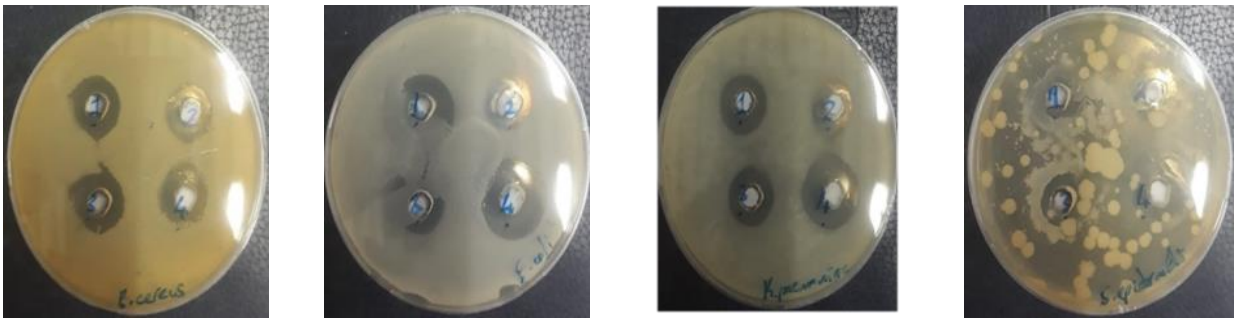

(a) **(b)** **(c)** **(d)**

Figure 8. Observation of the antimicrobial effect of ZnO NPs obtained from two different plant samples (S1, S2 in well 2,3) on **(a)** *B. cereus*, **(b)** *E. coli*, **(c)** *K. pneumonia*, **(d)** *S. epidermidis*

For *Bacillus cereus*, the inhibition zone decreased from 18 mm in sample S1 to 16 mm in sample S2, suggesting a slight reduction in antimicrobial activity of the ZnO NPs synthesized from linden compared to those from apple. In the case of *Escherichia coli*, the inhibition zone increased from 17 mm in S1 to 20 mm in S2, indicating that the ZnO NPs derived from linden extract exhibited stronger antimicrobial activity against *E. coli* than those obtained from apple extract. For *Klebsiella pneumoniae*, the inhibition zone expanded markedly from 16 mm in S1 to 21 mm in S2, demonstrating a significant enhancement of antimicrobial efficacy in the linden-derived ZnO NPs. Similarly, against *Staphylococcus epidermidis*, the inhibition zone increased from 12 mm in S1 to 16 mm in S2, suggesting improved antimicrobial activity of the linden-derived ZnO NPs compared to the apple-derived counterparts.

Overall, these findings suggest that zinc oxide nanoparticles synthesized from different plant sources. Those derived from linden extract (Sample S2) generally exhibit stronger antimicrobial activity against the tested microorganisms compared to the apple-derived sample (S1). However, the extent of this enhancement varies depending on the specific microorganism.

The investigation of the antimicrobial effects of zinc oxide nanoparticles synthesized from different plant sources has produced noteworthy findings. The comparison between the two samples, S1 and S2, offers valuable insights into the influence of plant-derived precursors on the antimicrobial efficacy of ZnO NPs. Variations in inhibition zone sizes clearly indicate differences in biological activity depending on the source of synthesis. For example, *Bacillus cereus* exhibited a reduction in inhibition zone size from 18 mm in S1 to 16 mm in S2, suggesting a slight decrease in effectiveness when the NPs were synthesized from linden extract. In contrast, both *Escherichia coli* and *Klebsiella pneumoniae* displayed significant increases in inhibition zone diameters in S2 compared to S1, indicating enhanced antimicrobial activity of linden-derived ZnO NPs. Similarly, *Staphylococcus epidermidis* showed an increase from 12 mm to 16 mm, suggesting improved efficacy against this Gram-positive bacterium in the S2 sample.

Collectively, these results demonstrate that the antimicrobial potential of ZnO NPs is influenced by the choice of plant extract used in green synthesis. While certain microorganisms exhibited reduced sensitivity, others showed markedly enhanced susceptibility, highlighting the importance of plant source selection in tailoring the biological activity of ZnO NPs.

The plants used in ZnO NP synthesis contain flavonoids and phytochemicals, most notably the yellow pigment quercetin. While pure ZnO is characteristically white, these phytochemicals impart a slightly yellow hue to the reaction mixture. Because the phytochemicals are present only in trace amounts, ZnO remains the dominant component. Importantly, it is nearly impossible to synthesize 100% pure nano-ZnO from different plant extracts, as the resulting product inevitably contains residual biomolecules from the extract. Consequently, the biological activity, such as antimicrobial efficacy, varies, as the final product is effectively a mixture named biomass.

The composition of the plant extract used for synthesis, therefore, plays a critical role, as it determines the nature of residual biomolecules that interact with bacteria. Variations in pH, organic constituents, and molecular structures across different plant sources influence these interactions, ultimately leading to differences in the antibacterial activity of ZnO NPs synthesized from apple (S1) and linden (S2) extracts.

5. Conclusion

In conclusion, it was not possible to obtain fully pure ZnO nanoparticles using the environmentally friendly, chemical-free green synthesis approach applied in this study. Instead, the process yielded a mixture of nano ZnO and biomass powder containing varying phytochemical components, depending on the plant source. This compositional variation accounts for the differences in the biological activities observed.

The biomass obtained from *Malus domestica* (apple) demonstrated topoisomerase inhibition, thereby suppressing replication enzyme activity and indicating its potential as an anticancer agent. In contrast, the biomass derived from linden exhibited notable interactions with DNA and bacteria, suggesting significant antibacterial activity and highlighting its potential as a therapeutic agent. Overall, the findings of this study contribute valuable insights into the development of novel antimicrobial agents and enzyme inhibitors, with promising applications in health and biotechnology.

Author Contributions

All the authors equally contributed to this work. They all read and approved the final version of the paper.

Conflict of Interest

All the authors declare no conflict of interest.

Ethical Review and Approval

No approval from the Board of Ethics is required.

Acknowledgment

XRD, SEM, and FTIR analyses in this study were carried out at the Erciyes University Technology Research Application Center. This study was supported by the project numbered TSA-2022-1066 submitted to the Kayseri University Scientific Research Projects Coordination Unit. We would like to thank the Proofreading & Editing Office of the Dean for Research at Erciyes University for the copy editing and proofreading service for this manuscript.

References

[1] H. Agarwal, S. Venkat Kumar, S. Rajeshkumar, *A review on green synthesis of zinc oxide nanoparticles – An eco-friendly approach*, Resource-Efficiency and Technologies 3 (4) (2017) 406–413.

[2] R. Prasad, A. Bhattacharyya, Q. D. Nguyen, *Nanotechnology in sustainable agriculture: Recent developments, challenges, and perspectives*, Frontiers in Microbiology 8 (2017) 1014.

[3] C. O. Dimkpa, P. S. Bindraban, *Fortification of micronutrients for efficient agronomic production: a review*, Journal of Agricultural and Food Chemistry 36 (2016) 7.

[4] G. Marslin, K. Siram, Q. Maqbool, R. K. Selvakesavan, D. Kruszka, P. Kachlicki, G. Franklin, *Secondary metabolites in the green synthesis of metallic nanoparticles*, Materials 11 (6) (2018) 940.

[5] S. Gunalan, R. Sivaraj, V. Rajendran, *Green synthesized ZnO nanoparticles against bacterial and fungal pathogens*, Progress in Natural Science: Materials International 22 (6) (2012) 693–700.

[6] N. Bala, S. Saha, M. Chakraborty, M. Maiti, S. Das, R. Basu, P. Nandy, *Green synthesis of zinc oxide nanoparticles using Hibiscus subdariffa leaf extract: effect of temperature on synthesis, anti-bacterial activity and anti-diabetic activity*, Royal Society of Chemistry Advances 5 (7) (2015) 4993-5003.

[7] A. A. Zahir, A. A. Rahuman, *Evaluation of different extracts and synthesised silver nanoparticles from leaves of Euphorbia prostrata against Haemaphysalis bispinosa and Hippobosca maculata*, Veterinary Parasitology 187 (3-4) (2012) 511–520.

[8] K. Gudikandula, S. Charya Maringanti, *Synthesis of silver nanoparticles by chemical and biological methods and their antimicrobial properties*, Journal of Experimental Nanoscience 11 (9) (2016) 714–721.

[9] S. Kunjiappan, R. Chowdhury, C. Bhattacharjee, *A green chemistry approach for the synthesis and characterization of bioactive gold nanoparticles using Azolla microphylla methanol extract*, Frontiers of Materials Science 8 (2014) 123–135.

[10] M. Gomathi, P. V. Rajkumar, A. Prakasam, K. Ravichandran, *Green synthesis of silver nanoparticles using Datura stramonium leaf extract and assessment of their antibacterial activity*, Resource Efficiency and Technologies 3 (2017) 280–284.

[11] G. Bagherzade, M. M. Tavakoli, M. H. Namae, *Green synthesis of silver nanoparticles using aqueous extract of saffron (Crocus sativus L.) wastages and its antibacterial activity against six bacteria*, Asian Pacific Journal of Tropical Biomedicine 7 (3) (2017) 227–233.

[12] M. Yasir, J. Singh, M. K. Tripathi, P. Singh, R. Shrivastava, *Green Synthesis of Silver Nanoparticles Using Leaf Extract of Common Arrowhead Houseplant and Its Anticandidal Activity*, Pharmacognosy Magazine 13 (Suppl 4) (2018) 840–844.

[13] S. Swain, S. K. Barik, T. Behera, S. K. Nayak, S. K. Sahoo, S. S. Mishra, P. Swain, *Green Synthesis of Gold Nanoparticles Using Root and Leaf Extracts of Vetiveria zizanioides and Cannabis sativa and its Antifungal Activities*, BioNanoScience 6 (2016) 205–213.

[14] B. Kumar, K. Smita, L. Cumbal, A. Debut, *Green synthesis of silver nanoparticles using Andean blackberry fruit extract*, Saudi Journal of Biological Sciences 24 (1) (2017) 45–50.

[15] N. Nazar, I. Bibi, S. Kamal, M. Iqbal, S. Nouren, K. Jilani, M. Umair, S. Ata, *Cu nanoparticles synthesis using biological molecule of P. granatum seeds extract as reducing and capping agent: Growth mechanism and photo-catalytic activity*, International Journal of Biological Macromolecules 106 (2018) 1203–1210.

[16] K. Cheirmadurai, S. R. Murali, P. Thanikaivelan, *Green synthesis of copper nanoparticles and conducting nanobiocomposites using plant and animal sources*, Royal Society of Chemistry Advances 4 (2014) 19507–19511.

[17] M. Nasrollahzadeh, S. Mohammad Sajadi, *Pd nanoparticles synthesized in situ with the use of Euphorbia granulate leaf extract: Catalytic properties of the resulting particles*, Journal of Colloid and Interface Science 462 (2016) 243–251.

[18] M. Nasrollahzadeh, S. M. Sajadi, M. Maham, *Green synthesis of palladium nanoparticles using Hippophae rhamnoides Linn leaf extract and their catalytic activity for the Suzuki–Miyaura coupling in water*, Journal of Molecular Catalysis A: Chemical 396 (2015) 297–303.

[19] B. Zheng, T. Kong, X. Jing, T. Odoom-Wubah, X. Li, D. Sun, F. Lu, Y. Zheng, J. Huang, Q. Li, *Plant-mediated synthesis of platinum nanoparticles and its bioreductive mechanism*, Journal of Colloid and Interface Science 396 (2013) 138–145.

[20] D. Suresh, P.C. Nethravathi, Udayabhanu, H. Rajanaika, H. Nagabhushana, S. C. Sharma, *Green synthesis of multifunctional zinc oxide (ZnO) nanoparticles using Cassia fistula plant extract and their photodegradative, antioxidant and antibacterial activities*, Materials Science in Semiconductor Processing 31 (2015) 446–454.

[21] K. Elumalai, S. Velmurugan, *Green synthesis, characterization, and antimicrobial activity of zinc oxide nanoparticles from the leaf extract of Azadirachta indica (L.)*, Applied Surface Science 345 (2015) 329–336.

[22] R. Dobrucka, J. Dlugaszewska, *Biosynthesis and antibacterial activity of ZnO nanoparticles using Trifolium pratense flower extract*, Saudi Journal of Biological Sciences 23 (4) (2016) 517–523.

[23] M. Anbuvannan, M. Ramesh, G. Viruthagiri, N. Shanmugam, N. Kannadasan, *Anisochilus carnosus leaf extract mediated synthesis of zinc oxide nanoparticles for antibacterial and photocatalytic activities*, Materials Science in Semiconductor Processing 39 (2015) 621–628.

[24] P. C. Nagajyothi, T. V. M. Sreekanth, C. O. Tettey, Y. I. Jun, S. H. Mook, *Characterization, antibacterial, antioxidant, and cytotoxic activities of ZnO nanoparticles using Coptidis Rhizoma*, Bioorganic & Medicinal Chemistry Letters 24 (17) (2014) 4298–4303.

[25] V. V. Gawade, N. L. Gavade, H. M. Shinde, S. B. Babar, A. N. Kadam, K. M. Garadkar, *Green synthesis of ZnO nanoparticles by using Calotropis procera leaves for the photodegradation of methyl orange*, Journal of Materials Science: Materials in Electronics 28 (2017) 14033–14039.

[26] P. Rajiv, S. Rajeshwari, R. Venckatesh, Bio-Fabrication of zinc oxide nanoparticles using leaf extract of Parthenium hysterophorus L. and its size-dependent antifungal activity against plant fungal pathogens, Spectrochimica Acta Part A: Molecular and Biomolecular Spectroscopy 112 (2013) 384–387.

[27] A. Raza, X. Xu, L. Xia, C. Xia, J. Tang, Z. Ouyang, *Quercetin-iron complex: synthesis, characterization, antioxidant, DNA binding, DNA cleavage, and antibacterial activity studies*, Journal of Fluorescence 26 (2016) 2023–2031.

[28] M. Tan, J. Zhu, Y. Pan, Z. Chen, H. Liang, H. Liu, H. Wang, *Synthesis, Cytotoxic Activity, and DNA Binding Properties of Copper (II) Complexes with Hesperetin*, Naringenin, and Apigenin, Bioinorganic Chemistry and Applications 2009 (1) (2009) 347872.

[29] G. Marslin, R. K. Selvakesavan, G. Franklin, B. Sarmento, A. C. P. Dias, *Antimicrobial activity of cream incorporated with silver nanoparticles biosynthesized from Withania somnifera*, International Journal of Nanomedicine 10 (1) (2015) 5955–5963.

[30] S. Jain, M. S. Mehata, *Medicinal Plant Leaf Extract and Pure Flavonoid Mediated Green Synthesis of Silver Nanoparticles and their Enhanced Antibacterial Property*, Scientific Reports 7 (2017) 15867.

[31] G. Krishnan, J. Subramaniyan, P. C. Subramani, B. Muralidharan, D. Thiruvengadam, *Hesperetin conjugated PEGylated gold nanoparticles exploring the potential role in anti-inflammation and anti-proliferation during diethylnitrosamine-induced hepatocarcinogenesis in rats*, Asian Journal of Pharmaceutical Sciences 12 (5) (2017) 442–455.

[32] B. Zhao, X. Cao, R. De La Torre-Roche, C. Tan, T. Yang, J. C. White, H. Xiao, B. Xing, L. He, *A green, facile, and rapid method for microextraction and Raman detection of titanium dioxide nanoparticles from milk powder*, Royal Society of Chemistry Advances 7 (35) (2017) 21380–21388.

[33] D. Xiao, C. Zhang, D. Yuan, J. He, J. Wu, K. Zhang, R. Lin, H. He, *Magnetic solid-phase extraction based on Fe3O4 nanoparticle retrieval of chitosan for the determination of flavonoids in biological samples coupled with high performance liquid chromatography*, Royal Society of Chemistry Advances 4 (110) (2014) 64843–64854.

[34] E. Abbasi, M. Milani, S. F. Aval, M. Kouhi, A. Akbarzadeh, H. T. Nasrabadi, P. Nikasa, S. W. Joo, Y. Hanifehpour, K. Nejati-Koshki, M. Samiei, *Silver nanoparticles: Synthesis methods, bio-applications and properties*, Critical Reviews in Microbiology 42 (2) (2016) 173–180.

[35] B. Kumar, K. Smita, L. Cumbal, A. Debut, *Green Approach for Fabrication and Applications of Zinc Oxide Nanoparticles*, Bioinorganic Chemistry and Applications 2014 (1) (2014) 523869.

[36] M. A. Hossain, S. Islam, *Synthesis of carbon nanoparticles from kerosene and their characterization by SEM/EDX, XRD and FTIR*, American Journal of Nanoscience and Nanotechnology 1(2) (2013) 52-56.

[37] M. N. S. Abdelaziz, M. G. Zayda, A. T. Maung, M. El-Telbany, T. N. Mohammadi, S. Z. C. Lwin, K. Z. Linn, C. Wang, L. Yuan, Y. Masuda, K. Honjoh, T. Miyamoto, *Genetic characterization, antibiotic resistance, and virulence genes profiling of Bacillus cereus strains from various foods in Japan*, Antibiotics 13(8) (2024) 774.

[38] S. Z. Öner, İ. Kaleli, M. Demir, A. Çalışkan, E. Mete, H. Şenol, *Gram-negative bacilli isolated from blood cultures and antimicrobial resistance*, Journal of the Turkish Microbiology Society 54(4) (2024) 274-281.

[39] R. Abbas, M. Chakkour, H. Z. E. Dine, E. F. Obaseki, S. T. Obeid, A. Jezzini, G. Ghssein, Z. Ezzeddine, *General overview of Klebsiella pneumonia: epidemiology and the role of siderophores in its pathogenicity*, Biology 13(2) (2024) 78.

[40] M. Moradinezhad, E. A. Montazeri, A. H. Ashtiani, R. Pourlotfi, V. Rakhshan, *Biofilm formation of Streptococcus mutans, Streptococcus sanguinis, Staphylococcus epidermidis, Staphylococcus aureus, Lactobacillus casei, and Candida Albicans on 5 thermoform and 3D printed orthodontic clear aligner and retainer materials at 3 time points: an in vitro study*, BMC Oral Health 24(1) (2024) 1107.

[41] A. M. Abu-Dief, R. M. El-Khatib, T. El-Dabea, M. Feizi-Dehnayebi, I. O. Barnawi, A. H. Alsehli, K. Al-Ghamdi, M. A. E. A. A. A. El-Remaily, *Design, preparation, physicochemical characterization, structural conformational, biological evaluation, and DNA interaction for some new benzimidazole complexes*, Applied Organometallic Chemistry 38(3) (2024) e7358.

[42] C. Perez, M. Pauli, P. Bazerque, *An antibiotic assay by the agar-well diffusion method*, Acta Biologica et Medica Experimentalis 15 (1990) 113–115.

[43] T. Keleş, B. Barut, A. Özel, Z. Bıyıklıoğlu, *Synthesis of water soluble silicon phthacyanine, naphthalocyanine bearing pyridine groups and investigation of their DNA interaction, topoisomerase inhibition, cytotoxic effects and cell cycle arrest properties*, Dyes and Pigments 164 (2019) 372–383.

[44] J. G. Deng, T. Li, G. Su, Q.-P. Qin, Y. Liu, Y. Gou, *Co(III) complexes based on α-N-heterocyclic thiosemicarbazone ligands: DNA binding, DNA cleavage, and topoisomerase I/II inhibitory activity studies*, Journal of Molecular Structure 1167 (2018) 33–43.

[45] S. Joulaee, M. Mirzaei, A. Hassanpour, H. Safardoust-Hojaghan, A. Khani, *Efficient removal of anionic and cationic dyes from waste water using green ZnO/NiO/graphene quantum dots nano photocatalyst*, Optik 290 (2023) 171324.

[46] C. Tshangana, M. Chabalala, A. Muleja, E. Nxumalo, B. Mamba, *Shape-dependant photocatalytic and antimicrobial activity of ZnO nanostructures when conjugated to graphene quantum dots*, Journal of Environmental Chemical Engineering 8 (4) (2020) 103930.

[47] D. Santana-Camacho, F. A. Barrios-Navarro, A. Moreno-Meza, A. Villegas-Fuentes, A. R. Vilchis-Nestor, P. A. Luque, *Photocatalytic properties of ZnO semiconductor nanoparticles green synthesized employing Ipomoea stans leave extracts*, Ceramics International: Part C 50 (21) (2024) 44426–44439.

[48] G. Marslin, R. K. Selvakesavan, G. Franklin, B. Sarmento, A. C. Dias, *Antimicrobial activity of cream incorporated with silver nanoparticles biosynthesized from Withania somnifera*, International Journal of Nanomedicine 10 (1) (2015) 5955–5963.

[49] S. Jain, M. S. Mehata, *Medicinal Plant Leaf Extract and Pure Flavonoid Mediated Green Synthesis of Silver Nanoparticles and their Enhanced Antibacterial Property*, Scientific Reports 7 (2017) 15867.

Journal of New Results in Science
dergipark.org.tr/en/pub/jnrs
Open Access

ISSN: 1304-7981 14 (2) (2025) 181-188 doi.org/10.54187/jnrs.1705103

Investigation of Pesticide Residues in Natural Comb Honey from Tokat Province

Yaşar Gülmez[1], Seher Dilek Koçak[2]

Article Info
Received: 23 May 2025
Accepted: 07 Aug 2025
Published: 31 Aug 2025
Research Article

Abstract − Pesticides used in agricultural production pose a threat to bee health and may lead to residue issues in honey. While foraging for food, bees can carry chemicals to the hive from the environment, which may result in pesticide residues in bee products. In this study, 24 samples of natural comb honey collected from beekeepers in various districts of Tokat province, including Almus, Artova, Erbaa, Merkez, Niksar, Reşadiye, Pazar, Turhal, and Zile, were analyzed for 261 different pesticide residues. Natural comb honey samples were preferred to avoid potential pesticide contamination from the foundation comb or beeswax. Pesticide analyses were conducted at the Central Laboratory of Gaziosmanpaşa University in Tokat. In a sample from the Reşadiye district (Re-15), tebuconazole fungicide was detected at 0.025 mg/kg and pirimicarb insecticide at 0.469 mg/kg, both exceeding Maximum Residue Limit (MRL) values. However, all other samples tested had pesticide residues below detectable levels. The results suggest that the natural comb honey produced in Tokat province is safe, and the region is conducive to pesticide-free honey production.

Keywords − *Tokat, natural comb honey, pesticide, residue*

1. Introduction

Pesticides are commonly used in agriculture to control harmful organisms and minimize their impact on crop production. However, these chemicals not only affect the target pests but also have detrimental effects on non-target organisms over a wide area. Pesticides can contaminate groundwater and spread into the atmosphere, posing risks to bees and other pollinators, which are crucial for ecosystem health [1]. Bees and their products are indicators of environmental pollution, reflecting the presence of pesticides in the environment [2, 3, 4]. Pesticides can enter bee colonies through various routes, including contaminated pollen and nectar consumption, contact with treated plants and soil, inhalation during flight, drinking contaminated water, and direct exposure to sprayed pesticides [5,6].

The foraging behavior of honey bees, which involves collecting nectar and pollen from various sources, exposes them to environmental pollutants that can be transported back to the hive [7]. Their long-distance flights in search of food further increase the risk of pesticide exposure. The social structure of bee colonies, with food sharing and close contact among individuals, facilitates the rapid spread of contamination within the colony. Pesticides can harm bees by affecting their behavior, immune system, and ability to reproduce, leading to weakened or collapsed colonies, mainly due to worker bee deaths. Contaminated be products can also pose health risks to humans, causing short-term symptoms like skin and eye irritation, headaches, vomiting, and

[1]e-mail: yasar.gulmez@gop.edu.tr (Corresponding Author); [2] e-mail: seherdilekkocak@gmail.com
[1]Department of Biology, Faculty of Arts and Sciences, Tokat Gaziosmanpaşa University, Tokat, Türkiye
[2]Graduate Education Institute, Tokat Gaziosmanpaşa University, Tokat, Türkiye

long-term health issues such as cancer, diabetes, asthma, Parkinson's disease, and genetic mutations [7,8]. Furthermore, decreasing pollinator populations, including bees, can reduce pollination and lower crop yields.

Various pesticides, including insecticides, fungicides, herbicides, bactericides, and acaricides, have been detected in apiaries [9-11]. The levels of pesticide residues tend to increase from honey to pollen and beeswax [4,12]. Regularly monitoring pesticide levels in honey is crucial for consumer health and guides producers [6]. The maximum allowable pesticide residue limit in honey is 0.01 mg/kg according to the "Turkish Food Codex Honey Communiqué" [13]. Exceeding these limits in bee products can also result in export issues, financial losses, and health problems.

According to the Turkish Food Codex Honey Communiqué, honey produced by bees with their combs without using a foundation comb is defined as “natural comb honey” [13]. Due to its lipophilic nature, Beeswax can accumulate pesticides and absorb volatile chemicals [8]. During the maturation process, honey is stored in beeswax cells, and the combs are reused in honey production in subsequent years, accumulating pesticide residues in old combs [19]. As a result, natural comb honey is considered less risky in terms of pesticide residues compared to other types of honey.

As far as we know, no pesticide analysis has been conducted on natural comb honey yet. The aim of this study is to determine the pesticide contents of natural comb honey produced in Tokat province. The paper is structured as follows: Section 2 provides a brief overview of sample collection and analyses. Section 3 discusses the results and implications, highlighting the issue of pesticide residues in honey in Turkey and the production of pesticide-free honey. Finally, Section 4 concludes the study by summarizing key findings, proposing future research directions, and offering recommendations to beekeepers.

2. Materials

A total of 24 natural comb honey samples were gathered from various districts in Tokat province, including Almus, Artova, Erbaa, Merkez, Niksar, Reşadiye, Pazar, Turhal, and Zile, once from each locality between August 2023 and September 2023 (Table 1). Prior to the honey season, beekeepers in these districts were provided with frames known as 'hoop bee frame' without basic combs. The bees were allowed to fill these frames with honey by constructing beeswax combs within them. Subsequently, the natural comb honey samples from the frames were collected, each weighing approximately 250 g, and stored in sealed jars using the leakage method at room temperature until analysis. The samples were properly labeled and sent to the Tokat Gaziosmanpaşa University Central Laboratory for further testing.

Table 1. Honey sample collection locations and dates in Tokat

Sample district	Sample locality	Proximity to	Sample number	Date
Almus	Almus	5km	Al-01	September 2023
Artova	Artova	11km	Ar-02	September 2023
Artova	Artova	200m	Ar-03	September 2023
Artova	Artova	100m	Ar-04	September 2023
Erbaa	Evciler village	12km	Er-05	September 2023
Erbaa	Karayaka village	8km	Er-06	September 2023
Erbaa	Erbaa	100m	Er-07	September 2023
Niksar	Başçiftlik	50m	Ni-08	September 2023
Niksar	Çamiçi plateau	20km	Ni-09	September 2023
Niksar	Hanyeri village	100m	Ni-10	September 2023
Niksar	Şıhlar village	7km	Ni-11	September 2023
Pazar	Kalaycık village	500m	Pa-12	September 2023
Pazar	Pazar	100m	Pa-13	September 2023
Reşadiye	Karaağaç village	20km	Re-14	September 2023
Reşadiye	Karlıyayla village	2km	Re-15	September 2023
Reşadiye	Özlüce village	25km	Re-16	September 2023

Table 1. (Continue) Honey sample collection locations and dates in Tokat

Sample district	Sample locality	Proximity to	Sample number	Date
Tokat Merkez	Aydoğdu village	8km	To-17	September 2023
Tokat	Tokat	2km	To-18	August 2023
Turhal	Yazıtepe village	10km	Tu-19	August 2023
Turhal	Çivril village	12km	Tu-20	August 2023
Turhal	Turhal	250m	Tu-21	August 2023
Zile	Karakuzu village	100m	Zi-22	August 2023
Zile	Kervansaray village	500m	Zi-23	August 2023
Zile	Ağılcık village	50m	Zi-24	August 2023

3. Methods

In the present study, pesticide residue analyses of honey samples were conducted using the method described for dried fig samples by Yeladı et. al. [15] at Tokat Gaziosmanpaşa University Central Laboratory. A total of 24 honey samples were tested for 261 different pesticide residues. The names of the pesticides screened are listed in Table 2.

Table 2. Pesticides analyzed in the study

2,4-D	Diafenthiuran	Hexaconazole	Pirimicarb
Abamectin	Diazinon	Hexaflumuron	Primiphos -ethyl
Acephate	Dichlofluanid	Hexythiazox	Primiphos -methyl
Acequinocyl	Dichlorfos	Imazalil sulfate	Prochloraz
Acetamiprid	Diclofop -methyl	Imazapyr	Profenefos
Acetochlor	Dicrotophos	Imidacloprid	Profoxydim-lithium
Acrinathrin	Diethofencarb	Indoxacarb	Promecarb
Alachlor	Difenacozole	Iodosulfuron-methyl-sodium	Prometryn
Aldicarb	Diflubenzuran	Ioxynil	Propaquizafob
Aldicarb-sulfone	Dimethenamid	Isocarbofos	Propargite
Aldicarb-sulfoxide	Dimethoate	Kresoxim Methyl	Propazine
Ametoctradin	Dimethomorph	Lenacil	Propiconazole
Amitraz	Diniconazole	Linuron	Propoxur
Atrazine	Dinocap	Lufenuron	Propyzamide
Azinphos-ethyl	Dioxacarb	Malaoxon	Prothiophos
Azinphos-methyl	Diphenamid	Malathion	Pymetrozine
Azoxystrobin	Diphenylamine	Mandipropamid	Pyraclostrobin
Benalaxyl	Diuron	MCPA	Pyrazophos
Benfuracarb	DMF	Mecarbam	Pyridaben
Benomyl	Dodine	Mepanipyrim	Pyridaphenthion
Bensulfuron-methyl	Emamectin benzoate	Mepanipyrim-hyroxypropyl	Pyridate
Bentazone	EPN	Metaflumizone	Pyrimethani
Bifenazate	Epoxiconazole	Metalaxyl M	Quinalphos
Bitertanol	EPTC	Metamitron	Quizalofop-ethyl
Boscalid	Ethiofencarb	Methacrifos-poz	Rimsulfuron
Bromoxynil	Ethion	Methamidophos	Sethoxydim
Bromuconazole	Ethirimol	Methidathion	Simazine
Buprimate	Etofenprox	Methiocarb	Spinosyn A
Buprofezin	Etoxazole	Methiocarb-sulfone	Spinosyn D
Butralin	Famaxadone	Methiocarb-sulfoxide	Spirodiclofen
Butylate	Fenamidone	Methomyl	Spiromesifen
Cadusafos	Fenamiphos	Methoxyfenozide	Spiroxamine
Carbaryl	Fenamiphos-sulfone	Metolachlor-S	Sulfoxaflor
Carbendazim	Fenamiphos-sulfoxide	Metosulam	Tebuconazole
Carbofuran	Fenarimol	Metrafenone	Tebufenozide
Carbofuran-3-hydroxy	Fenazaquin	Metribuzin	Tebufenpyrad

Table 2. (Continue) Pesticides analyzed in the study

Carbosulfan	Fenbuconazole	Mevinphos	Teflubenzuron
Carboxin	Fenbutatin oxide	Molinate	Tepraloxydim
Carfentrazone-ethyl	Fenhexamide	Monocrotophos	Terbutryn
Chlorantraniliprole	Fenoxycarb	Monolinuron	Terbutylazine
Chlorbufam	Fenoxyprob -ethyl	Myclobutanil	Tetraconazole
Chlorfenvinhos	Fenpropathrin	Novaluron	Tetramethrin
Chlorfluazuron	Fenproxymate	Nuarimol	Thiabendazole
Chloridazon	Fenthion	Omethoate	Thiacloprid
Chlorpyrifos	Fenthion-sulfone	Oxadixyl	Thiamethoxam
Chlorsulfuron	Fenthion-sulfoxide	Oxamyl	Thifensulfuron-
Clethodim	Fipronil	Oxycarboxin	Thiobencarb
Clodinofop-propargyl	Fipronil-sulfone	Oxydemeton-methyl	Thiodicarb
Clofentezine	Fluazifop-p-butyl	Paclobutrazol	Thiophanate-methyl
Clothianidine	Fluazinam	Paraoxon-ethyl	Tolclofos-methyl
Cyantraniliprole	Flubendiamide	Paraoxon-methyl	Tolfenpyrad
Cyazofamid	Fludioxinil	Parathion-ethyl	Tolyfluanid
Cycloate	Flufenoxuron	Penconazole	Tralkoxydim
Cycloxydim	Fluopicolide	Pencycuron	Triadimefon
Cyflufenamid	Fluopyram	Pendimenthalin	Triadimenol
Cyhalothrin	Fluquinconazole	Permethrin	Triasulfuron
Cymoxanil	Fluroxypyr	Phenmedipham	Triazophos
Cypermethrin	Flusilazole	Phenthoate	Tribenuron methyl
Cyproconazole	Flutriafol	Phorate	Trichlorfon
Cyprodinil	Forchlorfenuron	Phorate-sulfone	Trifloxystrobin
Dazomet	Formetanete hydrochloride	Phorate-sulfoxide	Triflumizole
Deltamethrin	Fosthiazate	Phosalone	Triflumuron
Demeton-s-methyl	Furathiocarb	Phosmet	Triticonazole
Demeton-S-methyl-sulfone	Haloxyfop-R-methyl	Phosphamidon	
Desmedipham	Heptenophos	Pirimicarb-Desmethyl	

4. Results and Discussion

In this study, natural comb honey samples taken from beekeepers in nine districts of Tokat province in 2023 were examined for pesticide residues. Natural comb honey samples were chosen to prevent contamination from honey produced in frames with foundation combs or repeatedly used frames, guaranteeing that any pesticide residues detected in the honey samples came from nectar or pollen sources in the environment.

In this study, 24 natural comb honey samples were analyzed for 261 different pesticide residues. According to results, only one sample (Re-15) exceeded the Maximum Residue Limit (MRL) for Pirimicarb and Tebuconazole pesticides (0.469 mg/kg and 0.025 mg/kg, respectively) (Figure 1). The remaining samples had pesticide levels below detectable limits. Despite heavy pesticide use in Tokat province, most of our samples (23 out of 24) were found free of pesticide residues. The detected pesticides, Tebuconazole and Pirimicarb, are moderately harmful to human health according to the World Health Organization [16]. The presence of these chemicals in the honey sample suggests contamination from agricultural pesticides used in the vicinity of the apiary. Our findings are consistent with previous studies that detected pirimicarb in honey samples from Egypt [17] and tebuconazole in honey samples from Italy [18]. These two pesticides have not been detected in the studies conducted so far in Türkiye.

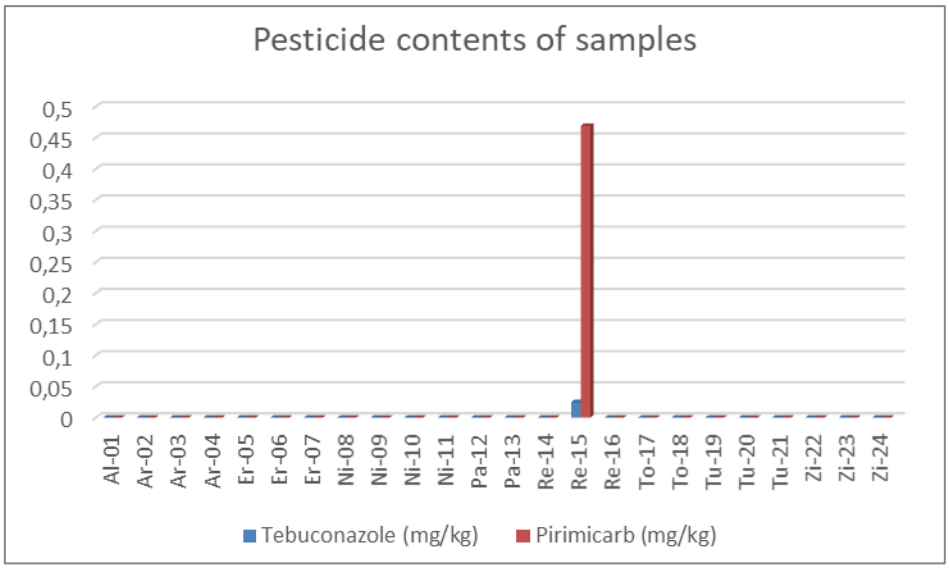

Figure 1. Pesticide contents of honey samples (mg/kg)

The distances of sample collection locations to industrial and agricultural areas are given in Table 1. Out of the samples analyzed, eleven were located in areas at least 5 km away from industrial or agricultural zones where pesticides were not used, while thirteen of them were close to pesticide-use areas. Beekeepers applied pesticides to control hive parasites either before the honey flow season or after harvesting honey. This practice likely explains why no chemical residues from hive treatments were detected in the honey samples analyzed. Furthermore, the natural comb honey samples were free from any contamination of pesticides by beeswax, as they were not produced in frames containing previously used beeswax or foundation comb.

In a study in Tokat province [19], pesticide residues were found in three out of 24 flower honey samples, likely due to in-hive spraying, pesticides, or environmental pollutants. Natural comb honeys have lower pesticide residue risk compared to extracted honeys, with old combs more likely to be contaminated. Nevertheless, additional research is required to investigate the potential transfer of pesticides through beeswax. To make a more relevant comparison, it would be beneficial to analyze natural comb honey and basic/old comb honey from the same hives.

Pesticides carried by bees to hives mainly accumulate in beeswax, with residue levels increasing from honey to pollen and beeswax [4,12]. A study found that honey had lower contamination levels compared to propolis from the same region [20]. Although pesticides in honey were mainly detected at low levels and not considered a health risk, honey serves as a biological indicator of environmental pollution [17, 21]. The study revealed that most honey samples from Tokat province, near agricultural areas, were free of pesticide residues, indicating their suitability for natural honey production. Possible reasons for the absence of residues include pesticide application outside the honey production season, lack of residues on visited plants, or minimal contamination of honey.

Recent studies on pesticide residues in honey in Türkiye have shown that some honeys contain pesticide residues, while others do not. The findings of these studies are briefly discussed below. Pesticides like malathion, ethion, cypermethrin, and deltamethrin were found in seven out of 20 flower honeys tested in Isparta. Diazinon and chlorpyrifos were also detected above the Maximum Residue Limit (MRL). These chemicals are commonly used insecticides in the region for apple and cherry cultivation [22].

Carbendazim, chlorpyrifos, imazalil, metalaxyl, and thiabendazole were found in 20 citrus honeys from various regions in Türkiye, including Antalya, Alanya, Aydın, Bozdoğan, Adana, and Kozan. The levels of imazalil and thiabendazole exceeded the Maximum Residue Limits (MRL) in these samples [23]. Specifically, imazalil was detected at 10.96 ng/g and thiabendazole at 12.11 ng/g, slightly above the MRL values.

In a study conducted in Gümüşhane province, Cyfluthrin, Cypermethrin, Malathion, and Deltamethrin were detected in various flower honeys. Cyfluthrin, Cypermethrin, and Malathion were found in two honey samples, while Deltamethrin was found in four honey samples [24].

As mentioned above, some studies have reported pesticide residues in honeys from Türkiye. On the other hand, no pesticide residues were detected in honey samples collected from the provinces of Adana, Hatay, Mersin, [25], Çanakkale [26], Antalya [27], Muş [28], and Tekirdağ [29].

Health risk assessments indicate that the levels of pesticides in honey are below the acceptable daily intake and pose minimal risk to consumers [17]. However, exposure to multiple chemicals simultaneously can lead to synergistic toxic effects in the body [30]. Therefore, it is crucial for honey production to be pesticide-free and for continuous monitoring of honey quality to ensure food safety.

5. Conclusion

The findings show that Tokat province has suitable conditions for producing pure natural honey. Beekeepers in Tokat province are well-organized through the Tokat Beekeeping Association, following seasonal maintenance schedules, hive treatments, and production practices. The low presence of pesticide residues in the honey samples, except for one, reflects the beekeepers' awareness.

The production of natural comb honey is limited among beekeepers, with many using basic or old combs, which may contain pesticide residues. Encouraging beekeepers to produce natural comb honey or "log hive" honey can reduce the risk of pesticide contamination. Beekeepers should source basic combs from reliable sources, avoid areas with pesticide use, and maintain hygiene in beekeeping practices. Education on producing additive-free honey, especially natural comb honey, is crucial for consumer health and environmental sustainability. Promoting the production of safe honey products is essential. It is recommended to produce safe products and time pesticide applications when bees are less active to protect their health.

Future studies should include the analysis of pollen, bee bread, and beeswax samples for pesticide residues in beehives. Comparing these bee products, particularly those from the same hives, can provide more precise information on the source of pesticide residues.

Author Contributions

The first author wrote and edited the manuscript and interpreted the results. The second author conducted the literature search, collected samples, and wrote the results. This article is based on the second author's master's thesis. Both authors reviewed and approved the final version of the paper.

Conflict of Interest

All the authors declare no conflict of interest.

Ethical Review and Approval

No approval from the Board of Ethics is required.

Acknowledgment

This work was supported by the Office of Scientific Research Projects Coordination at Tokat Gaziosmanpaşa University, Grant number: 2023/40.

References

[1] B. Polat, M. Özüiçli, H. Çetin, L. Aydın, *The effects of pesticide usage on honey bee health and products*, Journal of Research in Veterinary Medicine 39 (2) (2020) 128–134.

[2] Z. Barganska, M. Slebioda, J. Namiesnik, *Honeybees and their products: Bioindicators of environmental contamination*, Critical Reviews in Environmental Science and Technology 46 (3) (2016) 235–248.

[3] S. Girotti, S. Ghini, E. Ferri, L. Bolelli, R. Colombo, G. Serra, C. Porrini, S. Sangiorgi, *Bioindicators and biomonitoring: Honeybees and hive products as pollution impact assessment tools for the Mediterranean area*, Euro-Mediterranean Journal for Environmental Integration 5 (2020) 62.

[4] G. Sonmez Oskay, G. S. Uygur, D. Oskay, N. Arda, *Impact of stress factors internal and external to the hive on honey bees and their reflection on honey bee products: a review*, Journal of Apicultural Research 64 (1) (2023) 226–241.

[5] S. T. O'Neal, T. D. Anderson, J. Y. Wu-Smart, *Interactions between pesticides and pathogen susceptibility in honey bees*, Current Opinion in Insect Science 26 (2018) 57–62

[6] K. Kerkich, B. Bouargane, A. El Laghdach, B. Souhail, Y. Kadmi, *Recent advances in the extraction, purification and analysis of emerging pesticides in honey products: a review*, Journal of Food Composition and Analysis 127 (2024) 105947.

[7] A. Sharma, K. Pant, D. S. Brar, A. Thakur, V. Nanda, *A review on Api-products: current scenario of potential contaminants and their food safety concerns*, Food Control 145 (2023) 109499.

[8] R. Vegh, M. Csoka, M. Zsuzsanna, L. Sipos, *Pesticide residues in bee bread, propolis, beeswax and royal jelly – A review of the literature and dietary risk assessment*, Food and Chemical Toxicology 176 (2023) 113806.

[9] F. Sanchez-Bayo, K. Goka, *Pesticide residues and bees – A risk assessment*, PLoS One 9 (4) (2014) e94482.

[10] F. Sánchez-Bayo, D. Goulson, F. Pennacchio, F. Nazzi, K. Goka, N. Desneux, *Are bee diseases linked to pesticides? — A brief review*, Environment International 89–90 (2016) 7–11.

[11] Y. El-Nahhal, *Pesticide residues in honey and their potential reproductive toxicity*, Science of the Total Environment 741 (2020) 139953.

[12] C. A. Mullin, M. Frazier, J. L. Frazier, S. Ashcraft, R. Simonds, D. Vanengelsdorp, J. S. Pettis, *High levels of miticides and agrochemicals in North American apiaries: implications for honey bee health*, PloS One 5 (3) (2010) e9754.

[13] Official Gazette 31107, Turkish Food Codex Honey Communiqué (2020), https://www.resmigazete.gov.tr/eskiler/2020/04/20200422-13.htm, Accessed 23 May 2025.

[14] M. S. Seğmenoğlu, E. Baydan, *Medicine residues and contaminants found in honey*, Journal of Adana Veterinary Control Institute 2 (2012) 24–28.

[15] A. Yelaldı, K. Kara, T. Balkan, *Investigation of insecticide residues in fig and health rist assessment*, Turkish Journal of Entomology 48 (3) (2024) 319–326.

[16] World Health Organization, The WHO Recommended Classification of Pesticides by Hazard and guidelines to classification, 2019 edition (2020), https://www.who.int/publications/i/item/9789240005662, Accessed 23 May 2025.

[17] F. Eissa, S. El-Sawi, N. E. Zidan, *Determining pesticide residues in honey and their potential risk to consumers*, Pol. J. Environ. Stud. 23 (5) (2014) 1573–1580.

[18] M. Saitta, G. Di Bella, M. R. Fede, V. Lo Turco, A. G. Potortì, R. Rando, M. T. Russo, G. Dugo, *Gas chromatography-tandem mass spectrometry multi-residual analysis of contaminants in Italian honey samples,* Food Addit Contam Part A Chem Anal Control Expo Risk Assess 34 (5) (2017) 800–808.

[19] F. Kara, C. Kaya, E. E. Yücel, S. Topuz, M. Bayram, *Determination of some physicochemical properties of honeys from Tokat region and their compliance with the Turkish food codex,* Uludag Bee Journal 22 (2) (2022) 148–165.

[20] I. Simsek, O. Kuzukiran, B. Yurdakok-Dikmen, U. T. Sireli, M. Beykaya, A. Filazi, *Comparison of selected lipophilic compound residues in honey and propolis,* Journal of Food Composition and Analysis 102 (2021) 104068.

[21] A. M. K. Nassar, Y. M. Salim, E. Nour-Eldeen, M. S. Younis, M. M. Kelany, M. A. Shebl, A. S. Shafey, H. F. Abou-Sharara, *Seasonal screening of pesticide residues in beehive products collected from different districts in Egypt,* Environ Monit Assess 196 (2024) 297.

[22] H. Seçimiş Canbay, S. Öğüt, M. Yılmazer, E. Küçüköner, *Analysis of selected some pesticides in honey samples*, Süleyman Demirel University Journal of Natural and Applied Sciences 16 (1) (2012) 1–5.

[23] İ. Toptancı, A. Bayrak, *Determination of pesticide residue levels in citrus honeys,* Academic Food Journal 10 (3) (2012) 22–25.

[24] Y. Şahin, V. Armağan, A. Yılmaz Aslantürk, *Missing link in environmental policy: Honey bees,* Contemporary Local Governments 32 (2) (2023) 31–54.

[25] C. Muku, G. Güçlü, S. Selli, *Determination of pesticide and naphthalene residues in eastern Mediterranean honey by LC/MS/MS and HS-SPME GC/MS*, Çukurova Journal of Agriculture and Food Sciences 34 (2) (2019) 142–148.

[26] İ. Polat, *The investıgatıon of the antimicrobial, antioxidant activities and the contamination of pesticide and antibiotic residues of some honey produced in South Marmara region*, Master's Thesis Balıkesir University (2011) Balıkesir.

[27] E. Çakar, F. Gürel, *Comparison of liquid and comb honeys for pesticide, naphthalene and antibiotic residues,* Mediterranean Agricultural Sciences 32 (3) (2019) 453–459.

[28] M. A. Kutlu, A. Ş. Bengü, *Determination of antibiotic and pesticide residues and some quality criteria in honey produced in Muş province*, BÜSAD 1 (1) (2020) 1–6.

[29] N. Ozdemir, M.N. Muz, *Neonicotinoid Analysis in Sunflower (Helianthus annuus) Honey samples collected around Tekirdag in Turkey,* International Journal of Analytical Chemistry 2023 (1) (2023) 429449.

[30] S. A. Ashraf, D. Mahmood, A. E. O. Elkhalifa, A. J. Siddiqui, M. I. Khan, F. Ashfaq, M. Patel, M. Snoussi, M. Kieliszek, M. Adnan, *Exposure to pesticide residues in honey and its potential cancer risk assessment,* Food Chem Toxicol 180 (2023) 114014.

Journal of New Results in Science
dergipark.org.tr/en/pub/jnrs
Open Access

ISSN: 1304-7981 14 (2) (2025) 189-200 doi.org/10.54187/jnrs.1707677

Microstructure, Thermal and Mechanical Properties of Novel Nanocrystalline Al-B-Si Alloy

Celal Kurşun[1]

Article Info

Received: 27 May 2025

Accepted: 07 Aug 2025

Published: 31 Aug 2025

Research Article

Abstract − In this study, a nanostructured Al50B45Si5 alloy was produced by the mechanical alloying technique from mixtures of high-purity Al, B, and Si powders. The thermal behavior, structural evolution, and mechanical properties of the powders were examined through X-ray diffraction (XRD), scanning electron microscopy-energy dispersive X-ray (SEM-EDX), differential scanning calorimetry (DSC), differential thermal analysis (DTA), transmission electron microscopy (TEM), and Vickers microhardness measurements. The XRD results revealed that all crystalline peaks belonging to the Al, B, and Si elements disappeared during mechanical alloying and were eventually replaced by peaks from intermetallic phases such as AlB_2, B_4Si, and AlB_{12} in the supersaturated Al(Si) matrix. The crystalline size of the $Al_{50}B_{45}Si_5$ alloy was calculated by the Debye Scherrer equation, and it was determined to be 9.5 nm, consistent with TEM measurements. The microhardness value of the alloy was 219±10 HV, while the hardness increased to 345±9 HV with heat treatment. Therefore, a nanostructured $Al_{50}B_{45}Si_5$ alloy with high hardness, good thermal stability, and homogeneity was favorably synthesized by mechanical alloying for use in industrial applications.

Keywords − *Al alloys, nanocrystalline, microhardness, mechanical alloying, TEM*

1. Introduction

Al and Al-based alloys are ones of the most commonly used materials for many applications in the world because of their properties which are low density and thus lightweight, high strength, easy processing, excellent formability, very good corrosion resistance, thermal and electrical conductivity [1-8] Due to their perfect properties and applications in industry, new Al-based alloys have been continuously researched especially metastable materials which are amorphous, nanocrystalline and quasicrystalline. It is well known that the metastable alloys have exposed superior mechanical features, great electrical and thermal conductivities, and good corrosion resistance compared with crystalline materials. However, synthesis of these alloys is not easy owing to the low melting point of the Al element, specifically for alloys that consist of components with high melting points.

Al-based alloys can be manufactured by many methods: physical vapor deposition, conventional solidification, rapid solidification, suction casting, and mechanical alloying [2,4,5]. However, the mechanical alloying technique is the only one that differs among them because of the production of high-quality powders by well-controlled microstructures and morphologies [9,10]. In this technique, it is very easy to produce nanostructured materials. Moreover, it is not necessary to melt constituents of the alloy systems. It is a solid-solid reaction

[1]celalkursun@ksu.edu.tr (Corresponding Author)
[1]Department of Physics, Faculty of Science, Kahramanmaras Sutcu Imam University, Kahramanmaras, Türkiye

without any melting processes. This technique also has a very good advantage by comparison with other techniques, especially related to elements of low melting point. As an example, the Al element has a low melting point (660 ˚C); however, the melting temperature of B is 2075 ˚C, extremely high compared with that of Al. In the alloy production process, it is probable that Al will be evaporated at the melting point of B or a higher temperature.

In the present study, for the first time, a new nanocrystalline $Al_{50}B_{45}Si_5$ alloy was produced in powder form by the mechanical alloying technique. The mechanical and thermal properties, phase structure, and crystallite size of the alloy were characterized to understand the nature of Al-B-Si alloy systems. Al-Si, Al-Nb, Al-Ce binary alloys [11,12,13], and Al–Mg–Si, Al-Zn-Mg, Al–Ti–B ternary alloys [14,15,16] were studied before. However, Al-B-Si alloys, which are constituents of the lowest density elements used commonly in the industry, need to be studied to be used effectively in many applications. Therefore, it is expected that the $Al_{50}B_{45}Si_5$ alloy might be a guide to both researchers and industry for work in the future.

The rest of this work is categorized as mentioned below: Section 2 provides the properties of the powders, like purities, composition ratios, and the information of the instrument used in the alloy production process. Section 3 presents microstructural evaluation, crystallite size evaluation, thermal behavior, and microhardness evaluation of the Al-B-Si alloy. Section 4 mentions the results of the analysis by summarizing.

2. Materials and Methods

Ternary Al–B–Si powders with the determined composition of $Al_{50}B_{45}Si_5$ (at. %) were mechanically alloyed under argon (Ar) atmosphere in planetary ball mills. The production process was carried out by Fritsch Pulverisette 5. Alloy components of Al (99.9%), B (99.8%), and Si (99.7%) were exactly weighted according to the planned alloy system. The whole powder using stainless steel balls was loaded into a stainless-steel cup, 125 ml under Ar. For the mechanical alloying (MA) process, it was carried out at room temperature at a speed of 300 rotations per minute by a ball-to-powder ratio of 5:1. The MA process went on for 100 h; however, this process was discontinued for 20 minutes to chill the vials after each 20 minutes of ball milling.

The crystallite size change during mechanical milling (MM), and also depending on this, phase transformation of the alloying process was characterized by X-ray diffraction (XRD) analysis using a diffractometer with Copper K_α radiation (wavelength = 1.54 Å) at 40 kV and 30 milliampere. To analyze the morphology of the Al-B-Si powder alloy, scanning electron microscopy-energy dispersive X-ray (SEM-EDX) analysis was used with a JEOL-JCM-5000 scanning electron microscope at an acceleration voltage of 10 kilovolts. To produce the transmission electron microscopy (TEM) material, a drop of powder alloy solution (0.05 mg/mL) containing 1 wt.% of phosphotungstic acid was deposited onto a 200 mesh Cu-grid covered by carbon (C), then it was dried at room temperature. The TEM investigation was done by a Philips CM-20, performing at an acceleration voltage of 200 kilovolts.

The thermal behavior of the alloy at different stages of alloying was analyzed by differential scanning calorimetry (DSC) using a Perkin-Elmer's Sapphire DSC-7 at a constant heating rate of 20 °C from 250 °C to 675 °C. In addition to DSC for thermal analysis, differential thermal analysis (DTA), Perkin-Elmer's Diamond TG/DTA, was performed at a constant heating rate of 20 °C from 200 °C to 1100 °C at different stages of milling under a flowing argon atmosphere. After production processes with mechanical milling, $Al_{50}B_{45}Si_5$ alloy was heated by the heating rate of 30 °C min^{-1} from room temperature to 500 °C, 800 °C, and 1000 °C, where the alloy was annealed for 1 h in a furnace separately for each temperature under Ar atmosphere. To measure the microhardness of the alloy, powders were pressed into the cylindrical mold for five minutes. Then, the pressed alloy was put into the other mold, which was used to obtain a holder for polishing, and liquid bakelite was molded into the mold. The mold with the sample, after solidification of liquid bakelite, was polished, and therefore, the alloy was prepared for microhardness measurement. The microhardness

measurement, Vickers of the alloy, was carried out with Shimadzu HMV 2, performing an applied load of 0.98 N by a dwell time of 10 seconds at 5 different spots.

3. Results and Discussions

3.1. Microstructural Evaluation

The phase transformation of $Al_{50}B_{45}Si_5$ powders was investigated by XRD. The XRD patterns of $Al_{50}B_{45}Si_5$ alloy are shown in Figure 1. According to Figure 1, the powder alloy exhibits certain behaviors throughout MA owing to the movement of curving lines, the rise of peak enlargement, and the loss of diffraction lines of solute. The reasons for these behaviors are severe deformation, recurrent fractures, and following cold welding. The peaks of Al, B, and Si elements of the pure crystal are exhibited in the XRD pattern of unmilled powder (0h of milling). These diffraction peaks can still be clearly seen for 10h of milling time, while the peak intensities and broadening of the sharp Al, B, and Si peaks are decreasing. After 20h of milling time, the peaks of Al, B, and Si were missing due to the formation of a nanostructured solid solution [7]. At this stage, the α-Al (Si) solid solution phase was obtained by dissolving Si into Al. With increasing milling time to 50 h, the new phases, such as AlB_2 and B_4Si, occurred, and they were marked by symbols from Figure 1. The AlB_2 phase transformed into the AlB_{12} intermetallic phase after 100 h of milling time. Similar transformation in the mechanical alloying system was also detected in the earlier studies [17-19]. As can be seen in Figure 1, 50 h of alloying followed by at least 100 h of alloying is required for the formation of the nanocrystalline structure and the AlB_2, B_4Si, and AlB_{12} phases. In other words, it is not possible to obtain the relevant phases with less than 100 h of alloying.

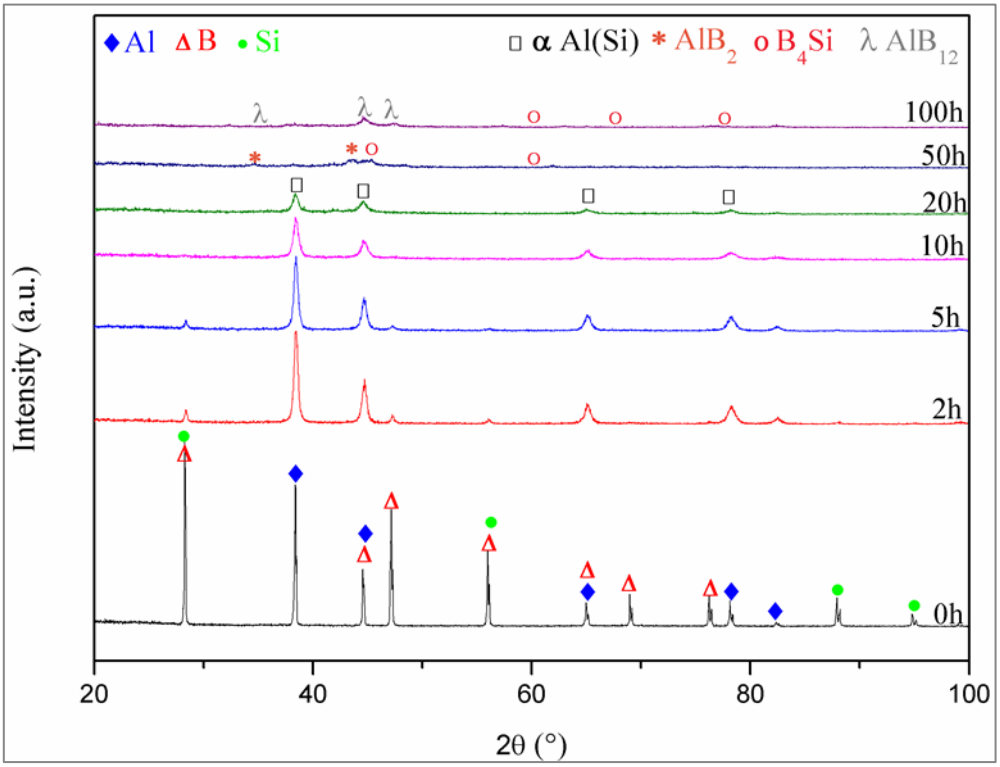

Figure 1. XRD traces of $Al_{50}B_{45}Si_5$ alloy as a function of MA time

The morphological changes of $Al_{50}B_{45}Si_5$ powder were investigated by SEM. Figure 2 demonstrates the images of the powders during mechanical alloying. As seen in Figure 2, the morphology and particle sizes of the powders, which have different shapes and sizes in the initial (in Figure 2a), changed owing to the cold welding and fracturing of the particles with increasing milling time. After 20 h of milling time (in Figure 2b), the particle size of the powder increased because of the cold welding. As shown in Figure 2c, with further milling

time, the particle size of the powders decreased by fracturing, and this stage is also the step of obtaining new phases such as AlB2 and B4Si, which were defined by XRD. The powder of alloy became smaller with a spherical shape and uniform after 100 h of milling time (in Figure 2d). The powder particles of the alloy are approximately 2 μm, and the homogeneity is so high when the final stage is reached.

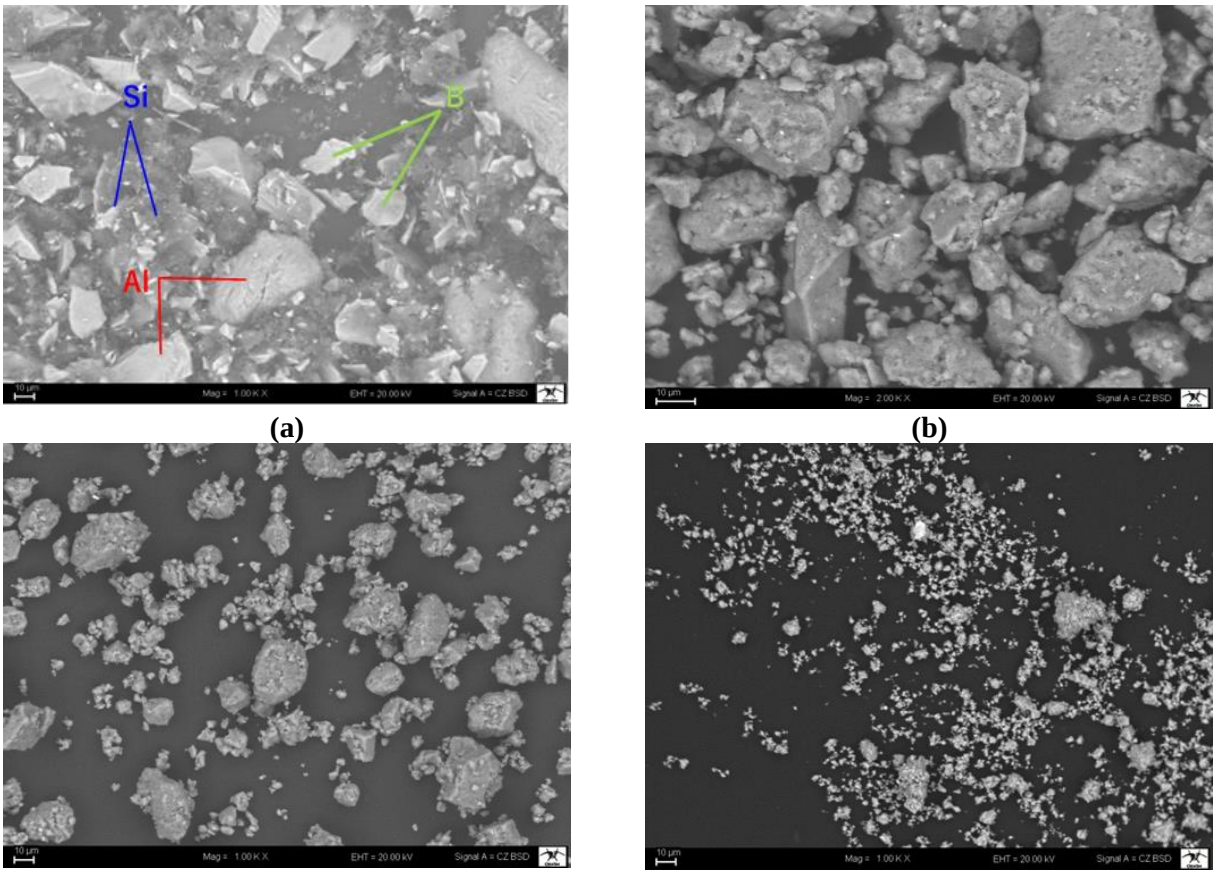

Figure 2. SEM images of the $Al_{50}B_{45}Si_5$ alloy as a function of the milling time
(a) 0h, **(b)** 20h, **(c)** 50h, **(d)** 100 h

The production of $Al_{50}B_{45}Si_5$ alloy by mechanical alloying is exhibited by a schematic drawing in Figure 3. The pure powders of Al, B, and Si elements in a container, stainless-steel stay between steel balls, as seen in Figure 3. The steel balls collide with both the powders and each other because of the opposite direction of the steel cups and the planetary disk. Due to the colliding balls, the Al, B, and Si powders are diffused into each other. Afterwards, the structures of the powder subjected to the steel ball collisions change during milling operations. These operations are also schematized in Figure 4. As seen in Figure 4, the Al, B, and Si powders have certain particle sizes and shapes at 0h of milling time. The particle sizes and the shapes of the powders start to change by diffusing into each other, owing to cold welding and fracturing of the powders after 2h of milling. These changes continue with further milling time (20h and 50h). It might be clearly perceived that, after 100 h of milling time, the particles of the Al-B-Si alloy become smaller and they have spherical shapes. The powders also have the highest homogeneity in this stage.

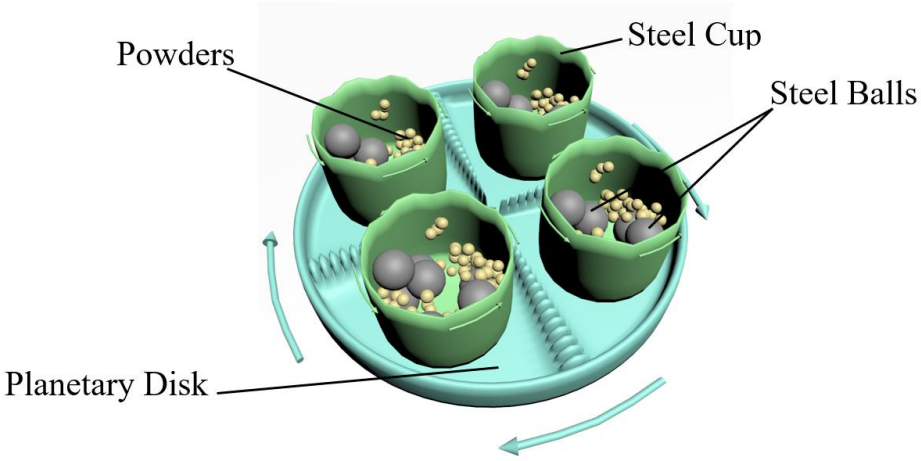

Figure 3. Schematic diagram of mechanical alloying for the production of an Al-B-Si alloy

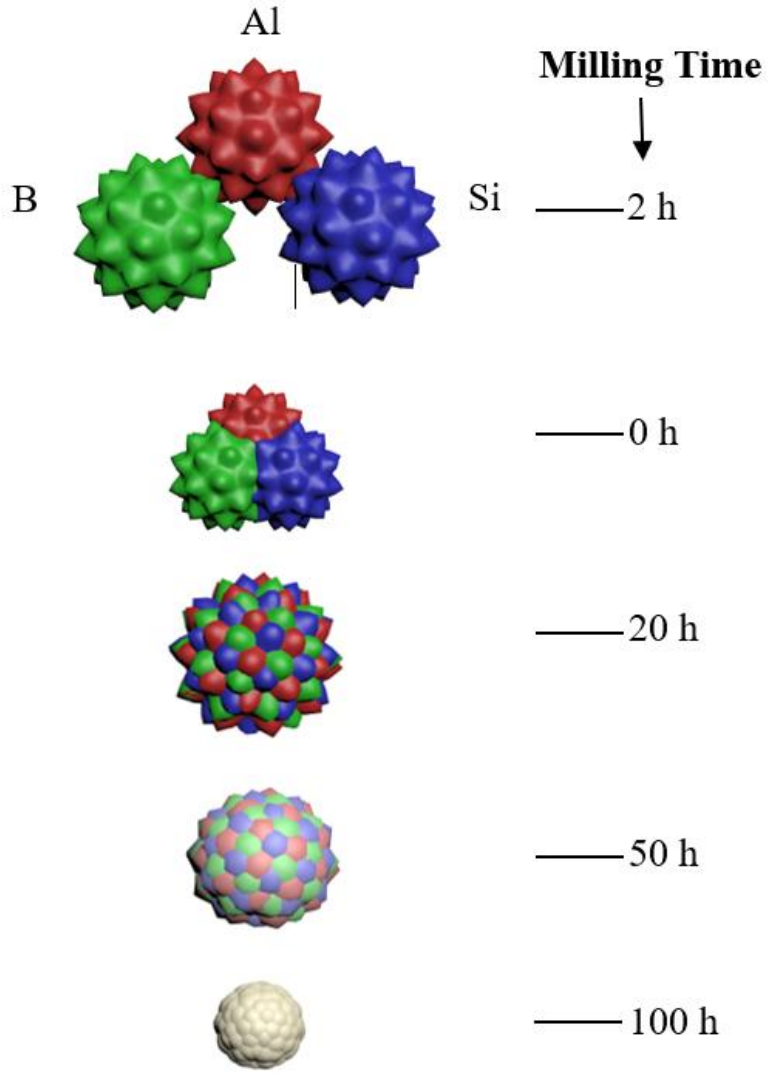

Figure 4. Schematic diagram of the microstructure evolution for Al, B, and Si powders during MA process

It is well known that the homogeneousness of the materials is very substantial for applications. The materials used effectively in industry have to be produced with high homogeneity. Therefore, the compositional homogeneity of the $Al_{50}B_{45}Si_5$ alloy was evaluated using field scanning with EDX. Figure 5 presents the EDX result of the alloy. According to Figure 5 and the table inset, the homogeneity of the alloy is so high that it is very close to the initially intended alloy composition rates.

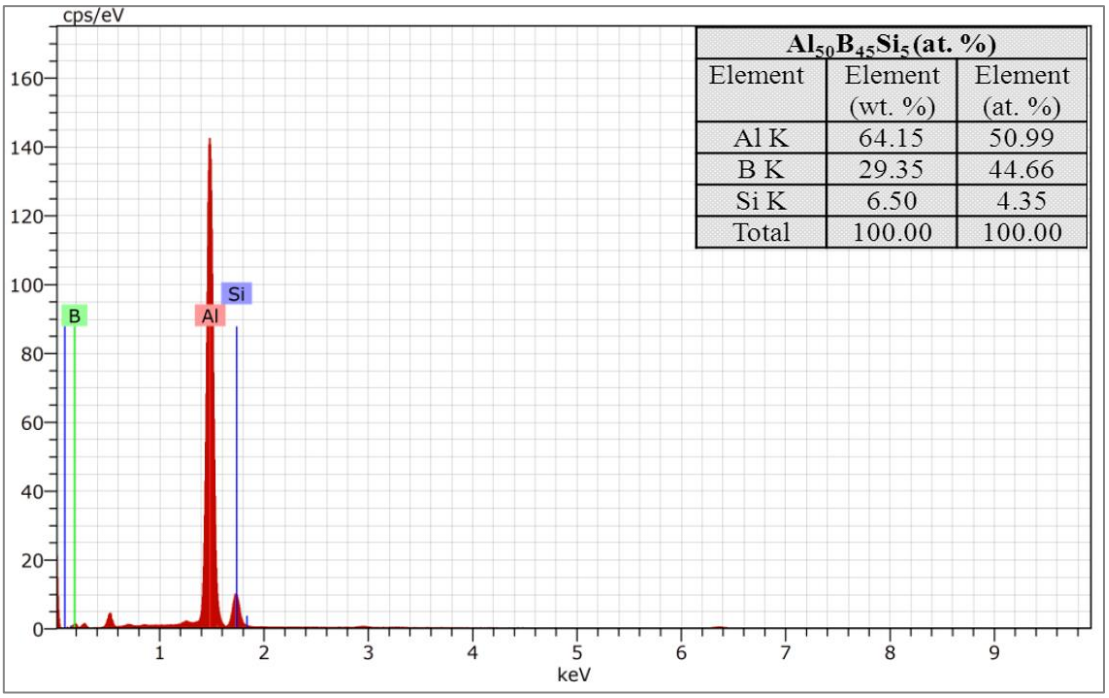

Figure 5. EDX analysis of the $Al_{50}B_{45}Si_5$ powders

3.2. Crystallite Size Evaluations

Figure 6 shows the crystallite size of the $Al_{50}B_{45}Si_5$ alloy during MA. As seen in Figure 6, the crystallite size, which was calculated by Debye Scherrer using XRD data, of the powders decreased by increasing milling time [20, 21]. Accordingly, the crystallite size of the alloy was calculated to be 35.8 ± 3 nm, 30.5 ± 2.5 nm, 15.4 ± 2.6 nm, and 10.2 ± 1.8 nm, respectively, after 5h, 10h, 20h, and 50h of milling time. However, the average crystallite size of the powder alloy was determined to be ~9.5 ± 0.8 nm for the final product, after 100 h of milling time. The changes in the crystallite sizes of the Al50B45Si5 alloy by increasing milling time are also listed in Table 1.

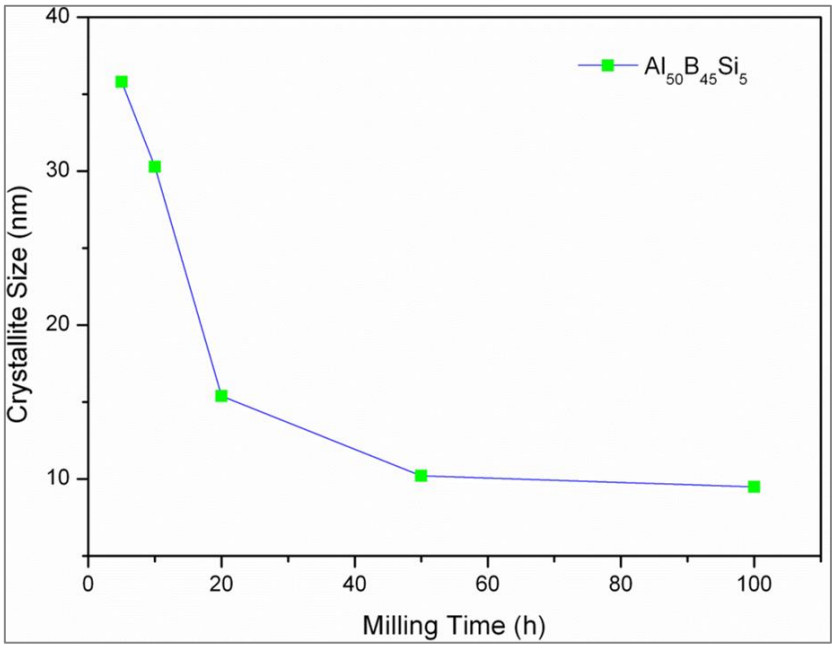

Figure 6. Crystallite size of $Al_{50}B_{45}Si_5$ powders as a function of milling time

Table 1. Crystallite size changes during mechanical alloying

Mechanical Alloying (hour)	Crystallite Size(nm)
	$Al_{50}B_{45}Si_5$
5	35.8 ± 3
10	30.3 ± 2.5
20	15.4 ± 2.6
50	10.2 ± 1.8
100	9.5 ± 0.8

The crystallite size of the $Al_{50}B_{45}Si_5$ alloy was observed by TEM to confirm the crystallite size obtained by the Debye Scherrer equation using XRD data, as well. Figure 7 shows the bright field TEM micrograph of $Al_{50}B_{45}Si_5$ alloy after 100 h of milling time. From the TEM micrograph, it can be seen clearly that the crystallite size of the powder alloy is approximately 10 nm. This result reveals two conclusions; one of them is the crystallite size of the powder alloy, confirmed by observing with TEM analysis. The other one is the good agreement between the determination of crystallite size by using XRD data and TEM observation. This agreement is also shown in previous works [10, 22].

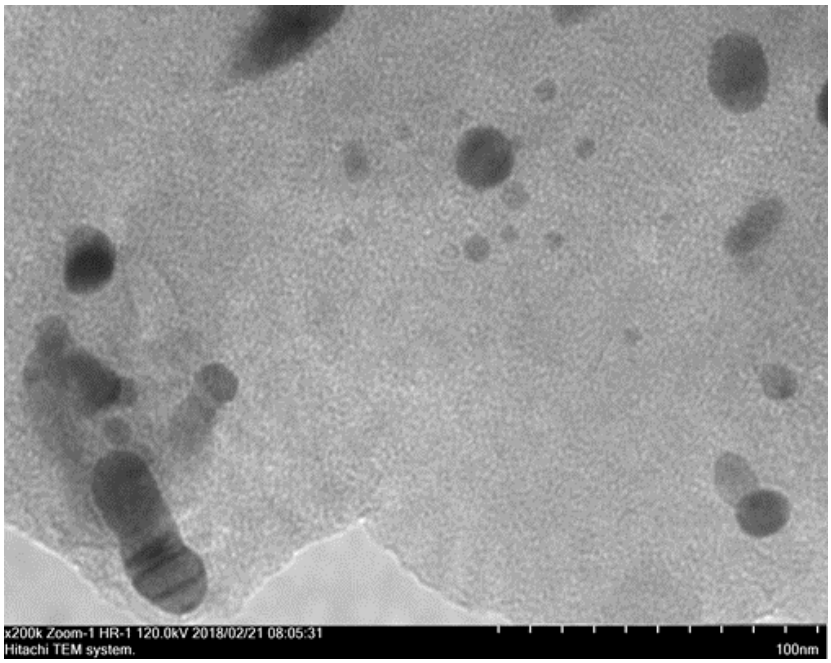

Figure 7. Bright field TEM micrograph of nanocrystalline $Al_{50}B_{45}Si_5$ alloy after 100 h of milling time

3.3. Thermal Analysis

Thermal behaviors of the nanocrystalline $Al_{50}B_{45}Si_5$ alloy were investigated by DSC and DTA throughout continuous heating at a heating rate of 20 ℃/minutes. Figure 8 shows the DSC curves of the $Al_{50}B_{45}Si_5$ alloy. As seen from Figure 8, an endothermic peak at 660 ℃ belonging to the melting temperature of Al appeared for unmilled powders (0h of milling). After 10h of milling time, a new endothermic peak in the vicinity of 575 - 600 ℃ was observed, as well as at 660 ℃. This peak belongs to the invariant eutectic temperature in the Al-Si binary phase diagram, inferring that some amount of Si got dissolved substitutionally in Al, resulting in α-Al(Si) solid solution. A similar thermal behavior was also observed for powders subjected to 20 h of milling. Any exothermic or endothermic peaks didn't appear from DSC traces of the $Al_{50}B_{45}Si_5$ alloy after 50 h and 100 h of milling time. This is because the new phases, such as AlB2, B4Si, and AlB12, identified by XRD diffraction have a higher melting point than 700 ℃.

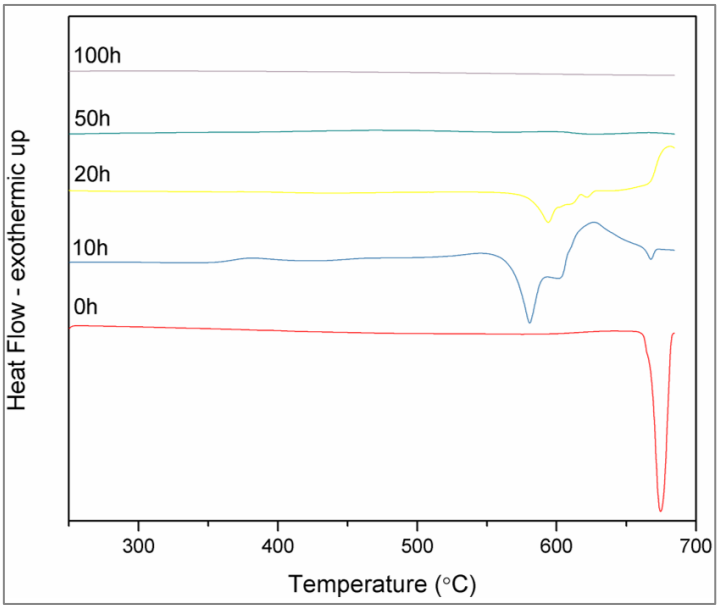

Figure 8. DSC traces of nanocrystalline $Al_{50}B_{45}Si_5$ powders

To further characterize the thermal behavior of the nanocrystalline $Al_{50}B_{45}Si_5$ powder, DTA analysis was performed from 200 ℃ to 1100 ℃. Figure 9 exhibits DTA traces of $Al_{50}B_{45}Si_5$ alloy. According to Figure 9, the DTA trace of unmilled powder exhibited only one endothermic peak at 660 ℃, which is the melting point of Al. The DTA trace of the powder after 50 h of milling time showed an exothermic peak and two endothermic peaks. The endothermic peaks at 890 ℃ and 945 ℃ belong to the AlB_2 phase [23, 24]. This phase was also observed in the XRD results of the powder alloy for 50 h of milling time in Figure 1. AlB_2 phase was also determined in previous works; thus, this result is in accordance with both XRD results of $Al_{50}B_{45}Si_5$ alloy and literature [23-25]. The final stage of $Al_{50}B_{45}Si_5$ powders, after 100 h milling time, the DTA trace exhibited two exothermic peaks at 650 ℃ and 950 ℃. When these peaks are evaluated with XRD patterns at 100h of milling of the powders, it can be concluded that the exothermic peaks belong to B_4Si or AlB_{12}.

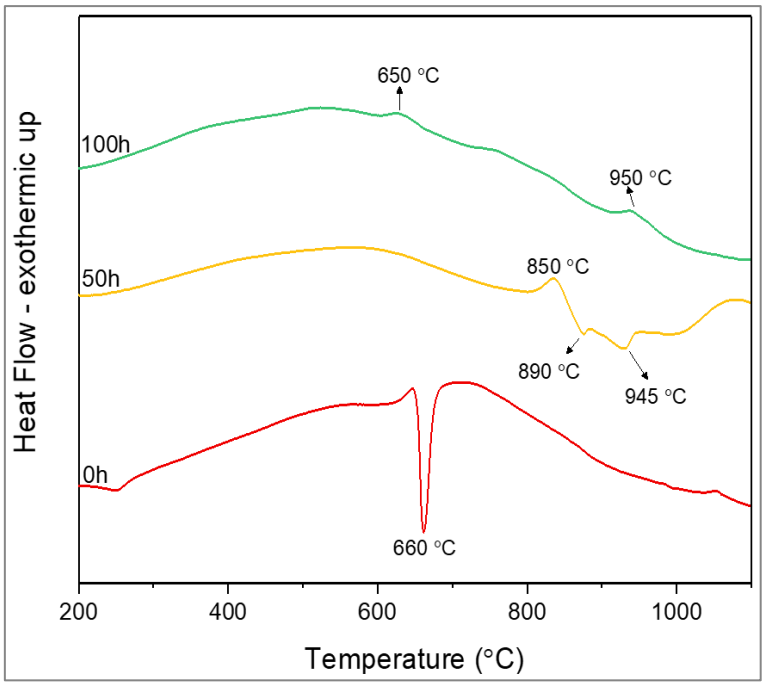

Figure 9. DTA traces of nanocrystalline $Al_{50}B_{45}Si_5$ powders

3.4. Microhardness Evaluation

The mechanically alloyed $Al_{50}B_{45}Si_5$ powders were characterized by Vickers HV measurements. Vickers from 3.1 was used to calculate the microhardness of the powder alloy.

$$HV = \frac{2P\,sin(\theta/2)}{d^2} = \frac{1.8544(P)}{d^2} \tag{3.1}$$

where P: the indentation force, d: the diagonal length, 1.854: geometrical factor for the diamond pyramid [26].

Figure 10 demonstrates the microhardness values of the alloy for the final product (100h of milling time) as a function of heat. From Figure 10, it can be obviously understood that the microhardness values increase with increasing heating. Therefore, the microhardness of the mechanically alloyed $Al_{50}B_{45}Si_5$ powders was measured as 219 ±10 HV at 25 ˚C, 225±8 HV at 500 ˚C, 295±7 HV at 800 ˚C, and 345±9 HV at 1000 ˚C. These results revealed two significant changes compared with the microhardness of pure Al element. One of them is related to the microhardness of the Al element, which is 40.2 HV [27] at room temperature; after 100 h of milling time, the microhardness of nanocrystalline $Al_{50}B_{45}Si_5$ alloy was calculated to be 219 ±10 HV. Thus, this value is ~5.5 times more than pure Al. On the other hand, after annealing at 1000 ˚C, the microhardness value of the $Al_{50}B_{45}Si_5$ alloy increased from 219 ±10 HV to 345±9 HV, which is ~8.6 times more than Al, as the second significant change. Therefore, the mechanical properties of the $Al_{50}B_{45}Si_5$ alloy were improved in a nanocrystalline form by using the MA technique. Moreover, it is possible to mention that the other reason for this improvement is the obtaining of the new phases, B4Si and AlB12, as well as production in a nanocrystalline form, and the annealing process of the powder alloy. These results revealed that the mechanical properties of nanocrystalline Al-based alloy were much better than well-known crystalline Al element whose atoms are arranged in a highly ordered structure. After annealing processes of $Al_{50}B_{45}Si_5$ alloy, an increase in its microhardness values also revealed that the annealing process of the alloys is very important to improve their mechanical features. Besides, the microhardness value (345±9 HV) of the $Al_{50}B_{45}Si_5$ alloy is also so high compared to previously Al-based alloys which are reported 56.1 HV for Al-3wt%SiC [25], 146.89 HV for $Al_{64}Cu_{24}Fe_{12}$ alloy [28], 142 HV for Al−6Si−6Cu−0.3Mg alloy [29], 165.04 HV for Al-4.6Zn-1.2Mg alloy [30] and 260 HV for Al–22.5Mg–23.5Zn alloy [31] in literature.

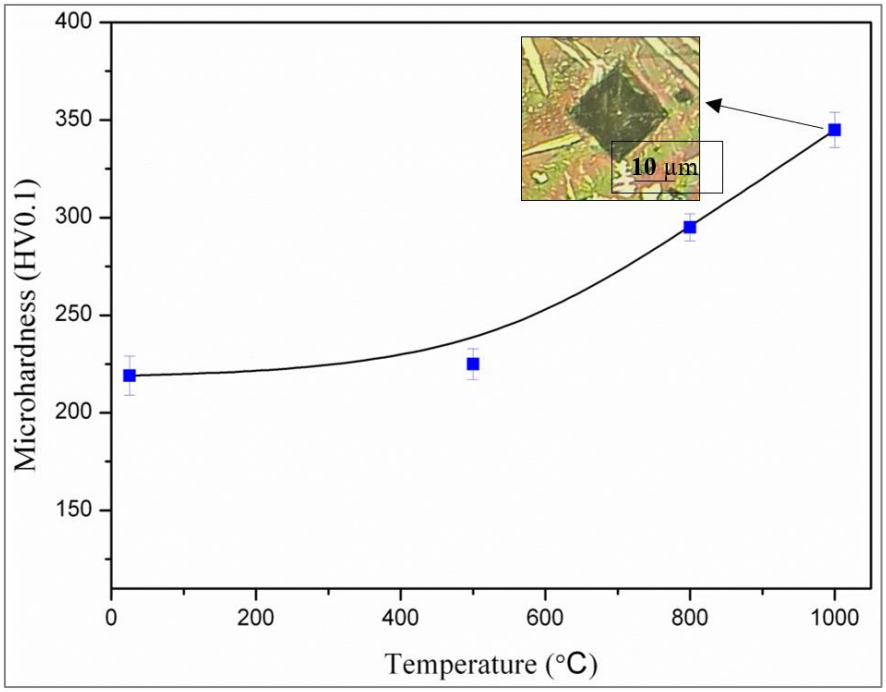

Figure 10. Microhardness changes of the ball-milled $Al_{50}B_{45}Si_5$ powder (100 h) as a function of heating. The inset: OM image of a microhardness indent mark on the alloy

4. Conclusion

In this study, the $Al_{50}B_{45}Si_5$ alloy was successfully manufactured from elemental powders by mechanical alloying for several stages of time from 0 h to 100 h. The microstructural evaluation, thermal behavior, mechanical properties, and crystallite size of the powder alloy were examined by several analysis techniques. The following conclusions are drawn:

- The microstructure of the powder alloy changed during mechanical alloying. Because of this change, four intermetallic phases, such as AlB2, B4Si, AlB12, and Al (Si), were obtained after 100 h of milling time.
- The homogeneity of the $Al_{50}B_{45}Si_5$ alloy increased with increasing milling time. Therefore, it was detected that each constituent of the alloy was homogeneously distributed.
- The crystallite size of the alloy reduced throughout MA. The lowest crystallite size value was determined to be 9.5 nm for the final powder. This value was confirmed by TEM.
- From the thermal analysis of the $Al_{50}B_{45}Si_5$ alloy, endothermic and ectothermic peaks were observed. It was determined that these peaks belonged to the new phases obtained during mechanical alloying.
- The microhardness values of the $Al_{50}B_{45}Si_5$ alloy increased with increasing heating. Thus, microhardness values of the alloy were measured in the range of 219 – 345 HV.

In future work, the composition ratio and components of the alloy can be changed properly to improve its properties by considering the usable area. This also gives an opportunity to compare this work with other studies in the literature.

Author Contributions

The author read and approved the final version of the paper.

Conflict of Interest

The author declares no conflict of interest.

Ethical Review and Approval

No approval from the Board of Ethics is required.

Acknowledgment

I greatly appreciate the financial support from Kahramanmaras Sutcu Imam University. I would like to thank F. S. Uludag for assistance to draw certain figures.

References

[1] T. Xu, D. Zuo, G. Zhang, *Modeling of anisotropic fracture forming limit strain for high-strength aluminum alloys in sheet metal forming*, Materials Today Communications 47 (2025) 113012.

[2] J. Min, F. Xie, Y. Liu, Z. Hou, J. Lu, J. Lin, *Experimental study on cold forming process of 7075 aluminum alloy in W temper*, CIRP Journal of Manufacturing Science and Technology 37 (2022) 11–18.

[3] L. Pezzato, M. Dabala, K. Brunelli, *Microstructure and corrosion properties of PEO coatings produced on AM-aluminum alloys*, Key Engineering Materials 813 (2019) 298–303.

[4] A. Mahabubadsha, K. Anandavelu, *Exploring the impact of AGG on the strength of AA2014 aluminium alloy FSW joints*, Emerging Materials Research 14 (2) (2025) 190–197.

[5] Zulfadhli, A. Akhyar, N. Ali, Arhami, M. R. Pahlevi, *Variations in casting temperatures effect of re-melted 6061 aluminum alloy on tensile strength*, Results in Materials 26 (2025) 100691.

[6] Y. Sun, *In-fire material properties of wire-arc additively manufactured 3D-printed structural aluminum alloys*, Construction and Building Materials 474 (2025) 140946.

[7] A. D. Iams, J.S. Wweaver, B.M. Lane, L.A. Giannuzzi, F. Yi, D.L. LaPlant, J.H. Martin, F. Zhang, *Microstructural features and metastable phase formation in a high-strength aluminum alloy fabricated using additive manufacturing*, Journal of Alloys and Compounds 1025 (2025) 180281.

[8] S. Çağlar, *Impact of B4C reinforcement on the microstructure, wear, hardness, corrosion behavior, and radiation shielding properties of Al-40Sm2O3 hybrid composites*, Nuclear Engineering and Technology 57 (8) (2025) 103566.

[9] C. Kursun, M. Gogebakan, C*haracterization of nanostructured Mg–Cu–Ni powders prepared by mechanical alloying*, Journal of Alloys and Compounds 619 (2015) 138–144.

[10] Y. K. Yadav, M. A. Shaz, N. K. Mukhopadhyay, T. P. Yadav, *High entropy alloys synthesized by mechanical alloying: A review*, Journal of Alloys and Metallurgical Systems 9 (2025) 100170.

[11] J.G. Jung, S.-H. Lee, J.-M. Lee, Y.-H. Cho, S.-H. Kim, W.H. Yoon, *Improved mechanical properties of near-eutectic Al-Si piston alloy through ultrasonic melt treatment*, Materials Science and Engineering: A 669 (2016) 187–195.

[12] F. Czerwinski, *Thermal stability of aluminum–cerium binary alloys containing the Al–$Al_{11}Ce_3$ eutectic*, Materials Science & Engineering A 809 (2021) 140973.

[13] Z. Chen, H. Kang, G. Fan, J. Li, Y. Lu, J. Jie, Y. Zhang, T. Li, X. Jian, T. Wang, *Grain refinement of hypoeutectic Al-Si alloys with B*, Acta Materialia 120 (2016) 168–178.

[14] Y. Birol, *A novel Al–Ti–B alloy for grain refining Al–Si foundry alloys*, Journal of Alloys and Compounds 486 (1-2) (2009) 219–222.

[15] V. Vilamosa, A.H. Clausen, T. Børvik, S.R. Skjervold, O.S. Hopperstad, *Behaviour of Al-Mg-Si alloys at a wide range of temperatures and strain rates*, International Journal of Impact Engineering 86 (2015) 223–239.

[16] M. Cheminguia, M. Khitouni, G. Mesmacque, A.W. Kolsi, *Effect of heat treatment on plasticity of Al-Zn-Mg alloy: Microstructure evolution and mechanical properties*, Physics Procedia 2 (3) (2009) 1167–1174.

[17] K.B. Gerasimov, V.V. Boldyrev, *On mechanism of new phases formation during mechanical alloying of Ag-Cu, Al-Ge and Fe-Sn systems*, Materials Research Bulletin 31 (10) (1996) 1297–1305.

[18] J. Wang, *Mechanical alloying of amorphous Al–SiO_2 powders*, Journal of Alloys and Compounds 456 (1-2) (2008) 139–142.

[19] Y.C. Kim, J.C. Lee, P.R. Cha, J.P. Ahn, E. Fleury, *Enhance glass forming ability and mechanical properties of new Cu-based bulk metallic glasses*, Materials Science and Engineering: A 437 (2) (2006) 248–253.

[20] N. Badar, H. M. Yusoff, K. Elong, N. Kamarulzaman, *Crystallite size reduction of Cr doped Al_2O_3 materials via optimized high-energy ball milling method*, Advanced Powder Technology 34 (8) (2023) 104102.

[21] C. Kursun, M. Gogebakan and H. Eskalen, *Mechanical properties, microstructural and thermal evolution of $Mg_{65}Ni_{20}Y_{15-x}Si_x$ (X=1,2,3) alloys by mechanical alloying*, Materials Research Express 5 (3) (2018) 036512.

[22] C. Kursun, M. Gogebakan, E. Uludag, M. S. Bozgeyik and F. S. Uludag, *Structural, electrical and magnetic properties of Nd – A – CoO_3 (A = Sr, Ca) Perovskite Powders by Mechanical Alloying*, Scientific Reports 8 (1) (2018) 13083.

[23] E. J. Felten, *The preparation of aluminum diboride, AlB_2[1]*, Journal of the American Chemical Society 78 (23) (1956) 5977–5978.

[24] J. Fjellstedt, and A.E.W. Jarfors, *Experimental and theoretical study of the Al-rich corner in the ternary Al-Ti-B system and reassessment of the Al-rich side of the binary Al-B phase diagram*, International Journal of Materials Research 92 (6) (2001) 563–571.

[25] O.N. Carlson, *The Al-B (Aluminum-Boron) system*, Bulletin of Alloy Phase Diagrams 11 (1990) 560–566.

[26] C. Kursun, M. Gogebakan, *Structure and mechanical behaviour of Cu-Zr-Ni-Al amorphous alloys produced by rapid solidification*, in: B. Movahedi (Ed.), Metallic Glasses - Formation and Properties, InTechOpen, London, 2016, Ch. 5, pp. 97–108.

[27] X. Zeng, W. Liu, B. Xu, G. Shu, Q. Li, *Microstructure and Mechanical Properties of Al–SiC Nanocomposites Synthesized by Surface-Modified Aluminium Powder*, Metals 8 (4) (2018) 253.

[28] Y.F. Wang, H. Hou, Y.H. Zhao, J.Z. Tian, *Microstructure and mechanical properties of an Al-Si alloy reinforced by $Al_{64}Cu_{24}Fe_{12}$ quasi-crystalline particles*, Materialwissenschaft und Werkstofftechnik 49 (2) (2018) 225–234.

[29] M. S. Salleh, M. Z. Omar, *Influence of Cu content on microstructure and mechanical properties of thixoformed Al−Si−Cu−Mg alloys*, Transactions of Nonferrous Metals Society of China 25 (2015) 3523−3538.

[30] M. Chemingui, M. Khitouni, G. Mesmacque, A.W. Kolsi, *Effect of heat treatment on plasticity of Al-Zn-Mg alloy: Microstructure evolution and mechanical properties*, Physics Procedia 2 (3) (2009) 1167–1174.

[31] N. Takata, T. Okano, A. Suzuki, M. Kobashi, *Microstructure of intermetallic-reinforced Al-Based alloy composites fabricated using eutectic reactions in Al–Mg–Zn ternary system*, Intermetallics 95 (2018) 48–58.